The influence of morphology, AGN and environment on the quenching histories of galaxies

Rebecca Jane Smethurst

Pembroke College

University of Oxford

A thesis submitted for the degree of

Doctor of Philosophy

Michaelmas 2016

Oy with the poodles already!

Acknowledgements

Thank ALLL TEH people. Including, for inspiration and the help with perseverance: T. Swift, B. Springsteen, C. Martin et al., Dr M. Grey, L. Gilmore, R. Gilmore, A. Haim et al., E. Sheeran,

Abstract

GZ shit happens.

Contents

List of Figures

Chapter 1

Introduction

Understanding the physical processes which shaped our Universe is the fundamental goal of all fields in Astrophysics. A successful theory of the Universe must describe how it evolved from the primordial soup of matter present just after the Big Bang to the multitude of galaxy properties we see today.

The most widely accepted cosmological model is the Λ-CDM (Λ- cold dark matter) model which describes a flat Universe made of only $\sim 5\%$ baryonic ("normal") matter, $\sim 26\%$ cold dark matter and $\sim 69\%$ dark energy (Planck Collaboration, 2016). In such a Universe, tiny quantum fluctuations in the early Universe grow with time, becoming overdense and laying the foundations for galaxy formation (Guth & Pi, 1982; Hawking, 1982; Linde, 1982; Starobinsky, 1982). Given the relatively small fraction of baryonic matter in the Universe, its gravitational contribution to this process is often neglected, greatly simplifying the problem. Structure in simulations is then observed to form hierarchically (Press & Schechter, 1974; Gott & Rees, 1975; White & Rees, 1978; Aarseth et al., 1979; Gott et al., 1979; Turner et al., 1979; Efstathiou & Eastwood, 1981; Davis et al., 1985). At the overdense regions in the early Universe, matter collapses dissipationally under its own gravity forming a dark matter 'halo', which then grows through smooth accretion and mergers of other halos to produce the large scale structure of galaxy filaments, clusters and voids we observe today (see comprehensive review by Frenk & White, 2012).

Adding in localised baryonic physics into this picture however, complicates matters. Galaxies are, unfortunately, not just simple smooth dark matter halos; they are

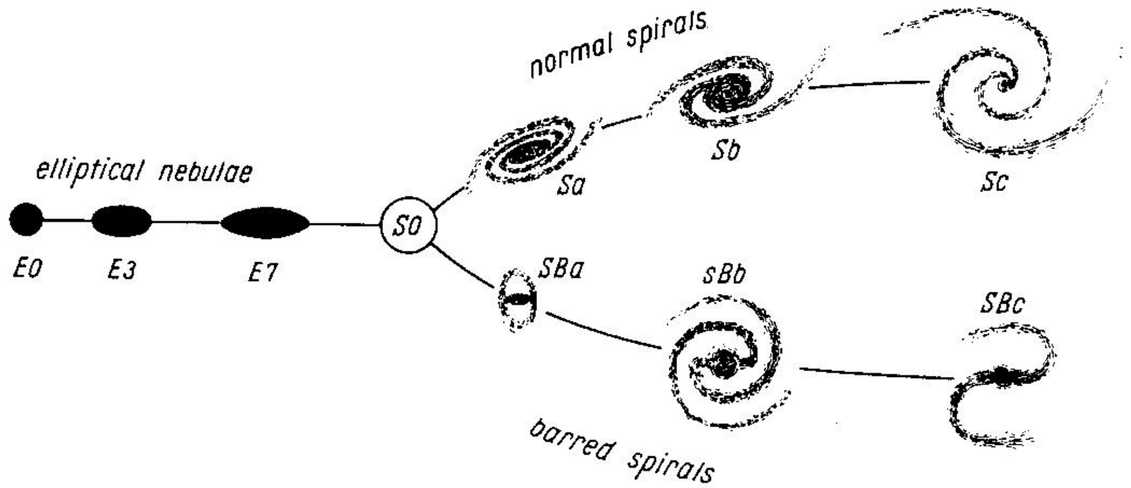

Figure 1.1: The Hubble sequence of galaxy morphology shown on his famous 'tuning fork diagram' as published in Hubble (1936).

thought to start life when baryons cool and condense at the centre of a dark matter halo. Further accretion of matter will cause a gravitational collapse (if angular momentum is present as a result of tidal torques then a rotating gas disc will form Fall & Efstathiou, 1980; Barnes & Efstathiou, 1987), and stars will form as hydrogen gas cools and coalesces. From this moment a galaxy will evolve, its shape changing depending on its encounters (or lack thereof) with other galaxies.

Today we observe galaxies of a multitude of shapes, or morphologies, across all redshift ranges. Hubble (1936) classified galaxies based on their shape, producing the widely adopted 'tuning fork diagram', now known as the Hubble sequence and shown in Figure 1.1. Hubble noticed that galaxies could by broadly categorised as either elliptical in shape or as a disc with spiral arms and/or barred structures. He referred to these categories as early-types (placed to the left of his diagram, in keeping with time axis conventions) and late types respectively, as he thought that as galaxies evolved they developed spiral structure. However, as discussed above, cosmological studies have concluded that galaxies start life as a rotating gas disc and so instead, Hubble's diagram is often read from right to left (with some debate over the placement of the S0 galaxies in this picture; Kormendy & Bender, 1996). Connecting this picture of pure gas disc galaxies in their infancy with the plethora of galaxy structures we see today, is the focus of this thesis.

However, the structure alone is not enough to describe a galaxy's evolution. The magnitude (used as a proxy for stellar mass), star formation rate (SFR), metallicity

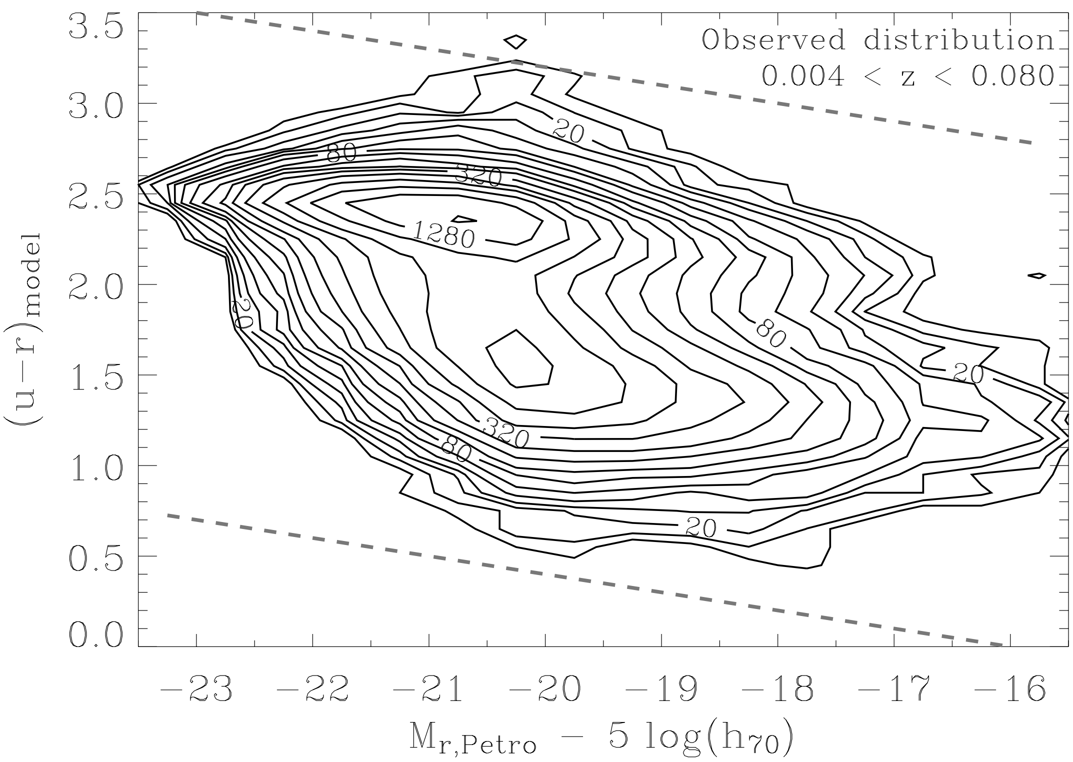

Figure 1.2: The galaxy colour magnitude diagram as observed by Baldry et al. (2004). The figure has been adapted from Figure 1 in Baldry et al. and annotated to show the locations of the red sequence and blue cloud. A lower magnitude corresponds to a higher mass and a large $u - r$ value corresponds to a redder colour.

(Z) and environment are all crucial to describing a galaxy's current state. By studying these galaxy properties, insight into the processes which govern galaxy evolution can be gained.

Large scale surveys of galaxies have first revealed a bimodality in the optical colour-magnitude diagram (CMD) of galaxies finding two distinct populations (see Figure 1.2); one at relatively low mass, with blue optical colours and another at relatively high mass, with red optical colours (Baldry et al., 2004, 2006; Willmer et al., 2006; Ball et al., 2008; Brammer et al., 2009). These populations were dubbed the 'blue cloud' and 'red sequence' respectively (Chester & Roberts, 1964; Bower et al., 1992; Bell et al., 2004; Driver et al., 2006; Faber et al., 2007). The sparsely populated colour space between these two populations was dubbed the 'green valley'.

The majority of disc galaxies were found in the blue cloud and the majority of ellipticals on the red sequence, with colour often used as a proxy for morphology. The Galaxy Zoo project (Lintott et al., 2008, 2011), which produced morphological classifications for a million galaxies, helped to confirm that this colour bimodality is not entirely morphology driven (Strateva et al., 2001; Salim et al., 2007; Schawinski et al., 2007a; Constantin et al., 2008; Bamford et al., 2009; Skibba et al., 2009), detecting larger numbers of spiral galaxies in the red sequence (Masters et al., 2010a) and elliptical galaxies in the blue cloud (Schawinski et al., 2009) than had previously been observed.

Second, large galaxy surveys revealed that star forming galaxies are also observed to lie on a well defined 'star forming sequence' (SFS) in the stellar mass vs. star formation rate (SFR) plane (Brinchmann et al., 2004; Salim et al., 2007; Daddi et al., 2007). The majority of blue cloud galaxies are found to lie on this SFS with the majority of the red sequence lying well below it with very low SFRs. The intermediate colours of the green valley have therefore been interpreted as evidence of recent suppression of star formation (SF; Salim et al., 2007). This suppression of SF and subsequent transition of a galaxy from blue cloud to red sequence must therefore also be intrinsically tied with a possible change in morphology from a disc galaxy to an elliptical galaxy.

The discovery of the fundamental plane (Dressler et al., 1987; Djorgovski & Davis, 1987), wherein the stellar velocity dispersion is correlated with the luminosity and effective radius of an elliptical, further constrained the mechanisms responsible for galaxy formation. The fundamental plane can be reproduced in simulations of major mergers (Bekki, 1998; Nipoti et al., 2003; Boylan-Kolchin et al., 2005; Robertson et al., 2006; Hilz et al., 2012; Taranu et al., 2015), lending support to the theory of hierarchical structure formation through mergers of dark matter halos.

Similarly, galaxies are often found huddled together in groups (Zwicky, 1938, 1952; Abell, 1958), all sharing one large dark matter halo (groups with 100 or more galaxies are referred to as clusters Bower & Balogh 2004). Conversely some galaxies are found isolated from others in less dense environments (often referred to as the field), either because they are fossil groups (where all members have eventually merged Ponman et al., 1994; Jones et al., 2000, 2003) or have truly been isolated for their entire lifetimes. This environmental density is found to be correlated not only with morphology (Dressler, 1980; Smail et al., 1997; Poggianti et al., 1999; Postman et al.,

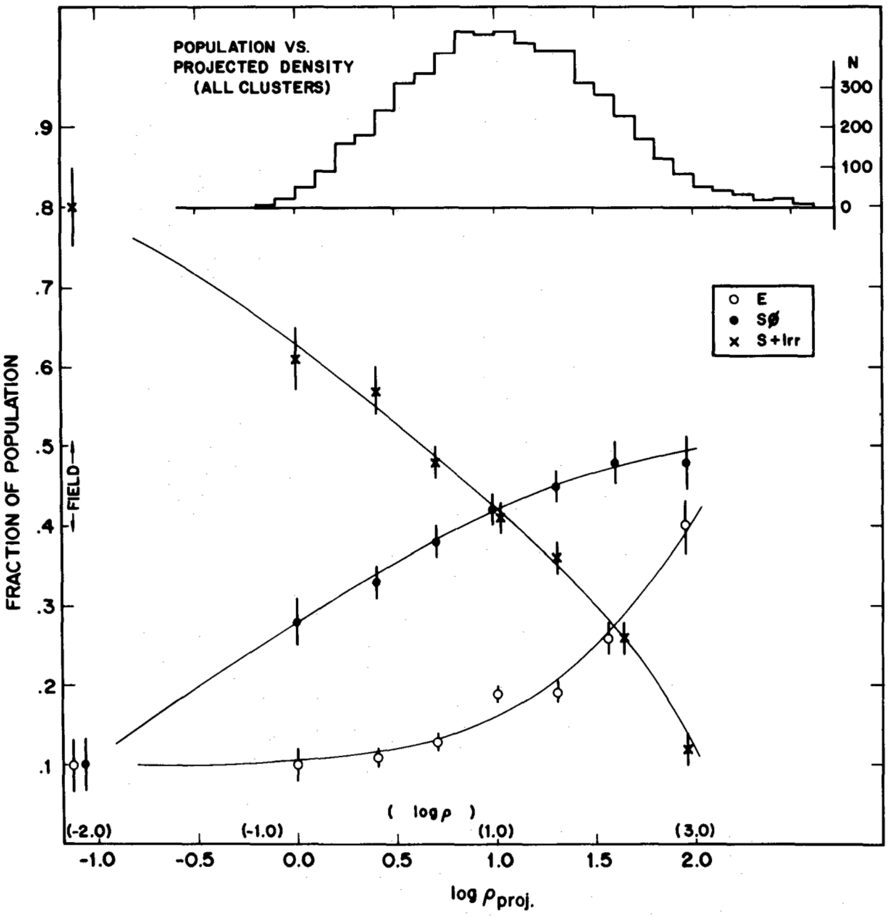

Figure 1.3: The morphology-density relation from Figure 4 of Dressler (1980) showing how the fraction of ellipticals (E) increases with increasing environmental density and the fraction of spirals (S + Irr) decreases.

2005; Bamford et al., 2009, and see Figure 1.3), but also colour (Butcher & Oemler, 1978; Pimbblet et al., 2002), quenched galaxy fraction (Kauffmann et al., 2003b; Baldry et al., 2006; Peng et al., 2012; Darvish et al., 2016) and SFR (Gómez et al., 2003) suggesting that the environment may drive this transition from blue cloud to red sequence due to the nature of hierarchical structure formation.

However, within this framework of hierarchical structure formation, the observed mass-metallicity relation (Tremonti et al., 2004) cannot be reproduced. This relationship describes how higher mass galaxies have higher metal contents. Simulations have shown that this phenomenon cannot be reproduced by the merging of galaxies alone, since mergers dilute the metallicity (Pipino & Matteucci, 2008; Rupke et al., 2010; Montuori et al., 2010; Torrey et al., 2012). This is also supported by observations showing that metallicities in galaxy pairs are suppressed by ~ 0.05 dex (Ellison et al., 2008; Michel-Dansac et al., 2008; Scudder et al., 2012). There must therefore be processes other than mergers occurring which are responsible for the colours, SFRs, masses, metallicities and morphologies of galaxies observed.

Further insight has also recently been revealed by the number of integral field unit (IFU) surveys which have come online in the past couple of years. These include the completed ATLAS^{3D} survey (Cappellari et al., 2011), which targeted a small sample of 260 early-type galaxies, and the larger, ongoing surveys of MaNGA (Bundy et al., 2015), SAMI (Croom et al., 2012) and CALIFA (Sánchez et al., 2012). Upon completion at the end of the decade, these surveys are expected to revolutionise the field of galaxy evolution, providing spatially resolved maps of the SFR in over $10,000$ galaxies.

Until that time, by studying galaxies which have just left the SFS sequence, the mechanisms governing galaxy evolution, including both the suppression of SF and the possible transformation of galaxy structure, can be revealed. Green valley galaxies have long been thought of as the 'crossroads' of galaxy evolution, a transition population between the two main galactic stages of the star forming blue cloud and the 'dead' red sequence. Bell et al. (2004) were the first to recognise that green valley galaxies may be a transitional population between the blue cloud and red sequence. Wyder et al. (2007) confirmed that galaxy bimodality also appears in NUV-optical colour space, with Schiminovich et al. (2007) investigating the morphological dependence in this parameter space and Martin et al. (2007) using it to constrain the flux of galaxies transitioning through the green valley. Faber et al. (2007) suggested that the build up of the red sequence has to occur via a mixture of suppression of star formation of galaxies in the blue cloud and mergers on the red sequence, which was confirmed by Mendez et al. (2011) who showed that mergers alone are not responsible for the transition from the blue cloud. This transition was theorised to occur on rapid timescales, otherwise there would be an accumulation of galaxies residing in the green valley (Gonçalves et al., 2012); however Schawinski et al. (2014) concluded that this was only true for elliptical galaxies, with disc galaxies transitioning much more slowly. The morphological dependence and causes of this transition are therefore still the cause of much debate.

I will refer to the suppression of a galaxy's SFR as *quenching* and processes which can cause this suppression as *quenching mechanisms.*

1.1 Possible quenching mechanisms

There are many theorised mechanisms which can cause quenching. They are often referred to as either *internal* mechanisms (caused by the galaxy's *nature*) or *external* mechanisms (caused by the way the galaxy is *nurtured*). The properties of a galaxy and its environment are often thought to control which mechanisms will affect a galaxy throughout its lifetime and subsequently affect the morphology.

1.1.1 Internal Quenching Mechanisms

1.1.1.1 AGN feedback as a quenching mechanism

An active galactic nucleus (AGN) is an actively growing supermassive black hole in the centre of a galaxy. There are many observed spectral classes of AGN which are explained by the viewing angle in the theory of unification (see review by Netzer, 2015). The basic structure of an AGN is an accretion disc of cold material which is formed around the black hole. The friction built up by the rotating gas causes the accretion disc to heat up and emit huge amounts of energy. The accretion disc is also surrounded by clouds of gas and an absorption region (often referred to as the torus) which can both re-emit and absorb the emitted light from the accretion disc (for a diagram depicting AGN structure see Beckmann & Shrader 2012). Type 2 Seyfert AGN are those which are viewed approximately edge on to their accretion disc and so have the majority of their emitted light absorbed by the torus. Some light is scattered off the surrounding gas clouds, resulting in the detection of broadened spectral emission lines. Type 1 Seyfert AGN however are those which are viewed perpendicular to their accretion disk and so are unobscured by the torus; light from both the accretion disc and/or emitted radiation jets can be observed.

There are tight correlations between properties of galaxies, such as the bulge mass, total stellar mass & stellar velocity dispersion, and the black hole mass (Magorrian et al., 1998; Marconi & Hunt, 2003; Häring & Rix, 2004). This implies a co-evolution between the black hole and its host galaxy therefore suggesting that changes in the SFR and structure of a galaxy could also be tied to black hole activity.

If we consider a 'back of the envelope' calculation of the ratio between the total energy of the black hole and the binding energy of the galaxy, we can determine if output from the black hole will be able to have a significant effect on its host galaxy (see p.649 of Mo et al., 2010). The total energy output by a black hole in its lifetime can be expressed as $E_{BH} = \bar{\epsilon} M_{BH} c^2$, where $\bar{\epsilon}$ is the mean efficiency of the black hole of mass M_{BH}. The galaxy binding energy can be approximated as $E_{gal} \approx M_* \sigma^2$, where M_* is the stellar mass of the galaxy with stellar velocity dispersion σ. Taking the average values of $M_{BH} \sim 10^{8.0}$ $\mathrm{M}_\odot$, $M_* \sim 10^{10.8}$ $\mathrm{M}_\odot$ and $\sigma \sim 200$ km s^{-1} of the 30 galaxies observed by Häring & Rix (2004), we can estimate the ratio $E_{BH}/E_{gal} \sim \bar{\epsilon} 10^3$. The energy of the black hole can therefore easily surpass the binding energy of its galaxy, suggesting that a black hole can indeed impact its host. This is thought to occur via AGN feedback where the output of energetic material and radiation from the black hole is theorised to either heat or expel gas needed for SF in a galaxy, causing a quench. Energy from a black hole is observed to be ejected in narrow, collimated jets of material out of the plane of a galaxy (see review by Homan, 2012), but for AGN feedback to be effective these jets would somehow need to impact the gas in the entire galaxy.

AGN feedback was first suggested as a mechanism for regulating star formation due to the results of simulations wherein galaxies could grow to unrealistic stellar masses (Silk & Rees, 1998; Bower et al., 2006; Croton et al., 2006; Somerville et al., 2008). Without a prescription for the effects of AGN feedback, the shape of the galaxy luminosity function could therefore not be matched at the high luminosity end (Baugh et al., 1998, 2005; Kauffmann et al., 1999a,b; Somerville et al., 2001; Kitzbichler & White, 2006). A similar problem was also encountered at the low end of the luminosity function, which was rectified by the inclusion of the effects of supernova wind feedback (Dekel & Silk, 1986; Powell et al., 2011). This is illustrated in Figure 1.4 taken from Silk & Mamon (2012).

Indirect observational evidence has now been found for both positive and negative feedback in various systems (see the comprehensive review from Fabian 2012). The strongest being the indirect evidence that the largest AGN fraction is found in the green valley (Cowie & Barger, 2008; Hickox et al., 2009; Schawinski et al., 2010), suggesting a link between AGN activity and the process which moves a galaxy from the blue cloud to the red sequence. However, concrete statistical evidence for the effect of AGN feedback on the host galaxy population has so far been elusive.

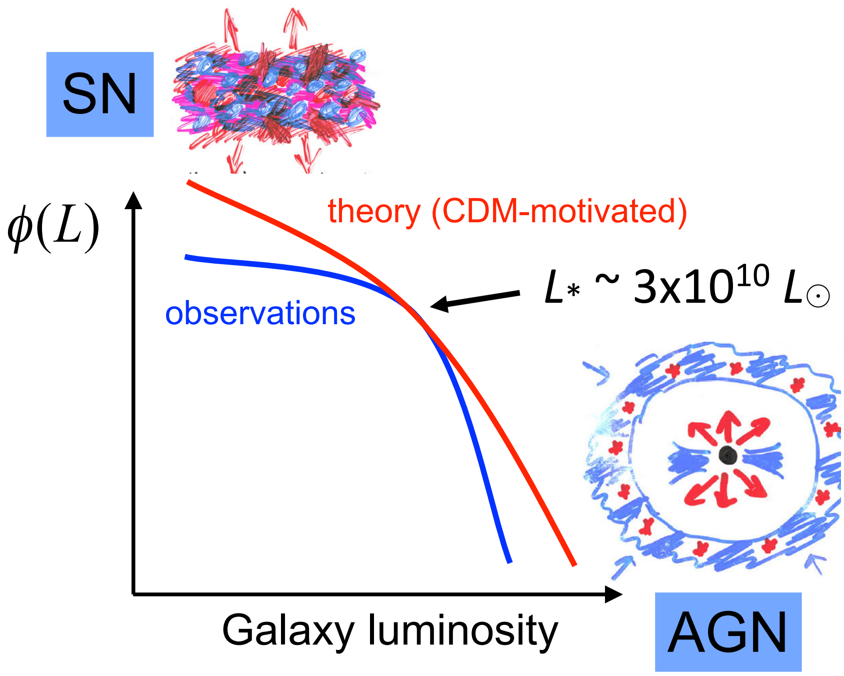

Figure 1.4: Cartoon of the role of feedback in modifying the observed luminosity function of galaxies with respect to theoretical predictions. Supernova winds are thought to be responsible at the low mass end, with AGN feedback responsible at the high mass end. Figure 1 in Silk & Mamon (2012).

1.1.1.2 Mass quenching

Mass quenching is defined by Peng et al. (2010, 2012) as any quenching mechanism which is independent of a galaxy's environment, but not of its mass. However, there is still much debate over the exact mechanism which is the cause of such a quench. Darvish et al. (2016) suggest that non-AGN driven feedbacks (for example supernova feedback) are responsible for the correlation observed between the mass quenching efficiency and SFR in Peng et al. (2010). However, Gabor & Davé (2015) suggest that this is driven by "halo quenching processes" whereby the inflow of cool gas from the galaxy halo is either cut off or hindered from cooling at $M_{halo} > 10^{12}$ M$_{\odot}$ (Birnboim & Dekel, 2003; Dekel & Birnboim, 2006). If this happens, a galaxy uses up the rest of its available gas for star formation via the Kennicutt-Schmidt law (Schmidt, 1959; Kennicutt, 1998) and consequently grows in mass.

In the rest of this thesis, I refer to mass quenching as a cut off of gas inflow, resulting in a gradual consumption of gas in star formation. This definition of mass quenching is thought to be a dominant mechanism for isolated galaxies in the field (Kormendy & Kennicutt, 2004). However, it is also thought that as a galaxy infalls in to a group or cluster over long timescales, gas reservoirs can also be depleted via a mass quenching process (Peng et al., 2012).

1.1.1.3 Morphological quenching

Morphological quenching (or 'secular' quenching, referring to slow, non-violent processes) is the process by which the internal structure of a galaxy can have a negative impact on its own SFR[1]. This is theorised to occur in galaxies hosting bars; the bar funnels gas to the centre of the galaxy (Athanassoula, 1992a) where gas is exhausted by star formation effectively quenching the galaxy (Zurita et al., 2004; Sheth et al., 2005). This process is thought to be responsible for large numbers of red spirals and supported by observations of increasing bar fraction with red colours (Masters et al., 2011).

This process is also theorised to be caused by bulges (Bluck et al., 2014) whereby the large gravitational potential of the bulge prevents the disc from collapsing and forming stars (Fang et al., 2013). Recent observational evidence from Hart et al. (2016) also suggests that spiral structure can also cause morphological quenching. Hart et al. propose that many armed spiral structures can trigger galaxy wide starbursts thereby rapidly using up gas for future star formation; similarly two armed spirals are observed with redder colours, suggesting that this spiral phase is much longer lived and may funnel gas into the centre of the galaxy to be exhausted in star formation over longer timescales.

1.1.2 External Quenching Mechanisms

1.1.2.1 Mergers as a quenching mechanism

Major mergers have been intrinsically linked to the formation of elliptical galaxies since Toomre & Toomre (1972) showed this was possible with a simulation of the merger of two equal mass disc galaxies. Since Λ-CDM relies on the idea of hierarchical

[1] Essentially shooting itself in the foot.

structure formation through the merger of dark matter halos for its description of galaxy formation, it also follows that galaxy evolution should be further influenced by mergers.

The hypothesis is as follows. When two galaxies merge, the influx of cold gas funnelled by the forces in the interaction often results in energetic starbursts (Mihos & Hernquist, 1994, 1996; Hopkins et al., 2006a, 2008b,a; Snyder et al., 2011; Hayward et al., 2014; Sparre & Springel, 2016), which can exhaust the gas required for star formation, effectively quenching the post-merger remnant. This remnant galaxy will also have formed a dynamically hot bulge through the dissipation of angular momentum in the merger (Toomre, 1977; Walker et al., 1996; Kormendy & Kennicutt, 2004; Hopkins et al., 2012; Martig et al., 2012). The mass ratio of the two galaxies merging is thought to affect the size of the bulge that is formed in the remnant (Cox et al., 2008; Hopkins et al., 2009; Tonini et al., 2016), with the most massive major mergers with a 1:1 mass ratio producing fully elliptical galaxies (Toomre & Toomre, 1972; Barnes & Hernquist, 1996; Mihos & Hernquist, 1996; Kauffmann, 1996; Pontzen et al., 2016).

Such a scenario is also intrinsically linked to the triggering of an AGN due to the influx of gas in the merger which can fuel the black hole accretion (Sanders et al., 1988; Di Matteo et al., 2005; Hopkins & Hernquist, 2009; Treister et al., 2012). Many studies have therefore focussed on investigating the growth of black holes due to mergers (e.g. Veilleux et al., 2002; Bellovary et al., 2013; Ellison et al., 2013; Medling et al., 2015; Gabor et al., 2016). Simulations of mergers with AGN have lead many to believe that a merger which triggered both a starburst and an AGN can quench a galaxy in extremely rapid timescales (Springel et al., 2005; Bell et al., 2006). Recent simulations have also suggested that feedback from the triggered AGN (see Section 1.1.1.1) is necessary to fully remove (or heat) all the available gas, otherwise the SFR will recover back to the SFS post-merger (Pontzen et al., 2016; Sparre & Springel, 2016).

1.1.2.2 Environment driven quenching

The environment of a galaxy has long been considered a key *nurturing* aspect of galaxy evolution. Correlations of galaxy morphology (Dressler, 1980; Smail et al., 1997; Poggianti et al., 1999; Postman et al., 2005; Bamford et al., 2009), colour (Butcher &

Oemler, 1978; Pimbblet et al., 2002) and the quenched galaxy fraction (Kauffmann et al., 2003b; Baldry et al., 2006; Peng et al., 2012; Darvish et al., 2016) with the environmental density all suggest that the environment is in some way responsible for the build up of the red sequence through quenching.

The proposed quenching mechanisms under the umbrella of environmental quenching are numerous and varied. Together with the typical gravitational galaxy-galaxy interactions (Moore et al., 1996), including galaxy mergers which are expected to be more frequent in a dense environment, environmental quenching also includes hydrodynamic interactions occurring between the cold inter stellar medium (ISM) of the in-falling galaxy and the hot intergalactic medium (IGM) of the group or cluster. Such hydrodynamic interactions include ram pressure stripping (Gunn & Gott, 1972), viscous stripping (Nulsen, 1982), and thermal evaporation (a rapid rise in temperature of the ISM due to contact with the IGM; Cowie & Songaila, 1977). Another such process is starvation (Larson et al., 1980) which can remove the outer galaxy halo cutting off the star formation gas supply to a galaxy. Preprocessing occurs when all of the above mechanisms take place in a group of galaxies which then merges with a larger group or cluster (Dressler, 2004).

The most likely candidate (and therefore the most studied) mechanism for the cause of the environmental density-morphology and SFR relations is ram pressure stripping (RPS; Abadi et al., 1999; Poggianti et al., 1999). However, there has been mounting evidence that RPS can only strip a galaxy of $40 - 60\%$ of its gas supply (Fillingham et al., 2016) and so may not be as effective of a quenching mechanism as first thought (Emerick et al., 2016). Therefore investigations of other environmentally driven quenching mechanisms, such as strangulation (Peng et al., 2015; Hahn et al., 2016; Maier et al., 2016; Paccagnella et al., 2016; Roberts et al., 2016; van de Voort et al., 2016) and harassment (Bialas et al., 2015; Smith et al., 2015a) are having a recent resurgence.

1.2 Using star formation histories to investigate quenching

In order to understand how a galaxy is quenched, the star formation history (SFH) is often modelled. This approach requires the inference of the global SFH of a galaxy from a its current stellar population. While in nearby galaxies it is possible to observe resolved stellar populations with the Hubble Space Telescope (HST) to pinpoint the main sequence turn off (an indicator of the age of a stellar population) on the Hertzsprung Russel diagram, this is not possible in more distant galaxies. Instead, reliance is placed upon the correlation between the integrated total light of a galaxy and its SFH (Searle et al., 1973). Adopting a global SFH for a galaxy is a big assumption, especially since recent IFU studies have shown that bulges and discs have vastly different SFHs (see for example Johnston et al., 2016). However, these differences will smear out across the integrated light of a galaxy and so inferring the SFH in this way will give an estimate of the average global SFH of the galaxy.

Many studies have employed this technique using either photometric broadband colours or spectral data as indicators of the integrated SFH (for example de Jong, 1996; Madau et al., 1998; Kauffmann et al., 2003b; Dressler, 2004; MacArthur et al., 2004; Martin et al., 2007; Pérez & Sánchez-Blázquez, 2011; Sánchez-Blázquez et al., 2011; McDermid et al., 2015). However, this technique is sensitive to the degeneracies between age and metallicity (Worthey, 1994) and the effects of dust (Ganda et al., 2009; Pastrav et al., 2013) on the integrated light.

The turn of the millennium therefore saw the development of full spectral energy density (SED) fitting codes to infer the SFH (without having to make any prior assumptions on its form) such as MOPED (Heavens et al., 2000), STARLIGHT (Cid Fernandes et al., 2005), VESPA (Tojeiro et al., 2007), and more recently FIREFLY (Wilkinson, 2015). In the absence of spectral data however, broadband colours are still effective at inferring the global SFHs of galaxies, especially when wavebands across the spectrum, such as ultra-violet, optical and infrared colours, are used simultaneously (Madau et al., 1998).

This method is achieved by modelling the observed SED of a galaxy using a combination of SEDs of simple stellar populations (SSP) at various ages. SSPs assume stars are coeval and form with the same metallicity and comprehensive knowledge of stellar evolutionary tracks and initial mass functions (IMF; Salpeter, 1955; Chabrier, 2003) are therefore needed to calculate the spectrum of a SSP at a given age (Chen et al., 2010; Kriek et al., 2010). Luckily, some astronomers have made the study of these SSPs their life's work (Bruzual & Charlot, 2003; Maraston, 2005; Vázquez & Leitherer, 2005; Conroy et al., 2009, for example), therefore once an IMF and a SFH function have been assumed, the SED of a model galaxy can be predicted at any point in its history (Chen et al., 2010). This technique also assumes a universal IMF, which recent studies have shown may not be appropriate (van Dokkum, 2008; Conroy & van Dokkum, 2012; Cappellari et al., 2012; Smith et al., 2015b). Whilst the choice of an IMF and metallicity of a SSP will affect the output SED (Conroy et al., 2009; Kriek et al., 2010), the choice of the functional form of the SFH will have the greatest impact.

Many possible forms for global galaxy SFHs have been assumed in previous studies, including an exponential decline (Tinsley, 1972; Gavazzi et al., 2002; Weiner et al., 2006; Martin et al., 2007; Noeske et al., 2007; Kriek et al., 2010; Schawinski et al., 2014; Hart et al., 2016), the extended (or delayed) exponential model (Gavazzi et al., 2002; Oemler et al., 2013; Simha et al., 2014), a Gaussian distribution (Feuillet et al., 2016) or a log normal distribution (Gladders et al., 2013; Abramson et al., 2016). These models are by no means a perfect description of a galaxy's SFH (Lee et al., 2010; Boquien et al., 2014; Smith & Hayward, 2015), as they generalise the localised bursts of SF across a galaxy's lifetime into a global SFH, but they still allow some insight to be gained on the complex processes responsible for the SFHs seen across the galaxy population.

In this thesis I will assume an exponentially declining SFH for galaxies with morphological classifications from Galaxy Zoo. Using Bayesian methods, I will use optical and NUV photometry to infer the dependence of quenching histories on the morphology across the colour magnitude diagram. I will also investigate the quenching histories of galaxies hosting AGN and those in dense environments to help constrain the quenching mechanisms responsible for galaxy evolution.

1.3 Data

In the following section I describe the data sources for the optical & NUV colours and morphologies used throughout this study.

1.3.1 Sloan Digital Sky Survey

The Sloan Digital Sky Survey (SDSS; York et al. 2000) is an optical imaging and spectroscopic survey of $8,000$ square degrees of sky, which was completed using a 2.5m telescope at Apache Point Observatory in New Mexico, USA. SDSS Data Release 8 (Aihara et al., 2011) provided publicly available optical magnitudes across 5 broadband filters, *ugriz* for over 1 million galaxies in the 'main galaxy' sample. Here I utilise the Petrosian magnitudes, `petroMag`, values for the u ($3,543$Å) and r ($6,231$Å) wavebands provided by the SDSS pipeline. Spectral data is available for a significant proportion of the SDSS main galaxy sample but the spectral fibre is a set size. Therefore across a population of galaxies the fibre will cover varying radii at different distances and of different sizes. Therefore the usual spectral star formation indicators cannot be utilised in this study as they will over- or under-estimate the global average SFR of a galaxy.

Magnitudes are corrected for galactic extinction (Oh et al., 2011) by applying the Cardelli et al. (1989) law, giving a typical correction of $u - r \sim 0.05$. K-corrections are also adopted to $z = 0.0$ and absolute magnitudes obtained from the NYU-VAGC (Blanton et al., 2005; Padmanabhan et al., 2008; Blanton & Roweis, 2007), giving a typical $u - r$ correction of ~ 0.15 mag. The change in the $u - r$ colour due to both corrections therefore ranges from $\Delta(u - r) \sim 0.2$ at low redshift, increasing up to $\Delta(u - r) \sim 1.0$ at $z \sim 0.25$, which is consistent with the expected k-corrections shown in Figure 15 of Blanton & Roweis (2007). These corrections were calculated by Bamford et al. (2009) for a subset of galaxies in the SDSS survey. These corrections are a crucial aspect of this work since a $\Delta(u - r) \sim 1.0$ can cause a galaxy to change whether it is class as blue cloud, green valley or red sequence.

Star formation rates and stellar masses, where available, were obtained from the MPA-JHU catalog (Kauffmann et al., 2003b; Brinchmann et al., 2004). These SFRs are derived from emission lines using the method of Charlot & Longhetti (2001). All SFRs are corrected for aperture size by fitting to the photometry outside the fibre with stochastic models as in Salim et al. (2007). SFRs for non star forming galaxies and AGN were derived indirectly using the $4,000$Å break. Those galaxies with emission lines with low signal-to-noise ratio, the SFR was estimated indirectly using a conversion factor likelihood distribution between the luminosity of the Hα Balmer emission line and the SFR. Masses are obtained from fits to the photometry with a large grid of SFHs produced using the Bruzual & Charlot (2003) models. In this thesis these values are obtained for interest to compare samples; they are never used to infer the SFHs of galaxies due to the circular nature of the modelling used to derive the values. I use the average values of AVG SFR and AVG MASS from the inferred likelihood distributions for each galaxy.

1.3.2 Galaxy Evolution Explorer

The Galaxy Evolution Explorer (GALEX; Martin et al. 2005) is an ultra-violet space based telescope which imaged galaxies simultaneously in two broadband filters: both the far ultra-violet (FUV) with an effective wavelength of $1,516$Å and in the NUV with an effective wavelength of $2,267$Å. Sources detected with GALEX were matched with a search radius of $1''$ to the SDSS data in right ascension and declination. The `auto` magnitudes provided by the GALEX pipeline are used in this study (for a discussion of aperture bias between different surveys see Hill et al. 2011). All magnitudes are k-corrected and extinction corrected as described in Section 1.3.1.

1.3.3 Galaxy Zoo

Galaxy Zoo (GZ) is a citizen science project enlisting the help of thousands of members of the public to voluntarily classify galaxy images online[2]. The first version of GZ classified just under 1 million SDSS galaxy images as either ellipticals, spirals or mergers within approximately 6 months of launch (Lintott et al., 2008, 2011). In the second version, GZ2 (Willett et al., 2013), volunteers were asked to make more detailed morphological classifications of $304,022$ images from the SDSS DR8 (a subset of those classified in the first Galaxy Zoo; GZ1). These images were all classified by *at least* 17 independent volunteers, with the mean number of classifications standing at ~ 42. GZ is now in its tenth year of classifying and its fifth incarnation, after classifying images from Hubble Space Telescope Legacy surveys in GZ:Hubble (Willett et al., 2016) and the CANDELS survey galaxies in GZ:CANDELS (Simmons et al., 2016). At the time of writing, images from the DeCALS[3] survey and Illustrius simulation (Vogelsberger et al., 2014; Genel et al., 2014) are being classified by volunteers.

[2] `http://galaxyzoo.org`

[3] `http://legacysurvey.org/`

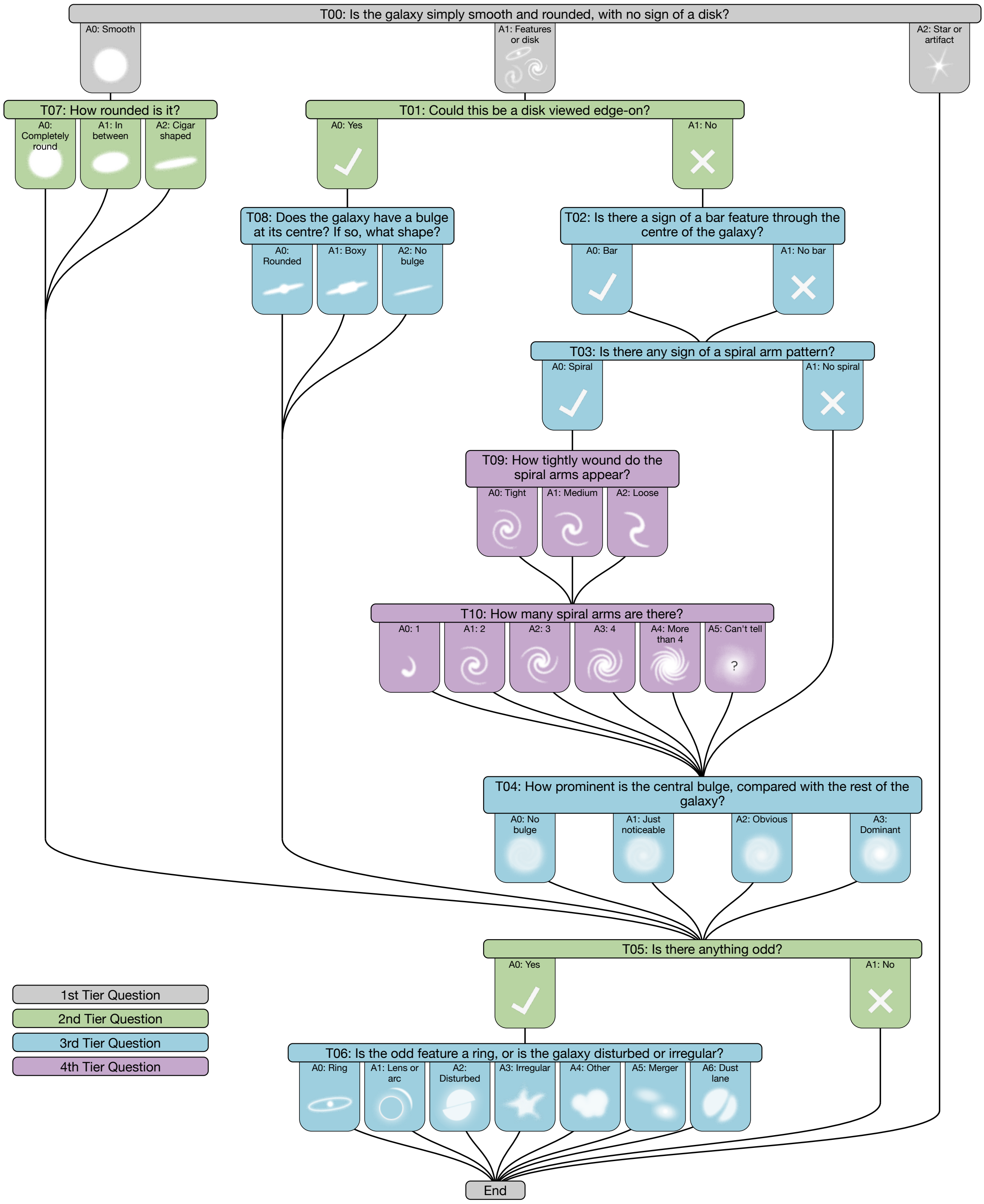

Figure 1.5: Flowchart of the classification tree for GZ2, beginning at the top with Task 0. Tasks are colour-coded by their relative depths in the decision tree with tasks in green, blue and purple respectively one, two or three steps below branching points in the decision tree.

From GZ2 onwards, all projects have collected classification data via a multi-step decision tree, shown in Figure 1.5. Each individual step in a tree is a *task*, which consists of a *question* with a finite number of possible *answers*. The selection of an answer is called the volunteer's *vote*. The first task of GZ2 asks volunteers to choose whether a galaxy is mostly smooth, is featured and/or has a disc or is a star/artefact. Every volunteer who classifies a galaxy image will complete this task, therefore the most statistically robust classifications are available at this level.

The classifications from volunteers produces a vote fraction for each galaxy; for example if 80 of 100 people thought a galaxy was featured and/or had a disc, whereas 20 out of 100 people thought the same galaxy was mostly smooth (i.e. elliptical), that galaxy would have raw vote fractions $p_s = 0.8$ and $p_d = 0.2$. In this example this galaxy would be included in the *'clean'* disc sample ($p_d \geq 0.8$) according to Willett et al. (2013) and would be considered a late-type galaxy. Similar vote fractions can be produced at each stage in the tree, such as $\{p_{\rm bar}, p_{\rm no\ bar}\}$, $\{p_{\rm spiral}, p_{\rm no\ spiral}\}$ and $\{p_{\rm odd}, p_{\rm not\ odd}\}$. Selecting a sample of galaxies with a specific feature using these vote fractions becomes a trade off between purity and completeness. Since not every volunteer will submit a response to a 2nd, 3rd or 4th tier question (see Figure 1.5), the number of classifiers recording a response must be considered, in order to reduce noise in cases where only a small number of people answered that task.

For example imagine that a galaxy is classified by 40 people, 38 of whom say that the galaxy is mostly smooth in answer to the first question. However, 2 people decide that the galaxy is featured and/or has a disc, both of whom subsequently respond to Task 2 to say that there is a sign of a bar in the same galaxy. This would give a $p_{\rm bar} = 1$, despite the fact that the $p_s = 0.95$. This is an unlikely situation, but highlights the need for not only consideration of the number of respondents for a task but also the vote fractions of previous tasks when using a threshold to identify a subset of features. Appropriate values for these thresholds given the number of respondents are shown in Table 1.1 (reproduced from Table 3 in Willett et al. 2013) and are adopted where relevant throughout this study.

All previous Galaxy Zoo projects have also incorporated extensive analysis of volunteer classifications to measure classification accuracy and bias. A weighting is computed for each volunteer based on their classification history and the redshit of each galaxy considered in order to produce debiased vote fractions for each galaxy (for

Task	Previous task	Vote fraction $N_{task} \geq 10$	Vote fraction $N_{task} \geq 20$
00	–	–	–
01	00	0.227	0.430
02	00,01	0.519	0.715
03	00,01	0.519	0.715
04	00,01	0.519	0.715
05	–	–	–
06	05	0.263	0.469
07	00	0.223	0.420
08	00,01	0.326	0.602
09	00,01,03	0.402	0.619
10	00,01,03	0.402	0.619

Table 1.1: Thresholds for determining well-sampled galaxies in GZ2. Thresholds depend on the number of respondents for a task, including the thresholds that should be applied to previous task(s) for both 10 and 20 respondents. As an example, to select galaxies that may or may not contain bars, cuts for $p_{\mathrm{features/disc}} > 0.430$, $p_{\mathrm{not\ edgeon}} > 0.715$, and $N_{\mathrm{not\ edgeon}} \geq 20$ should be applied. No thresholds are given for Tasks 01 and 06, since these are answered for every classification in GZ2. The task numbers are those defined in Figure 1.5.

a detailed description of redshift debiasing and consistency-based volunteer weightings, see either Section 3 of Lintott et al. 2009 or Section 3 of Willett et al. 2013). This produces highly accurate and robust detailed morphological classifications and is a significant statistical improvement over efforts completed using only a small number of expert classifiers (Schawinski et al., 2007b; Nair & Abraham, 2010a; Ann et al., 2015). These classifications can now be used as machine learning training sets (Dieleman et al., 2015) to improve future automated classifications of galaxies.

The debiased GZ2 p_d and p_s vote fractions encompass the continuous spectrum of morphological features (as shown in Figure 1.6), rather than a simple binary classification separating elliptical and disc galaxies (see Section 6.1). These classifications allow each galaxy to be considered as a probabilistic object with both bulge and disc components. I utilise the debiased GZ2 vote fractions in this study to facilitate future work studying more detailed galaxy structures.

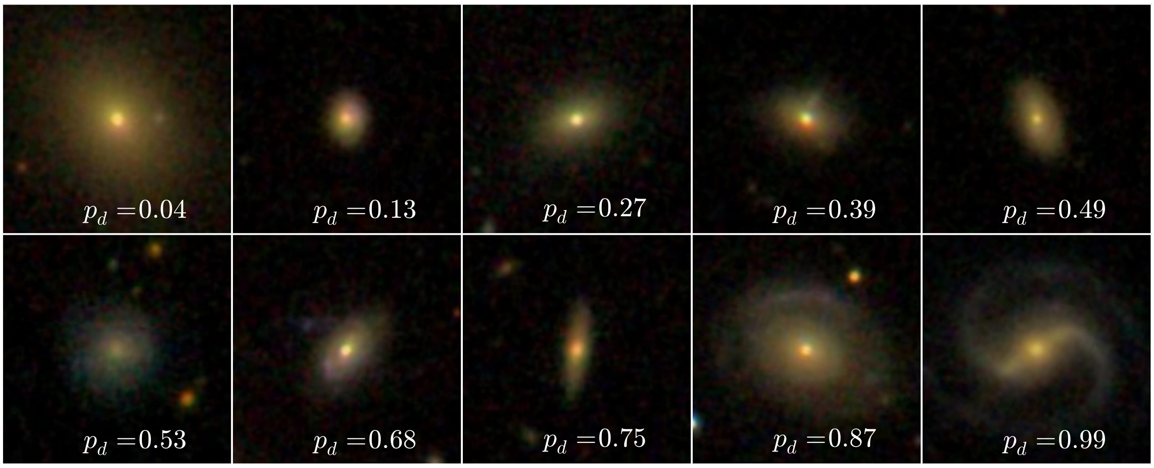

Figure 1.6: Randomly selected SDSS *gri* composite images showing the continuous probabilistic nature of the Galaxy Zoo sample from a redshift range $0.070 < z < 0.075$. The debiased disc vote fraction for each galaxy is shown. The scale for each image is 0.099 arcsec/pixel.

1.3.4 Defining the GZ2-GALEX main galaxy sample

I require a sample of galaxies with optical and NUV photometry from SDSS and GALEX respectively, along with morphologies from GZ2 in order to study the morphological dependence of galaxy quenching histories. The GZ2 sample consists of $304,022$ SDSS galaxies which were selected to include the brightest ($m_r < 17$), largest (radius containing 90% of the Petrosian flux, $r_{90} > 3''$) and nearest ($0.005 < z < 0.25$) galaxies in order to achieve robust detailed morphological classifications. I first removed those objects considered to be stars or artefacts in Task 0 or merging pairs in Task 6 (using the thresholds defined in Table 1.1) from this GZ2 sample. Further to this, I required NUV photometry from the GALEX survey, within which $\sim 42\%$ of the GZ2 sample galaxies were observed, giving a total sample size of $126,316$ galaxies. This will be referred to as the GZ2-GALEX sample.

The completeness of the GZ2-GALEX sample is shown in Figure 1.7 with the u-band absolute magnitude against redshift, compared with the SDSS data set. Despite the GZ2 selection for the brightest and largest galaxies and the cross match to GALEX (which has a higher magnitude limit than SDSS) typical Milky Way L_* galaxies with $M_u \sim -20.5$ are still included in the GZ2 subsample out to the highest redshift of $z \sim 0.25$; however dwarf and lower mass galaxies are only detected at the lowest redshifts. The redshift is taken into account during the SFH modelling (see Section 2.1).

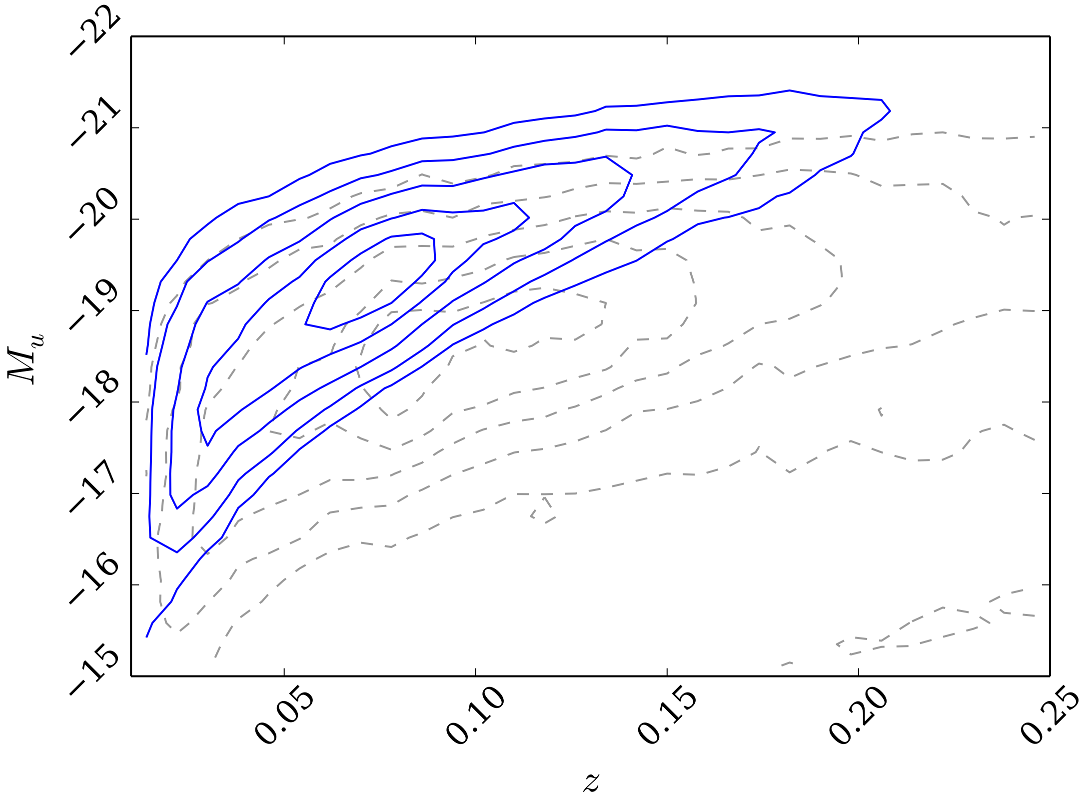

Figure 1.7: Absolute u-band magnitude against redshift for the whole of SDSS (grey dashed lines) in comparison to the GZ2 subsample (blue solid lines). Typical Milky Way L_* galaxies with $M_u \sim -20.5$ are still included in the GZ2 subsample out to the highest redshift.

Galaxy colours were not corrected for intrinsic dust attenuation. This is of particular consequence for disc galaxies, where attenuation increases with increasing inclination. Buat et al. (2005) found the median value of the attenuation in the GALEX NUV passband to be ~ 1 mag. Similarly Masters et al. (2010b) found a total extinction from face-on to edge-on spirals of 0.7 and 0.5 mag for the SDSS u and r passbands and show spirals with $\log(a/b) > 0.7$ have signs of significant dust attenuation. For the GZ2-GALEX sample I find $\sim 29\%$ of discs (with $p_d > 0.5$) have $\log(a/b) > 0.7$, therefore we must be aware of possible biases in the results due to dust.

I shall use the GZ2-GALEX sample to probe how different quenching mechanisms cause galaxies of different morphologies and environments to transition from the SFS to quiescence.

1.4 Thesis Summary

This thesis proceeds as follows. In Chapter 2 I describe the SFH model used to characterise the colours of quenching galaxies, along with the statistical methods used to determine the distribution of quenching histories in a population of galaxies. In Chapter 3 I apply this method across the red sequence, green valley and blue cloud and investigate the morphological dependence of quenching histories in these populations. Chapter 4 is split into two parts. In Section 4.1 I investigate the effect of AGN feedback on the quenching histories of a population of AGN host galaxies. In Section 4.2 I investigate the proposed slow co-evolution of galaxies with their central black holes, by measuring the black hole masses of a sample of bulgeless galaxies, which have assumed merger free histories. In Chapter 5 I return to investigating the quenching histories of galaxies, this time focussing on the effect of the group environment on satellite galaxies in comparison to centrals and those in the field. In Chapter 6 I discuss how the implications of my results in the context of galaxy evolution and propose ideas for future work.

Where necessary I adopt the Planck 2015 cosmological results (Planck Collaboration, 2016) with $(\Omega_m, \Omega_\lambda, h) = (0.309 \pm 0.006, 0.691 \pm 0.006, 0.677 \pm 0.005)$.

Chapter 2

STARPY: Bayesian inference of a galaxy's star formation history

The work in the following chapter has been published in Smethurst et al. (2015).

2.1 Star Formation History Models

The quenched star formation history (SFH) of a galaxy can be simply modelled as an exponentially declining star formation rate (SFR) across cosmic time ($0 \leq t$ [Gyr] ≤ 13.8) as:

$$SFR = \begin{cases} I_{sfr}(t_q) & \text{if } t \leq t_q \\ I_{sfr}(t_q) \times exp\left(\frac{-(t-t_q)}{\tau}\right) & \text{if } t > t_q \end{cases} \tag{2.1}$$

where t_q is the onset time of quenching, τ is the timescale over which the quenching occurs and I_{sfr} is an initial constant star formation rate dependent on t_q. A smaller τ value corresponds to a rapid quench, whereas a larger τ value corresponds to a slower quench. This model is not a fully hydrodynamical simulation, it is a deliberately simple model built in order to test our understanding of the evolution of galaxy populations. This SFH model has previously been shown to appropriately characterise quenching galaxies (Weiner et al., 2006; Martin et al., 2007; Noeske et al., 2007; Schawinski et al., 2014). However. it is not expected to accurately determine the SFH of every galaxy in the GZ2-GALEX sample, in particular galaxies which have not undergone any quenching.

Here, I assume that all galaxies formed at a time $t = 0$ Gyr with an initial burst of star formation, $I_{sfr}(t_q)$. This initial constant star formation rate must be defined in order to ensure the 'model' galaxy has a reasonable stellar mass by $z \sim 0$. This value will be dependent on the epoch at which quenching is modelled to occur, hence the $I_{sfr}(t_q)$ in Equation 2.1. To tackle this problem, I looked to the literature; Peng et al. (2010, Equation 1) define a relation between the average specific SFR (sSFR = SFR/M$_*$) and redshift (cosmic time, t) by fitting to measurements of the mean sSFR of blue star forming galaxies from SDSS, zCOSMOS and literature values at increasing redshifts (Elbaz et al., 2007; Daddi et al., 2007):

$$sSFR(m,t) = 2.5 \left(\frac{m}{10^{10} M_{\odot}} \right)^{-0.1} \left(\frac{t}{3.5 \text{ Gyr}} \right)^{-2.2} \text{Gyr}^{-1}. \tag{2.2}$$

Beyond $z \sim 2$ the characteristic SFR flattens and is roughly constant back to $z \sim 6$. This flattening can be seen across similar observational data (Peng et al., 2010; González et al., 2010; Béthermin et al., 2012); the cause is poorly understood but may reflect a physical limit to the sSFR of a galaxy.

Motivated by these observations, the relation defined in Peng et al. (2010) is taken up to a cosmic time of $t = 3$ Gyr (z $\sim$ 2.3) and prior to this a constant average SFR is assumed (see middle panel of Figure 2.1). At the point of quenching, t_q, the SFH models are therefore defined to have an $I_{sfr}(t_q)$ which lies on this relationship for the sSFR, for a galaxy with mass, $m = 10^{10.27} M_{\odot}$ (the mean mass of the GZ2-GALEX sample; see left panel of Figure 2.1). This choice of $I_{sfr}(t_q)$ is an important one, however does not impact on the predicted colours output by the model (see below) as it is merely a normalisation factor on the SFH; $[t_q, \tau]$, which set the shape of the SFH, are the crucial parameters.

Under these assumptions the average SFR of these models will result in a lower value than the relation defined in Peng et al. (2010) at all cosmic times as each galaxy only resides on the 'main sequence' at the point of quenching. However galaxies cannot remain on the 'main sequence' from early to late times throughout their entire lifetimes given the unphysical stellar masses and SFRs that would result in the local Universe (Béthermin et al., 2012; Heinis et al., 2014). If prescriptions for starbursts, mergers, AGN etc. were included in this model, the reproduction of the average SFR across cosmic time would improve; however I have chosen to focus first on the simplest possible model.

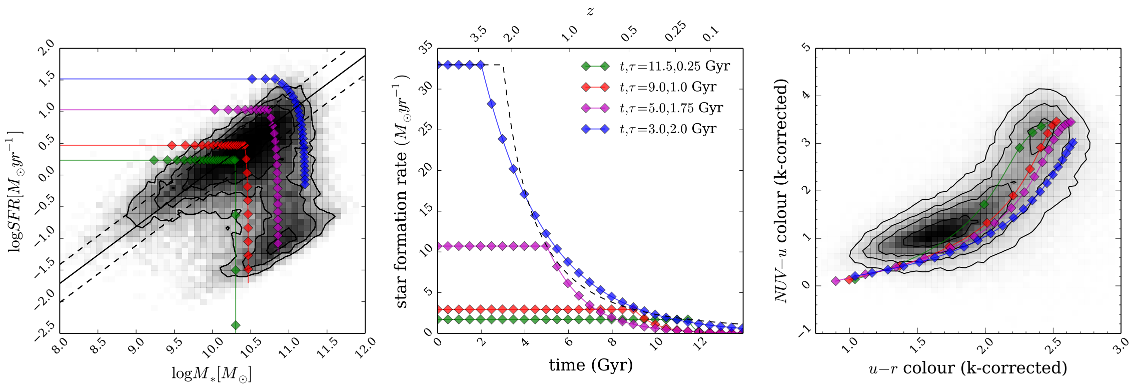

Figure 2.1: Left panel: SFR-stellar mass plane for all 126,316 galaxies in the GZ2-GALEX sample (shaded contours), with model galaxy trajectories shown by the coloured lines, with each point representing a time step of 0.5 Gyr. The 'main sequence' of star formation as defined by Peng et al. (2010) is shown by the solid line with $\pm 1\sigma$ (dashed lines). Middle panel: The SFHs of the models are shown, where the SFR is initially constant before quenching at time t_q and thereafter exponentially declining with a characteristic timescale τ. The SFR at the point of quenching is set to be consistent with the typical SFR of a star-forming galaxy at the quenching time, t_q (dashed curve; Peng et al. 2010). Right panel: The full range of models can reproduce the observed colour-colour properties of the GZ2-GALEX sample; for clarity the figures show only 4 of the possible models explored in this study. Note that some of the model tracks produce colours redder than the apparent peak of the red sequence in the GZ2 subsample; however this is not the *true* peak of the red sequence due to the necessity for NUV colours from GALEX (see Section 3.1.)

Once this SFH is obtained, it is convolved with the Bruzual & Charlot (2003) population synthesis models to generate a model SED at each time step. The observed features of galaxy spectra can be modelled using simple stellar population techniques which sum the contributions of individual, coeval, equal-metallicity stars. The accuracy of these predictions depends on the completeness of the input stellar physics. Comprehensive knowledge is therefore required of (i) stellar evolutionary tracks and (ii) the initial mass function (IMF) to synthesise a stellar population accurately.

These stellar population synthesis (SPS) models are an extremely well explored (and often debated) area of astrophysics (Maraston, 2005; Eminian et al., 2008; Conroy et al., 2009; Falkenberg et al., 2009; Chen et al., 2010; Kriek et al., 2010; Miner et al., 2011; Melbourne et al., 2012). In this work I have chosen to utilise the Bruzual & Charlot (2003) *GALEXEV* SPS models, along with a Chabrier IMF (Chabrier, 2003), across a large wavelength range ($0.0091 < \lambda$ [μm] < 160) with solar metallically (m62 in the Bruzual & Charlot (2003) models; hereafter BC03), to allow a direct comparison with Schawinski et al. (2014).

Flux from stars younger than 3 Myr in the SPS model is suppressed to mimic the large optical depth of protostars embedded in dusty formation clouds (as in Schawinski et al. 2014). Filter transmission curves are then applied to the fluxes to obtain AB magnitudes and ultimately colours. For a particular galaxy at an observed redshift, z, I calculate the observed time, t^{obs}, for that galaxy using the standard cosmological conversion between redshift and time provided in the ASTROPY *Python* module (Astropy Collaboration et al., 2013). The predicted colours of the SFH models at the observed redshift of each individual galaxy can then be compared to the observed colours directly, as in the right panel of Figure 2.1. Note that some of the SFHs shown produce colours redder than the apparent peak of the red sequence in the GZ2-GALEX sample; however this is not the *true* peak of the red sequence due to the necessity for NUV colours from GALEX (see Section 3.1). Star forming galaxies in this regime are fitted by a constant SFR up until $t_q \simeq t^{obs}$, with a very low probability.

Figure 2.2 shows these predicted optical and NUV colours at a time of $t^{obs} =$ 12.8 Gyr (the mean observed time of the GZ2-GALEX sample, $z \sim 0.076$) for the exponential SFH model. These predicted colours will be referred to as $d_{c,p}(t_q, \tau, t^{obs})$, where c={opt,NUV} and p = predicted. The SFR at a time of $t^{obs} = 12.8$ Gyr is also shown in Figure 2.2 to compare how this impacts on the predicted colours. The $u - r$ predicted colour shows an immediate correlation with the SFR, however the

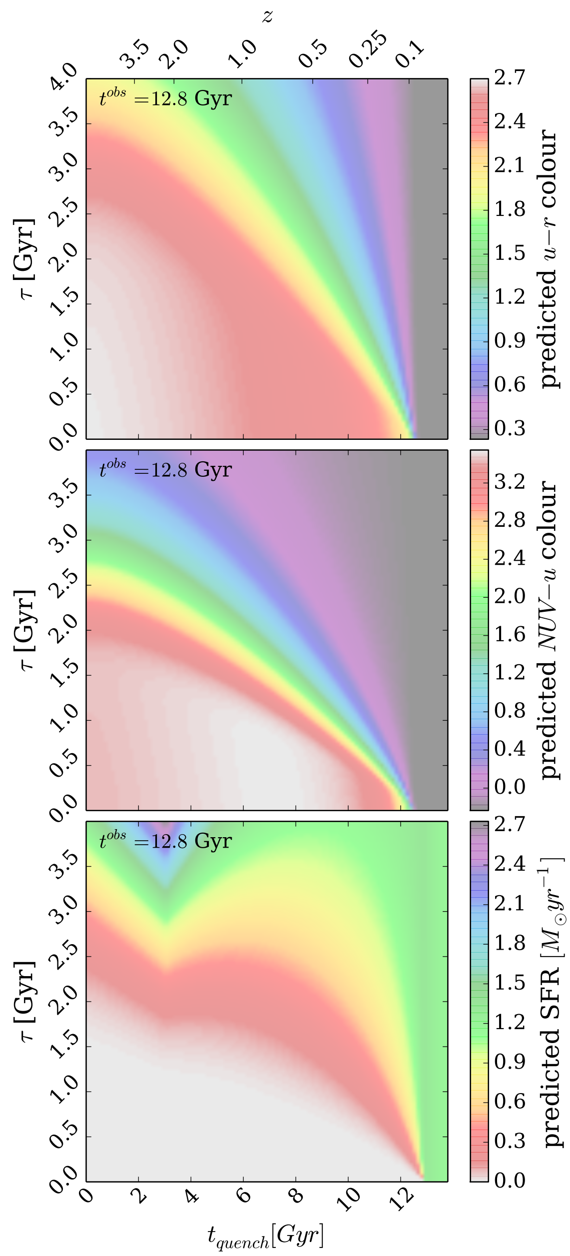

Figure 2.2: Quenching timescale τ versus quenching onset time t_q in all three panels for the quenched SFH models used in STARPY. Colour shadings show model predictions of the $u - r$ optical colour (top panel), $NUV - u$ colour (middle panel), and star formation rate (lower panel), at $t^{obs} = 12.8$ Gyr, the mean observed redshift of the GZ2 sample (see Section 2.1). The combination of optical and NUV colours is a sensitive measure of the $\theta = [t_q, \tau]$ parameter space. Note that all models with $t > 12.8$ Gyr are effectively un-quenched. The 'kink' in the bottom panel is due to the assumption that the sSFR is constant prior to $t \sim 3$ Gyr ($z \sim 2.2$).

$NUV - u$ colour is more sensitive to the value of τ and so is ideal for tracing any recent star formation in a population. At small τ (rapid quenching timescales) the $NUV - u$ colour is insensitive to t_q, whereas at large τ (slow quenching timescales) the colour is very sensitive to t_q. Together the two colours are ideal for tracing the effects of t_q and τ in a population.

2.2 Probabilistic Fitting Methods

In order to achieve robust conclusions I conducted a Bayesian analysis (Sivia & Skilling, 2006; Mackay, 2003) of the predicted colours from the SFH models in comparison to the observed colours of the GZ2-GALEX sample.

2.2.1 A short introduction to Bayesian statistics

Frequentist statistics allows you to test whether an event (i.e. a hypothesis) occurs or not and calculate the probability of it occurring over many trials of an experiment. The accuracy of the derived probability is also dependant on the number of experiment trials conducted. Conversely, a Bayesian approach allows you to directly test whether a hypothesis, θ, is true, given the data you already have, d, by relating this to something you can easily calculate: the probability that you would observe the data if the hypothesis was true. It does so by employing the rules of conditional probability into Bayes' theorem:

$$P(\theta|d) \propto P(d|\theta)P(\theta), \tag{2.3}$$

which is made up of three separate terms:

(i) $P(\theta)$, known as the *prior* probability which represents your knowledge (or ignorance) about the hypothesis before you have analysed any data.

(ii) $P(d|\theta)$, the *likelihood* function which gives the probability of observing the data you have given the hypothesis being tested.

(iii) $P(\theta|d)$, the *posterior* probability which summarises your knowledge of the hypothesis given your observed data.

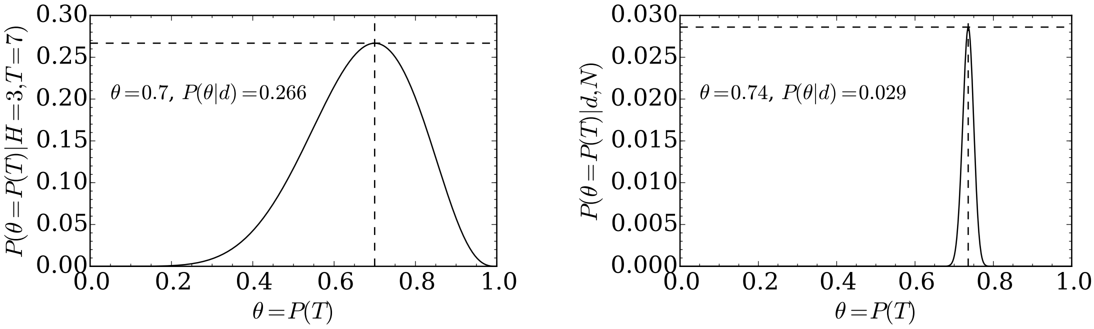

Figure 2.3: The unnormalised posterior probability calculated for multiple hypotheses for the probability of tossing a tails, $P(T)$ in the case of 10 data points (left) and 1000 data points (right). The dashed lines in both cases show the posterior probability values at the peak of the distribution.

The missing normalisation constant in Equation 2.3 doesn't explicitly depend on your hypothesis and so doesn't have to be calculated for model parameter estimation problems (for example, where your hypothesis, θ, is a model described by some number of parameters with the goal of emulating your data). Deciding on a prior and likelihood function is very much dependent on the problem you are trying to solve; the decision is often informed by your knowledge of the problem.

This difference between frequentist and Bayesian statistics is often highlighted by the example of a coin being tossed; if I toss a coin 10 times and get 3 heads ($H = 3$) and 7 tails ($T = 7$) what is the probability that the coin is weighted? With frequentist statistics, you are limited by the fact that I only tossed the coin 10 times; I haven't repeated the experiment enough for you to be sure of your response that the probability of tossing a tails, $P(T) = 0.7$. Perhaps if I'd tossed the coin a 1000 times and recorded 720 tails then you could be more certain that the coin was weighted. Herein lies the problem of frequentist statistics; not only is your answer dependent on the number of experiment trials but you also can't quantify how likely your answer is of being correct.

To quantify this you can use Bayesian statistics; first you need to choose your likelihood, $P(d|\theta)$, and your prior distributions, $P(\theta)$, but there are many choices available. For example, given that most coins that you encounter are not weighted, you might choose a Gaussian as your prior distribution, centered on $P(T) = 0.5$. Or, you may decide that all scenarios are equally likely and therefore choose a flat prior distribution.

For the likelihood function you need to think about what hypothesis (or model, θ) best describes your problem. In this case you might choose a Bernouilli likelihood distribution, e.g.

$$P(d|\theta, N) = \theta^d \ (1 - \theta)^{N-d}, \tag{2.4}$$

where d is the number of tails flipped, θ is our guess (or hypothesis) for $P(T)$, i.e. how biased the coin is, and N is the number of flips of the coin. If you calculate this likelihood, $P(d|\theta, N)$ for many possible values of $\theta = P(T)$ and multiply it by your flat prior distribution, you get the unnormalised posterior probability distribution shown in the left panel of Figure 2.3. From this you can see that $P(T) = 0.7$ is indeed the most likely value for the probability of tossing a tails given the 10 data points you have. Not only have you been able to determine the best model to describe the coin, given the data you have, but have also been able to say how certain you are of this model (since this is an unnormalised posterior distribution you can't give a definitive probability but can say how certain you are in comparison to other θ values). As you increase the number of trials in the experiment, N, you become more certain of your result, as in the right panel of Figure 2.3.

This is the strength of using a Bayesian method over a frequentist one. In particular, the output of a Bayesian analysis is probabilistic in nature, returning the posterior probability distribution across the model parameter space, θ (in the example in Figure 2.3 this is demonstrated in one dimension, but this can be visualised over as many dimensions as needed in the problem). This distribution encodes a huge amount of useful information that can be utilised in the analysis of the hypothesis.

Since this investigation is focussed on finding the most likely star formation history model in a very degenerative parameter space for a large sample of galaxies, the obvious choice of method for analysis is therefore a Bayesian one.

2.2.2 STARPY

For the SFH problem at hand, using this Bayesian approach requires consideration of all possible combinations of the model parameters $\theta \equiv (t_q, \tau)$ (the hypothesis in this instance). Assuming that all galaxies formed at $t = 0$ Gyr with an initial burst of star formation, we can assume that the 'age' of each galaxy in the GZ2 sample is equivalent to an observed time, t_k^{obs}. I then used this 'age' to calculate the predicted model colours at this cosmic time for a given combination of θ: $d_{c,p}(\theta_k, t_k^{obs})$ for both optical and NUV ($c = opt, NUV$) colours. The predicted model colours can now directly be compared with the observed GZ2-GALEX sample colours, so that for a single galaxy k with optical $(u-r)$ colour, $d_{opt,k}$ and NUV $(NUV-u)$ colour, $d_{NUV,k}$, I have chosen the likelihood of a given model $P(d_k|\theta_k, t_k^{obs})$ to be:

$$
\begin{aligned}
P(d_k|\theta_k, t_k^{obs}) = \frac{1}{\sqrt{2\pi\sigma_{opt,k}^2}} \frac{1}{\sqrt{2\pi\sigma_{NUV,k}^2}} \exp\left[-\frac{(d_{opt,k} - d_{opt,p}(\theta_k, t_k^{obs}))^2}{\sigma_{opt,k}^2}\right] \\
\exp\left[-\frac{(d_{NUV,k} - d_{NUV,p}(\theta_k, t_k^{obs}))^2}{\sigma_{NUV,k}^2}\right].
\end{aligned}
\tag{2.5}
$$

Here I have assumed that $P(d_{opt}|\theta_k, t_k^{obs})$ and $P(d_{NUV}|\theta_k, t_k^{obs})$ are independent of each other and that the errors on the observed colours are also independent. To obtain the probability of a combination of θ values given the GZ2 data: $P(\theta_k|d_k, t^{obs})$, i.e. how likely a single SFH model is given the observed colours of a single GZ2 galaxy, I utilise Bayes' theorem as:

$$
P(\theta_k|d_k, t^{obs}) = \frac{P(d_k|\theta_k, t^{obs})P(\theta_k)}{\int P(d_k|\theta_k, t^{obs})P(\theta_k)d\theta_k}. \tag{2.6}
$$

I assume a flat prior on the model parameters so that:

$$
P(\theta_k) = \begin{cases} 1 & \text{if } 0 \leq t_q \text{ [Gyr] } \leq 13.8 \text{ and } 0 \leq \tau \text{ [Gyr] } \leq 4 \\ 0 & \text{otherwise.} \end{cases} \tag{2.7}
$$

As the denominator of Equation 2.6 is a normalisation factor, comparison between likelihoods for two different SFH models (i.e., two different combinations of $\theta_k = [t_q, \tau]$) is equivalent to a comparison of the numerators. Markov Chain Monte Carlo (MCMC; Mackay 2003; Foreman-Mackey et al. 2013; Goodman & Weare 2010) analysis provides a robust comparison of the likelihoods between θ values.

MCMC allows for a more efficient exploration of the parameter space by avoiding those areas with low likelihood. A large number of 'walkers' are started at an initial position (i.e. an initial hypothesis, θ), where the likelihood is calculated; from there they individually 'jump' a randomised distance to a randomised new area of parameter space. If the likelihood in this new position is greater than the original position then

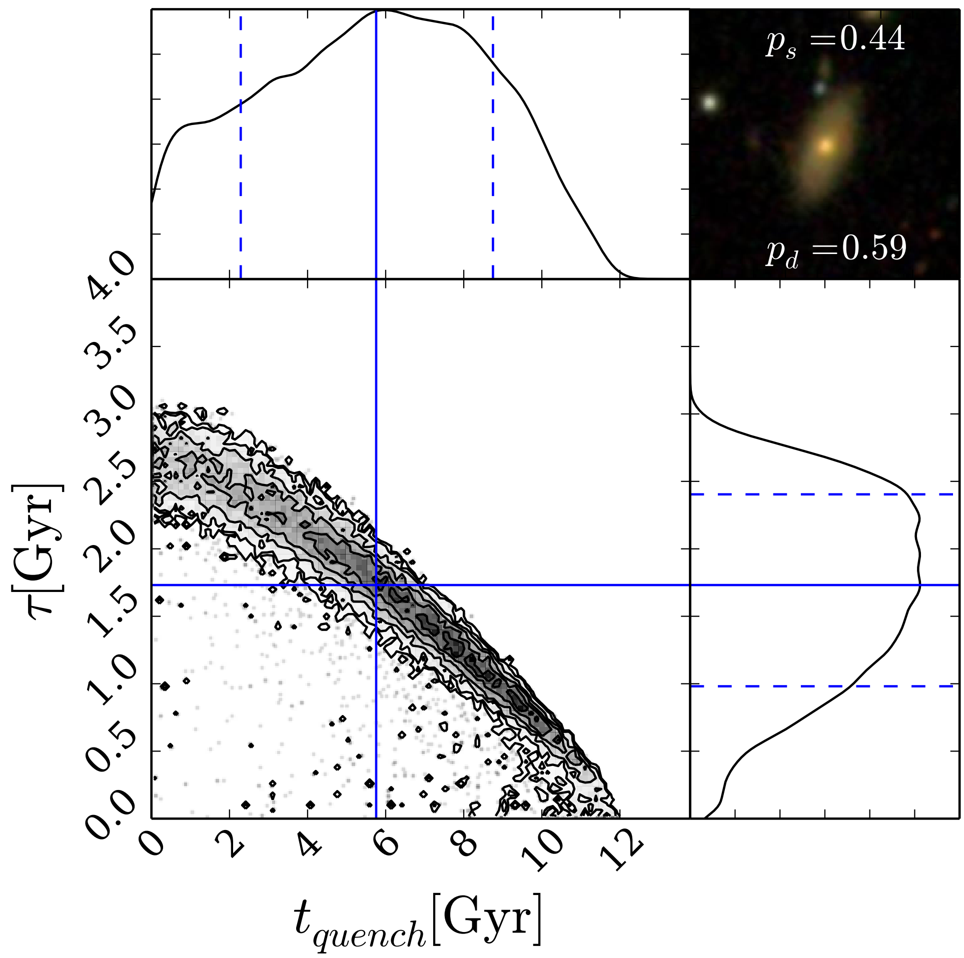

Figure 2.4: Example output from STARPY for a galaxy within the red sequence. The contours show the positions of the 'walkers' in the Markov Chain (which are analogous to the areas of high probability) for the quenching models described by $\theta = [t_q, \tau]$. The histograms show the 1D projection along each axis. Solid (dashed) blue lines show the best fit parameters (with $\pm 1\sigma$) to the data. The postage stamp image from SDSS is shown in the top right along with the debiased vote fractions for smooth (p_s) and disc (p_d) from Galaxy Zoo 2.

the 'walkers' accept this change in position. Any new position then influences the direction of the 'jumps' of other walkers (this is the case in ensemble MCMC as used in this investigation but not for simple MCMC, which is much slower at converging). This is repeated for the defined number of steps after an initial 'burn-in' phase. The length of this burn-in phase is determined after sufficient experimentation to ensure that the 'walkers' had converged on a region of parameter space. I chose to use *emcee*,[1] a Python module which implements an affine invariant ensemble sampler to explore the parameter space, written by Foreman-Mackey et al. (2013). *emcee* outputs the positions of these 'walkers' in the parameter space, which are analogous to the regions of high posterior probability.

The routine outlined above has been coded using the *Python* programming language into a package named STARPY which has been released with an open source license[2]. An example output from this module for a single galaxy from the GZ2-GALEX sample in the red sequence is shown in Figure 2.4 wherein the degeneracies of the SFH model can be clearly seen and reflect those seen in the colours in Figure 2.2. These degeneracies are present for all galaxies run through STARPY therefore if differences in the distributions arise when comparing two galaxies (or two populations), this is due to intrinsic differences in their SFHs and not due to the degeneracies of the model.

2.3 Testing STARPY

In order to test that STARPY can find the correct quenching model for a given observed colour, 25 synthesised galaxies were created with known SFHs (i.e. known values of $\theta = [t_q, \tau]$) from which optical and NUV colours were generated using the BC03 SPS models. These were input into STARPY to test whether the known values of θ were reproduced, within error, for each of the 25 synthesised galaxies. Figure 2.5 shows the results for each of these synthesised galaxies, with the known values of θ shown by the red lines (the largest difference between the known and derived values being $[\Delta t_q, \Delta\tau] \approxeq [4.5, 2.0]$). In some cases this red line does not coincide with the inferred best fit θ values shown by the blue lines, however in all cases the intersection of the red lines (i.e. the known or true values input) resides within the parameter space explored

[1] `dan.iel.fm/emcee/`

[2] `github.com/zooniverse/starpy`

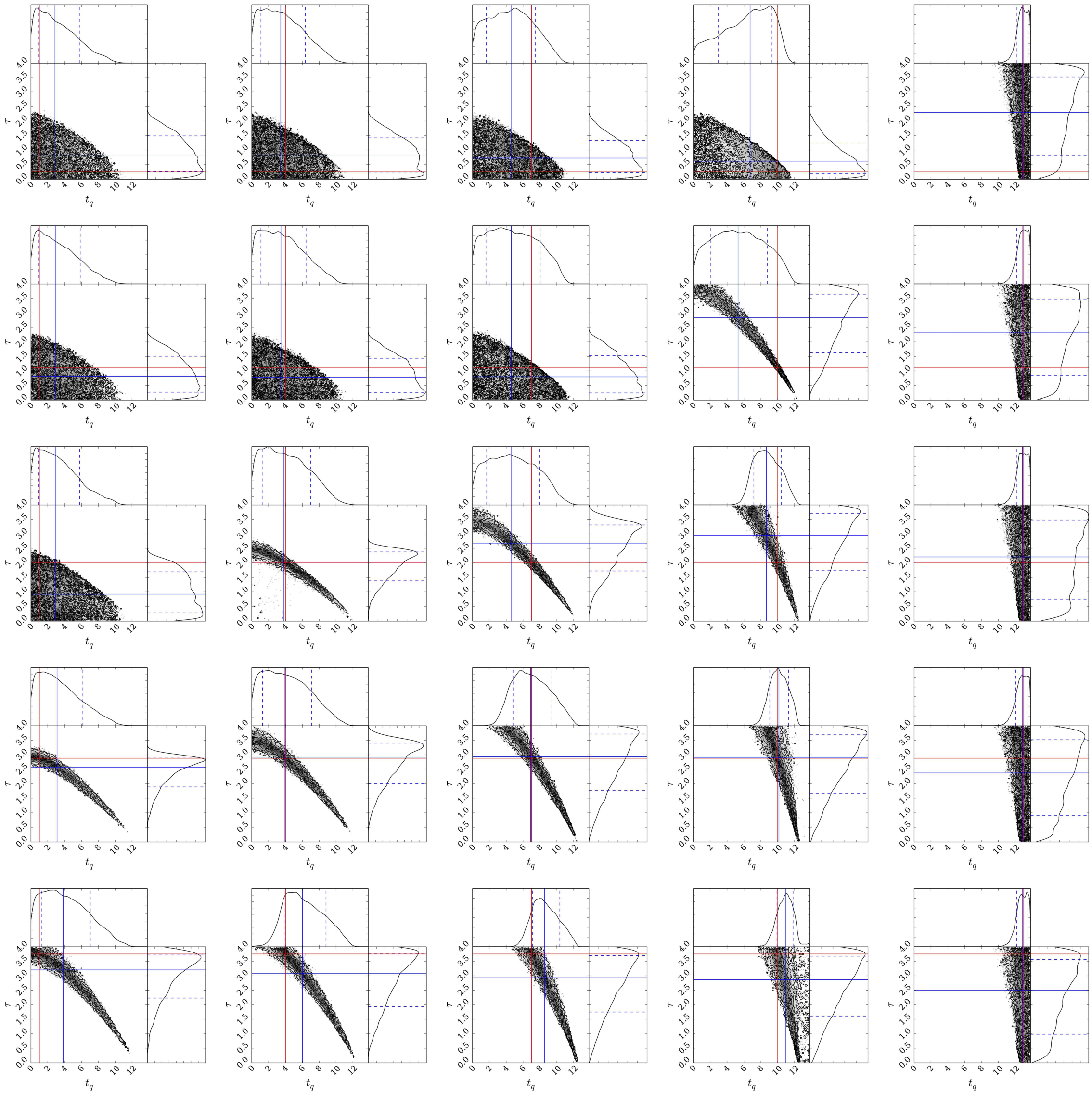

Figure 2.5: Results from STARPY for an array of synthesised galaxies with known, i.e. <u>true</u>, t_q and τ values (marked by the red lines) using the complete function to calculate the predicted colour of a proposed set of θ values in each MCMC iteration, assuming an error on the calculated known colours of $\sigma_{u-r} = 0.124$ and $\sigma_{NUV-u} = 0.215$ (the average errors on the GZ sample colours). I also assume that each synthesised galaxy has been observed at a redshift of $z = 0$. In each case STARPY succeeds (50th percentile best fit parameters are shown by the blue lines) in locating the true parameter values within the degeneracies of the star formation history model.

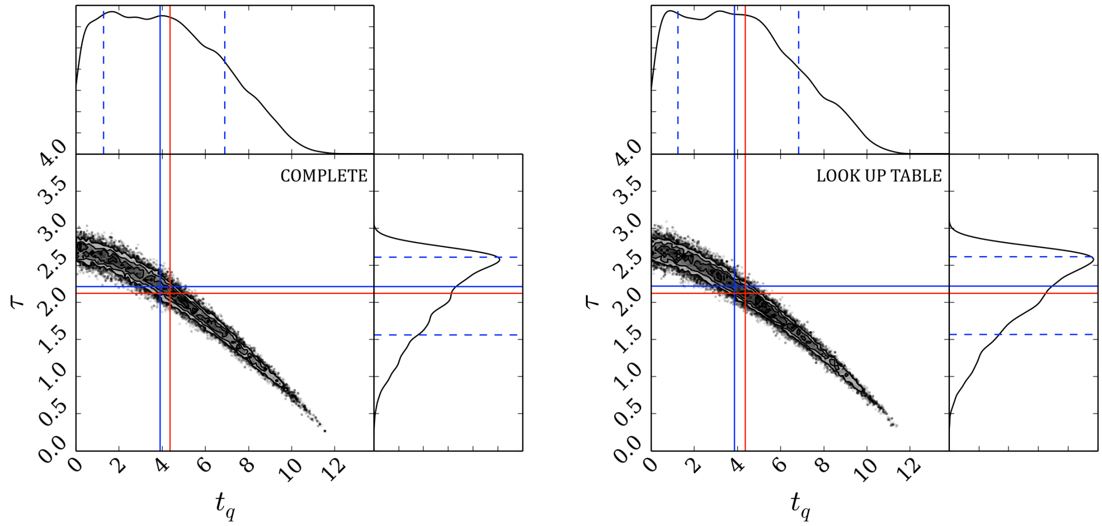

Figure 2.6: Left panel: Results from STARPY for true t_q and τ values (red lines) using the complete function to calculate the predicted colour of a proposed set of θ values in each MCMC iteration. The median walker position (the 50th percentile of the Bayesian probability distribution) is shown by the solid blue line with the dashed lines encompassing 68%($\pm 1\sigma$) of the samples (the 16th and 84th percentile positions). The time taken to run for a single galaxy using this method is approximately 2 hours. Right panel: Results from STARPY for true t_q and τ values using a look up table generated from the complete function to calculate the predicted colour of a proposed set of θ values in each MCMC iteration. The time taken to run for a single galaxy using this method is approximately 2 minutes.

by the walkers, which trace the region of highest posterior probability. Therefore STARPY succeeds in locating the true parameter values within the degeneracies of the SFH model.

2.4 Speeding up STARPY

I wish to consider the SFH model parameters for a large populations of galaxies across the colour magnitude diagram, however for each combination of θ values which *emcee* proposes for a single galaxy, a new SFH must be built, prior to convolving it with the BC03 SPS models at the observed age and then predicted colours calculated from the resultant SED. For a single galaxy this takes up to 2 hours on a typical

Table 2.1: Median walker positions (the 50th percentile; as shown by the blue solid lines in Figure 2.6) found by STARPY for a single galaxy, using the complete star formation history function and a look up table to speed up the run time. The errors quoted define the region in which 68% of the samples are located, shown by the blue lines in Figure 2.6. The known true values are also quoted, as shown by the red lines in Figure 2.6. All values are quoted to three significant figures.

	t_q	τ
True	4.37	2.12
Complete	$3.893\pm^{3.014}_{2.622}$	$2.215\pm^{0.395}_{0.652}$
Look up table	$3.850\pm^{2.988}_{2.619}$	$2.218\pm^{0.399}_{0.649}$

desktop machine for long Markov Chains. A 3-dimensional look-up table was therefore generated at 50 t^{obs}, 100 t_{quench} and 100 τ values; which were interpolated over for a given observed galaxy's age and proposed θ values at each step in the Markov Chain. This ensured that a single galaxy SFH takes approximately 2 minutes to infer on a typical desktop machine.

Figure 2.6 shows one example of how using the look up table in place of the full function does not affect the results to a significant level. Table 2.1 quotes the median walker positions (the 50th percentile of the Bayesian probability distribution) along with their $\pm 1\sigma$ ranges for both methods in comparison to the true values specified to test STARPY. The uncertainties incorporated into the quoted values by using the look up table are therefore minimal with a maximum $\Delta = 0.043$ (the difference between the complete & look up table derived values quoted in Table 2.1). This test was run with 1000 randomised $[t_q, \tau]$ values across the entire parameter space; the example shown in Figure 2.6 (with values quoted in Table 2.1) was found to have the largest difference between complete and look up table derived values, Δ.

Using this lookup table, each of the 126,316 total galaxies in the GZ2-GALEX sample was run through STARPY on multiple cores of a computer cluster to obtain the Markov Chain positions (analogous to $P(\theta_k|d_k)$) for each galaxy, k (see Figure 2.4). In each case the Markov Chain consisted of 100 'walkers' which took 400 steps in the 'burn-in' phase and 400 steps thereafter, at which point the MCMC acceptance fraction was checked to be within the range $0.25 < f_{acc} < 0.5$ (the fraction of proposed walker 'jumps' that were accepted), which was true in all cases. This acceptance fraction ensures that the walkers are sampling the probability space correctly as they explore. If $f_{acc} \sim 0$ then all the walker jumps are rejected and so the walkers won't move from their initial starting positions and the output will not represent the posterior distribution accurately. If $f_{acc} \sim 1$ then all jumps are accepted and the walkers will just perform a random walk around the parameter space, which again will not represent the posterior distribution accurately. The range of $0.25 < f_{acc} < 0.5$ used in this case is the general rule of thumb stated by Gelman, Roberts, & Gilks (1996).

2.5 POPSTARPY: studying populations of galaxies with STARPY

To study the SFH of a large population of galaxies, the individual galaxy walker positions output by STARPY (analogous to the posterior probability distribution) are combined across $[t_q, \tau]$ space. The Markov Chain walker positions are binned and weighted by their corresponding logarithmic posterior probability $\log[P(\theta_k|d_k)]$, provided by the *emcee* package, in order to emphasise the features and differences between various populations. This weighting by $\log[P(\theta_k|d_k)]$ is to minimise the contribution of galaxies poorly fit by this exponentially declining SFH (e.g. star forming galaxies). This is no longer inference of model parameters but merely a method to visualise the results across a population of galaxies (see Section 2.5.1).

I also discard those walker positions with a corresponding normalised posterior probability of $P(\theta_k|d_k) < 0.2$ in order to exclude galaxies which are not well fit by the quenching model. Therefore, galaxies which reside on the main sequence will not contribute to the final population distribution of quenching parameters. This raises the issue of whether I exclude a significant fraction of the GZ2-GALEX sample and whether those galaxies reside in a specific location of the colour-magnitude diagram. The fraction of galaxies which had all or more than half of their walker positions discarded due to low probability are shown in Table 2.2. Using the $P(\theta_k|d_k) < 0.2$ constraint, 2.4%, 7.0% and 5.4% of green, red and blue galaxies respectively had *all* of their walker positions discarded.

This is not a significant fraction of any population, therefore the STARPY module is effective in fitting the majority of galaxies and this method of discarding walker positions ensures that poorly fit galaxies are removed from the analysis of the results. Figure 2.7 shows that these galaxies with discarded walker positions are also scattered

Table 2.2: The number of galaxies in each population which had walker positions discarded due to low posterior probability values in order to exclude those galaxies from the analysis which were poorly fit by the SFH quenching model.

	Red Sequence	**Green Valley**	**Blue Cloud**
All walkers discarded	1420 (7.00%)	437 (2.41%)	3109 (5.37%)
More than half walker positions discarded	2010 (9.92%)	779 (4.30%)	6669 (11.52%)

across the optical-NUV colour-colour diagram and therefore STARPY is also effective in fitting galaxies across this entire plane. The galaxies that are discarded can be seen to mostly lie outside the contours of the GZ2-GALEX sample in the colour-colour plane shown in Figure 2.7. This is due to the SPS models used to produce the SEDs of the model SFHs; these models are calibrated with typical galaxies rather than the extremes of galaxy evolution. Those galaxies with red (blue) optical colours but blue (red) NUV colours are oddities which cannot be explained by the SPS models and so STARPY has particular difficulty fitting a SFH to these galaxies.

Figure 2.5 shows how peaks in the histograms are found across all areas of the parameter space in both dimensions $[t_q, \tau]$, ensuring that any conclusions drawn from combined population distributions are due to a superposition of extended probability distributions, as opposed to a bimodal distribution of probability distributions across all galaxies.

I also utilise the GZ2 debiased user vote fractions to obtain separate population density distributions for both smooth and disc galaxies. This is obtained by also weighting by the morphology vote fraction of each individual galaxy when the binned walker positions of each galaxy in a population are combined. This ensures that the entirety of the GZ2-GALEX sample is used, negating the need for a threshold on the GZ2 vote fractions (e.g., $p_d > 0.8$ as used in Schawinski et al., 2014) to give two separate definitively disc and smooth galaxy populations. This ensures that those galaxies of intermediate morphology are still included in the analysis. The walkers of those galaxies with a higher morphological vote fraction, p_d (p_s), are weighted more heavily and so contribute more to the disc (smooth) weighted combined walker distributions. These distributions will be referred to as the population densities.

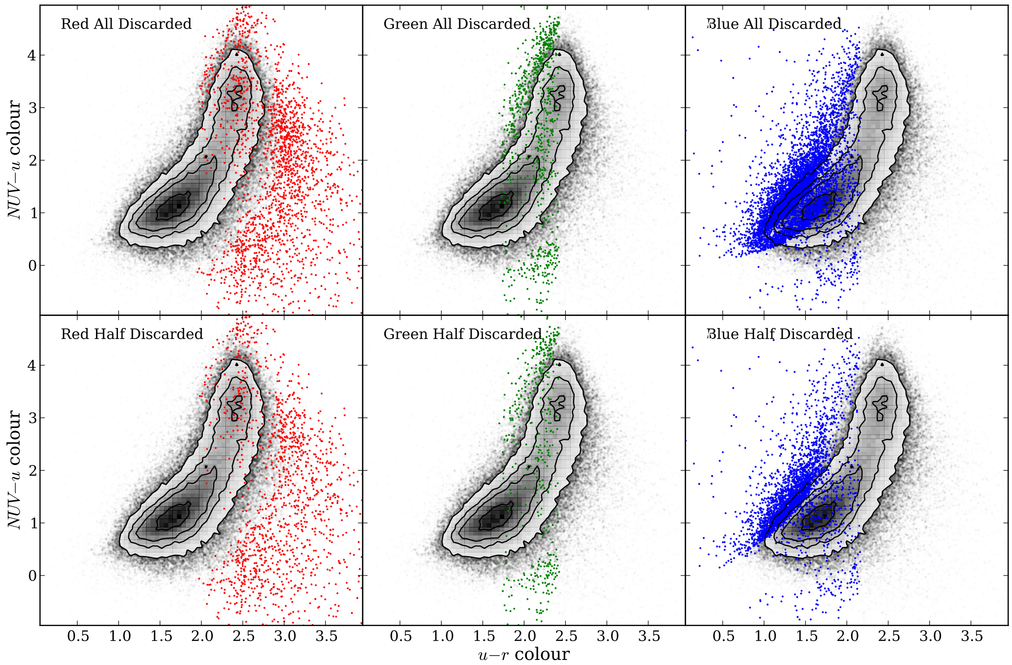

Figure 2.7: Contours show the GZ2-GALEX sample optical-NUV colour-colour diagram. The points show the positions of the galaxies which had all (top panels) or more than half (bottom panel) of their walker positions discarded due to their low probability for the red sequence (left), green valley (middle) and blue cloud (right).

For example, the galaxy shown in Figure 2.4 would contribute almost evenly to both the smooth and disc parameters due to the GZ2 vote fractions. Since galaxies with similar vote fractions contain both a bulge and disc component, this method is effective in incorporating intermediate galaxies which are thought to be crucial to the morphological changes between early- and late-type galaxies. It was the consideration of these intermediate galaxies which was excluded from the investigation by Schawinski et al. (2014).

2.5.1 Alternative Hierarchical Bayesian approach

The approach presented above relies upon a visualisation of the SFHs across each population, with no inference involved beyond the use of STARPY to derive the individual galaxy SFHs. An alternative approach to this problem would be to use a hierarchical Bayesian method to determine the 'hyper-parameters' that describe the distribution of the parent population $\theta' = [t'_q, \tau']$ that each individual galaxy's SFH is drawn from.

The posterior PDF for $\vec{\theta}'$ to describe such a galaxy population:

$$P(\vec{\theta}'|\vec{d}) = \frac{P(\vec{d}|\vec{\theta}')P(\vec{\theta}')}{P(\vec{d})}, \tag{2.8}$$

where $\vec{d}$ represents all of the optical and NUV colour data in a population $\{\vec{d}_k\}$. For one galaxy, k, the marginalised likelihood is:

$$P(d_k|\vec{\theta}') = \iint P(d_k|t_k, \tau_k)P(t_k, \tau_k|\vec{\theta}')\ \mathrm{d}t_k\ \mathrm{d}\tau_k \tag{2.9}$$

and for all galaxies, N, therefore:

$$P(\vec{d}|\vec{\theta}') = \prod_k^N P(d_k|\vec{\theta}'). \tag{2.10}$$

Using STARPY for an individual galaxy, k the output is the 'interim' posterior $P(t_k, \tau_k|d_k)$ which I can relate to $P(d_k|t_k, \tau_k)$ so that:

$$P(d_k|\vec{\theta}') = \iint P(t_k, \tau_k|d_k).P(d_k).\frac{P(t_k, \tau_k|\vec{\theta}')}{P(t_k, \tau_k)}\ \mathrm{d}t_k\ \mathrm{d}\tau_k. \tag{2.11}$$

In order to calculate this I draw N_s random samples, r, from each interim posterior, $P(t_k, \tau_k|d_k)$ so that Equation 2.11 can be expressed as a sum over a number of random samples, N_s (as with the calculation of an expected mean):

$$P(d_k|\vec{\theta}') = \frac{P(d_k)}{N_s} \sum_r^{N_s} \frac{P(t_{k,r}, \tau_{k,r}|\vec{\theta}')}{P(t_k, \tau_k)}, \tag{2.12}$$

for the r^{th} sample of N_s total samples taken from one galaxy's, k, interim posterior PDF. This fraction is known as the 'importance weight', w_r, in importance sampling.

However, I also have two morphological vote fractions that I can weight by to determine separate hyper-parameters, $\vec{\theta}' = [\vec{\theta}'_d, \vec{\theta}'_s]$, for both disc, d, and smooth, s, galaxies. Therefore:

$$w_r = \frac{P(t_{k,r}, \tau_{k,r}|\vec{\theta}')}{P(t_k, \tau_k)} = \frac{p_{d,k}P(t_{k,r}, \tau_{k,r}|\vec{\theta}'_d) + p_{s,k}P(t_{k,r}, \tau_{k,r}|\vec{\theta}'_s)}{P(t_k, \tau_k)} \tag{2.13}$$

If we substitute equation 2.12 into equation 2.8 we find that the $P(d_k)$ terms cancel and we are left with:

$$P(\vec{\theta}'|\vec{d}) = P(\vec{\theta}') \prod_k^N \frac{1}{N_{s,k}} \sum_r^{N_s} w_r, \tag{2.14}$$

where $P(\vec{\theta}')$ is the assumed prior on the hyper-parameters, which is assumed to be uniform.

This approach is heavily dependent on what shape is assumed for the hyper-distribution; a decision which is not trivial. It is often common for this function to take the form of a multi-component Gaussian mixture model (Mackay, 2003; Lahav et al., 2000). For example a two component Gaussian mixture model in $[t_q, \tau]$ space is described by eight hyper-parameters for a single morphology, $\vec{\theta}' = [\mu_{t,1}, \sigma_{t,1}, \mu_{\tau,1}, \sigma_{\tau,1}, \mu_{t,2}, \sigma_{t,2}, \mu_{\tau,2}, \sigma_{\tau,2}]$. This approach assumes no covariance between hyper-parameters for simplicity. The equations outlined above, combined with MCMC methods can be used to infer these eight $\vec{\theta}'$ parameters from which the hierarchical population distribution can be determined.

In order to test whether this assumption of a multi-component Gaussian mixture model is appropriate, I sampled the inferred hierarchical distributions to produce replica datasets in optical-NUV colour space. These are shown here in Figure 2.8

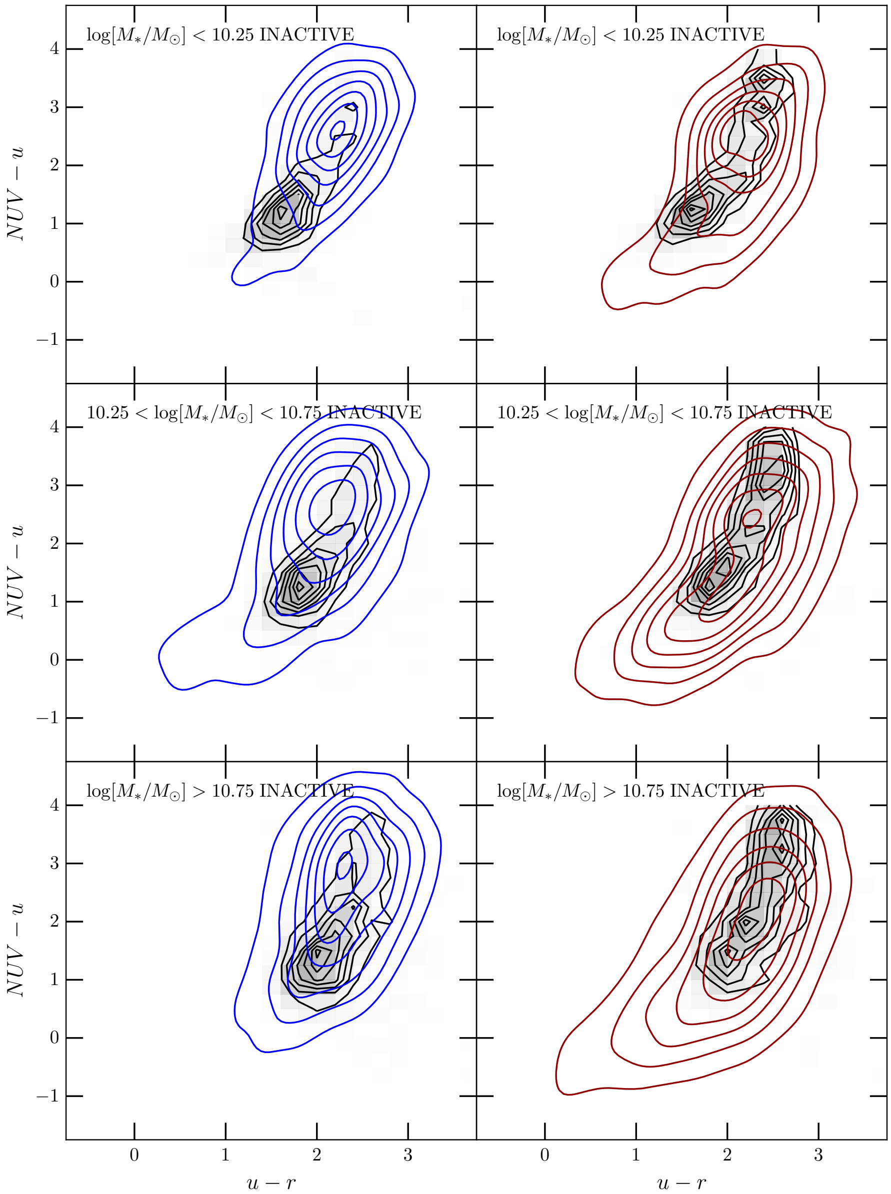

Figure 2.8: Optical-NUV colour-colour diagrams for the INACTIVE galaxies shown by the black contours, split into low mass (top), medium mass (middle) and high mass (bottom) galaxies weighted by p_d (left) and p_s (right). Kernel smoothing has been applied to the overlaid replica datasets, which are created by sampling from the **inferred 2 component Gaussian mixture model hierarchical parent distributions**. Gaussian random noise is also added to the inferred colours, with a mean and standard deviation of the errors on the observed colours of the respective sample. Contours are shown for samples taken from the disc (blue) and smooth weighted (red) inferred hierarchical distributions.

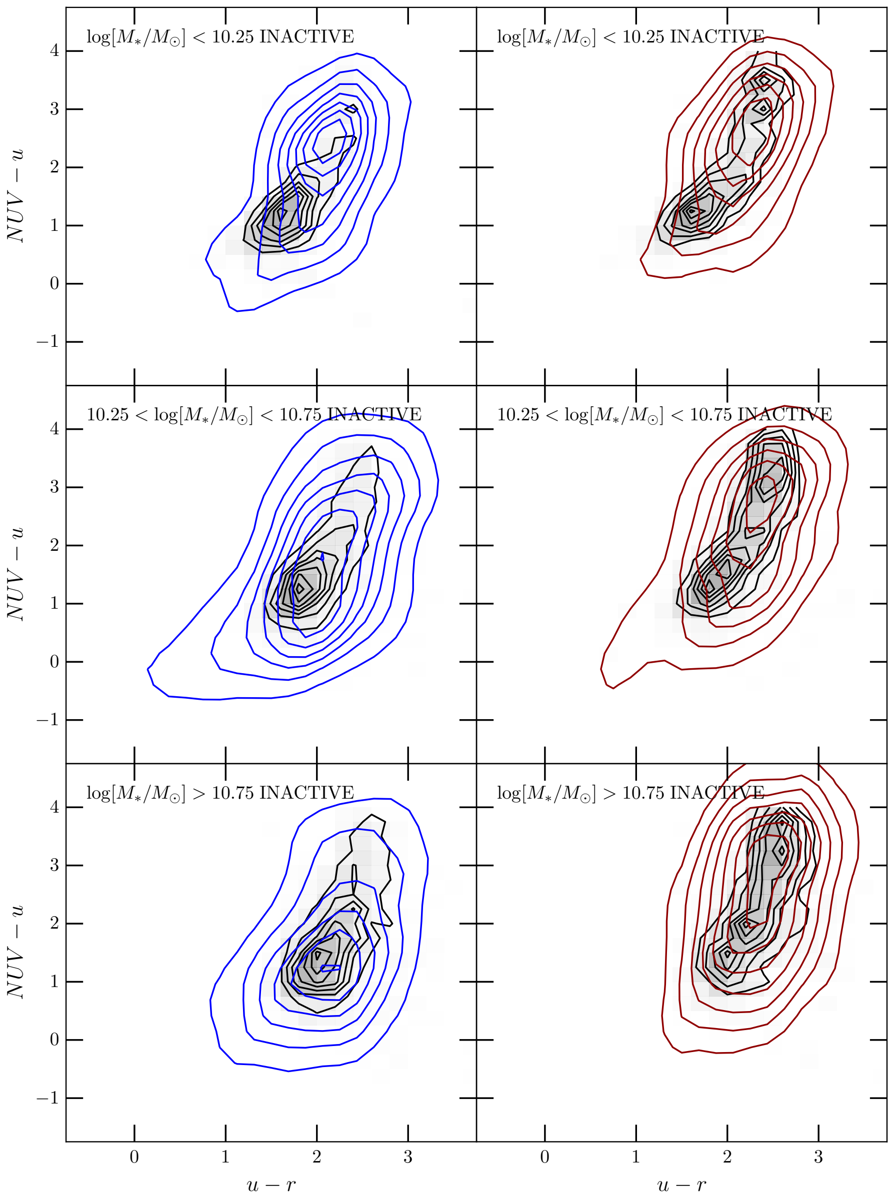

Figure 2.9: Optical-NUV colour-colour diagrams for the INACTIVE galaxies shown by the black contours, split into low mass (top), medium mass (middle) and high mass (bottom) galaxies weighted by p_d (left) and p_s (right). Kernel smoothing has been applied to the overlaid replica datasets, which are created by sampling from the **popstarpy population density distributions described in Section 2.5**. Gaussian random noise is also added to the inferred colours, with a mean and standard deviation of the errors on the observed colours of the respective sample. Contours are shown for samples taken from the disc (blue) and smooth weighted (red) inferred hierarchical distributions.

in comparison to the observed colour-colour distributions of the INACTIVE sample (a subset of $\sim 6,000$ galaxies from the GZ2-GALEX sample, see Section 4.1). For all masses and morphologies the replicated $u-r$ and $NUV-u$ colours do not accurately match the observed data.

I also varied the value of N_s and found that increasing the number of samples drawn did not improve this fit for the INACTIVE population. Similarly increasing the number of components in the Gaussian mixture model did not immediately improve the accuracy of the fit along with other functional forms which require too many assumptions to be made about the shape of the parent distribution. I therefore concluded that assuming any functional form of the population distribution was unsatisfactory.

The POPSTARPY approach described in section 2.5 was motivated by the investigation increasing the number of samples, N_s, drawn from the posterior of each galaxy, k, until the point where all the samples were drawn. Instead of attempting to infer parameters to describe this distribution, as above, I presented the combined distributions of all individual galaxies in a population (as described in Section 2.5). The distributions produced by this visualisation method reveal the complexity that the parent distribution must describe which, as concluded earlier, cannot be effectively modelled.

I also tested whether the POPSTARPY method is reasonable by producing replica datasets in optical-NUV colour space, as before, by drawing 1000 $[t_q, \tau]$ values from the population density distributions derived for the INACTIVE sample (see Section 4.1). These replica datasets are shown here in Figure 2.9 in comparison to the observed colour-colour distributions of the INACTIVE sample. Comparing these replica colours in Figure 2.9, with those produced by drawing from the inferred hierarchical distributions, shown in Figure 2.8, they can be seen to produce a more accurate match to the observed data for the majority of masses and morphologies.

Considering these issues with assuming a functional form for the hierarchical parent distribution, an expansion on this approach would be to perform 'heat map optimization', similar to image reconstruction, to determine the parent distribution for a given population. The population parameter space woul,d be divided into an $M \times M$ grid of pixels and the value of each pixel would be a model parameter to be inferred by hierarchical Bayesian methods. Each pixel would need a prior (e.g. a basic entropic prior) and the heat map would sum to unity. In order for this pixel map to accurately characterise the detail expected in the parent populations, this pixel grid would need to be sufficiently large, with at least a 50x50 grid of pixels (i.e. upwards of 2500 model parameters, θ', to be inferred). This is a significant expansion upon the work presented here and is something I wish to investigate in future work.

For the results presented in the following chapters, I therefore use the POPSTARPY method to visualise the population distribution, rather than quoting inferred values to describe it.

Chapter 3

The morphological dependance of quenching

The work in the following chapter has been published in Smethurst et al. (2015).

By studying the galaxies which have just left the 'star forming sequence' (SFS; see left panel of Figure 2.1), the nature of the quenching mechanisms which cause this departure can be probed. By investigating the *amount* of quenching that has occurred in the blue cloud, green valley and red sequence and by comparing that amount across the three populations, we can apply constraints to the many possible quenching mechanisms outlined in Chapter 1.

I have been motivated by a recent result suggesting that there are two contrasting evolutionary pathways through the green valley for different morphological types (Schawinski et al. 2014, hereafter S14). S14 used the exponentially declining star formation model, described in Section 2.1, to obtain predicted optical and NUV colours for four possible SFHs through the green valley; two with fast quenching rates ($\tau = [0.001, 0.25]$ Gyr) and two with slower quenching rates ($\tau = [1, 2.5]$ Gyr). These predicted optical and NUV colours were then compared to the observed colours of early- and late-type green valley galaxy colours. S14 then concluded that late-type galaxies quench with a slower rate and form a nearly static disc population in the green valley, whereas early-type galaxies quench with very rapid rates, transitioning through the green valley and onto the red sequence in ~ 1 Gyr (Wong et al., 2012).

Although this result showing morphologically dependent quenching is intriguing, the work of S14 is hindered for the following reasons: (i) the incompleteness of the galaxy sample; only definitively early- ($p_s \geq 0.8$) and late-type ($p_s \leq 0.8$) galaxies were studied, whereas galaxies of intermediate morphology were excluded, and (ii) the lack of statistics to support the conclusions. Here I use the same toy SFH model but implement STARPY in order to statistically study the star formation histories of galaxies of all morphologies across the colour magnitude diagram.

3.1 Defining the Green Valley

To define which of the 126,316 galaxies of the GZ2-GALEX sample are in the green valley, I looked to previous definitions in the literature defining the separation between the red sequence and blue cloud. For example, Baldry et al. (2004) traced this bimodality with a large sample of 66,846 local SDSS galaxies ($0.004 < z < 0.08$) by fitting double-peaked Gaussians to the colour magnitude diagram. Their relation between the $u - r$ colour, C'_{ur}, and r-band magnitude, M_r, to define the colour cut between the blue and red galaxy populations is defined in their Equation 11 as:

$$C'_{ur}(M_r) = 2.06 - 0.244 \tanh\left(\frac{M_r + 20.07}{1.09}\right). \tag{3.1}$$

Due to the necessity for NUV photometry in this study, matching to GALEX removed typical 'red and dead' galaxies from the GZ2-GALEX sample. This is apparent in the optical $u - r$ colour histograms shown in the right panels of Figure 3.1; the GZ2-GALEX sample is split in bins of absolute r-band magnitude and for each bin the position of the green valley at that M_r, as defined by Baldry et al. (2004) is shown. For the GZ2-GALEX sample at brighter r-band magnitudes (i.e. larger mass), this definition of the green valley seems to intersect with the observed peak at red colours.

However, for a more complete SDSS sample (from the MPA-JHU catalog; Kauffmann et al. 2003b; Brinchmann et al. 2004, left panels of Figure 3.1) the Baldry et al. (2004) green valley definition does not intersect with the peak at red colours, as this sample is complete, containing the high mass typical 'red and dead' galaxies of the red sequence. It would therefore not be appropriate to define the green valley by a visual fit to the colour magnitude diagram for this sample (this method was used in

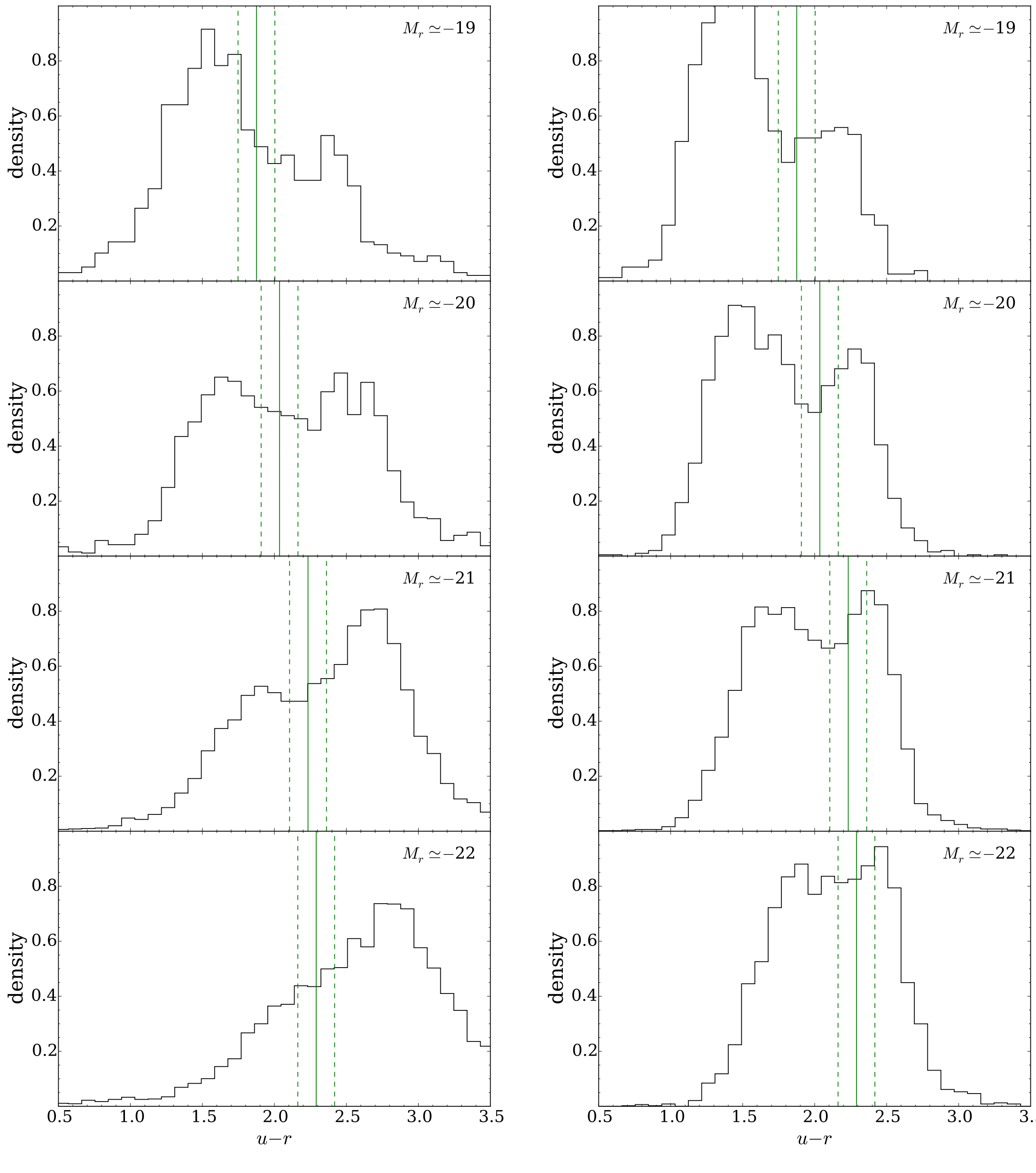

Figure 3.1: Optical $u - r$ colour histograms, sliced in absolute r-band magnitude for a complete SDSS sample (MPA-JHU catalog; left) and for the GZ2-GALEX sample (right). In each panel the definition between the blue cloud and the red sequence from Baldry et al. (2004) is shown by the dashed line (as defined in Equation 3.1); the solid lines show $\pm 1\sigma$ either side of this definition.

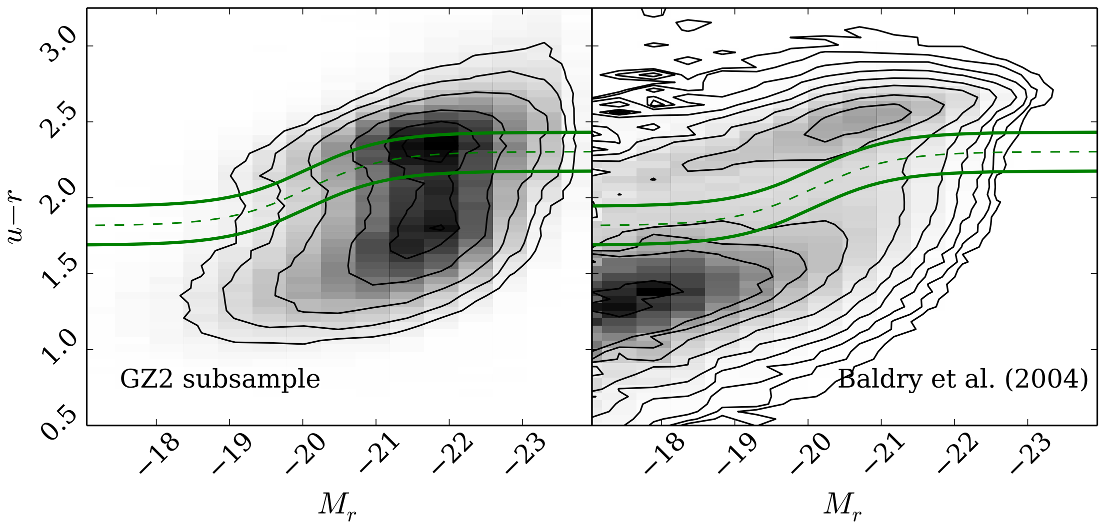

Figure 3.2: Colour-magnitude diagram for the GZ2-GALEX sample (left) and the SDSS sample from Baldry et al. (2004, right). In both panels the definition between the blue cloud and the red sequence from Baldry et al. (2004) is shown by the dashed line, as defined in Equation 3.1. The solid lines show $\pm 1\sigma$ either side of this definition; any galaxy within the boundary of these two solid lines is considered a green valley galaxy. The lack of red sequence galaxies due to the necessity for NUV GALEX colours skews the apparent location of the green valley in the GZ2-GALEX sample, therefore a literature definition of the green valley is used to ensure galaxies are correctly classified.

S14 and adopting it here would have allowed for a direct comparison to this previous work) as this would cause green valley galaxies to be misclassified as red sequence.

I therefore adopt the Baldry et al. (2004) green valley definition for this study, which is shown in Figure 3.2 by the dashed line, overlaid on both the GZ2-GALEX sample (left) and the SDSS data used by Baldry et al. (2004, right). I employ a conservative definition of the green valley; any galaxy within $\pm 1\sigma$ of the Baldry et al. relationship, shown by the solid lines in Figure 3.2, is therefore considered a green valley galaxy.

Despite the requirement for NUV photometry, the GZ2-GALEX sample still contains typical galaxies from across the entirety of the colour magnitude diagram, including the red sequence. Ko et al. (2013) show that in a sample of quiescent red-sequence galaxies without Hα emission (i.e. without spectral indication of recent star

Table 3.1: Table showing the decomposition of the GZ2-GALEX sample by galaxy type into the subsets of the colour-magnitude diagram.

	All	Red Sequence	Green Valley	Blue Cloud
Smooth-like ($p_s > 0.5$)	42453 (33.6%)	17424 (61.9%)	10687 (44.6%)	14342 (19.3%)
Disc-like ($p_d > 0.5$)	83863 (80.7%)	10722 (38.1%)	13257 (55.4%)	59884 (47.4%)
Early-type ($p_s \geq 0.8$)	10517 (8.3%)	5337 (18.9%)	2496 (10.4%)	2684 (3.6%)
Late-type ($p_s \geq 0.8$)	51470 (40.9%)	4493 (15.9%)	6817 (28.5%)	40430 (54.4%)
Total	**126316** (100.0%)	28146 (22.3%)	23944 (18.9%)	74226 (58.7%)

formation), 26% show NUV excess emission and that the fraction with recent star formation is 39%. Therefore this requirement for NUV photometry still allows for the selection of typical red sequence galaxies. Using the definition of the star forming SFS from Peng et al. (2010, see Section 2.1) I find that 94% of the red sequence galaxies in the GZ2-GALEX sample lie more than 1σ below the main sequence; see Table 3.2).

The decomposition of the GZ2-GALEX sample into red sequence, green valley and blue cloud galaxies is shown in Tables 3.1 and 3.2 along with further division by galaxy type and SFR (where available for the GZ2-GALEX sample from the MPA-JHU catalog) respectively. The tables also list the definitions I adopt henceforth for early-type ($p_s \geq 0.8$), late-type ($p_d \geq 0.8$), smooth-like ($p_s > 0.5$), disc-like ($p_d > 0.5$), quenched (SFR $< P - 5\sigma$), quenching ($P - 5\sigma <$ SFR $< P - \sigma$) and star forming (SFR $> P - \sigma$) galaxies, where P is the SFR as defined by Peng et al. (2010) for a given stellar mass and observed time (see Equation 2.2).

Figure 3.3 shows the SFR against the stellar mass for the GZ2-GALEX sample (where available from the MPA-JHU catalog) split into blue cloud, green valley, red sequence, late- and early-type populations. This figure (see bottom row, middle panel) confirms that the green valley galaxies in the GZ2-GALEX sample are indeed a population which have either left, or begun to leave, the star forming SFS. A relatively small fraction (20.6%; see Table 3.2) are also classified as star forming

Table 3.2: Table showing the decomposition of the GZ2-GALEX sample by their star formation rate in the subsets of the colour-magnitude diagram.

	All	Red Sequence	Green Valley	Blue Cloud
Quenched	24278	17018	6440	820
($\mathrm{SFR} < \mathrm{P} - 5\sigma$)	(19.7%)	(60.9%)	(27.5%)	(1.1%)
Quenching	34743	9277	12181	13285
($P - 5\sigma < \mathrm{SFR} < \mathrm{P} - \sigma$)	(28.2%)	(33.1%)	(51.9%)	(18.6%)
Star Forming	63957	1665	4828	57464
($\mathrm{SFR} > \mathrm{P} - \sigma$)	(52.0%)	(5.9%)	(20.6%)	(80.3%)
Total	**122,978**	27960	23449	71569
	(100.0%)	(22.7%)	(19.1%)	(58.2%)

galaxies, however the middle panel, bottom row of Figure 3.3 shows that these galaxies reside on the low SFR side of the SFS.

3.2 Results

The population density distributions for both smooth and disc weighted populations in the red sequence, green valley and blue cloud are shown in Figures 3.4, 3.5 & 3.7 respectively. The full two dimensional distributions in $[t, \tau]$ are shown in each case, along with a histogram showing the one dimensional projection for each individual parameter, marginalised over the other one. The percentages shown in Figures 3.4, 3.5 & 3.7 are calculated as the fractions of the population densities located in each region of parameter space for a given population.

Since the sample contains such a large number of galaxies, a peak in the population densities will be caused by a large number of galaxies with peaks in their individual posterior distribution at that location in parameter space. This will overwhelm contributions to this area of the population density from galaxies where this region of parameter space is not dominant in their individual posterior distributions. Therefore these fractions can be interpreted as broadly equivalent to the percentage of galaxies in a given population undergoing quenching at a rate within the stated range. Although this is not quantitatively exact, it is nevertheless a useful framework for interpreting the population densities.

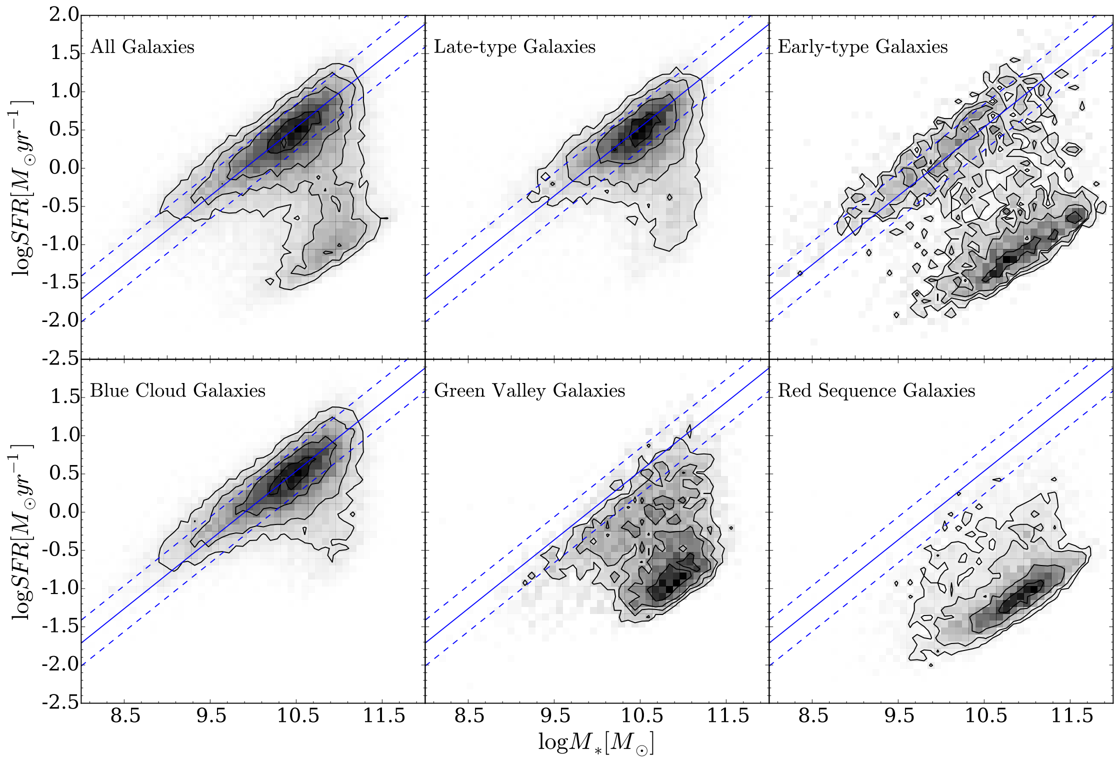

Figure 3.3: Star formation rate against stellar mass for the different populations of galaxies (top row, left to right: all galaxies, late-type galaxies, early-type galaxies; bottom row, left to right: blue cloud, green valley and red sequence galaxies) and how they contribute to the star forming sequence (from Peng et al. (2010), shown by the solid blue line with 0.3 dex scatter by the dashed lines). Based on positions in these diagrams, the green valley does appear to be a transitional population between the blue cloud and the red sequence. Detailed analysis of star formation histories can elucidate the nature of the different populations' pathways through the green valley.

Figure 3.8 shows the distribution of the median walker positions (the 50th percentile of the posterior probability distribution) of each individual galaxy, split into red, green and blue disc-like ($p_d > 0.5$) and smooth-like ($p_s > 0.5$; in order to incorporate the full GZ2-GALEX sample and still investigate the morphological dependance of the results) populations. Unlike in the POPSTARPY method (see Section 2.5) these plots were made without discarding any walker positions due to low probability and without weighting by the GZ2 morphological vote fractions. Figure 3.8 may therefore be more intuitive to understand than Figures 3.4, 3.5 & 3.7.

Although the quenching rates are continuous in nature, in this Section I will refer to rapid, intermediate and slow quenching rates which correspond to ranges of τ [Gyr] < 1.0, $1.0 < \tau$ [Gyr] < 2.0 and τ [Gyr] > 2.0 respectively for ease of discussion.

3.2.1 The Red Sequence

The top panel of Figure 3.4 reveals that the red sequence smooth weighted population density is dominated by rapid quenching rates across all cosmic time (with an estimated 49.5% of galaxies undergoing quenching at this rate; see Figure 3.4). At early quenching times (high redshift), the population density is dominated by slow and intermediate rates (top panel of Figure 3.4). Perhaps this is the influence of intermediate galaxies (with $p_s \sim p_d \sim 0.5$), which would explain why similar high density areas exist for both the smooth and disc weighted populations in both panels of Figure 3.4. This is especially apparent considering there are far more of these intermediate galaxies than those that are definitively early- or late-types (see Table 3.1).

The bottom panel of Figure 3.4 reveals a bimodal distribution for the disc weighted population density between rapid (31.3%) and slow (44.1%) quenching rates. The *very* slow ($\tau > 3.0$ Gyr) quenching rates present in the red disc population density (which are not seen in either the green valley or blue cloud, see Figures 3.5 and 3.7) with $[t, \tau] \sim [1, 3.5]$ Gyr take approximately 11.5 Gyr to transition to the red sequence in the SFH models. This suggests that these galaxies have only just reached the red sequence after a very slow evolution across the colour-magnitude diagram. Considering their limited number and the requirement for NUV emission, it is likely that these galaxies are currently on the edge of the red sequence having recently (and finally) moved out of the green valley.

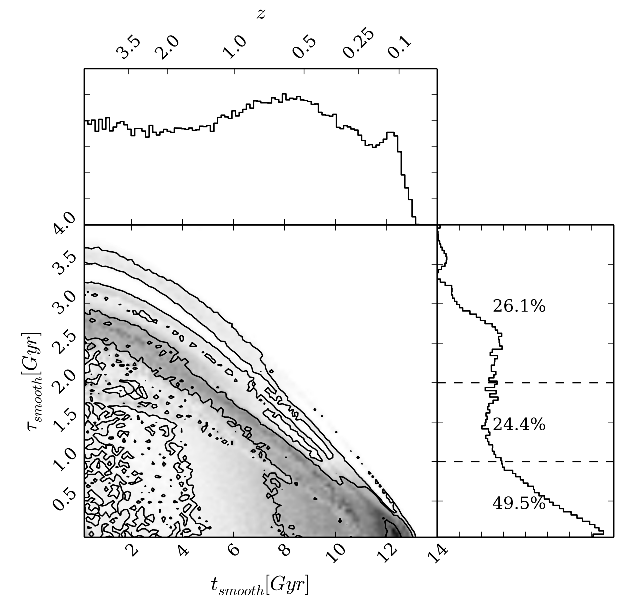

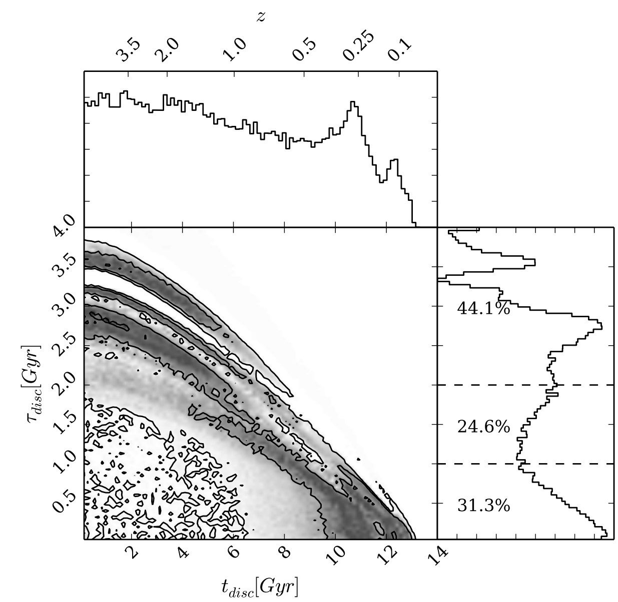

Figure 3.4: Contour plots showing the population densities for red sequence galaxies of the GZ2-GALEX sample, weighted by the morphological vote fractions from GZ2 to give both bulge (top) and disc (bottom) dominated distributions. The histograms show the projection into one dimension for each parameter. The dashed lines show the separation between rapid (τ [Gyr] < 1.0), intermediate ($1.0 < \tau$ [Gyr] < 2.0) and slow (τ [Gyr] > 2.0) quenching rates with the fraction of the combined posterior probability distribution in each region shown (see Section 2.2).

Tojeiro et al. (2013) used the VErsatile SPectral Analyses spectral fitting code (VESPA; Tojeiro et al. 2007) and found that red late-type spirals show 17 times more recent star formation than red elliptical galaxies. The results in Figure 3.4 can be tested against this finding by comparing the SFRs predicted by the inferred SFH model of both the smooth and disc weighted population densities (these SFRs are shown in Figure 2.2). For the peak at early times and slow quenching rates in the red disc weighted population density, this SFH model still has some residual star formation occurring with a SFR ~ 0.105 $\mathrm{M_{\odot}yr^{-1}}$. Whereas for the peak at recent times and rapid quenching rates in the red smooth weighted population density, this SFH model has a resultant SFR ~ 0.0075 $\mathrm{M_{\odot}yr^{-1}}$. This is approximately 14 times less than the residual SFR still occurring in the red disc weighted population; within error, this is in agreement with the findings of Tojeiro et al. (2013).

These results for the red sequence galaxies have many implications for green valley galaxies, as all of these systems must have passed through the green valley on their way to the red sequence.

3.2.2 Green Valley Galaxies

Figure 3.5 shows how the smooth weighted green valley population density is dominated by both intermediate quenching rates (40.6%) and slow quenching at rates early times ($z > 1$; 40.7%). The fraction of the population density at rapid quenching rates in this smooth weighted population has dropped by over a half compared to the red sequence smooth weighted population. This is caused, in part, by the fact that rapidly quenching galaxies will transition through the green valley very quickly. To quantify this I tested the time spent in the green valley across the $[t, \tau]$ parameter space assuming a stellar mass, $m = 10^{10.27} M_{\odot}$ (the mean mass of the GZ2-GALEX sample), which is shown in Figure 3.6. The galaxies with such a rapid decline in star formation rate spend very little time in the green valley, therefore fewer of these galaxies will reside in the green valley at any one time in comparison to those galaxies transitioning with slower quenching rates. However the amount of rapid quenching occurring across the entire galaxy population is not underestimated, as all galaxies which have undergone a rapid quenching history will now be found in the red sequence and detected there in the GZ2-GALEX sample. This contributes to the dominance of rapid quenching rates in the red sequence population densities (see Figure 3.4) and explains the observed

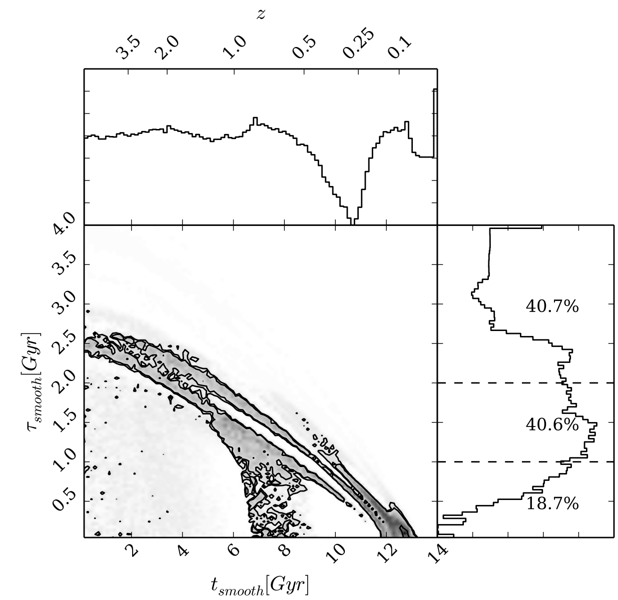

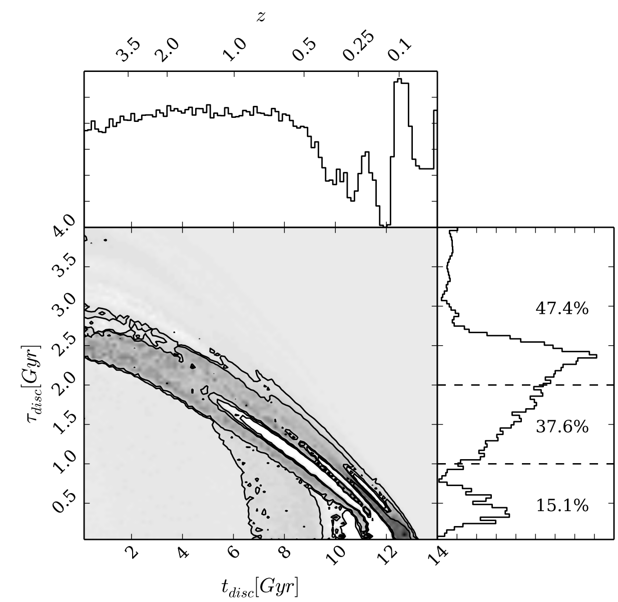

Figure 3.5: Contour plots showing the population densities for green valley galaxies in the GZ2-GALEX sample weighted by the morphological vote fractions from GZ2 to give both bulge (top) and disc (bottom) dominated distributions. The histograms show the projection into one dimension for each parameter. The dashed lines show the separation between rapid (τ [Gyr] < 1.0), intermediate ($1.0 < \tau$ [Gyr] < 2.0) and slow (τ [Gyr] > 2.0) quenching rates with the fraction of the combined posterior probability distribution in each region shown (see Section 2.2).

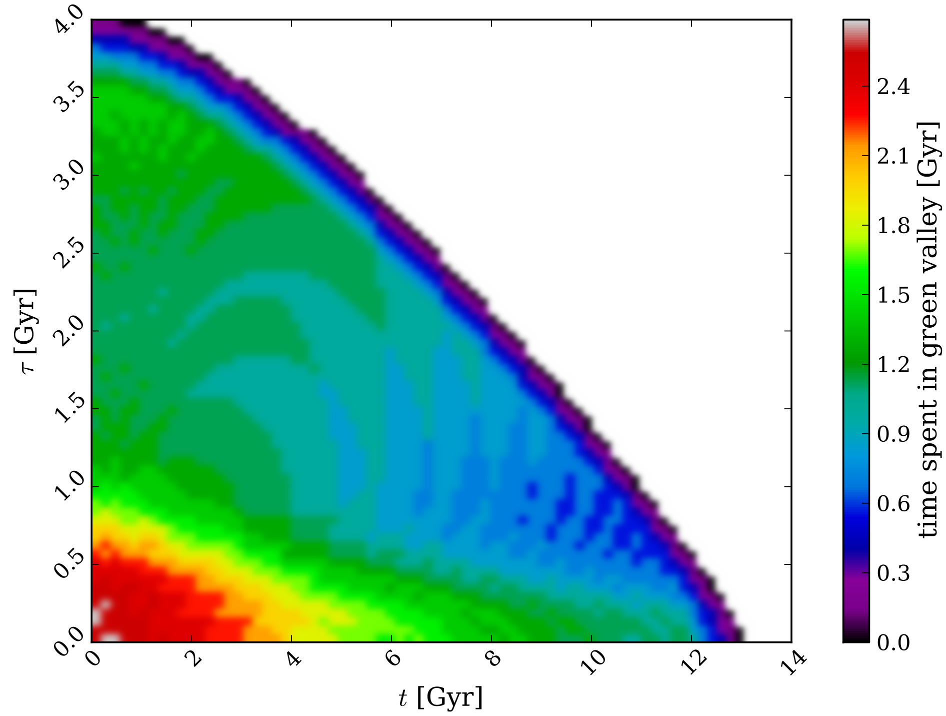

Figure 3.6: Plot showing the time spent in the green valley across the SFH model parameter space by the current epoch. This affects the observability of those galaxies which have quenched rapidly and recently and have passed too quickly through the green valley to be detected. The white region denotes those models with colours that do not enter the green valley by the present cosmic time.

number of intermediate morphology galaxies (see Table 3.1) which are present in the green valley (assuming a morphological change occurs during the quench).

The green valley disc weighted population density is completely dominated by slow quenching rates (47.4%) with a slightly smaller fraction of intermediate quenching rates detected than in the smooth weighted population (37.6%; see Figure 3.5).

If the population densities of Figures 3.5 & 3.4 are compared, quenching is detected at later cosmic times (lower redshift) in the green valley than in the red sequence for both morphological types. This therefore suggests that both morphologies are tracing the evolution of the red sequence (i.e. evolving with the same quenching histories just at a later time), confirming that the green valley is indeed a transitional population between blue cloud and red sequence regardless of morphology.

Given enough time ($t \sim 4 - 5$ Gyr), the current green valley disc galaxies will therefore eventually transition through to the red sequence (the right panel of Figure 2.1 shows galaxies with $\tau > 1.0$ Gyr do not approach the red sequence within 3 Gyr post quench). This is most likely the origin of the 'red spirals', attributed to the *very* slow quenching rates discussed in Section 3.2.1 (and see bottom panel of Figure 3.4). This is in contradiction to the conclusions of S14 who state that the disc population stall in the green valley.

Considering this result that the green valley is a transitional population, the ratio of smooth : disc galaxies that is currently observed in the green valley is expected to evolve into the ratio observed in the red sequence (assuming that the decreased number of galaxies detected in the red sequence due to matching to GALEX is independent of morphology). Table 3.1 shows the ratio of smooth-like : disc-like galaxies in the red sequence is 62 : 38, whereas in the green valley this ratio is 45 : 55. Making very simple assumptions that this ratio does not change with redshift and that quenching is the only mechanism which causes a morphological transformation, then 31.2% of the disc-like galaxies in the green valley would have to undergo a morphological change to a smooth-like galaxy.

Inspecting the disc weighted green valley population density (bottom panel of Figure 3.5) reveals that 29.4% of the distribution occupies the $\tau < 1.5$ Gyr parameter space. Since this is a similar fraction to the number of green valley disc-like galaxies which would have to undergo a morphological change to a smooth-like galaxy to match the ratio of smooth : disc galaxies in the red sequence, this suggests that quenching mechanisms with $\tau < 1.5$ Gyr are capable of destroying the disc-dominated structure of galaxies.

All of this evidence suggests that there are not just two contrasting evolutionary pathways through the green valley for different morphological types as concluded by S14. The intermediate quenching rates reside in the space between the extremes sampled by the optical-NUV colour-colour diagrams of S14. The inclusion of the intermediate galaxies in this investigation and the use of a statistical method, elucidates a continuum of quenching rates, with all galaxies transitioning through the green valley to the red sequence during quenching, regardless of morphology.

Therefore instead of concluding that *'the green valley is a red herring'* as in S14, I would conclude that the *'grass is always redder on the other side'*.

3.2.3 Blue Cloud Galaxies

Since the blue cloud by definition is made up of star forming galaxies, STARPY is expected to have some difficulty inferring any quenching model to describe them, as confirmed by Figure 3.7. The attempt to characterise a star forming galaxy with a quenched SFH model leads STARPY to attribute the extremely blue colours of the majority of these galaxies to a constant SFR until recent times and then a fast quench at the observed redshift (i.e. the colour has not had enough time to change from blue post-quench).

This is particularly apparent for the blue disc weighted population. Perhaps even galaxies which are currently quenching slowly across the blue cloud cannot be well fit by the quenching models implemented, as they still have high SFRs despite some quenching. By definition although a galaxy is undergoing quenching, star formation can still be occurring, just at a slower rate than at earlier times. This rate is described by τ.

A very small fraction of the blue smooth weighted population density is found to begin quenching at redshifts $z \gtrsim 0.5$ with slow quenching rates. These populations have been blue for a considerable period of time, slowly using up their gas for star formation by the Kennicutt−Schmidt law (Schmidt, 1959; Kennicutt, 1997). However the dominant fraction of the blue smooth weighted population density occurs at rapid quenching rates at recent times. This therefore provides some support to the theories for blue ellipticals as either merger-driven ($\sim 76\%$; like those identified as recently quenched ellipticals with properties consistent with a merger origin by McIntosh et al. 2014) or gas inflow-driven reinvigorated star formation that is now slowly decreasing ($\sim 24\%$; such as the population of blue spheroidal galaxies studied by Kaviraj et al. 2013).

The blue cloud is therefore primarily composed of both star forming galaxies of all morphologies and a smooth population undergoing a rapid quench, presumably after a previous event triggered star formation and turned them blue.

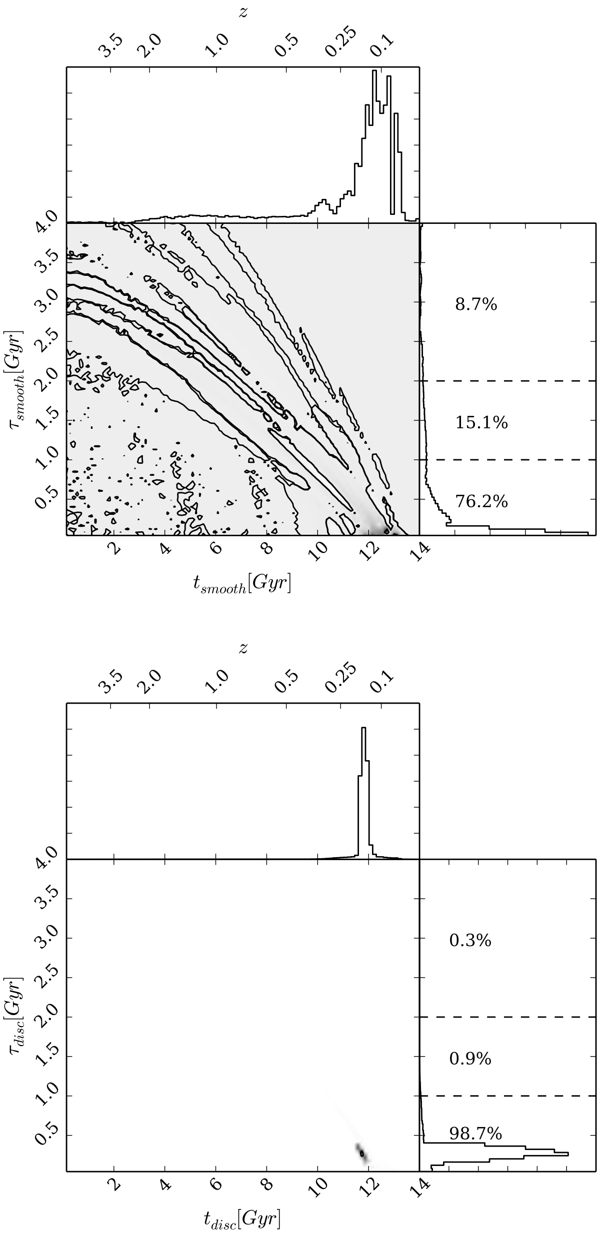

Figure 3.7: Contour plots showing the population densities for blue cloud galaxies in the GZ2-GALEX sample, weighted by the morphological vote fractions from GZ2 to give both bulge (top) and disc (bottom) dominated distributions. The histograms show the projection into one dimension for each parameter. The dashed lines show the separation between rapid (τ [Gyr] < 1.0), intermediate ($1.0 < \tau$ [Gyr] < 2.0) and slow (τ [Gyr] > 2.0) quenching rates with the fraction of the combined posterior probability distribution in each region shown (see Section 2.2). Positions with probabilities less than 0.2 are discarded as poorly fit models, therefore unsurprisingly blue cloud galaxies are not well described by a quenching star formation model.

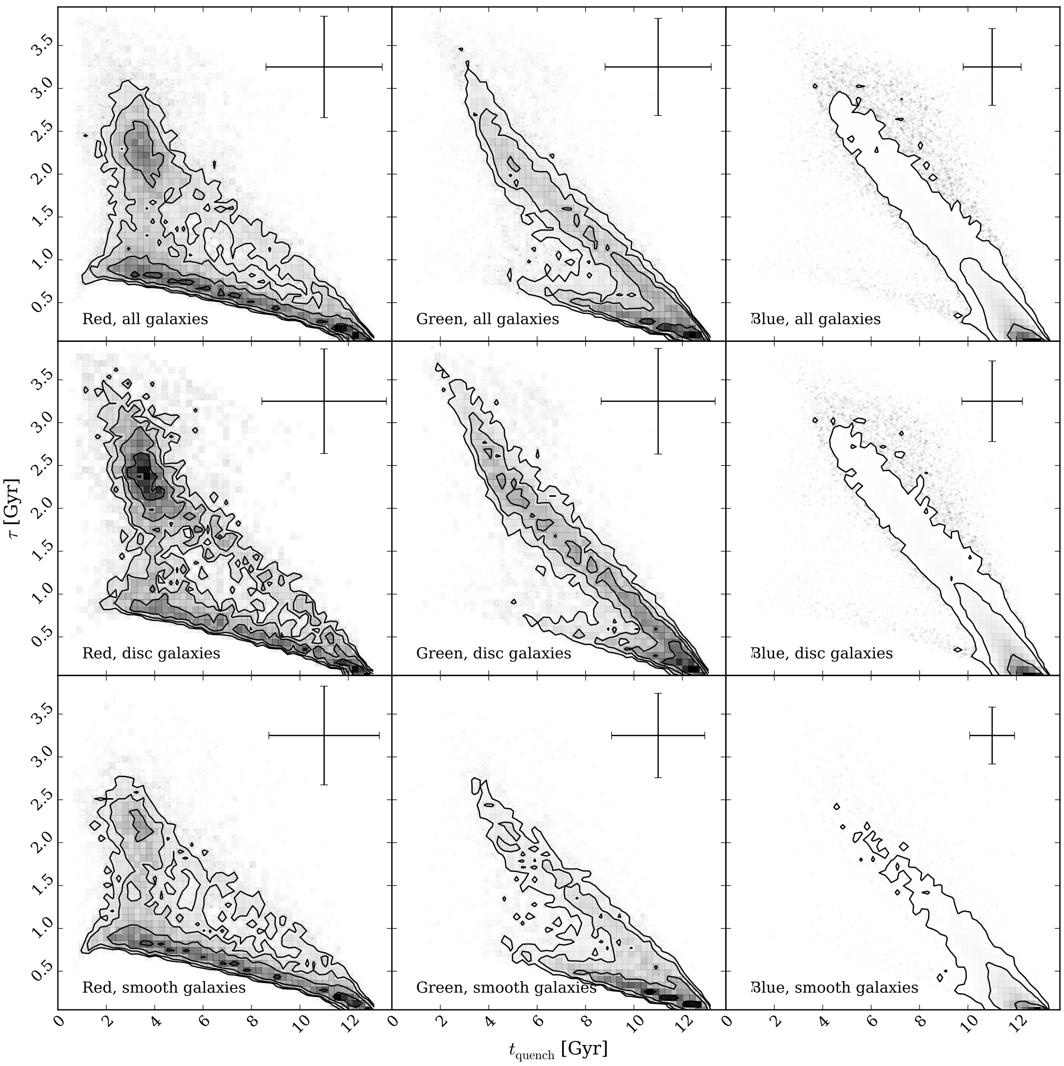

Figure 3.8: Contours showing the positions in the $[t, \tau]$ parameter space of the median walker position (the 50th percentile; as shown by the intersection of the solid blue lines in Figure 2.4) for each galaxy for all (top), disc ($p_d > 0.5$; middle), and smooth ($p_s > 0.5$; bottom) red sequence, green valley and blue cloud galaxies in the left, middle and bottom panels respectively. The error bars on each panel shows the average 68% confidence on the median positions (calculated from the 16th and 84th percentile, as shown by the blue dashed lines in Figure 2.4). These positions were calculated without discarding any walker positions due to low probability and without weighting by vote fractions, therefore this plot may be more intuitive than Figures 3.4, 3.5 & 3.7. The differences between the smooth and disc populations and between the red, green and blue populations remain clearly apparent.

Table 3.3: Table summarising the main results in Section 3.2 by describing the distributions derived for each population across the colour-magnitude diagram.

	Red Sequence	Green Valley	Blue Cloud
Smooth-weighted	Dominated by rapid quenching rates	Dominated by intermediate quenching rates	Dominated by rapid quenching rates
Disc-weighted	Bimodal between slow and rapid quenching rates	Dominated by slow quenching rates	-

3.3 Discussion

In the previous section I presented the results of using POPSTARPY to derive the distribution of quenching histories for galaxies across the colour magnitude diagram. I found differences between the SFHs of smooth- and disc-weighted populations of the red sequence, green valley and blue cloud. These results are summarised in Table 3.3. In this section I will speculate on the following question: what are the possible mechanisms driving these differences?

3.3.1 Rapid Quenching Rates

Rapid quenching is more dominant in the smooth weighted population densities than the disc weighted population (comparing top and bottom panels in Figures 3.4 & 3.5). The red sequence populations also have larger fractions of rapid quenching rates than green valley population densities (compare Figures 3.4 & 3.5).

This result suggests that rapid quenching mechanisms are accompanied by a change in morphology from a disc- to a smooth dominated galaxy as it quickly traverses the colour-magnitude diagram to the red sequence. This is supported by the number of disc galaxies that would need to undergo a morphological change in order for the smooth : disc ratio of galaxies in the green valley to match that of the red sequence (see Section 3.2.2). From this indirect evidence I suggest that this observed rapid quenching mechanism is major mergers. However, since a significant fraction of the red sequence disc weighted population density is found at rapid quenching rates (bottom panel Figure 3.4), this suggests that the quenching may have occurred more rapidly than the morphological change in such a merger.

In order to achieve such rapid quenching rates ($\tau \lesssim 0.5$) in a simulation of a major merger, Springel, Di Matteo, & Hernquist (2005) showed that feedback from black hole activity is necessary. As discussed in Chapter 1, powerful quasar outflows are thought to be able to remove much of the gas from the inner regions of the galaxy, terminating star formation on extremely short rates (this connection between quenching and AGN feedback is explored further in Chapter 4). Bell et al. (2006), using data from the COMBO-17 redshift survey ($0.4 < z < 0.8$), estimate a merger timescale of ~ 0.4 Gyr for the merger to go from being classified as a close galaxy pair to morphologically disturbed. Springel, Di Matteo, & Hernquist (2005) consequently find using hydrodynamical simulations that after ~ 1 Gyr the merger remnant has reddened to $u - r \sim 2.0$.

Under the simple assumption that the merger timescale will be $\sim$ quenching rate, these simulation results are in agreement with the simple exponential quenching models used here. Figure 2.1 shows that SFH models with $\tau < 0.4$ Gyr have reached $u - r \gtrsim 2.2$, within ~ 1 Gyr. This could explain the fraction of the red disc weighted population with very rapid quenching rates. These galaxies may have undergone a major merger recently but are still undergoing a morphological change from disc, to disturbed, to an eventual smooth galaxy (see also van der Wel et al. 2009). Similarly they may have retained their disc structure in a merger, such as in recent simulations by Pontzen et al. (2016). This possible connection between AGN feedback and rapid quenching rates is explored further in Chapter 4.

These rapid quenching rates, while found across all populations, do not fully characterise the entire red sequence or green valley populations. Dry (i.e. gas poor) major mergers therefore cannot fully account for the formation of any galaxy population, supporting the observational conclusions of Bell et al. (2007); Bundy et al. (2007); Kaviraj (2014b) and simulations by Genel et al. (2008).

3.3.2 Intermediate Quenching Rates

Intermediate quenching rates are found to be equally prevalent across both smooth and disc weighted populations across cosmic time and are particularly dominant in the green valley (see Figure 3.5). This suggests that this intermediate quenching rate must therefore be caused by mechanisms that both preserve and transform morphology. It is this result of another route through the green valley that is in contradiction with the findings of S14.

I propose that these intermediate quenching rates ($1 \leq \tau$ [Gyr] ≤ 2) are caused by any of the following: gas rich major mergers, major mergers without black hole feedback, minor mergers and galaxy interactions. This is supported by the findings of Lotz et al. (2011), who find in simulations that increasing the baryonic gas fraction in a merger (mass ratios $\sim 1:1-1:4$) causes the observability timescale of the merger to increase from ~ 0.2 Gyr (with little gas, as above for major mergers which can cause rapid quenching rates) up to ~ 1.5 Gyr (with large gas fractions).

Intermediate quenching rates are equally dominant for both smooth and disc populations across Figures 3.4 and 3.5. Lotz et al. (2008) show that the remnants of simulated equal mass gas rich disc mergers are observable for $\gtrsim 1$ Gyr post merger and state that they appear “disc-like and dusty” in the simulations, which is consistent with an “early-type spiral morphology”. Such galaxies are often observed to have spiral features with a dominant bulge, suggesting that such galaxies may divide the votes of the GZ2 users, producing vote fractions of $p_s \sim p_d \sim 0.5$. Such a vote fraction may also arise because the galaxy is at a large distance or because it is an S0 galaxy whose morphology can be interpreted by different GZ2 users in different ways. Willett et al. (2013) find that S0 galaxies expertly classified by Nair & Abraham (2010b) are more commonly classified as ellipticals by GZ2 users, but that the population has a significant tail to high disc vote fractions. A galaxy with these ambiguous GZ2 vote fractions will therefore contribute equally to the smooth and disc weighted population densities which may explain the dominance of these intermediate quenching rates across all populations.

By inspecting Figure 2.2, we find that SFH models with these intermediate quenching rates of $1.0 \lesssim \tau$ [Gyr] $\lesssim 2.0$ take approximately $2.5-5.5$ Gyr to reach the red sequence. In the simulations of Springel, Di Matteo, & Hernquist (2005) which do not include feedback from black holes, merger remnants can sustain low levels of star formation for several Gyrs if a small fraction of gas is not consumed in the merger triggered starburst (either because the mass ratio is not large enough or from the lack of strong black hole activity). The remnants from these simulations take ~ 5.5 Gyr to reach red optical colours of $u - r \sim 2.1$, providing support for the hypothesis that the intermediate quenching rates may be caused by minor mergers.

Observationally, Darg et al. (2010) showed an increase in the spiral to elliptical ratio for merging galaxies ($0.005 < z < 0.1$) by a factor of two compared to the typical galaxy population. They attribute this to the mergers of spirals being observable for much longer compared to mergers with elliptical galaxies. This supports the hypothesis that the slower quenching rates in the $\tau < 1.5$ Gyr region of the disc weighted green valley population density (see bottom panel of Figure 3.5) may be caused by a minor or wet major merger and eventually give rise to the morphological change needed to match the ratio of smooth:disc galaxies seen in the red sequence (see Section 3.2.2).

Darg et al. (2010) also show (in their Figure 6) that below a merger ratio of $1 : 10$ (up to $\sim 1 : 100$), green is the dominant average galaxy colour of visually identified merging pairs in GZ. These pairs are also dominated by spiral-spiral mergers as opposed to elliptical-elliptical and elliptical-spiral mergers. The remnants of these green spiral-spiral mergers would contribute to the green disc weighted population density in the bottom panel of Figure 3.5, where these intermediate quenching rates are found to be the dominant SFH. This lends more support to the idea that these intermediate quenching rates are caused in part by minor mergers.

For the smooth weighted green valley population (shown in the top panel of Figure 3.5), 40.6% of the distribution is found in the intermediate quenching rate regime. Similarly, Kaviraj (2014b,a) by studying SDSS photometry ($z < 0.07$) state that approximately half of the star formation in all galaxies is driven by minor mergers at $0.5 < z < 0.7$. These minor mergers would therefore exhaust available gas for star formation and consequently causing a gradual decline in the star formation rate. This is therefore complimentary to the fraction of smooth green valley galaxies found to be undergoing quenching at an intermediate rate in the top panel of Figure 3.5.

Assuming that rapid and intermediate quenching rates are therefore caused by major or minor mergers, the fraction of population density with $\tau \leq 2$ Gyr can provide an estimate for the percentage of galaxies with a merger dominated evolutionary history. This is calculated to be 73.9% and 59.3%, for the smooth weighted red sequence and green valley populations (top panels Figures 3.4 and 3.5) respectively. This estimate for the faction of smooth galaxies with merger dominated histories is supported by the earlier work of Kaviraj et al. (2011). They use multi wavelength photometry of galaxies in COSMOS (Scoville et al., 2007) to estimate that 70% of early-type galaxies appear morphologically disturbed, suggesting either a minor or major merger in their history. Note that the star formation model used here is a basic one and has no prescription for reignition of star formation post-quench. Such a reignition of star formation has been detected observationally by Kaviraj et al. (2011) and seen in simulations by Pontzen et al. (2016).

Any external event which can cause either a burst of star formation (depleting the gas available) or directly strip a galaxy of its gas, for example galaxy harassment, interactions, ram pressure stripping, strangulation and interactions internal to clusters, should also cause quenching with an intermediate rate. Such mechanisms would be the dominant cause of quenching in dense environments; considering that the majority of galaxies reside in groups or clusters (Coil et al. 2008 find that green valley galaxies are just as clustered as red sequence galaxies). It is not surprising therefore that the majority of the GZ2-GALEX galaxies ($\sim 50\%$) are considered intermediate in morphology (i.e., $p_d \sim p_s \sim 0.5$,see Table 3.1) and therefore may be undergoing or have undergone such an interaction. This obvious dependancy of the quenching parameters on the galaxy environment will be investigated further in Chapter 5.

3.3.3 Slow Quenching Rates

Although intermediate and rapid quenching rates are the dominant mechanisms across the colour-magnitude diagram, together they cannot completely account for the quenching of disc galaxies. S14 concluded that slow quenching rates were the most dominant mechanism for disc galaxies. However I show that: (i) intermediate quenching rates are equally important in the green valley (bottom panel Figure 3.5) and (ii) rapid quenching rates are equally important in the red sequence (bottom panel Figure 3.4). There is also a significantly lower fraction of slow quenching rates in the smooth weighted population densities (top panels of Figures 3.4 & 3.5). This suggests that the evolution (or indeed creation) of typical smooth galaxies is dominated by processes external to the galaxy. The exceptions are galaxies in the blue cloud where a small fraction of the smooth weighted population density is found at slow quenching rates (top panel Figure 3.7), which could be due to a reinvigoration of star formation that is slowly depleting the available gas (via the Kennicutt−Schmidt law).

Table 3.1 shows that 3.9% of the GZ2-GALEX sample are red sequence late-type galaxies, i.e. red late-type spirals. This is, within uncertainties, in agreement with the findings of Masters et al. (2010a), who find $\sim 6\%$ of late-type spirals are red when defined by a cut in the $g - r$ optical colour (rather than with $u - r$ as used in this investigation) and are at the 'blue end of the red sequence'. Bamford et al. (2009), using GZ1 vote fractions of galaxies in the SDSS, found a significant fraction of field galaxies are in fact high stellar mass red spiral galaxies. As these galaxies are isolated from the effects of interactions from other galaxies, the slow quenching mechanisms dominant in the disc weighted population densities (bottom panels of Figures 3.4 & 3.5) are most likely due to secular processes (i.e. mechanisms internal to the galaxy, in the absence of sudden accretion or merger events; Kormendy & Kennicutt 2004; Sheth et al. 2012). Bar formation in a disc galaxy is such a mechanism, whereby gas is funnelled to the centre of the galaxy by the bar over long rates where it is used for star formation (Masters et al., 2012; Saintonge et al., 2012; Cheung et al., 2013), consequently forming a 'pseudo-bulge' (Kormendy et al., 2010; Simmons et al., 2013).

I therefore speculate that these slow quenching rates are due to secular evolution, as such processes do not change the disc dominated nature of a galaxy.

3.4 Conclusions

I have used morphological classifications from the Galaxy Zoo 2 project to determine the morphology-dependent star formation histories of galaxies via a Bayesian analysis of an exponentially declining star formation quenching model. The most likely values were determined for the quenching onset time, t_q, and quenching timescale, τ, in this model for galaxies across the blue cloud, green valley and red sequence to trace the morphological dependance of galactic evolution across the colour-magnitude diagram.

The green valley is found to be a transitional population for all morphological types (in conflict with S14), however this transition proceeds slowly for the majority of disc dominated galaxies and occurs rapidly for the majority of smooth dominated galaxies in the red sequence (in agreement with S14). However, in addition to the results of S14, the inclusion of both (i) the entire GZ2-GALEX sample with no morphology thresholds, and (ii) a robust statistical analysis of the results has revealed a more nuanced result; specifically that the prevailing mechanism across all morphologies and populations is quenching with intermediate rates. The main findings are summarised as follows:

(i) Quenching within the red sequence population occurs at earlier quenching times (i.e. higher redshift) than in the green valley population regardless of morphology (see Figures 3.4 and 3.5). Therefore the quenching mechanisms currently occurring in the green valley were also active in creating the 'blue end of of the red sequence' at earlier times; confirming that the green valley is indeed a transitional population, regardless of morphology.

(ii) The red sequence is dominated by galaxies which are elliptical in morphology and have undergone a rapid to intermediate quench at some point in cosmic time, resulting in a very low current SFR (see Section 3.2.1).

(iii) The green valley as it is currently observed is dominated by very slowly evolving disc dominated galaxies along with intermediate and smooth dominated galaxies which pass across it with intermediate rates within $\sim 1.0 - 1.5$ Gyr (see Section 3.2.2).

(iv) There are many different mechanisms responsible for quenching, all causing a galaxy to progress through the green valley. These mechanisms are dependant on galaxy type, with the smooth and disc dominated galaxies each having different dominant star formation histories across the colour-magnitude diagram.

(v) Blue cloud galaxies are not well fit by a quenching model of star formation due to the continuous high star formation rates occurring (see Figure 3.7).

(vi) Rapid quenching rates are found at a lower fraction in the green valley population than the red sequence population (see Figures 3.4 & 3.5). I speculate that this quenching mechanism is caused by major mergers with black hole feedback, which are able to expel the remaining gas not initially exhausted in the merger-induced starburst and which can cause a change in morphology from disc- to bulge-dominated. The colour-change rates from previous simulations of such events agree with the derived quenching rates (see Section 3.3.1). These rapid quenching rates are instrumental in forming red galaxies, however galaxies at the current epoch passing through the green valley do so at more intermediate quenching rates (see Figure 3.5).

(vii) Intermediate quenching rates ($1.0 < \tau$ [Gyr] < 2.0) are found with constant density across red and green galaxies for both smooth- and disc-weighted populations, the rates for which agree with observed and simulated minor merger rates (see Section 3.3.2). I hypothesise that such rates can also be caused by a number of external processes, including gas rich major mergers, mergers without black hole feedback, galaxy harassment, interactions, strangulation and ram pressure stripping. The rates and observed morphologies from previous studies agree with the results, including that this is the dominant mechanism for intermediate morphology galaxies such as early-type spiral galaxies with spiral features but a dominant bulge, which split the GZ2 vote fractions (see Section 3.3.2).

(viii) Slow quenching rates are the most dominant mechanism in the disc galaxy population across the colour-magnitude diagram population (see bottom panels Figures 3.4 & 3.5). Disc galaxies are often found in the field, therefore I hypothesise that such slow quenching rates are caused by secular evolution and processes internal to the galaxy (see Section 3.2.3). A small amount of slow quenching rates is also detected for blue elliptical galaxies which is attributed to a reinvigoration of star formation, the peak of which has passed and has started to decline by slowly depleting the gas available (see Section 3.2.3).

Chapter 4

Black hole-galaxy co-evolution in the context of quenching

The following chapter is split into two parts; in Section 4.1 I investigate the connection between quenching parameters and the presence of an AGN and then follwing up on these results in Section 4.2 I investigate how black holes grow in disc galaxies with merger free evolutionary histories.

4.1 Rapid, recent quenching within a population of Type 2 AGN host galaxies

The work in the following chapter has been published in Smethurst et al. (2016).

In Chapter 3, rapid quenching rates were dominant across the smooth weighted population in Figures 3.5 & 3.4. In Section 3.3.1 I discussed how simulations suggest that such rapid quenching rates can only be achieved if AGN feedback is present in a major merger scenario. I therefore decided to investigate this possible connection between AGN feedback and rapid quenching rates further. I shall do so by analysing the SFHs of a population of AGN host galaxies with POPSTARPY in comparison to an inactive galaxy control sample. I aim to determine the following: (i) Have galaxies which currently host an AGN undergone quenching? (ii) If so, when and at what rate does this quenching occur? (iii) Is this quenching occurring at different times and

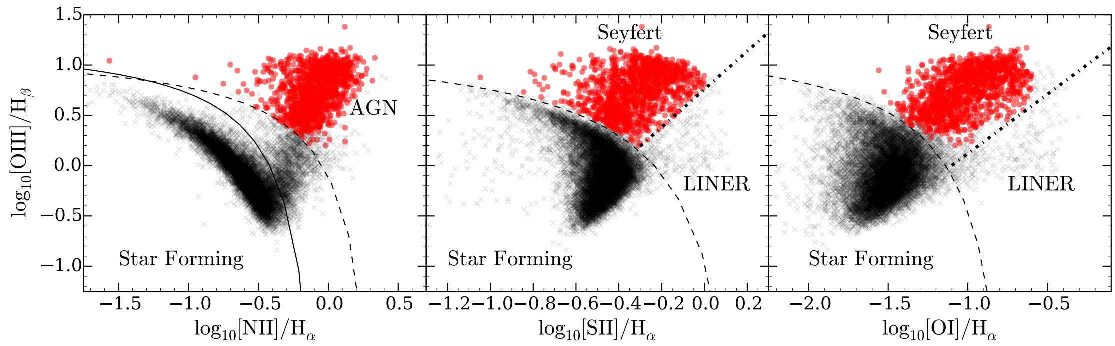

Figure 4.1: BPT diagrams for galaxies in the GZ2-GALEX sample (black crosses) with S/N > 3 for each emission line. Inequalities defined in: Kewley et al. (2001) to separate SF galaxies from AGN (dashed lines), Kauffmann et al. (2003a) to separate SF from composite SF-AGN galaxies (solid line) and Kewley et al. (2006) to separate LINERS and Seyferts (dotted lines). Galaxies are included in the AGN-HOST sample (red circles) if they satisfy all the inequalities to be classified as Seyferts. LINERs are excluded to ensure a pure sample of AGN.

rates compared to a control sample of inactive galaxies? This investigation builds on the work of Martin et al. (2007), who also investigate the quenching rates of AGN with spectral SF indicators but improves significantly on their statistical techniques.

4.1.1 AGN Sample

Obscured type 2 AGN were selected from the GZ2-GALEX sample using a BPT diagram (Baldwin, Phillips, & Terlevich, 1981) using line and continuum strengths for [OIII], [NII], [SII] and [OII] obtained from the MPA-JHU catalogue (Kauffmann et al., 2003b; Brinchmann et al., 2004). A BPT diagram uses emission line ratio diagnostics to determine whether a galaxy is a star forming galaxy, a Seyfert (i.e. hosting an AGN) or a LINER (a low-ionization nuclear emission-line region galaxy). This is possible because lines such as [NII] are forbidden transitions, and therefore only excited by the highest energy photons. Therefore an AGN, which is giving off higher energy photons than even the most massive stars in a galaxy, will produce a higher [NII]/Hα ratio.

In order to select a sample of AGN using a BPT diagram I use the following constraints. The signal-to-noise ratio of each emission line of the GZ2-GALEX sample

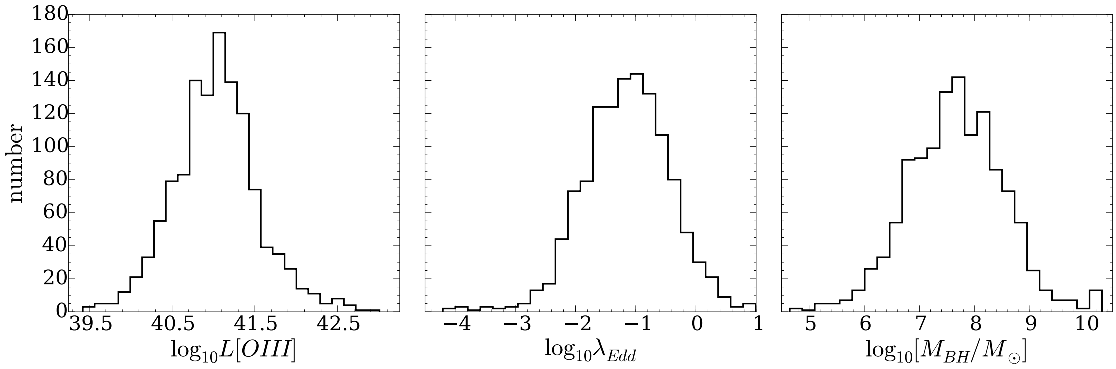

Figure 4.2: Distribution of the [OIII] luminosity (left), Eddington ratio (middle) and black hole masses (right) in the AGN-HOST sample.

galaxies was required to be S/N $>$ 3 as in Schawinski et al. (2010). Those galaxies which satisfied all of the inequalities (derived from theoretical spectral modelling of star forming galaxies and AGN) defined in Kewley et al. (2001, to separate SF galaxies from AGN) and Kauffmann et al. (2003a, to separate SF galaxies from composite SF-AGN galaxies) were selected as Type 2 AGN, giving $1,299$ host galaxies ($\sim 10\%$ of the GZ2-GALEX sample; in agreement with estimates of the local AGN fraction by Kauffmann et al. 2004; Pimbblet et al. 2013).

Sarzi et al. (2010), Yan & Blanton (2012) and Singh et al. (2013) have all demonstrated that LINERs are not primarily powered by AGN, therefore to ensure a pure sample of AGN, these galaxies were excluded from the sample using the definition from (Kewley et al., 2006, 55 galaxies total) with no significant change to the results. The remaining $1,244$ galaxies will hereafter be referred to as the AGN-HOST sample; Figure 4.1 shows the entire AGN-HOST and GZ2-GALEX samples with the selection criteria used on a BPT diagram.

I do not use Type 1 AGN in this investigation due to concerns about contamination of the observed galaxy colours, used in the SFH analysis, from potentially strong NUV emission by unobscured active nuclei. The obscuration of Type 2 AGN is highly efficient, considerably more so in the NUV than the optical (Simmons et al., 2011). Residual NUV flux from a Type 2 AGN can therefore be neglected in comparison to that of the galaxy. However, I did investigate the possibility of contamination of optical galaxy colours from unobscured AGN emission in the AGN-HOST sample and found that subtracting measured nuclear magnitudes (SDSS `psfMag`) from the

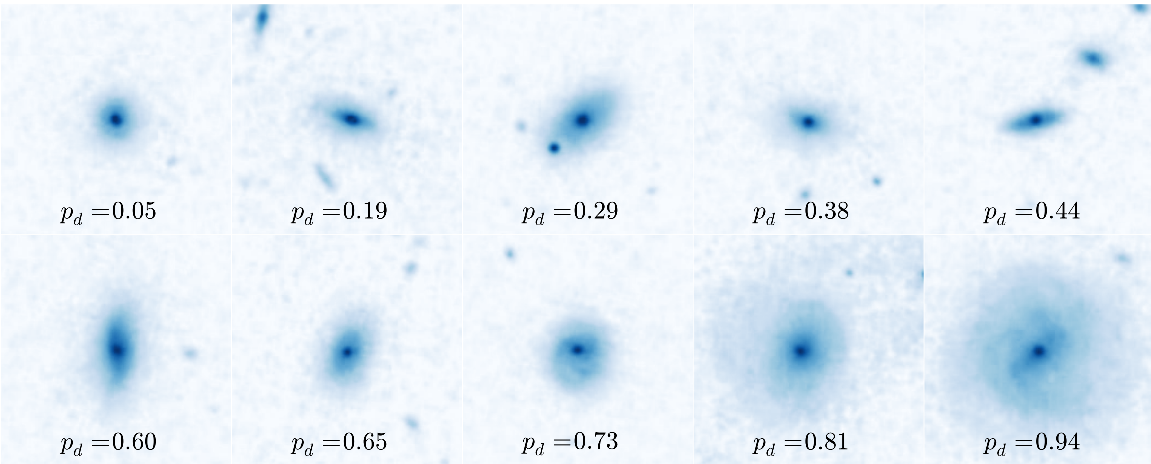

Figure 4.3: Randomly selected SDSS *gri* band composite images from the sample of $1,244$ Type 2 AGN in a redshift range $0.04 < z < 0.05$. The galaxies are ordered from least to most featured according to their debiased 'disc or featured' vote fraction, p_d (see Willett et al. 2013). The scale for each image is 0.099 arcsec/pixel.

total galaxy magnitude (SDSS `modelMag`) produces a negligible change in host galaxy colour ($\Delta(u-r) \sim 0.09$). I therefore use the total galaxy magnitudes (with extinction corrections as described in Section 1.3.4) to avoid unnecessary complexity and minimise the propagation of uncertainty from the observed colours through to the inferred SFHs. However, I note that using these corrected colours in the analysis does not change the results.

Since this investigation is focussed on whether an AGN can have an impact on the star formation of its host galaxy, possible selection effects must be considered. The extent to which star formation could obscure AGN emission was addressed by Schawinski et al. (2010). They showed, by simulating the addition of AGN emission of varying luminosities to a star-forming galaxy spectra, that BPT-based selection of AGN produces a complete sample at luminosities of $L[OIII] > 10^{40}$ erg s^{-1}. $\sim 98\%$ of the AGN-HOST sample have an $L[OIII]$ above this limit, therefore I therefore assume I have selected a complete sample of Type 2 AGN independent of host galaxy SFR.

Black hole masses of the AGN-HOST sample are derived from the $M_{BH} - \sigma$ relationship whereby black hole masses are tightly correlated with the galaxy's stellar velocity dispersion (Magorrian et al., 1998; Marconi & Hunt, 2003; Häring & Rix, 2004). McConnell et al. (2011), using archival measurements along with two more accurate measurements of black hole masses derived using reverberation mapping techniques, define the $M_{BH} - \sigma$ relationship as:

$$\log_{10}\left(\frac{M_{BH}}{M_{\odot}}\right) = 8.29 + 5.12\ \log_{10}\left(\frac{\sigma}{200\ \mathrm{km\ s^{-1}}}\right). \tag{4.1}$$

where the velocity dispersion, σ, is measured from the Balmer lines and is provided in the MPA-JHU catalog (Kauffmann et al., 2003b; Brinchmann et al., 2004) for the AGN-HOST sample.

The Eddington ratio, λ_{Edd}, describes the accretion rate of the black hole and is calculated with the proxy $\lambda_{Edd} = L_{bol}/L_{Edd}$, where L_{Edd} is the Eddington luminosity and L_{bol} is the bolometric luminosity. An accreting black hole is Eddington limited when the gravitional force, $F_{\mathrm{g}} = GM_{BH}m/R^2$, balances the radiation pressure force, $F_{\mathrm{rad}} = \kappa\ m \cdot \frac{L}{c} \cdot \frac{1}{4\pi R^2}$ (assuming spherical symmetry). Since the black hole is most likely accreting ionized hydrogen we can estimate $\kappa \approx \sigma_T/m_p$ where σ_T is the Thomson scattering cross section. Therefore the Eddington luminosity can be calculated as:

$$L_{Edd} = \frac{4\pi G M_{BH} c m_p}{\sigma_T}, \tag{4.2}$$

as outlined in Binney & Merrifield (1998). This equation then reduces to:

$$L_{Edd} = 3 \times 10^4 \left(\frac{M_{BH}}{M_{\odot}}\right) L_{\odot}. \tag{4.3}$$

To determine $\lambda_{Edd} = L_{bol}/L_{Edd}$, we still need to be able to calculate the bolometric luminosity, L_{bol}. For obscured (Type 2) AGN the bolometric luminosity cannot be directly measured and so is inferred from the luminosity of the [OIII] emission line, as derived by Heckman et al. (2004):

$$\log_{10} L_{bol} = 3.54 + \log_{10} L[OIII]. \tag{4.4}$$

The distributions of L[OIII], M_{BH} and λ_{Edd} of the AGN-HOST sample are shown in Figure 4.2. SDSS images for 10 randomly selected galaxies from the AGN-HOST sample are shown in Figure 4.3. The decomposition of the AGN-HOST sample into red sequence, green valley and blue cloud galaxies is shown in Tables 4.1 and 4.2 along with further division by galaxy type and SFR (where available for the AGN-HOST sample from the MPA-JHU catalog) respectively.

Table 4.1: Table showing the decomposition of the AGN-HOST sample by galaxy type into the subsets of the colour-magnitude diagram.

	All	Red Sequence	Green Valley	Blue Cloud
Smooth-like ($p_s > 0.5$)	340 (27.3%)	21 (25.0%)	105 (41.2%)	213 (23.5%)
Disc-like ($p_d > 0.5$)	871 (70.0%)	63 (75.0%)	148 (58.0%)	660 (72.9%)
Early-type ($p_s \geq 0.8$)	66 (5.3%)	1 (1.2%)	14 (5.5%)	51 (5.6%)
Late-type ($p_s \geq 0.8$)	569 (45.7%)	39 (46.4%)	74 (29.0%)	456 (50.4%)
Total	**1244** (100.0%)	84 (6.7%)	255 (20.5%)	905 (72.7%)

Table 4.2: Table showing the decomposition of the AGN-HOST sample galaxies by their star formation rate in the subsets of the colour-magnitude diagram.

	All	Red Sequence	Green Valley	Blue Cloud
Quenched (SFR $<$ P $- 5\sigma$)	14 (1.3%)	9 (12.5%)	4 (1.7%)	1 (0.1%)
Quenching ($P - 5\sigma <$ SFR $<$ P $- \sigma$)	335 (30.6%)	45 (64.3%)	139 (59.9%)	151 (19.1%)
Star Forming (SFR $>$ P $- \sigma$)	744 (68.0%)	16 (22.9%)	89 (38.4%)	639 (80.7%)
Total	**1093** (100.0%)	70 (6.4%)	232 (21.2%)	791 (72.4%)

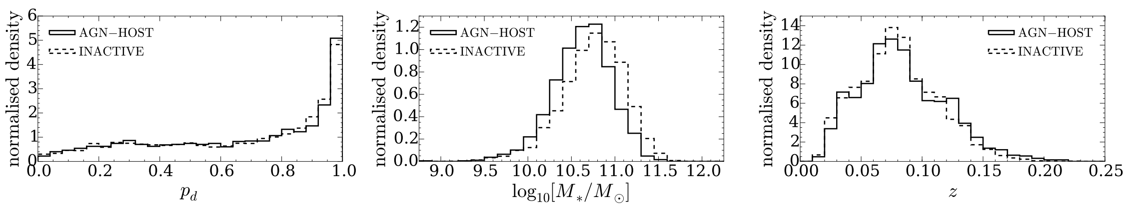

Figure 4.4: Distribution of the GZ2 disc vote fractions (p_d; left), stellar masses (middle) and redshift (left) in the AGN-HOST sample (solid lines) in comparison to the matched control INACTIVE sample (dashed lines).

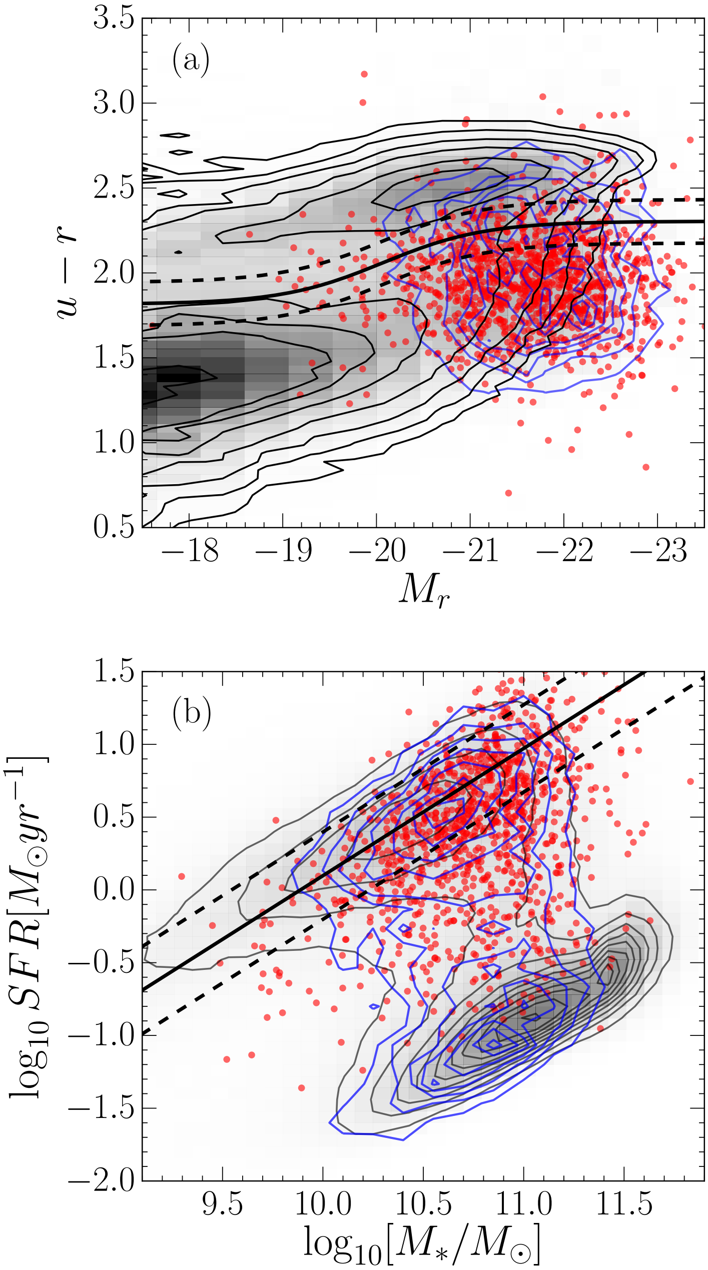

Figure 4.5: (a) Optical colour-magnitude diagram showing the SDSS DR7 (grey filled contours), the AGN-HOST sample (red circles) and INACTIVE sample (blue contours). The definition of the green valley from Baldry et al. (2006) (solid line) with $\pm 1\sigma$ (dashed lines) is shown. (b) SFR-stellar mass diagram showing the MPA-JHU measurements of SFR and M_* of SDSS DR7 galaxies (Kauffmann et al. 2003b; Brinchmann et al. 2004; black contours), the AGN-HOST sample (red circles) and INACTIVE sample (blue contours). The star forming 'main sequence' from Peng et al. (2010) is shown by the solid line for $t = 12.8$ Gyr, the average observed age of the GZ2-GALEX sample, with $\pm 1\sigma$ (dashed lines).

4.1.2 Defining a control sample

A control sample of inactive galaxies was constructed by removing from the GZ2-GALEX sample all galaxies with line strengths indicative of potential AGN activity (Kauffmann et al., 2003a), as well as sources identified as Type 1 AGN by the presence of broad emission lines (Oh et al., 2015). This is to ensure a pure sample of galaxies with no AGN activity. I selected a mass- and morphology-matched inactive sample by identifying up to 5 inactive galaxies for each AGN-HOST galaxy with the same stellar mass (to within $\pm 5\%$) and GZ2 smooth, p_s, and disc p_d, vote fractions (to within ± 0.1) giving 6107 galaxies. This sample will be referred to as the INACTIVE sample.

Figure 4.4 shows the GZ2 disc vote fraction (p_d; left), stellar mass (M_*; middle) and redshift (right) distributions of the AGN-HOST sample in comparison to the matched INACTIVE sample. A Kolmogorov-Smirnov test revealed that the redshift distributions of the INACTIVE and AGN-HOST samples are statistically indistinguishable ($D \sim 0.16$, $p \sim 0.88$).

The AGN-HOST and INACTIVE samples are also shown on both an optical colour-magnitude diagram and in the SFR-stellar mass plane in Figure 4.5 in comparison to the distribution of SDSS DR7 galaxies. SFRs and stellar masses are obtained from the MPA JHU catalog, where available, which follow the prescriptions outlined in Brinchmann et al. (2004) and Salim et al. (2007) for calculating the total aperture corrected galaxy SFR in the presence of an AGN.

The majority of the AGN-HOST sample would be defined as residing in the blue cloud ($\sim 73\%$) on the optical colour-magnitude diagram despite the fact that a significant proportion of the sample (32%) lie more than 1σ (0.3 dex) below the SFS as defined in Section 2.1 (Peng et al., 2010, see Figure 4.5 and Table 4.2).

4.1.3 Results

I use the POPSTARPY method to produce the distributions shown in Figure 4.6 for the AGN-HOST smooth and disc weighted populations which are split across three bins in Eddington ratio, λ_{Edd}, to investigate any trends with the accretion rate of the black hole. The bin boundaries were chosen to give equal numbers of AGN-HOST galaxies in each bin.

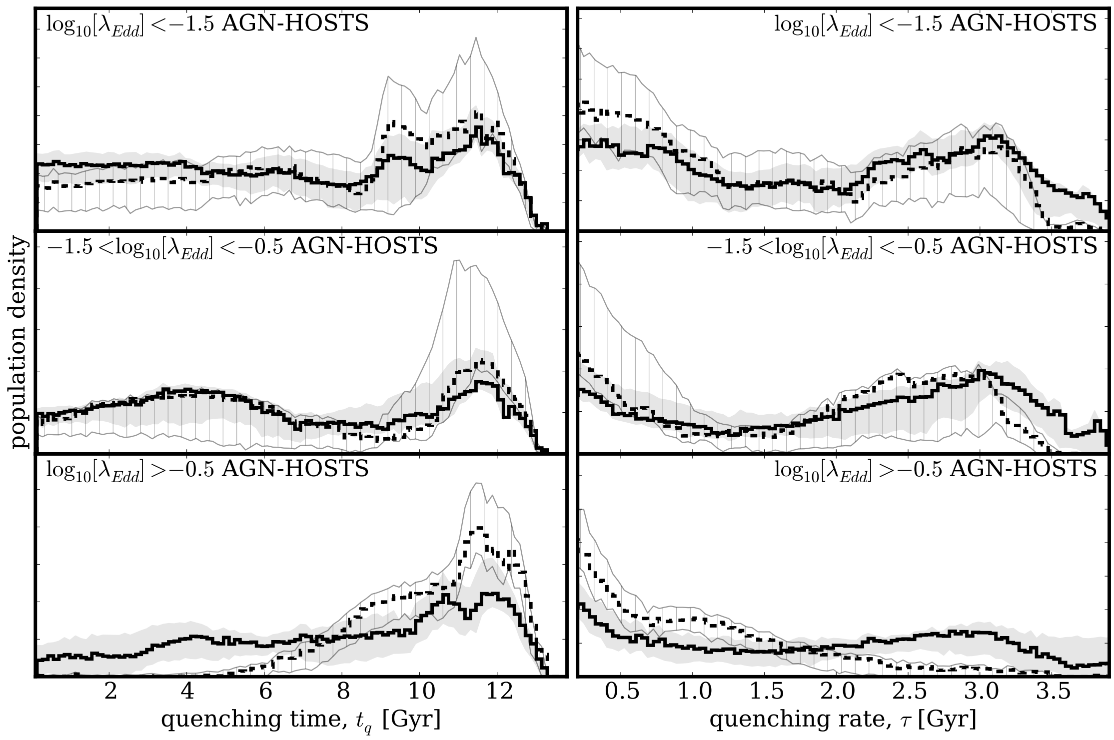

Figure 4.6: Population density distributions for the quenching time (t_q; left) and rate (τ; right), normalised so that the areas under the curves are equal. The AGN-HOST sample is split into low (top), medium (middle) and high (bottom) Eddington ratio, λ_{Edd}, for smooth (dashed) and disc (solid) galaxies. Uncertainties from bootstrapping are shown by the shaded regions for the smooth (grey striped) and disc (grey solid) population densities. A small (large) value of τ corresponds to a rapid (slow) quench.

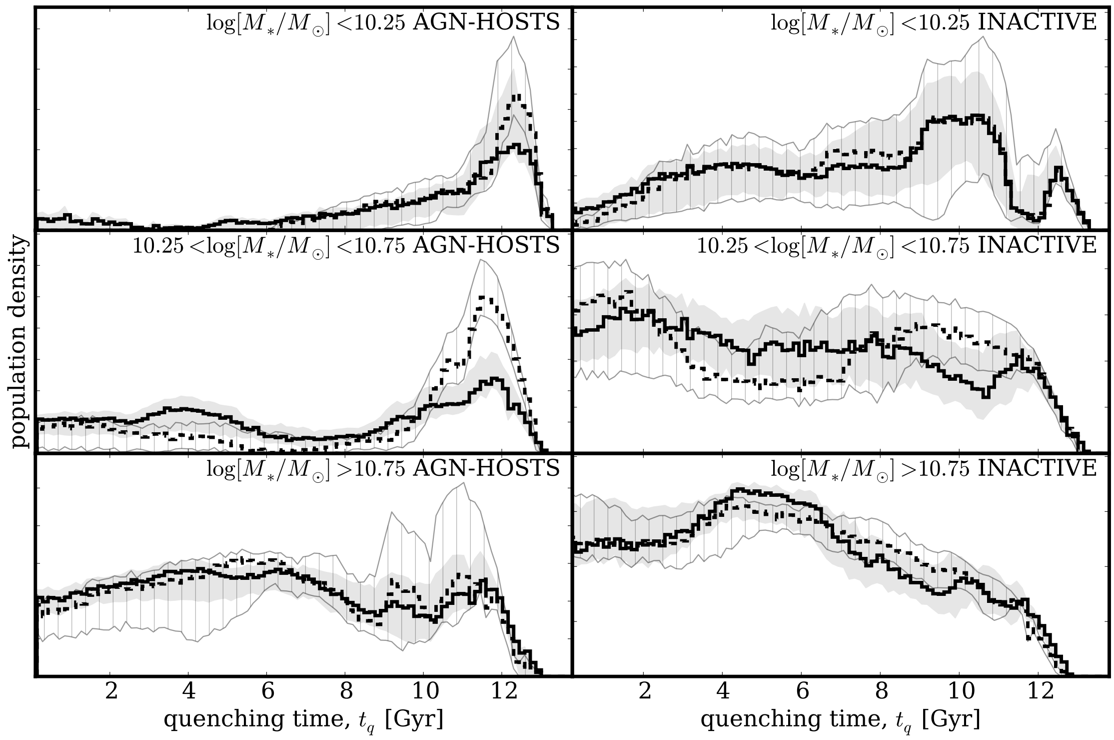

Figure 4.7: Population density distributions for the quenching time (t_q) parameter, normalised so that the areas under the curves are equal. AGN-HOST (left) and INACTIVE (right) galaxies are split into low (top), medium (middle) and high (bottom) mass for smooth (dashed) and disc (solid) galaxies. Uncertainties from bootstrapping are shown by the shaded regions for the smooth (grey striped) and disc (grey solid) population densities. A low (high) value of t_q corresponds to the early (recent) Universe.

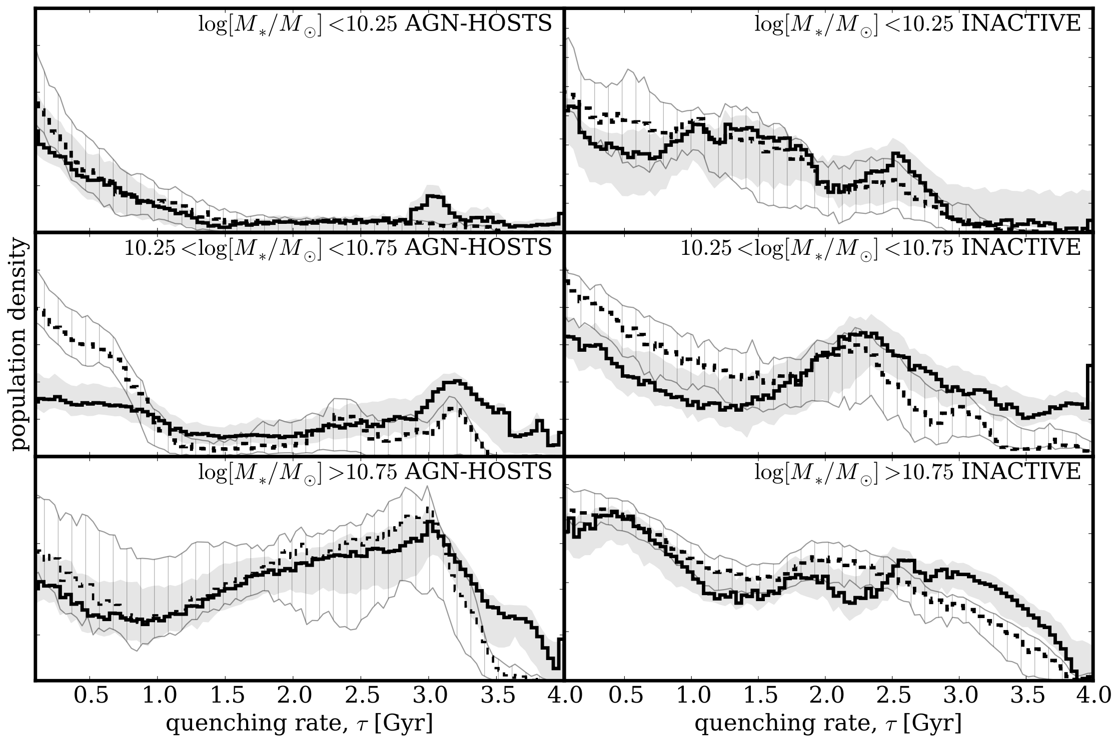

Figure 4.8: Population density distributions for the quenching rate (τ), normalised so that the areas under the curves are equal. AGN-HOST (left) host and INACTIVE (right) galaxies are split into low (top), medium (middle) and high (bottom) mass for smooth (dashed) and disc (solid) galaxies. Uncertainties from bootstrapping are shown by the shaded regions for the smooth (grey striped) and disc (grey solid) population densities. A small (large) value of τ corresponds to a rapid (slow) quench.

Table 4.3: Table showing the number of galaxies in each of the three mass bins for both the AGN-HOSTS and INACTIVE galaxy samples and the percentage of the distribution across each morphologically weighted population found in the rapid, intermediate and slow quenching regimes.

SAMPLE	MASS BIN	WEIGHTING	$\tau < 1$ [Gyr]	$1 < \tau$ [Gyr] < 2	$\tau > 2$ [Gyr]	NUMBER
AGN-HOSTS	$\log[M_*/M_\odot] < 10.25$	p_d	$60\pm^{23}_{5}$	$13\pm^{9}_{9}$	$28\pm^{6}_{19}$	165(13.3%)
		p_s	$69\pm^{14}_{6}$	$17\pm^{6}_{14}$	$14\pm^{3}_{7}$	
	$10.25 < \log[M_*/M_\odot] < 10.75$	p_d	$33\pm^{3}_{5}$	$15\pm^{4}_{4}$	$51\pm^{4}_{7}$	630(50.6%)
		p_s	$69\pm^{4}_{5}$	$7\pm^{4}_{4}$	$26\pm^{5}_{9}$	
	$\log[M_*/M_\odot] > 10.75$	p_d	$20\pm^{5}_{4}$	$25\pm^{7}_{5}$	$56\pm^{8}_{12}$	449(36.1%)
		p_s	$24\pm^{4}_{3}$	$26\pm^{5}_{6}$	$50\pm^{7}_{7}$	
INACTIVE	$\log[M_*/M_\odot] < 10.25$	p_d	$37\pm^{8}_{14}$	$39\pm^{8}_{6}$	$24\pm^{8}_{6}$	807(13.2%)
		p_s	$47\pm^{5}_{11}$	$36\pm^{9}_{5}$	$17\pm^{4}_{5}$	
	$10.25 < \log[M_*/M_\odot] < 10.75$	p_d	$30\pm^{4}_{3}$	$18\pm^{2}_{3}$	$51\pm^{4}_{4}$	3094(50.7%)
		p_s	$42\pm^{2}_{2}$	$29\pm^{3}_{3}$	$30\pm^{3}_{4}$	
	$\log[M_*/M_\odot] > 10.75$	p_d	$36\pm^{3}_{3}$	$24\pm^{3}_{4}$	$41\pm^{4}_{3}$	2206(36.1%)
		p_s	$38\pm^{2}_{2}$	$28\pm^{3}_{4}$	$34\pm^{3}_{3}$	

Similarly, in Figures 4.7 & 4.8 I use the POPSTARPY method to determine the AGN-HOST and INACTIVE smooth and disc weighted populations for the quenching time and rate, split between three mass bins to investigate any trends with mass. The bin boundaries were chosen to give roughly equal numbers of inactive galaxies in each bin, before mass matching to the AGN-HOST sample. This decision was made to ensure the mass bins were representative of 'typical' galaxies rather than being biased by the mass distribution of the AGN-HOST sample which tend to occupy higher mass galaxies.

Table 4.3 contains the percentages of the population densities shown in Figures 4.7 & 4.8 in the quenching regimes originally defined in Chapter 3 for rapid ($\tau < 1$ Gyr), intermediate ($1 < \tau$ [Gyr] < 2) and slow ($\tau > 2$ Gyr) quenching rates in each of the three mass bins. Uncertainties in the population densities (shown by the shaded regions) are determined from the maximum and minimum values spanned by $N = 1000$ bootstrap iterations, each sampling 90% of the galaxy population. 1σ uncertainties are quoted for the percentages in Table 4.3, calculated from the bootstrapped distributions.

At all masses, the population density for galaxies within the AGN-HOST population across the quenching time, t_q (left panels of Figure 4.7), is different from that of the inactive galaxies (right panels of Figure 4.7). Recent quenching ($t > 11$ Gyr) is the dominant history for low and medium mass AGN-HOST galaxies, particularly for the smooth weighted population hosting an AGN (solid lines, left panels Figure 4.7). However, this effect is less dominant in higher mass galaxies where quenching at earlier times also has high density (bottom left panel of Figure 4.7).

The population densities for the quenching rate, τ, in Figure 4.8 and Table 4.3 show the dominance of rapid quenching ($\tau < 1$ Gyr) within the AGN-HOST population, particularly for smooth galaxies (solid lines, left panels Figure 4.8). With increasing mass the dominant quenching rate becomes slow ($\tau > 2$ Gyr). Similar trends in the population density are observed for the INACTIVE population (right panels Figure 4.8) but the overall distribution is very different.

In Figure 4.6 there is no INACTIVE control sample to act as a comparison, since an Eddington ratio cannot be measured for a black hole that is not accreting. The population densities for the AGN-HOST samples however, show the dominance of rapid and recent quenching as the Eddington ratio increases (i.e. higher black hole accretion rates). A bimodal distribution can be seen for the low Eddington ratio AGN-HOST population (top right panel of Figure 4.6) between both rapid and slow quenching rates.

The population densities for the AGN-HOST galaxies therefore all show evidence for the dominance of rapid, recent quenching. This result implies the importance of AGN feedback for the evolution within this population.

4.1.4 Discussion

The differences between the population density distributions of the AGN-HOST and INACTIVE populations in Figures 4.7 & 4.8 reveal that an AGN can have a significant effect on the SFH of its host galaxy. Both recent, rapid quenching and early, slow quenching are observed in the population densities of the AGN-HOST population.

There are however minimal differences between the smooth and disc weighted distributions of the quenching parameters within the AGN-HOST population (comparing solid and dashed lines in the left panels of Figures 4.6 - 4.8). This is agreement with the conclusions of Kauffmann et al. (2003a) who found that the structural properties of AGN hosts depend very little on AGN power. Quenching caused by AGN feedback is therefore morphologically independent; this is unlike the mechanisms discussed in Chapter 3. This suggests that the morphological dependances observed across the quenching histories in Chapter 3 are not due to the effects of AGN feedback.

Quenching at early times is observed within the INACTIVE population (see right panels of Figure 4.7), where the population density is roughly constant until recent times where the distribution drops off. This drop-off occurs at earlier times with increasing mass, with a significant lack of quenching occurring at early times for low mass INACTIVE galaxies (top right panel Figure 4.7). This is evidence of downsizing within the INACTIVE galaxy population whereby stars in massive galaxies form first and quench early (Cowie et al., 1996; Thomas et al., 2010).

The population densities for smooth weighted higher mass (bottom left panels Figures 4.7 & 4.8) and lower Eddington ratio (top panels Figure 4.6) AGN-HOST galaxies are also dominated by slow, early quenching. This implies that AGN feedback is not responsible for the cessation of star formation within a proportion of these galaxies, as this quenching has occurred prior to the triggering of the current AGN. I speculate that this is also due to the effects of downsizing rather than being caused by the current AGN, as the shape of both the AGN-HOST and INACTIVE high mass population densities are very similar at these early times. Since the lower Eddington ratio AGN-HOST population is also dominated by this early quenching at slow rates (top panels Figure 4.6) this supports the idea that the AGN is not strong enough to be the cause of this quenching. This earlier quenching would slowly form a 'dead' galaxy typical of massive elliptical galaxies which could then have a recent infall of gas either through a minor merger, galaxy interaction or environmental change, triggering further star formation and feeding the central black hole, triggering an AGN (Kaviraj, 2014a). In turn this AGN can then quench the recent boost in star formation. This track is similar to the evolution history proposed for blue ellipticals (Kaviraj et al., 2013; McIntosh et al., 2014; Haines et al., 2015, and detected in the top panel of Figure 3.7). This SFH would then give rise to the distribution seen within the high mass smooth weighted AGN-HOST population for both time and rate parameters (bottom panels of Figures 4.7 & 4.8).

Alternatively in the high mass disc weighted AGN-HOST population, in which slow, early quenching is also observed (dashed lines bottom left panels of Figures 4.7 & 4.8) this evolution could be due to initially isolated discs evolving slowly by the Kennicutt-Schmidt law (Schmidt, 1959; Kennicutt, 1997). These can then undergo an interaction or merger to reinvigorate star formation, feed the central black hole and trigger an AGN (Varela et al., 2004; Emsellem et al., 2015). These galaxies would need a large enough gas reservoir to fuel both SF throughout their lifetimes and the recent AGN. These high mass galaxies also play host to the most luminous AGN (mean $\log(L[OIII]$ [erg s^{-1}]$) \sim 41.6$) and so this SFH challenges the typical merger driven co-evolution of luminous black holes and their host galaxies (see Section 4.2 for an investigation into an alternative merger free black hole-galaxy co-evolution).

In both these high mass disc and smooth galaxies, the recently triggered, low accretion rate AGN do not have have the ability to impact the SF across the entirety of a high mass galaxy in a deep gravitational potential (Ishibashi & Fabian, 2012; Zinn et al., 2013). This leads to the lower peak for recent, rapid quenching within the high mass, low Eddington ratio AGN-HOST population for both morphologies (left bottom panels of Figures 4.7 & 4.8 and top panels of Figure 4.6).

Conversely if we now consider the low mass (left top panel Figure 4.8) and high Eddington ratio (bottom left panel of Figure 4.6) AGN-HOST population, rapid quenching, possibly caused by the AGN itself through negative feedback, is the most dominant quenching history. Within the medium mass AGN-HOST population a bimodal distribution between these two quenching histories is seen (left middle panel Figure 4.8), highlighting the strength of this method which is capable of detecting such variation in the SFHs within a population of galaxies. These lower and medium mass galaxies have lower gravitational potentials from which gas may be more readily expelled or heated (Tortora et al., 2009) by jets launched by the strongly accreting AGN, suggesting that the AGN may be the cause of the quenching observed in the population densities.

Tortora et al. (2009) model the effects of this jet-induced AGN feedback on a typical early-type galaxy and observe a drastic suppression of star formation on a timescale of ~ 3 Myr. Comparing their synthetic colours with observed colours of SDSS elliptical galaxies, they find the time between the current galaxy age, $t_{\rm gal}$ and the time that the feedback began, $t_{\rm AGN}$, peaks at $t_{\rm gal} - t_{\rm AGN} \sim 0.85$ Gyr. In the top panel of Figure 4.7, the population density for low mass AGN-HOST galaxies has a difference between the peak of the distribution and the average age of the population (galaxy age is calculated as the age of the Universe at the observed redshift, by assuming all galaxies form at $t = 0$) of ~ 0.83 Gyr. This is in agreement with the timescales for AGN feedback driven quenching derived in the simulations by Tortora et al. (2009). The dominance of rapid quenching across the smooth AGN-HOST population (solid lines in left panels of Figure 4.8) supports the hypothesis discussed in Chapter 3 that a merger, having caused a morphological transformation to a smooth galaxy, can also trigger an AGN, causing feedback and cessation of star formation (Sanders et al. 1988; Pontzen et al. 2016).

Simulations by Sparre & Springel (2016) show that major merger remnants are only quenched when the prescription used for AGN feedback in the model is stronger than their initial fiducial level. They increase the strength of their AGN feedback by decreasing the metallicity, Z, of the gas accreted by the black hole; this impacts on the cooling function of the gas $\Lambda(T, Z)$ (see Section 2.1 of Sparre & Springel, 2016). This suggest that AGN feedback will therefore have a larger effect on galaxies with lower metallicity. Considering the mass-metallicity relation (Tremonti et al., 2004), it follows from this argument that AGN feedback will have a greater effect on galaxies with lower mass. This provides more support to the hypothesis that the dominance of rapid, recent quenching across the low and medium mass AGN-HOST population (left panels Figures 4.7 & 4.8) is caused directly by the AGN.

The mechanism of AGN feedback was originally proposed to regulate the number galaxies at the bright (or high mass) end of the luminosity function in cosmological simulations (see Chapter 1). The shape of the observed K-band luminosity function can be seen in Figure 4.9 (Figure 1 from Benson et al., 2003), falling away from model estimates below a K-band magnitude of $M_K - 5\log_{10} h \sim 23.5$, or above an approximate stellar mass of $\log_{10}[M_*/M_\odot] \gtrsim 10.3$, assuming a mass-to-light ratio of $(M/L)_K = 0.8$ (Brinchmann & Ellis, 2000). However, it is the low and medium mass AGN-HOST populations where this rapid recent quenching is dominant (see left panels Figures 4.7 & 4.8). At first this seems contradictory to the arguments posed to constrain the shape of the luminosity function, but with some thought the two results can be reconciled.

The knee of the luminosity function is the point at which AGN feedback starts to impact the masses of galaxies; this occurs at $\log_{10}[M_*/M_\odot] \gtrsim 10.3$, which lies at the lower edge of the medium mass AGN-HOST population studied here. The quenching observed in the low and medium mass AGN-HOST populations will stop the stellar masses of these galaxies from growing any larger in the future. In turn these now quenched galaxies will contribute to dry mergers, which would otherwise have had high gas fractions; limiting the stellar mass of the merger remnants. The combination of these two effects, caused initially by the quench of a lower mass galaxy by negative AGN feedback, will reduce the number of galaxies which will be able to grow to populate the high mass end of the luminosity function.

However, there still remains the possibility that the AGN is not the cause of the quenching observed, but merely a *consequence* of an alternative quenching mechanism.

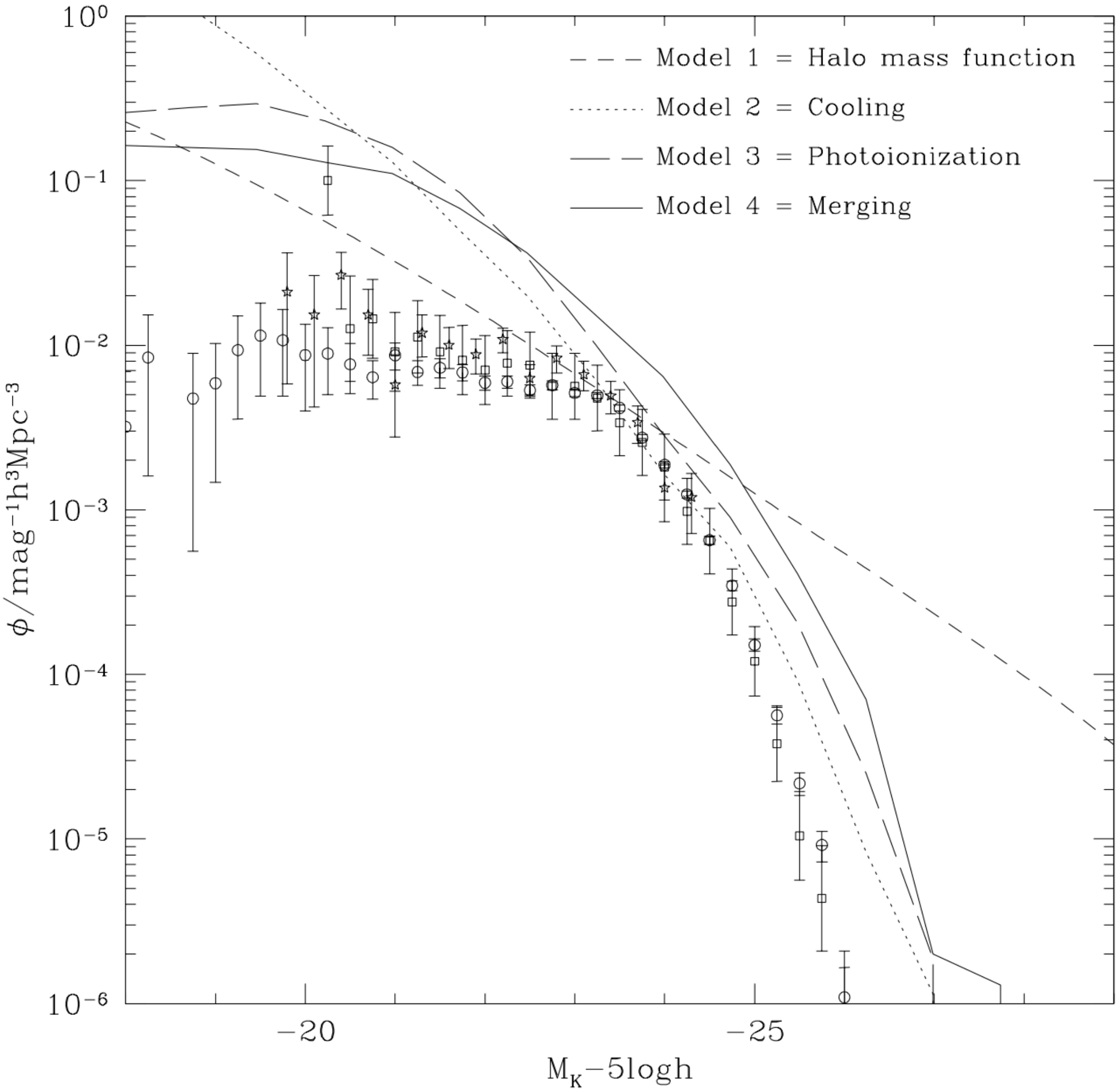

Figure 4.9: Figure 1 from Benson et al. (2003) showing the K-band luminosity function of galaxies, with $h = 0.65$. The points show the observational determinations of (Cole et al., 2001, circles), (Kochanek et al., 2001, squares), and (Huang et al., 2003, $z < 0.1$, stars). Lines show model results investigated by Benson et al. (2003) to determine what shapes this luminosity function; they concluded that including prescriptions for AGN feedback (supernova feedback winds) can help match the simulations to the data at the bright (faint) end of the luminosity function. The knee of the function occurs at $M_K - 5\log_{10} h \sim 23.5$, which is an approximate stellar mass of $\log_{10}[M_*/M_\odot] \sim 10.3$, assuming a mass-to-light ratio of $(M/L)_K = 0.8$ (Brinchmann & Ellis, 2000).

This idea is supported by simulations showing that the exhaustion of gas by a merger fuelled starburst could cause such a rapid quench in star formation and in turn also trigger an AGN (Croton et al., 2006; Wild et al., 2009; Snyder et al., 2011; Hayward et al., 2014). Yesuf et al. (2014) also showed that AGN are more commonly hosted by post starburst galaxies, with the peak AGN activity appearing $\geq 200 \pm 100$ Myr after the starburst. Such a SFH is not accounted for in the models presented here (see Section 6.2 for a discussion), however this scenario is still consistent with the results presented in this paper; that AGN which are *currently* active have been detected in host galaxies ~ 1 Gyr after the onset of quenching. Solving this issue of *cause* vs. *consequence* will not be possible with the currently available SDSS photometry. The advent of Integral Field Unit (IFU) surveys with many aperture fibres per galaxy per observation (such as the MaNGA (Bundy et al., 2015), SAMI (Croom et al., 2012) and CALIFA (Sánchez et al., 2012) surveys) will allow this problem to be studied by observing the change in quenching parameters with increasing distance from the galaxy nucleus (see Section 6.3 for a more detailed discussion).

Not all galaxies in the AGN-HOST and INACTIVE samples are quenching ($\sim 50\%$, as seen in Figure 4.5) with a significant proportion of both the AGN-HOST and INACTIVE samples lying on the SFS. A galaxy can therefore still maintain star formation whilst hosting an AGN. The results presented in Section 4.1.3 only reflect the trends for galaxies that have undergone or are currently undergoing quenching within the AGN-HOST population and can therefore be accurately fit by an exponentially declining SFH. This prevalence of star forming AGN host galaxies, combined with the results above allows us to consider that either: (i) the AGN are the cause of the rapid quenching observed but only in gas-poor host galaxies where they can have a large impact, (ii) the AGN are a consequence of another quenching mechanism but can also be triggered by other means which do not cause quenching, or (iii) the SFR of a galaxy can recover post-quench and return to the star forming sequence after a few Gyr (see recent simulations by Pontzen et al. 2016 and Sparre & Springel 2016). Further investigation will therefore be required to determine the nature of this quenching (see Section 6.3 for a discussion of proposed future work with IFU survey data).

4.2 Bulgeless galaxies hosting growing black holes

The work in the following chapter is in preparation for submission to MNRAS in Simmons, Smethurst & Lintott (in prep.). I was responsible for the spectral data reduction and statistical analysis and assisted in the interpretation of the results.

Although the study of large populations of galaxies provides crucial information to constrain the processes governing galaxy evolution, valuable insight can still be discerned from detailed observations of a smaller sample of rare objects.

The strong correlations that exist between black hole mass and velocity dispersion (Magorrian et al., 1998; Merritt & Ferrarese, 2001; Hu, 2008; Kormendy et al., 2011; McConnell et al., 2011), bulge stellar mass (Marconi & Hunt, 2003; Häring & Rix, 2004), and total stellar mass (Cisternas et al., 2011) suggest that galaxies co-evolve with their central super massive black holes (SMBH). Since mergers can grow both bulges and black holes these correlations have been interpreted as the result of a few mergers within a Hubble time (Peng, 2007; Hopkins et al., 2008b; Jahnke & Macciò, 2011). A growing black hole must accrete matter and is therefore observed as an AGN during this time period. Understanding the triggering mechanisms of AGN which kick-start this process of simultaneous galaxy and black hole evolution and possible subsequent feedback from the AGN, is therefore important. However, in Section 4.1, I presented the argument that disc galaxies currently hosting an AGN could have started quenching at early times with very slow quenching rates, suggesting an alternative to the typical rapid and violent merger driven galaxy-black hole coevolution scenario (Hopkins et al., 2008b).

A secular co-evolution of galaxy and black hole has been proposed by previous works (Greene et al., 2010; Jiang et al., 2011b; Cisternas et al., 2011; Simmons et al., 2011; Schawinski et al., 2011; Kocevski et al., 2012) and was investigated by Simmons et al. (2013) who studied 13 AGN residing in disc dominated host galaxies, whose accretion histories are assumed to be merger free. In the following work I examine a larger sample of disc galaxies, visually identified as bulgeless or disc dominated, hosting an AGN and investigate the locations of these galaxies on typical galaxy-black hole scaling relations. Since the disc galaxies in this sample will have different dynamical histories to bulge dominated galaxies, their black hole masses are not expected to correlate in the same way to their stellar masses if different dynamical histories lead to different mechanisms for black hole growth.

4.2.1 Observational Data

The goal of this study is to investigate black hole growth in galaxies whose growth histories have been dominated by relatively calm, slow processes. A sample of growing (i.e. active) black holes hosted in disc-dominated galaxies is therefore required. Optimally, the AGN should have broad emission lines to facilitate measurement of black hole masses via well-established relations between line flux and width and black hole mass. Previously, Simmons et al. (2013) investigated a sample of 13 pure disc galaxies hosting AGN. The selection method used in that study selected against very massive black holes with unobscured emission: only 2 AGN of 13 showed clear signs of broadened line emission in their SDSS spectra, leading to calculated black hole masses of $4 \times 10^6 \mathrm{M}_\odot$ and $1 \times 10^7 \mathrm{M}_\odot$. Here the aim is to select AGN hosted in disc-dominated galaxies at all masses with broad emission lines that can be used to calculate black hole masses through virial assumptions (see Section 4.2.2.4). Below the methods used to select both a disc dominated AGN sample along with a control sample of typical AGN host galaxies are described.

4.2.1.1 Selecting disc-dominated AGN host galaxies

Asample of unobscured AGN with broad emission lines must first be selected, so that black hole masses may be measured from well-established correlations between emission line properties, such as the FWHM of the broadened $H\alpha$ emission line, and black hole masses (e.g., Greene & Ho, 2007; Jiang et al., 2011a; Xiao et al., 2011; Peterson, 2014).

These unobscured AGN have characteristic colours in multi-wavelength imaging, particularly in X-ray, optical and infrared bands (Kauffmann et al., 2003a; Stern et al., 2005; Goulding & Alexander, 2009; Kauffmann & Heckman, 2009; Aird et al., 2012; Mendez et al., 2013; Azadi et al., 2016; Cowley et al., 2016; Harrison et al., 2016). Given the existence of all-sky surveys at many of the wavelengths relevant to the selection of unobscured AGN, it is now possible to construct larger samples of sources identified as unobscured AGN with high likelihood.

An initial sample of AGN was selected using the W2R sample of Edelson & Malkan (2012), comprised of $4,316$ sources identified using multi-wavelength data from the *Wide-field Infrared Survey Explorer* (*WISE*; Wright et al., 2010), Two Micron All-Sky

Survey (2MASS; Skrutskie et al., 2006), and *ROSAT* all-sky survey (RASS; Voges et al., 1999). This multi wavelength photometric, all-sky selection, selects unobscured AGN at > 95 per cent confidence (Edelson & Malkan, 2012).

Following this selection of $4,316$ sources, galaxies imaged by the Sloan Digital Sky Survey are then further sub-selected. There are $1,844$ W2R sources with positional matches having reported coordinates within $3''$ of a source in the SDSS (York et al., 2000) Data Release 8, a fraction consistent with the fractional area of the SDSS versus an all-sky catalog.

Each of the $1,844$ SDSS ugriz colour images were then examined to identify disc-dominated features. 101 disc-dominated AGN host galaxies were identified on the basis of clearly identifiable spiral arms, bars or obvious edge-on discs. I shall refer to these galaxies as the DISCDOM sample. Figures 4.10 & 4.11 collectively show the SDSS postage stamps for all galaxies in the sample, with all images showing the expected bright nebular emission of the unobscured AGN.

4.2.1.2 Spectra

Of the 101 disc-dominated AGN host galaxies with SDSS imaging, 96 have spectra from SDSS Data Release 9 (Ahn et al., 2012). 23 of which were first identified as AGN by Shen et al. (2008) and Edelson & Malkan (2012). Example spectra centred around the broad $H\alpha$ emission at $6562\mathring{A}$ for 5 of these SDSS spectra are shown in Figure 4.12.

The broad $H\alpha$ emission for 5 additional sources was measured using long-slit spectra techniques with the Intermediate Dispersion Spectrograph (IDS) on the Isaac Newton Telescope (INT) from 21st-23rd May 2014. I reduced these spectra using the standard reduction pipeline of Massey, Valdes & Barnes (1992) using IRAF modules to debiase, dark subtract, flat field, calibrate, sky subtract, flux calibrate and finally extract spectra for the central regions of each galaxy. The redshift of these sources was also measured from the reduced spectra, using the peak of the broadened $H\alpha$ emission to measure λ_{obs}. These reduced spectra, centred around the broad $H\alpha$ emission at $6563\mathring{A}$, are shown in Figure 4.13 for the 5 galaxies observed.

Figure 4.14 shows the redshift distribution of all 101 sources for which we have spectra; the mean redshift of the sample is $\langle z \rangle = 0.129$, with the highest-redshift

Figure 4.10: Postage stamp SDSS images of the 96 galaxies within the DISCDOM sample for which SDSS spectra were available, sorted from lowest redshift ($z = 0.03$; top left) to highest redshift ($z = 0.24$; bottom right). The scale for each image is shown by the 5" ruler in the top left panel.

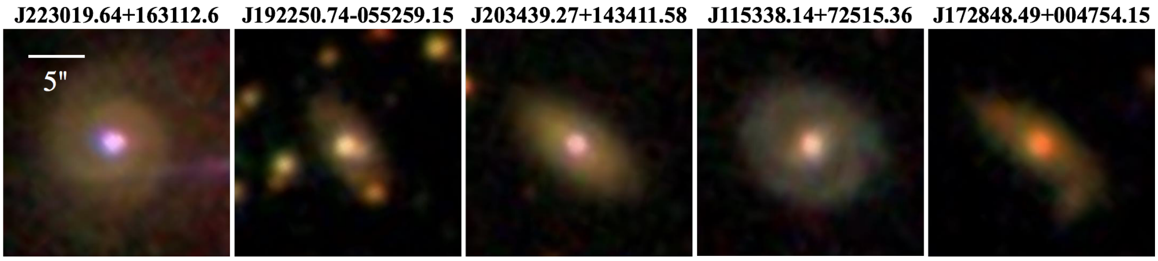

Figure 4.11: Postage stamp SDSS images of the 5 galaxies observed with the IDS on the INT within the DISCDOM sample. The scale for each image is shown by the 5" ruler in the left panel.

source having $z = 0.244$.

4.2.1.3 Selecting a Control Sample

Since the majority of the galaxies in the DISCDOM sample have been observed using SDSS, I constructed a control sample from the SDSS quasar catalog of Shen et al. (2011). Using this sample I compiled a sample of 191 galaxies which were redshift matched to within $\pm 5\%$ of the DISCDOM sample. I shall refer to these galaxies as the QSOCONTROL sample. 124 of the QSOCONTROL sample also had measured $(B/T)_r$ ratios from Simard et al. (2011, matched with a $3''$ search radius, see Section 4.2.2.2).

This provides a control sample of 'typical' AGN host galaxies representative of the population in the redshift range probed in this study.

4.2.2 Galaxy and Black Hole Properties

In order to study the relation between the galaxies and their SMBHs in these disc dominated systems, their properties shall be compared to well tested black hole-galaxy scaling relations. In the following section I therefore describe how the photometry, black hole masses, total and bulge stellar masses, bolometric luminosities and Eddington ratios were derived for each galaxy in the DISCDOM sample.

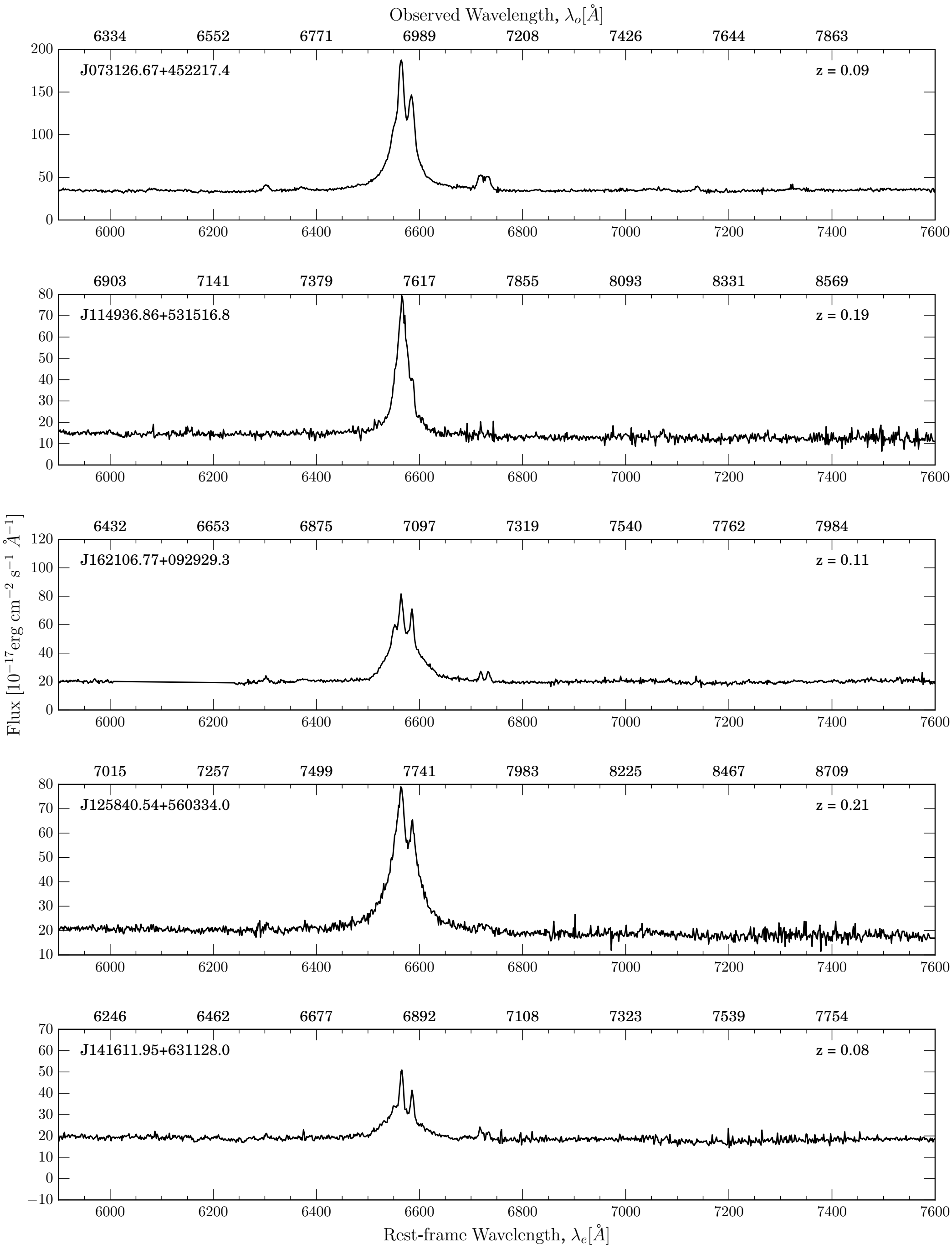

Figure 4.12: 5 example SDSS spectra from with the corresponding measured redshift values shown. Each panel shows the same rest-frame wavelength range (bottom axis of each panel); observed wavelengths are shown on the top axis of each panel. All spectra show broadened $H\alpha$ emission, confirming that the multi-wavelength AGN selection employed here efficiently selects unobscured AGN.

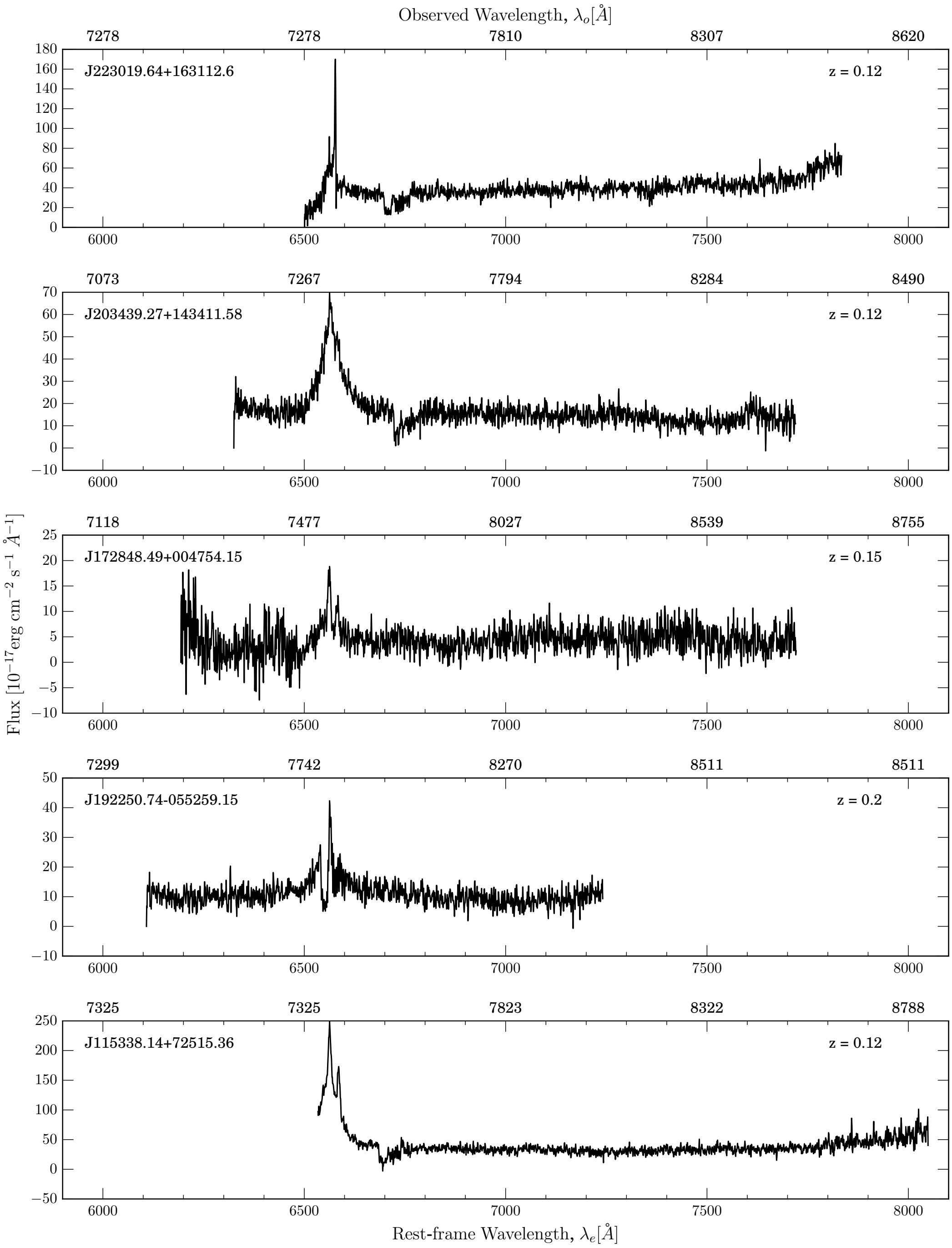

Figure 4.13: Reduced spectra from the IDS on the INT for the 5 galaxies observed. Each panel shows the same rest-frame wavelength range (bottom axis of each panel); observed wavelengths are shown on the top axis of each panel, with redshifts in the top right of each panel. All spectra one again show broadened $H\alpha$ emission, confirming that the multi-wavelength AGN selection employed here efficiently selects unobscured AGN.

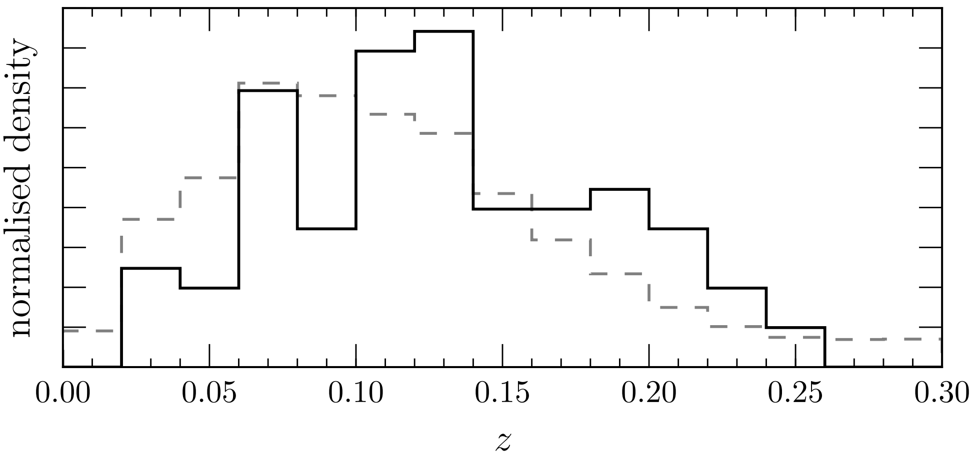

Figure 4.14: Normalised redshift distribution for all 101 sources (solid) for which we have spectra, either from SDSS or measurements with the IDS on the INT. Also shown is the overall redshift distribution of SDSS DR7 in the relevant redshift range of our sources (dashed).

4.2.2.1 Photometry

The AGN contribution to the magnitude of each galaxy, m_{gal}, is calculated by subtracting the flux in the SDSS `psfMag`, m_{psf}, from the flux in `modelMag`, m_{model} in a given wave band, b as follows:

$$m_{\text{b,gal}} = -2.5\log_{10}\left[10^{\left(\frac{m_{\text{b,model}}}{-2.5}\right)} - 10^{\left(\frac{m_{\text{b,psf}}}{-2.5}\right)}\right], \tag{4.5}$$

since the normalisation constants in the flux-magnitude conversion will be constant for different sized apertures in a given band. `psfMag` is the best estimate of unresolved emission, while `modelMag` is the optimal quantity for computing aperture-matched source colours[1]. A galaxy magnitude in both the SDSS u and r bands was calculated in order to determine the galaxy $u - r$ colour.

A similar NUV galaxy magnitude can be calculated using the GALEX apertures, however matching these apertures to those provided by SDSS cannot be done with a large enough degree of accuracy to derive a reliable galaxy $NUV - u$ colour. This therefore means that STARPY cannot be run on these unobscured AGN host galaxies of

[1]https://www.sdss3.org/dr10/algorithms/magnitudes.php

the DISCDOM sample. However, the locations of the DISCDOM sample on the optical colour-magnitude diagram can still be explored; this is studied in Section 5.2 (see Figure 4.22).

4.2.2.2 Total stellar masses

Total stellar masses are calculated using the well-studied relation between stellar mass, absolute galaxy r-band magnitude, $M_{\rm r,gal}$, and $u-r$ galaxy colour (corrected for galactic extinction; Schlegel et al., 1998), following the method of Baldry et al. (2006, see Section **??**). Uncertainties are propagated from the colour-magnitude relationship and due to the subtraction of the central AGN component. The average uncertainty on each measurement is ~ 0.3 dex. The distribution of the stellar masses calculated for the DISCDOM sample is shown in the right panel of Figure 4.17.

4.2.2.3 Bulge stellar masses

Calculation of the bulge stellar mass for the DISCDOM sample is more complicated than the total stellar mass calculation described in the previous section. The nuclear emission (as estimated via comparison of `psfMag` to `modelMag`) is generally between 20 to 200 per cent of the galaxy-only emission. The presence of the luminous AGN therefore severely compromises the estimates of the bulge-to-total ratio, (B/T), in the host galaxy provided by, e.g., the `fracDeV` parameter reported in the SDSS catalogs. The `fracDeV` parameter estimates that $\sim 80\%$ of the galaxies in this sample are pure de Vaucouleurs (1953) bulges in the r-band, despite the fact that the sample was selected on the basis of clear visual signatures of dominant discs (see Figure 4.10). None of the photometric parameters derived by the SDSS pipeline allow for the dual presence of an AGN and a host galaxy. Without such considerations the unresolved AGN light is likely to be attributed to the compact bulge component in a bulge-disc model fit (Simmons & Urry, 2008; Koss et al., 2011) leading to an overestimate of the bulge stellar mass.

AGN-host decomposition based on 2-dimensional image fitting (e.g., Simard, 1998; Peng et al., 2002, 2010) is more reliable (e.g. McLure et al., 1999; Urry et al., 2000; McLure & Dunlop, 2001; Sánchez et al., 2004; Pierce et al., 2007; Gabor et al., 2009; Simmons et al., 2011, 2013; Koss et al., 2011). However even in high-resolution *Hubble*

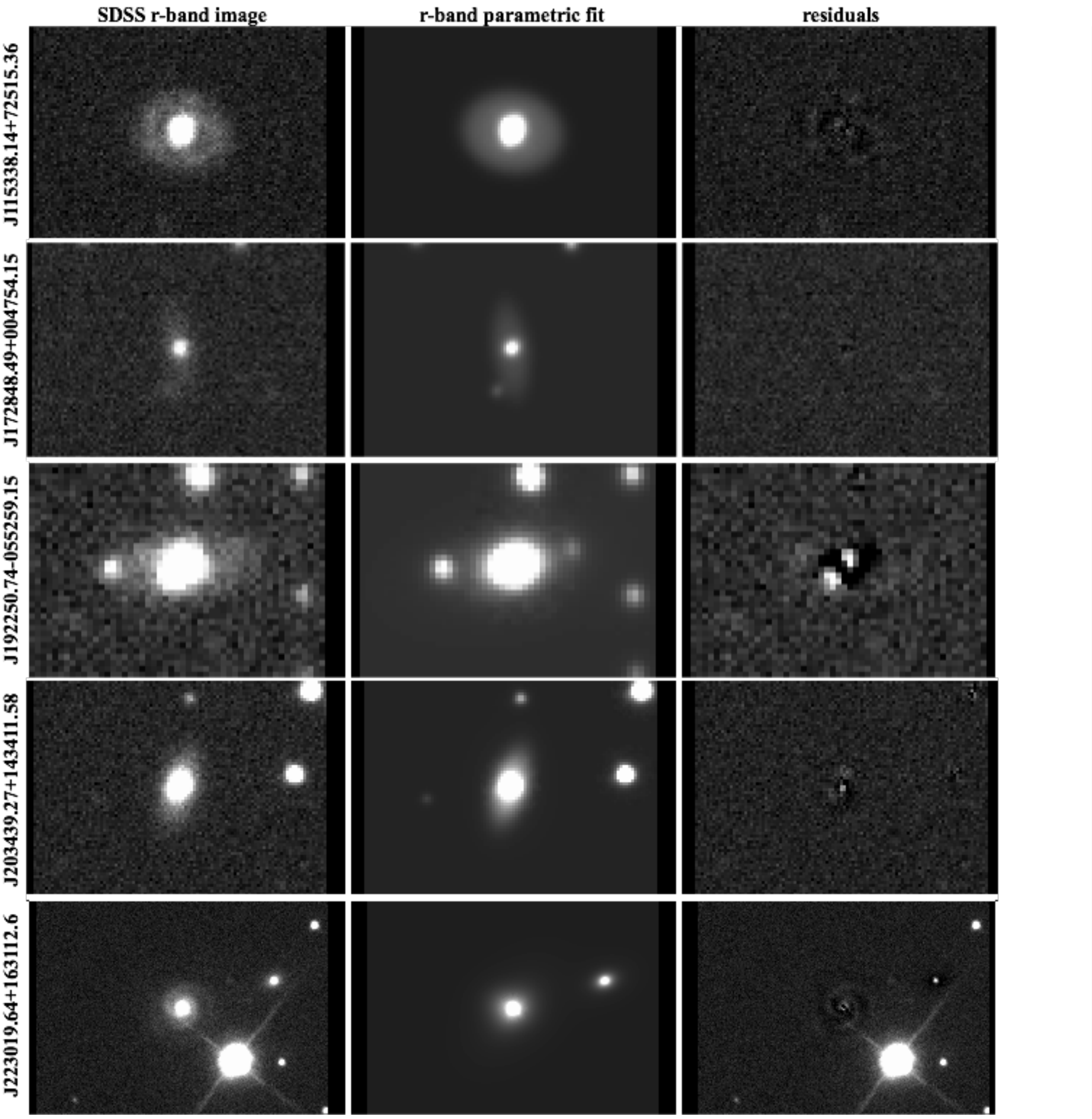

Figure 4.15: SDSS r-band images (left), with the 3 component parametric fits from GALFIT (middle) and the residuals (right; with the same scale as the original image) for the 5 galaxies observed with the IDS on the INT. Stable, but uncertain, bulge-to-total ratios were only recovered for the galaxies in the top two rows. In the bottom three rows the nuclear emission was too bright and image resolution too low to derive a reliable estimate of the bulge-to-total ratio.

Space Telescope (HST) images (Simmons & Urry, 2008) or SDSS imaging at $z \gtrsim 0.06$ (Koss et al., 2011; Simmons et al., 2013) the recovered bulge-to-total ratio can be highly uncertain, particularly for disc-dominated galaxies with a very small bulge or pseudo-bulge (Kormendy & Kennicutt, 2004) component. While the AGN-host decompositions of the galaxies studied by Simmons et al. (2013) recovered reliable bulge-to-total ratios for 11 of the 13 galaxies, their sources were at substantially lower redshift than the DISCDOM sample (with the majority at $z < 0.08$), and their AGN significantly less luminous ($L_{bol} \lesssim 10^{44}$erg s^{-1}, whereas in the DISCDOM sample $L_{bol} \gtrsim 10^{44}$erg s^{-1}, see Section 4.2.2.5).

Bulge-to-total fits were first attempted for the 5 galaxies in the DISCDOM sample which were observed with the IDS on the INT using the GALFIT software (Peng et al., 2002); the results of which are shown in Figure 4.15. I used a Sérsic light profile (Sérsic, 1968) to model bulge and disc components, defined by an effective radius, R_e, and light concentration index, n, as:

$$I(R) = I_e \exp\left(-b_n\left[\left(\frac{R}{R_e}\right)^{1/n} - 1\right]\right), \tag{4.6}$$

where I_e is the intensity at the effective radius, R_e and b_n is a constant defined in relation to the Sérsic index, n. Typical disc (bulge) light profiles have $n \approxeq 1$ ($n \approxeq 3$). Each of the galaxies observed with the INT were fitted with a disc, bulge and PSF component (to account for the bright nuclear emission of the AGN). PSFs were extracted from the SDSS FITS images using the standard `read_PSF` IDL code provided by the SDSS pipeline[2]. Initial guesses of $n = 2.5$ are used on the first pass of the GALFIT algorithm, which uses a χ^2 minimisation method to determine the best fit Sérsic index, effective radius, magnitude and position for each of the 3 components. This first pass allows the positions of the components to be determined, which are then fixed on a second pass of the algorithm to ensure accurate magnitudes, radii and Sérsic indices are then inferred. From these models, the GALFIT r band magnitudes of the bulge, $m_{r,\mathrm{bulge}}$, and disc, $m_{r,\mathrm{disc}}$, components were used to calculate the bulge-to-total ratio, $(B/T)_r$, as follows:

$$(B/T)_r = \frac{10^{\left(\frac{m_{r,\mathrm{bulge}}}{-2.5}\right)}}{\left[10^{\left(\frac{m_{r,\mathrm{bulge}}}{-2.5}\right)} + 10^{\left(\frac{m_{r,\mathrm{disc}}}{-2.5}\right)}\right]}. \tag{4.7}$$

[2] `http://www.sdss.org/dr12/algorithms/read_psf/`

Stable, but highly uncertain, bulge-to-total ratios were recovered for only 2 of the 5 galaxies (the top two rows in Figure 4.15). In the remaining 3 cases the nuclear emission was too bright and the image resolution too low for a reliable bulge-to-disc decomposition. Detailed AGN host fits to the SDSS images in the rest of the DISCDOM sample, which lie at similar redshifts, are therefore not likely to produce useful measurements of bulge masses. *HST* imaging would enable these measurements, and although currently not available for the galaxies in this sample, observations are currently underway in Cycle 24 (ID: 14606).

Nevertheless, it is possible to constrain the bulge contribution to the host galaxies using existing structural parameters from large-scale studies performing bulge-disc decompositions of SDSS galaxies. While such studies do not account for the presence of an AGN, their tendency to overestimate the bulge-to-total ratio as a result means that bulge masses derived from these quantities may be taken to be conservative upper limits.

Simard et al. (2011) fit multiple models to 1.12 million galaxies in the SDSS catalog to determine best-fit structural parameters for each galaxy. Their r-band bulge-to-total ratio of the best-fit model is taken as an upper limit to the true bulge-to-total ratio of the DISCDOM sample. To convert limits on bulge luminosities to limits on bulge masses, we assume the mass-to-light ratio of the bulge is equal to the mass-to-light ratio of the disc. This is a reasonable assumption for disc-dominated galaxies, where many of the "bulge" components, if present, are likely to be rotationally-supported pseudo-bulges (Kormendy & Kennicutt, 2004) with stellar populations similar to that of the disc (e.g., Graham, 2001).

The bulge-to-total ratio upper limits of the 89 galaxies in the DISCDOM sample which were included in the Simard et al. (2011) study, range from $0.13 \leq (\mathrm{B/Tot})_{r,\mathrm{max}} \leq 1.0$, with a mean value of 0.5. Inspection of the morphologies of the galaxies shown in the images in Figure 4.10 reveals how such a range in $(\mathrm{B/Tot})_{r,\mathrm{max}}$ is clearly an over-estimate of the bulge contribution to these galaxies. Applying these bulge-to-total limits to the stellar masses derived in Section 4.2.2.2, results in bulge mass upper limits of $3 \times 10^9 \mathrm{M}_\odot < \mathrm{M}_{\mathrm{bulge}} < 7 \times 10^{10} \mathrm{M}_\odot$. The distribution of bulge-to-total ratios in the DISCDOM sample are shown in the middle panel of Figure 4.17

4.2.2.4 Black hole mass estimates

The selection of unobscured AGN facilitates the accurate estimate of black hole masses using a viral assumption. Unobscured AGN have broad emission lines originating from within the black hole sphere of influence; this photoionized broad line region (BLR) can be used as a dynamical tracer of the black hole mass. The viral black hole mass (Peterson, 2014) can be expressed simply as:

$$M_{BH} = f\frac{R\Delta v^2}{G}, \tag{4.8}$$

where Δv is the velocity dispersion of the emitting BLR, which is assumed to be spherical with radius R. The factor, $f = 0.75$ (Netzer, 1990) then corrects for this simplifying assumption. The velocity dispersion of the BLR can be inferred from the FWHM of a broad line, such as $H\alpha$ or $H\beta$, and the radius inferred from the luminosity of the same broad line. This radius-luminosity relationship is calibrated using the more precise black hole mass measurement technique of reverberation mapping (Blandford & McKee, 1982; Peterson, 2001; Barth et al., 2015) in which the radii are measured based on the observed delay between variations in the AGN continuum and the BLR emission (Kaspi et al., 2005; Bentz et al., 2006). Masses derived with this virial method, under these simplifying geometric assumptions, have been shown to be accrate to within a factor of ~ 3 when compared to masses derived using the M_{BH}-σ method (Ferrarese et al., 2001; Nelson et al., 2004; Onken et al., 2004, and see Section 4.1.1).

Using the M_{BH}-σ relation to calculate black hole masses (as in Section 4.1.1) is not possible in this case since I am trying to investigate how these galaxies evolve in comparison to the 'typical' AGN host galaxy population used to fit the M_{BH}-σ relation. Instead I employ the established relation between the black hole mass and the FWHM and luminosity in the broad Hα line of Greene & Ho (2007):

$$M_{BH} = (3.0^{+0.6}_{-0.5}) \times 10^6 \left(\frac{L_{H\alpha}}{10^{42}\ \mathrm{erg\ s^{-1}}}\right)^{0.45\pm0.03} \left(\frac{\mathrm{FWHM_{H\alpha}}}{10^3\ \mathrm{km\ s^{-1}}}\right)^{2.06\pm0.06} M_{\odot}, \tag{4.9}$$

derived using the virial method described above.

To obtain an estimate of the FWHM of the broadened $H\alpha$ lines, I performed spectral fitting on each of the SDSS and INT spectra described in Section 4.2.1.2 to recover narrow- and broad-line strengths and widths of the Hα 6563 Å line, by using `GANDALF` (Sarzi et al., 2006) to fit multiple simultaneous lines as well as the continuum of the spectra. GANDALF is optimised for use with SDSS spectra and so using the program with the INT spectra required minimal data re-formatting; I logarithmically re-binned and de-redshifted the spectra. From the continuum-subtracted best fit provided by GANDALF}, I determine the FWHM and line flux of the broad and narrow components of the Hα line simultaneously, one again employing emcee[3], the Python MCMC ensemble sampler by Foreman-Mackey et al. (2013), described in Chapter 2.

The uncertainties reported by emcee encapsulate the separation of narrow and broad line components in measurement of the FWHM. The reported uncertainties on black hole masses include this source of uncertainty as well as the reported uncertainties in the black hole-broad line relation (Greene & Ho, 2007). There are other sources of uncertainties, such as those involved in implicitly assuming the fixed geometric correction factor, $f = 0.75$ (Netzer, 1990) for each SMBH, the spectral noise, and the error introduced by assuming a Gaussian line profile for all measured broad lines. Determining uncertainties for the last two is outside the scope of this study; based on visual inspection of the line fits, the first is very small compared to the other uncertainties. These fits to the broad and narrow line Hα components in the INT spectra are shown in Figure 4.16.

The black hole masses for the 101 galaxies of the DISCDOM sample range from $10^6.2\mathrm{M}_\odot \leq \mathrm{M}_{\mathrm{BH}} \leq 2 \times 10^9.5\mathrm{M}_\odot$ and the distribution is shown in the left panel of Figure 4.17 in comparison to those from the QSOCONTROL sample.

4.2.2.5 Bolometric Luminosities

Bolometric luminosities are calculated from the wavelength-dependent bolometric corrections of Richards et al. (2006) using the conversion from the $12\mu m$ infrared luminosities, $L_{12\mu m}$:

$$L_{bol} \approx 8 \times L_{12\mu m}. \tag{4.10}$$

The infrared luminosity, $L_{12\mu m}$, is calculated from the WISE W3 magnitudes, M_{W3}, for which all of the DISCDOM sources have a detection, as follows:

$$L_{12\mu m} = \left(\frac{4\pi d^2}{10^{-2}\ \mathrm{m}^2}\right)\left(\frac{c}{\lambda}\right)\left(\frac{F_{\nu,0}}{1 \times 10^{23}\ \mathrm{Jy}}\right)10^{\left(\frac{M_{W3}}{-2.5}\right)}. \tag{4.11}$$

[3] dan.iel.fm/emcee/

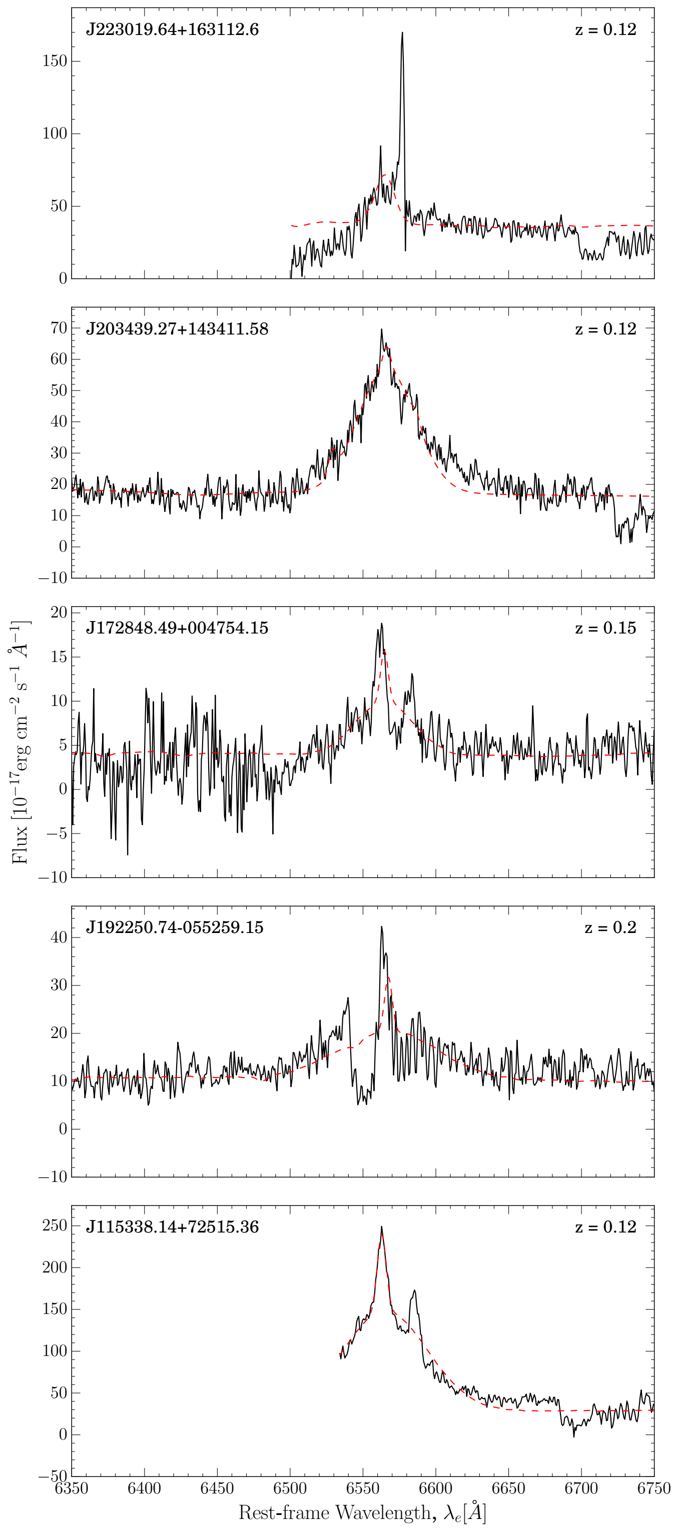

Figure 4.16: Reduced spectra from the IDS on the INT for the 5 galaxies observed with the corresponding measured redshift values shown. Spectra are aligned with the broad $H\alpha$ emission line, the gaussian fits to which are shown by the dashed red line.

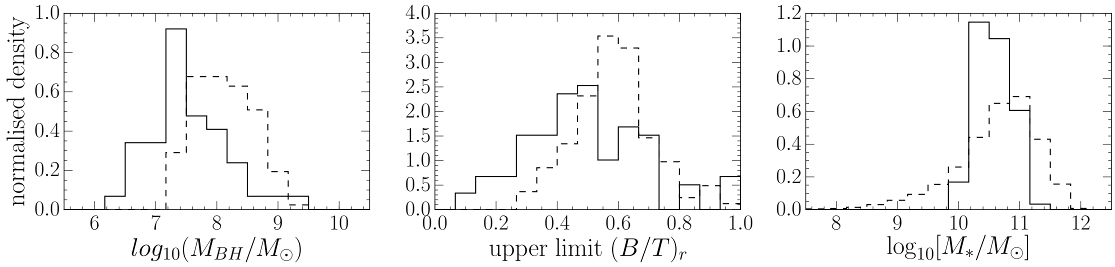

Figure 4.17: Distributions of black hole mass (left), upper limits on the r-band bulge-to-total mass ratio from Simard et al. (2011, middle) and stellar mass (right) of the DISCDOM sample (solid) in comparison to the QSOCONTROL sample (dashed).

The derived bolometric luminosities were first used to calculate Eddington ratios, λ_{Edd}, for the DISCDOM sample (using the method outlined in Section 4.1.1), and then the black hole mass accretion rate, $\dot{m}$, using a simple matter to energy conversion:

$$L = \frac{E}{t} = f \cdot \frac{mc^2}{t}, \tag{4.12}$$

where $f = 0.15$ (Elvis et al., 2002), is a lower limit on the radiative efficiency factor (i.e. what fraction of the accreted mass can be turned into radiated energy). The black hole mass accretion rate, $\dot{m}$ is therefore calculated as:

$$\frac{m}{t} = \left(\frac{\dot{m}}{\mathrm{M}_{\odot}\ \mathrm{yr}^{-1}}\right) = \left(\frac{1.58 \times 10^{-26}}{f}\right) \left(\frac{\mathrm{cm\ s}^{-1}}{c}\right)^2 \left(\frac{L_{\mathrm{bol}}}{\mathrm{erg\ s}^{-1}}\right). \tag{4.13}$$

All of these derived galaxy and black hole properties of the DISCDOM sample are now compared to those of QSOCONTROL sample in Section 5.2.

4.2.3 Results

The total stellar mass and estimated bulge masses (see Section 4.2.2.2) are plotted against the black hole masses for the DISCDOM sample in Figures 4.18 & 4.19 respectively. I fit a multiple linear regression model to both of these relations using an inference method which encompasses the uncertainties on both x- and y-dimensions and the intrinsic scatter in the data. The full method is outlined in Kelly (2007) and is publicly available as a *Python* module LINMIX[4]; a brief outline of the method is provided below.

[4] `http://linmix.readthedocs.org/`

A multiple linear regression model assumes a simple linear relationship between two independent variables, x and y, where both variables are unknown, with added noise, ϵ, from an unknown unobserved random variable. In the LIMMIX package this is modelled with the following form:

$$\eta = \alpha + \beta * x_i + \epsilon \tag{4.14}$$

$$x = x_i + x_{err} \tag{4.15}$$

$$y = \eta + y_{err}. \tag{4.16}$$

Here α and β are the regression coefficients to be inferred (like m and c in a traditional $y = mx + c$ linear regression), x_{err} is the error on the measured values x_i, and y_{err} is the error on the measured values η. ϵ is assumed to be normally-distributed, centred around zero, with a variance σ^2. x_{err} and y_{err} are also assumed to be normally-distributed and centred around zero with variances σ_x^2 and σ_y^2, respectively and covariance xy_{cov}. This linear regression method can also incorporate the upper limits on the bulge mass measurements of the 89 SDSS galaxies measured by Simard et al. (2011, see Section 4.2.2.2), by treating them as 'censored values' (see Section 7.2 of Kelly, 2007), shown by the solid line in Figure 4.19.

Using LINMIX, I also fit to the observations of 30 early-type galaxies from Häring & Rix (2004). Despite the fact that galaxies in the DISCDOM sample are disc dominated and contain either no bugle or a pseudo-bulge, they preferentially lie above the relationship between black hole and bulge stellar mass derived using the bulge dominated galaxies of Häring & Rix (2004), as seen in Figure 4.19.

I consider how the black hole mass relates to the bolometric luminosity of the DISCDOM sample, compared with the QSOCONTROL sample in Figure 4.20. The galaxies of the DISCDOM sample have both lower black hole masses and lower bolometric luminosities in comparison to the QSOCONTROL sample, however the Eddington ratios are very similar, as shown by the distributions in Figure 4.21. In fact, the Eddington ratios of the redshift matched QSOCONTROL sample are on average, lower than that for the DISCDOM sample. I can reject the null hypothesis that the disc dominated galaxies are drawn from the same distribution as the QSOCONTROL sample but not for the entire quasar sample of Shen et al. (2011).

Within the QSOCONTROL sample, 108 galaxies were morphologically classified by the Galaxy Zoo 1 project Lintott et al. (2008, 2011), all of which have a debiased

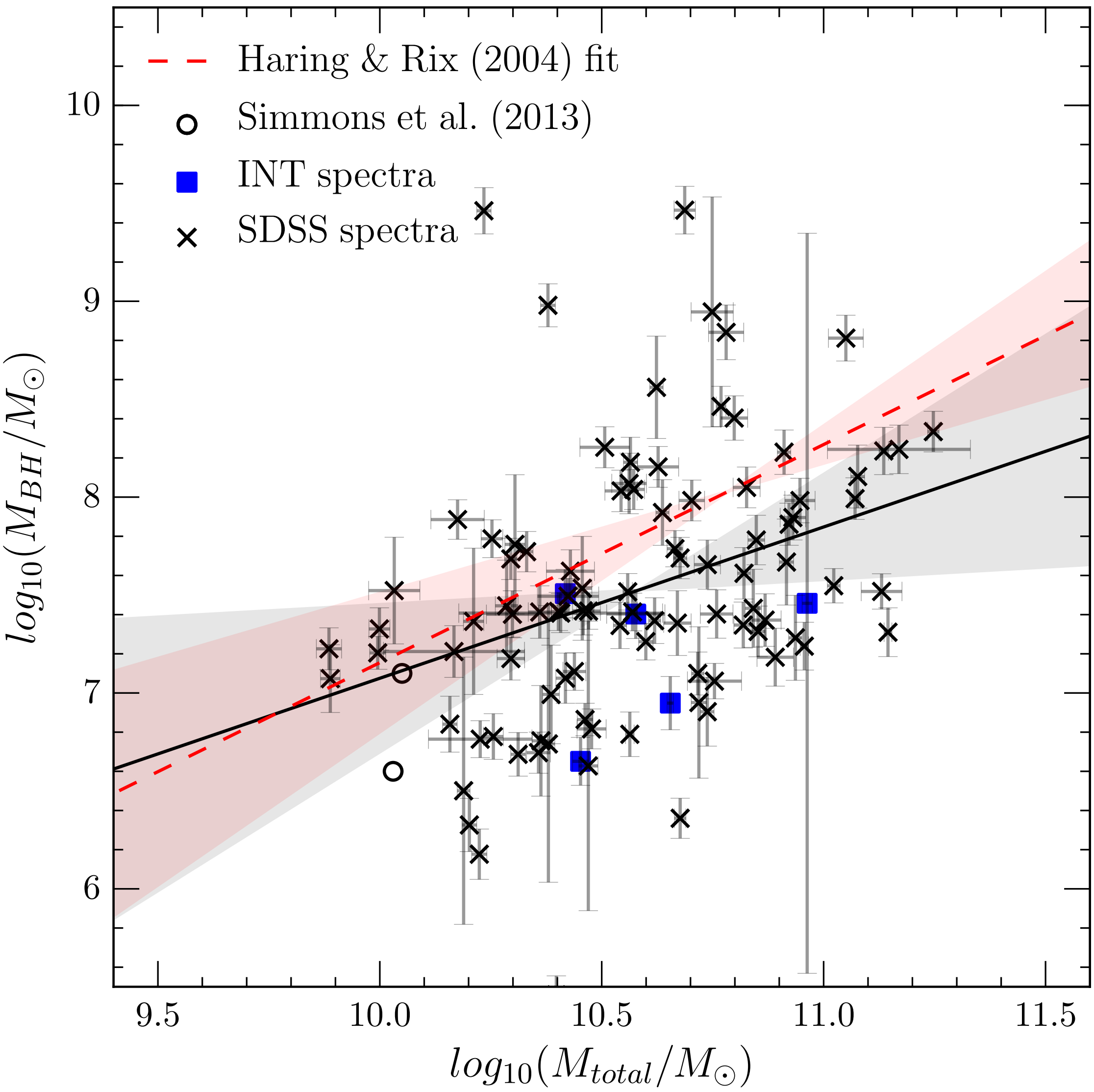

Figure 4.18: Total stellar mass against the black hole mass of the 101 galaxies, including those observed by SDSS (crosses), with the IDS on INT (blue squares) and detections from Simmons et al. (2013, open cirlces). The best fit line to the data points and two-dimensional errors from linear regression is shown (solid line) with $\pm 3\sigma$ (grey shaded). I also show the best fit found using this same method to the early-type galaxies of Häring & Rix (2004) (dashed line) with $\pm 3\sigma$ (red shaded) and the measured values shown by the red circles. Despite the fact that these galaxies are predominantly disc dominated they are found in the same region of parameter space as the bulge dominated systems used to derive the Häring & Rix (2004) relationship (see discussion in Section 4.2.4).

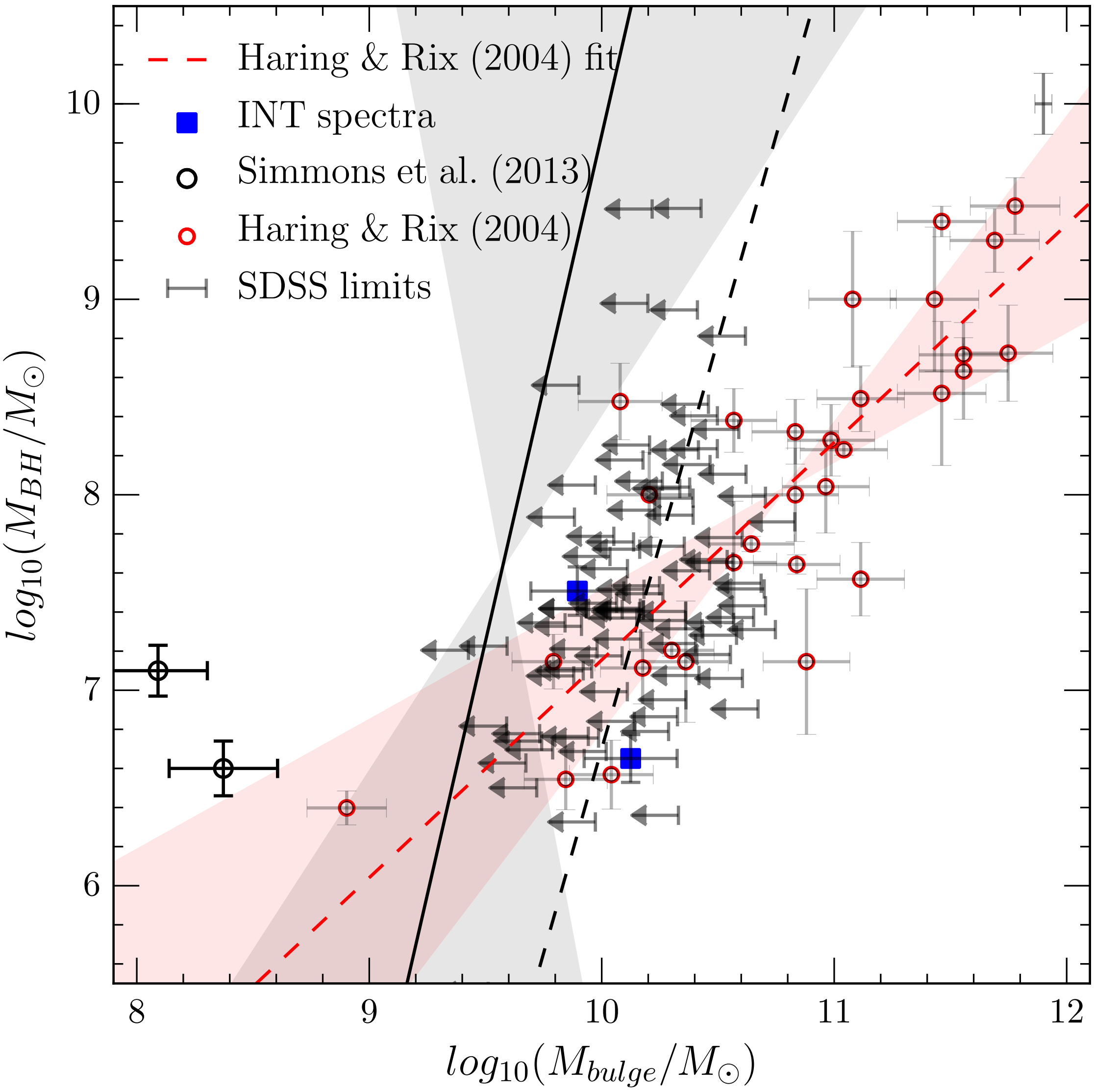

Figure 4.19: The upper limits on the calculated bulge masses are plotted against the black hole mass with the best fit to these upper limits and two-dimensional errors using linear regression methods (solid line) shown with $\pm 3\sigma$ (grey shaded). The dashed line shows the fit if the upper limits are not treated as such. I also show the best fit found using this same method to the early-type galaxies of Häring & Rix (2004) (dashed line) with $\pm 3\sigma$ (red shaded) and the measured values shown by the red circles. Despite the fact that these galaxies are predominantly disc dominated they will are most likely to lie above the Häring & Rix (2004) relationship found for bulge dominated systems (see discussion in Section 4.2.4).

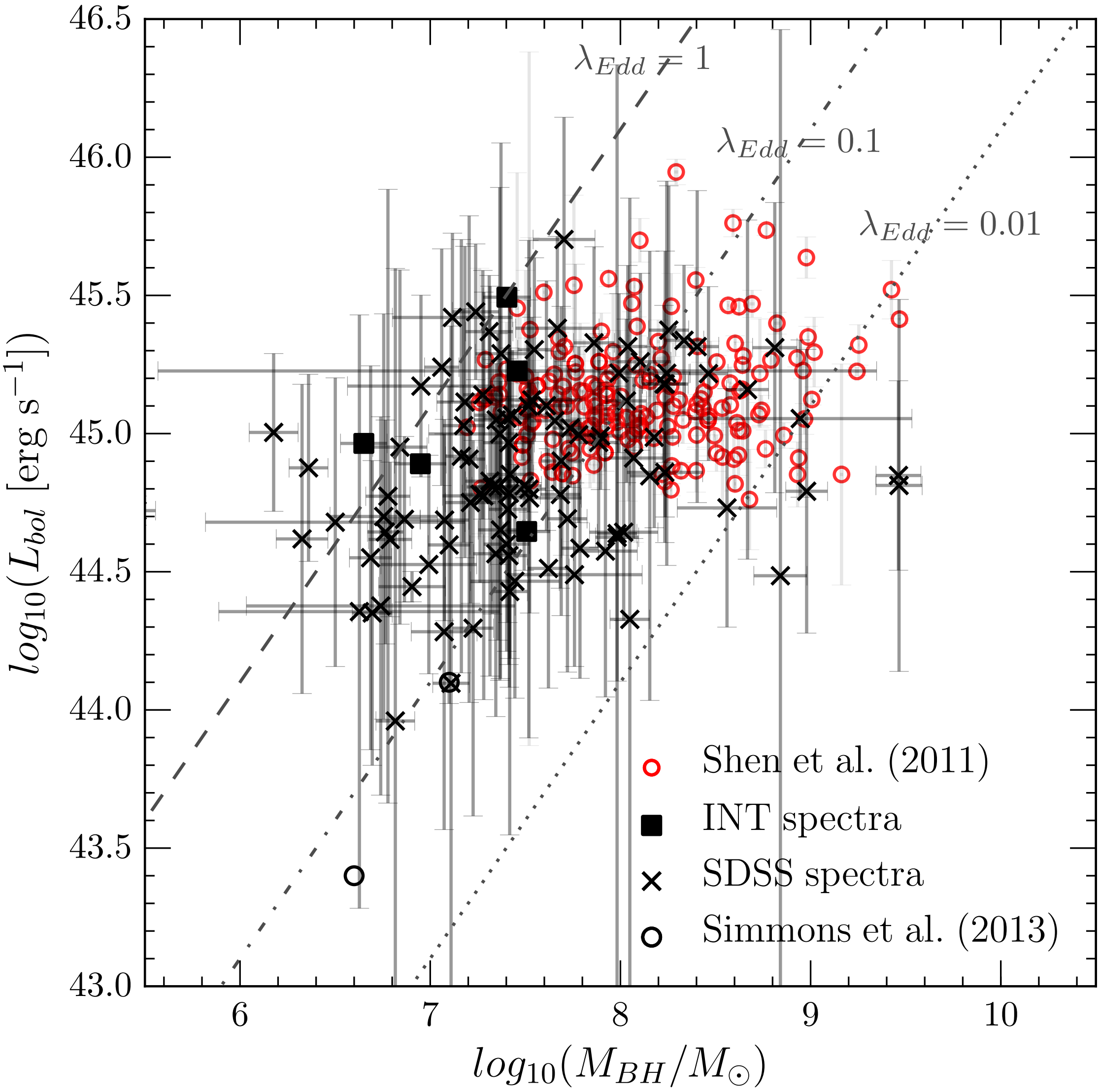

Figure 4.20: Black hole mass against bolometric luminosity for the 101 galaxies, including those observed by SDSS (crosses) and with the IDS on INT (squares). We also show detections from Simmons et al. (2013) (open circles) and those from the redshift matched sample of Shen et al. (2011). For reference we show lines of example Eddington ratios of $\Lambda_{Edd} = 1$ (dashed), $\Lambda_{Edd} = 0.1$ (dot-dashed) and $\Lambda_{Edd} = 0.01$ (dotted).

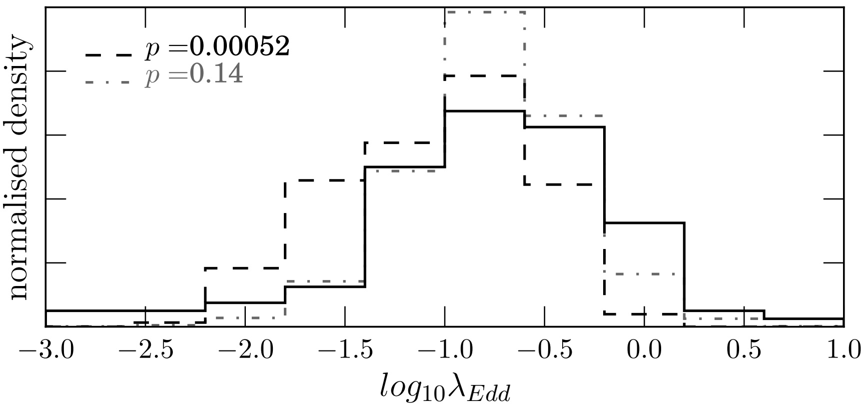

Figure 4.21: Normalised distributions of logarithmic Eddington ratio for the sample of 101 disc dominated galaxies (solid line), compared with that for the redshift matched sample from Shen et al. (2011; dashed line) and the entire sample (dot-dashed line) We also provide the p-values of a 2 sample KS test between the disc dominated sample and each of the quasar samples. We reject the null hypothesis that the two samples are drawn from the same population for the redshift matched quasar sample but accept the null hypothesis for the entire quasar sample of Shen et al. (2011).

combined spiral vote fraction (Galaxy Zoo 1 did not ask whether a galaxy was a disc, therefore we can approximate the combined spiral vote fraction as a disc vote fraction) of $p_{CS} < 0.5$ and mean value of $\langle p_{CS} \rangle = 0.17$. The QSOCONTROL sample is therefore mainly comprised of bulge dominated galaxies unlike the DISCDOM sample. Slightly higher accretion rates are therefore occurring in the AGN of the galaxies in the DISCDOM sample than in a bulge dominated QSOCONTROL sample.

The colour magnitude diagram for the DISCDOM sample is also shown in Figure 4.22 in comparison to the SDSS sample and green valley definition from Baldry et al. (2004). The unobscured AGN host galaxies of the DISCDOM sample are found across the entirety of this parameter space, however those with higher black hole mass accretion rates are found preferentially in the green valley and at brighter r-band magnitudes.

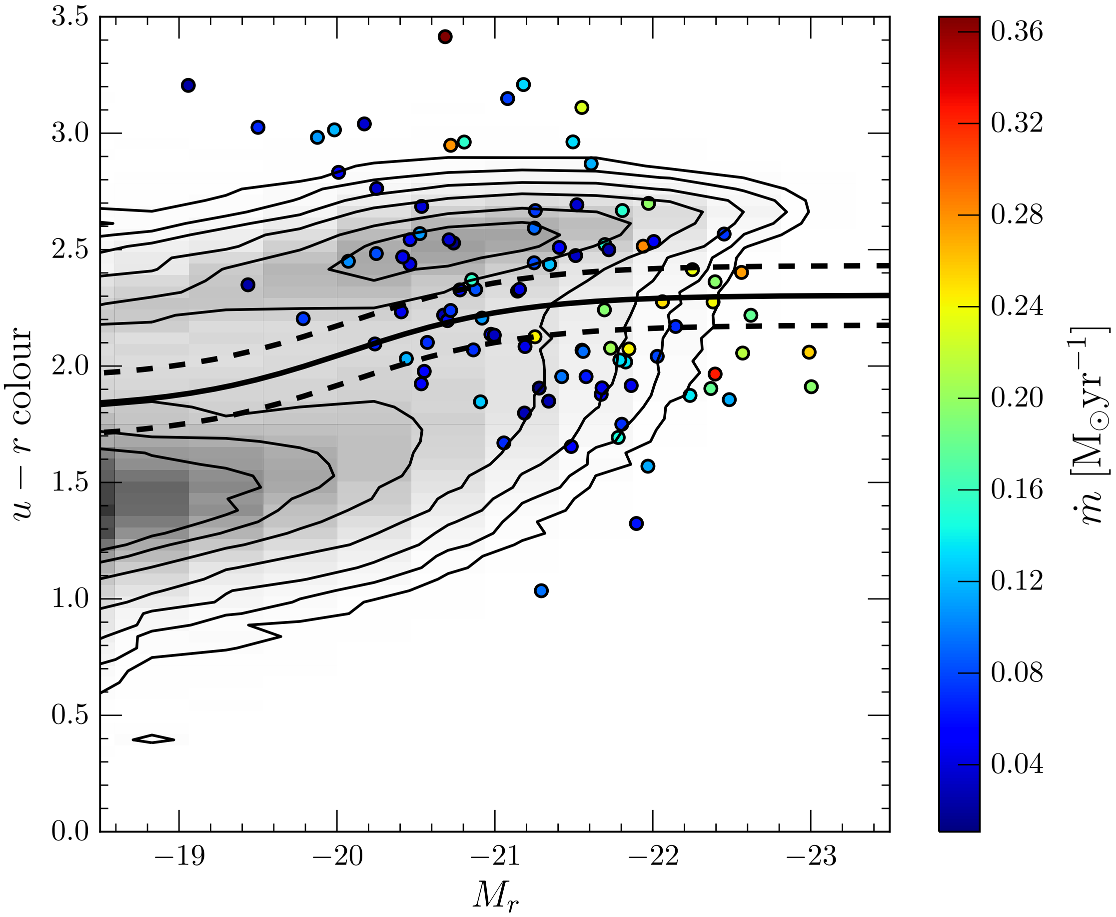

Figure 4.22: Optical colour-magnitude diagram showing the positions of the DISCDOM sample (circles) in comparison to the SDSS DR7 sample from Baldry et al. (2004). The galaxies of the DISCDOM sample are coloured by their black hole mass accretion rate, $\dot{m}$ (see Equation 4.13). The definition between the blue cloud and red sequence from Baldry et al. (2004) is shown by the solid line (as defined in Equation 3.1) with $\pm$ 1σ shown by the dashed lines. The DISCDOM sample are found across the colour magnitude diagram, however those with higher mass accretion rates are found preferentially in the green valley and at brighter r-band magnitudes.

4.2.4 Discussion

The relatively large number of purely disc galaxies of the DISCDOM sample hosting growing SMBHs provides a very powerful probe of the simultaneous evolution of galaxies and their black holes driven without typical bulge-forming mechanisms. Despite the rarity of the morphology of these DISCDOM galaxies, they are found in common areas of black-hole-galaxy scaling relations, as seen in Figures 4.18, 4.19 & 4.20, frequented by typical AGN host galaxies of all morphologies (they also lie in the common regions of the local $M_{BH} - \lambda_{Edd}$ plane shown in Figure 1 of the review paper of Alexander & Hickox 2012). Significant black hole growth has occurred up to masses of $M_{BH} \sim 10^8 - 10^9$ $M_\odot$ in the DISCDOM sample whilst the disc dominated nature of the galaxy has been preserved. Simulations have repeatedly shown that mergers with mass ratios larger than 1:10 (i.e. mergers where the mass of the satellite is greater than 10% of the main galaxy's mass) will form a classical bulge (Walker et al., 1996; Hopkins et al., 2012; Tonini et al., 2016); so how is this substantial mass growth possible in the absence of such a major merger dominated (and minor merger limited) formation history?

Using Equation 4.13, the black hole mass accretion rates are estimated to lie in the range $0.01 \leq \dot{m} \leq 0.37$ $M_\odot$ yr^{-1}. Simulations by Crockett et al. (2011), and more recently by Di Teodoro & Fraternali (2014), show that such accretion rates are completely achievable by cold accretion of minor satellites with mass ratios less than 1:10 (i.e. the mass of the satellite galaxy is less than 10% of the main galaxy mass). However, there is also evidence that such accretion rates may also be possible via merger free, secular processes alone. One such secular process, is bar driven gas inflow into the central regions of galaxies. Simulations of barred galaxies have repeatedly shown that gas inflow rates due to a morphological bar range from $\sim 0.1-$few $M_\odot$ yr^{-1} (Sakamoto, 1996; Maciejewski et al., 2002; Regan & Teuben, 2004; Lin et al., 2013) and may increase to up to ~ 7 $M_\odot$ yr^{-1} (Friedli & Benz, 1993) with increasing bar length, bar strength and axis ratio.

These simulations however, struggle to show that the gas funnelled to the central regions of the galaxy is actually accreted into the central few parsecs, and instead often accumulates in a nuclear ring wherein it causes a starburst (Regan & Teuben, 2004). Similarly, no observational correlation has yet been found between the presence of a bar and and that of an AGN either locally (Ho et al., 1997; Malkan et al., 1998; Erwin & Sparke, 2002; Lee et al., 2012; Cisternas et al., 2013) or out to $z \sim 1$ (Cheung et al., 2015). I estimate a bar fraction, f_{bar} in the DISCDOM sample (which is by no means complete), by visual inspection of the SDSS ugriz images (see Figure 4.10), of $f_{\mathrm{bar}} \sim 0.42$; a lower limit due to the edge on nature of some of the galaxies in the DISCDOM sample. In agreement with the studies above, this is no higher than the local bar fraction observed in the general local galaxy population (Masters et al., 2011).

Using these derived black hole mass accretion rates, the time required to grow the black holes in the DISCDOM sample from a seed mass of 10^2 M$_{\odot}$ can also be derived. This calculation assumes that the black holes have grown at the currently observed bolometric luminosity, since the mass at which that luminosity was the Eddington luminosity and prior to this underwent Eddington limited growth. This means that the accretion rates calculated, $\dot{m}$, will be the maximum rates at which the black holes have grown over their lifetimes. This is a conservative assumption but gives an estimate of the total time these black holes would need to spend in actively growing phase if the calculated rates are typical of black holes residing in disc dominated host galaxies. The mean (median) time taken for the black holes of the DISCDOM sample to grow from a seed black hole mass is ~ 1.68 Gyr (~ 0.37 Gyr). These times are considerably less than a Hubble time, with the SMBHs in the DISCDOM sample needing to spend only $\sim 10\%$ of their lifetimes in a growing phase to give the black hole masses currently measured. This is in agreement with the fraction of time predicted by simulations and observed by others (Kauffmann et al., 2003b; Hao et al., 2005; Hopkins et al., 2006b; Fiore et al., 2012; Simmons et al., 2013).

A time of ~ 38 Gyr was calculated for two of the most massive black holes in the DISCDOM sample, which have very low current Eddington ratios (see Figure 4.20). Since this time frame is well beyond the current estimates for the age of the Universe (~ 13.8 Gyr; Planck Collaboration, 2016), this value is clearly an overestimate of the time taken to grow these two black holes. Since AGN are believed to go through a duty cycle of varying accretion rates throughout their lifetimes (Martini & Weinberg, 2001; Yu & Tremaine, 2002; Schawinski et al., 2015), then we can assume that these two black holes were accreting at a higher rate at some point in their history. If these two black holes are assumed to have grown within the median (mean) time derived for the rest of the DISCDOM sample, then the past accretion rate will have been on the order of, $\dot{m} \sim 7.95$ (1.73) M$_{\odot}$ yr^{-1}. As discussed earlier, similar gas inflow rates caused by the presence of a bar have been seen in simulations (Friedli & Benz, 1993); suggesting once again that despite having large masses, these black holes could in theory be grown by secular processes. Unfortunately, the two host galaxies are at too high a redshift to allow the detection of a morphological bar in the SDSS ugriz image.

The black hole mass accretion rates are also shown in Figure 4.22, wherein the locations of the DISCDOM sample on the optical colour magnitude diagram are shaded by $\dot{m}$. Those galaxies hosting black holes with higher mass accretion rates are found preferentially in the green valley and at brighter r-band magnitudes. This once again supports the arguments of Section 4.1 that feedback from these AGN could cause galaxies to quench, and therefore transition through the green valley, due to a sustained period of high mass accretion.

Figures 4.20 & 4.21 show how the Eddington ratios of the DISCDOM sample are higher than those in the bulge dominated QSOCONTROL sample (which has mean combined spiral vote fraction from GZ1 of $\langle p_{CS} \rangle = 0.17$), so that the null hypothesis that the two Eddington ratio distributions are drawn from the same parent sample can be rejected. However, the same null hypothesis cannot be rejected for the full non-redshift matched AGN sample of Shen et al. (2011) which spans a redshift range of $0.06 < z < 5.46$. The Eddington ratios of the DISCDOM sample are therefore higher than bulge dominated systems in the same redshift range, and instead are consistent with black hole accretion rates occuring at earlier cosmic times. So, despite having merger free evolutionary histories, black hole growth in the DISCDOM galaxies is occurring at a higher rate than in typical local AGN host galaxies.

The black hole masses of the disc dominated host galaxies in the DISCDOM sample are not expected to correlate in the same way to their stellar masses as those in bulge dominated galaxies, if different dynamical histories lead to different mechanisms for black hole growth. However, Figure 4.18 shows how the black hole and total stellar masses of the DISCDOM sample occupy the same region of parameter space as the bulge dominated elliptical galaxies used to derive the Häring & Rix (2004) relationship. Similarly Figure 4.19 shows how the black hole masses of the DISCDOM sample (which contain either no bulge, or a possible small pseudo bulge) lie well above the Häring & Rix (2004) relationship, particularly when the upper limits on DISCDOM bulge masses are taken into account. In other words, given what we know about black hole growth mechanisms, the black holes in these disc dominated systems are $\sim 1-2$ dex more massive than they should be, given the mass (or lack thereof) of their bulge component.

This is in agreement with the results of Simmons et al. (2013) who found a similar excess in the black hole masses of $\sim$ 1.5 dex and $\sim$ 2 dex for the two measured black hole masses in their sample of 13 pure disc galaxies. Both this result and the results shown in Figures 4.18 & 4.19 at first seem to be in contradiction with previous works which find that galaxies with pseudo-bulges have lower black hole masses than predicted by typical scaling relations (see work by Greene et al., 2008; Hu, 2009; Jiang et al., 2011a; Mathur et al., 2012; Ho & Kim, 2014). However, all these studies are biased by their sample selection methods, first selecting based on black hole mass to produce a sample of low mass black holes ($M_{BH} < 10^6$ M$_\odot$) within which they hoped to find bulgeless or pseudo-bulge morphologies. Now, with the larger DISCDOM sample shown in Figure 4.19, we can see that the fitted relationship between their black hole masses and bulge mass upper limits (solid black line), intersects with the relationship derived for the bulge dominated Häring & Rix (2004) sample at $M_{BH} \sim 10^{6.4}$ M$_\odot$. At this point, the relationship predicts that for disc dominated galaxies the black hole masses will indeed be less than those predicted for bulge dominated systems, as concluded by the studies referenced above.

Splitting the AGN host population by morphology in this way however, leads to biased conclusions. As discussed in Chapter 3, the strength of the POPSTARPY method lies partly due to the fact that no thresholds are applied to the GZ morphological vote fractions, allowing the dominance of intermediate quenching rates across the colour magnitude diagram to be revealed (see Section 3.2). Similarly, if one does not "*discriminate*" against morphology in the black hole mass-bulge mass plane and fit a linear regression model to galaxies in both the DISCDOM (with proper consideration of upper limits) and Häring & Rix (2004) samples, the result is consistent with a vertical line in the bulge-black hole mass plane. This suggests that there is perhaps no intrinsic correlation between black hole mass and stellar bulge mass across the full morphological spectrum of galaxies.

This argument is supported by the agreement in Figure 4.18 between the relationships derived in the total stellar mass-black hole mass plane for the DISCDOM and bulge dominated Häring & Rix (2004) samples. This agreement arises despite the two extremes in galaxy formation histories. This indicates that the mechanisms driving the dynamical and morphological structure of the galaxy may not be fundamental to the growth of the black hole. The black hole-galaxy relations observed across the M_{BH}-σ, M_{BH}-$M_{\rm bulge}$ and M_{BH}-M_* planes, although demonstrating a correlation, have never implied a *causation*. All of these parameters however, share mutual correlations to the overall gravitational potential of the dark matter halo of the galaxy (Booth & Schaye, 2010; Volonteri et al., 2011), suggesting the true cause of the black-hole galaxy scaling relations is an outcome of hierarchical galaxy evolution (Jahnke & Macciò, 2011), regardless of the merger history of the galaxy.

4.3 Conclusions

In Section 4.1 I used morphological classifications from the Galaxy Zoo 2 project to determine the morphology-dependent SFHs of a population of $1,244$ Type 2 Seyfert AGN host galaxies, in comparison to an inactive galaxy population, via a Bayesian analysis of an exponentially declining SFH model. Using POPSTARPY I determined the population densities for the time and exponential rate that quenching occurs and find clear differences in the distributions, between INACTIVE and AGN-HOST galaxy populations and for host galaxies with AGN of different Eddington ratios. The main findings were:

(i) Quenching at early times is observed within the INACTIVE population (see right panels of Figure 4.7), where the population density is roughly constant until recent times where the distribution drops off at earlier times with increasing mass. This is evidence of downsizing within the INACTIVE galaxy population, which is also seen in the AGN-HOST smooth weighted population. This implies that AGN feedback is not responsible for the cessation of star formation within a proportion of these galaxies, as this quenching has occurred prior to the triggering of the current AGN.

(ii) Slow, early quenching is also observed in the disc weighted AGN-HOST population (dashed lines bottom left panels of Figures 4.7 & 4.8) and so this SFH challenges the typical merger driven co-evolution of luminous black holes and their host galaxies.

(iii) Rapid quenching, possibly caused by the AGN itself through negative feedback, is the most dominant history within the low mass (left top panel Figure 4.8) and high Eddington ratio (bottom left panel of Figure 4.6) AGN-HOST population.

This quenching history is particularly apparent for the smooth-weighted AGN-HOST population, supporting the hypothesis that a merger, having caused a morphological transformation to a smooth galaxy, can also trigger an AGN, causing feedback and cessation of star formation on rapid timescales (initially proposed in Chapter 3). Further work is required to determine if the AGN is indeed the cause of the quenching seen.

(iv) The prevalence of star forming AGN host galaxies, combined with the dominance of rapid, recent quenching seen across the AGN-HOST population allows us to consider that either: (i) the AGN are the cause of the rapid quenching observed but only in gas-poor host galaxies where they can have a large impact, (ii) the AGN are a consequence of another quenching mechanism but can also be triggered by other means which do not cause quenching, or (iii) the SFR of a galaxy can recover post-quench and return to the star forming sequence after a few Gyr.

In Section **??** I studied how black holes can grow in galaxies with merger free evolutionary histories, by investigating where AGN in disc dominated galaxies lie on typical black-hole galaxy scaling relations. Despite the fact that these disc dominated galaxies have different dynamical histories to bulge-dominated and elliptical shaped systems, they are found to lie in the same regions of parameter space are $\sim 1-2$ dex more massive than they should be, given the mass (or lack thereof) of their bulge component. The main findings were:

(i) Significant black hole growth has occurred up to masses of $M_{BH} \sim 10^8 - 10^9$ M$_{\odot}$ in the DISCDOM sample whilst the disc dominated nature of the galaxy has been preserved.

(ii) Eddington ratios of the DISCDOM sample are higher than those in the bulge dominated QSOCONTROL sample; despite having merger free evolutionary histories, black hole growth in the DISCDOM galaxies is occurring at a higher rate than in typical local AGN host galaxies.

(iii) Those galaxies hosting black holes with higher mass accretion rates are found preferentially in the green valley and at brighter r-band magnitudes. This once again supports the arguments of Section 4.1 that feedback from these AGN could cause galaxies to quench, and therefore transition through the green valley, due to a sustained period of high mass accretion.

(iv) Figures 4.18 & 4.19 show how the galaxies of the DISCDOM sample occupy the same region of the M_*-M_{BH} and M_{bulge}-M_{BH} parameter spaces, respectively, as the bulge dominated Häring & Rix (2004) sample. Given what we know about black hole growth mechanisms, the black holes in these disc dominated systems are $\sim 1-2$ dex more massive than they should be, given the mass (or lack thereof) of their bulge component. This suggests that there is perhaps no intrinsic correlation between black hole mass and galaxy bulge mass across the full morphological spectrum of galaxies and that the true cause of the black-hole galaxy scaling relations may be due to mutual correlations to the overall gravitational potential of the dark matter halo of the galaxy.

It is therefore clear that AGN can have a large impact on the evolution of their host galaxies, including causing quenching directly through AGN feedback across the entire population; which I have demonstrated here for the first time.

Chapter 5

The influence of galaxy environment

So far, I have considered galaxy mergers & interactions, morphology and AGN as causes of quenching across the galaxy population. While it is abundantly clear that these processes can strongly affect the SFHs of galaxies, the density of a galaxy's environment is also thought to be a driver of galaxy evolution.

The galaxy environment as a cause of quenching was proposed due to the correlation of environmental density with morphology (Dressler, 1980; Smail et al., 1997; Poggianti et al., 1999; Postman et al., 2005; Bamford et al., 2009), colour (Butcher & Oemler, 1978; Pimbblet et al., 2002) and the quenched galaxy fraction (Kauffmann et al., 2003b; Baldry et al., 2006; Peng et al., 2012; Darvish et al., 2016). Star forming disc galaxies tend to be located in low-density environments with quiescent elliptical galaxies in more dense environments. Although these correlations were originally interpreted as causation, recent evidence from simulations suggests that quenching mechanisms driven by the environment may not be dominant in the galaxy lifecycle (Kimm et al., 2009, 2011; Hirschmann et al., 2014; Wang et al., 2014; Phillips et al., 2015). Perhaps instead, the correlation of increased galaxy quenched fractions with environment is due to a superposition of the effects of mergers, interactions and both mass and morphology quenching.

In order to isolate the cause of the density-morphology and density-SFR correlations, I need to observe how morphology and galaxy quenching timescales change in dense environments with different properties in comparison to the field. Here, I consider the group environment, as this is a more typical environment for a galaxy than the relatively rare rich cluster environment (Carlberg, 2004). I construct a sample of both group and field galaxies and once again use STARPY to determine the quenching time and rate to describe a simple SFH for a galaxy given its photometry. However, dense environments are messy with many possible mechanisms at work, whose effects are difficult to disentangle.

I aim to determine the following: (i) How does the environment influence the detailed morphological structures of a galaxy? (ii) Is quenching which is directly caused by the environment occurring in galaxy groups?

5.1 Data and Methods

5.1.1 Group Identification

The construction of a robust cluster or group catalogue is a thesis in itself, with many studies attempting this across the SDSS (Merchán & Zandivarez, 2005; Miller et al., 2005; Berlind et al., 2006; Yang et al., 2007; Tago et al., 2008, 2010; Tinker et al., 2011; Muñoz-Cuartas & Müller, 2012; Tempel et al., 2014) and other large surveys (Tucker et al., 2000; Merchán & Zandivarez, 2002; Eke et al., 2004; Cucciati et al., 2010; Robotham et al., 2011; Knobel et al., 2012). The difficulties arise in removing projection effects, understanding the selection function used, covering large ranges in mass and redshift, and dealing with spectral fibre collisions (see the comprehensive review by Postman, 2002, for an in depth discussion). Various different methods have been employed to achieve robust cluster/group identification including clustering algorithms (e.g. Miller et al., 2005), galaxy colour modelling (Koester et al., 2007), adaptive filter halo modelling (Yang et al., 2005, 2007) and friends-of-friends algorithms (Goto, 2005b; Merchán & Zandivarez, 2005; Berlind et al., 2006).

Each group finding algorithm has to be tested for purity (how contaminated the groups are by non-members) and completeness (how often are true members excluded from a group). Campbell et al. (2015) compared the purity and completeness of two of the most frequently used group catalogues of Berlind et al. (2006, a friends-of-friends algorithm) and Yang et al. (2007, a halo modelling algorithm) and concluded that no sample could achieve perfect purity or completeness. Despite the different algorithms employed to identify group galaxies, Campbell et al. found that the two catalogues are remarkably similar. The Yang et al. catalogue has however, higher purity of satellites at lower halo masses (i.e. the low halo mass groups are less contaminated by non-members). For this reason the Yang et al. catalogue is the most commonly used in environment studies using data from the SDSS (including Hoyle et al., 2011; Pasquali et al., 2012; Wetzel et al., 2014; Shankar et al., 2014; Lacerna et al., 2014; Knobel et al., 2015; Fitzpatrick & Graves, 2015; Lan et al., 2016; Woo et al., 2016; Bluck et al., 2016; Weigel et al., 2016), but I find that when cross matched with the GZ2-GALEX sample (with a $3''$ search radius) only 38 galaxies (of $176,604$ possible galaxies) which belong to a group with 2 or more members are identified. This is most likely due to the necessity for GALEX NUV photometry in this study. The majority of NUV emission comes from massive, short lived stars and so in the cluster environment which is dominated by typical 'red and dead' quiescent galaxies, detecting NUV emission is less likely.

Instead I use the Berlind et al. (2006) catalogue, which when cross matched with the GZ2-GALEX sample and limited to $z < 0.1$[1], gives $14,199$ group galaxies with the number of group members, $N_{\text{group}} \geq 2$. Centrals were selected as the most massive galaxy in a group (as in Yang et al., 2007, 2009; Pasquali et al., 2010) with all other galaxies in a group designated as satellites.

The projected group-centric radius, R, of all satellite galaxies was calculated from the projected separations of the co-ordinates of a satellite from its central; this was then converted to kpc by using the observed spectroscopic redshift of the central galaxy. In order to compare groups of different sizes, the virial radius is used as a normalisation factor to this projected group-centric radius. Here I use a proxy to the virial radius, R_{200}(see Navarro et al., 1995), the radius within which the group mass overdensity is 200 times the critical density, $\rho_{\text{crit}}(z)$, as defined by Finn et al. 2005:

$$200\rho_{\text{crit}}(z) = \frac{M_{cl}}{\frac{4}{3}\pi R_{200}^3}, \tag{5.1}$$

where M_{cl} is the mass of the group. Finn et al. then use the redshift dependance of the critical density and the virial mass to relate the line-of-sight velocity dispersion,

[1]To ensure GALEX completeness of the red sequence, unlike in Chapter 3; see Wyder et al. 2007; Yesuf et al. 2014

σ_x, to the group mass so that R_{200} becomes:

$$R_{200} = 1.73 \left(\frac{\sigma_x}{1000 \mathrm{km\ s}^{-1}} \right) \cdot \frac{1}{\sqrt{\Omega_\Lambda + \Omega_o(1+z)^3}} \, h_{100}^{-1} \ \mathrm{Mpc}, \tag{5.2}$$

σ_x is calculated for a group as the standard deviation of the velocity dispersions $\sqrt{(v_i - \langle v_i \rangle)^2}$. Here v_i are the proper velocities of each galaxy, i as defined in Danese et al. (1980):

$$v_i = c \cdot \frac{z_i - z_{group}}{1 + z_{group}}, \tag{5.3}$$

where z_{group} is the mean redshift of all the group members. Since most groups in the sample have low N_{group}, using the mean redshift for z_{group}, rather than the central galaxy redshift is most appropriate in this case. These calculations resulted in a sample of $3,468$ centrals and $10,731$ satellites within a projected group-centric radius range of $0.02 < R/R_{200} < 24.9$ and $z < 0.084$ which shall be referred to as the GZ2-BERLIND sample. Note that for a galaxy (central or satellite) to be included in the GZ2-BERLIND sample, the rest of its group does not. However the properties of that group are still retained by the included galaxy.

Unlike in previous Chapters, here I will specifically focus on galaxies that are below the star forming sequence (SFS) in order to simplify the analysis (see Section 5.2.3). I therefore select a subsample of the GZ2-BERLIND galaxies that are 1σ below the SFS, giving $4,629$ satellite and $2,314$ central galaxies which will collectively be referred to as the GZ2-GROUP sample. These galaxies are shown in the panels of Figure 5.1 and can be seen to lie below the SFS.

I also compare the GZ2-BERLIND and GZ2-GROUP samples with a measurement of the projected neighbour density from Baldry et al. (2006), $\Sigma_N = N/4\pi d_N^2$, where d_N is the distance to the N^{th} nearest neighbour. Σ is a more direct probe of the local density of a galaxy's environment, and although it does not allow for the identification of groups and their properties, it is still a useful probe of the local density inside a group (see Muldrew et al., 2012, for a comparison of various environment parameterisations).

In this work I use the estimates of Bamford et al. (2009) who calcualted the local galaxy density, Σ, determined by averaging $\log \Sigma_N$ for $N = 4$ and $N = 5$ by the method outlined in Baldry et al. (2006), for the entirety of the GZ1 sample. 90% of the GZ2-BERLIND sample have $\log \Sigma > -0.8$ (the threshold quoted by Baldry et al. 2006 above which non-field galaxies tend to be found), suggesting a purity of

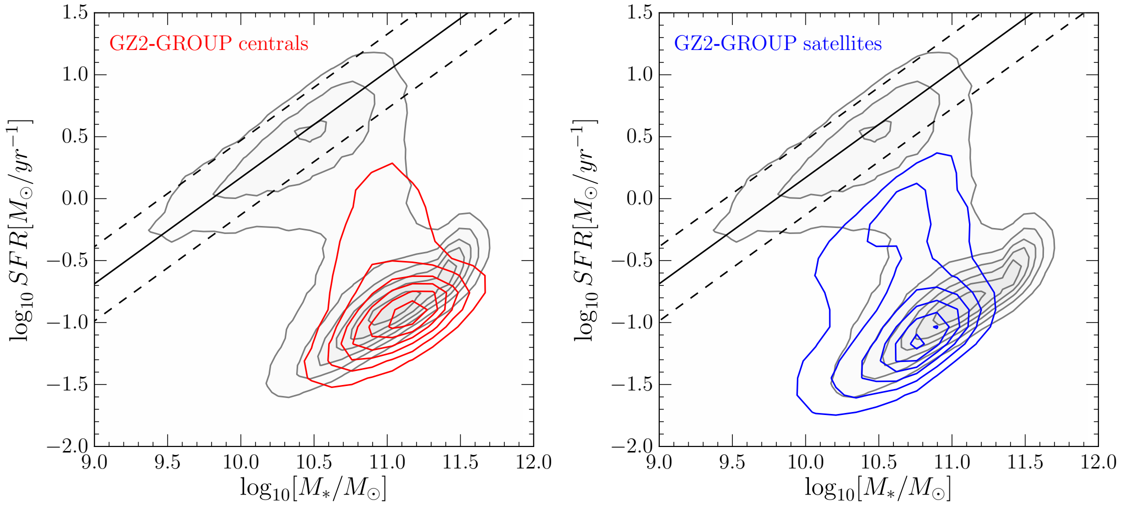

Figure 5.1: The stellar mass-SFR plane showing central (left; red contours) and satellite (right; blue contours) in the GZ2-GROUP sample. In both panels the entire SDSS sample from the MPA-JHU catalogue is shown by the grey contours. The definition of the SFMS from Peng et al. (2010) at $\bar{z} = 0.053$ (solid line, the mean redshift of the GZ2-GROUP sample) with $\pm 1\sigma$ (dashed lines) is shown.

$\sim 90\%$ for the GZ2-BERLIND sample. The distributions of $\log \Sigma$ for star forming and quenching/quenched centrals and satellites in the GZ2-BERLIND sample are shown in Figure 5.2. Star forming galaxies tend to reside in less dense local environments than their quenching/quenched counterparts. The satellite galaxies as a whole also seem to occupy denser local environments than centrals, however on investigation this seems to arise because the satellites in the GZ2-BERLIND sample reside in groups with larger N_{group} than the centrals. This is to be expected given the definition of a satellite galaxy.

5.1.2 Field sample

I constructed a sample of field galaxies for use as a control sample to the GZ2-GROUP sample. For all galaxies in the GZ2-GALEX sample, I calculated the smallest projected group-centric radii, R/R_{200}, from each of the central galaxies in the Berlind et al. (2006) catalogue (regardless of whether the central was included in the GZ2-BERLIND sample) and selected candidate field galaxies as those with (i) $R/R_{200} > 25$ and (ii) $\log \Sigma < -0.8$ (the threshold on the local environment density which selects field

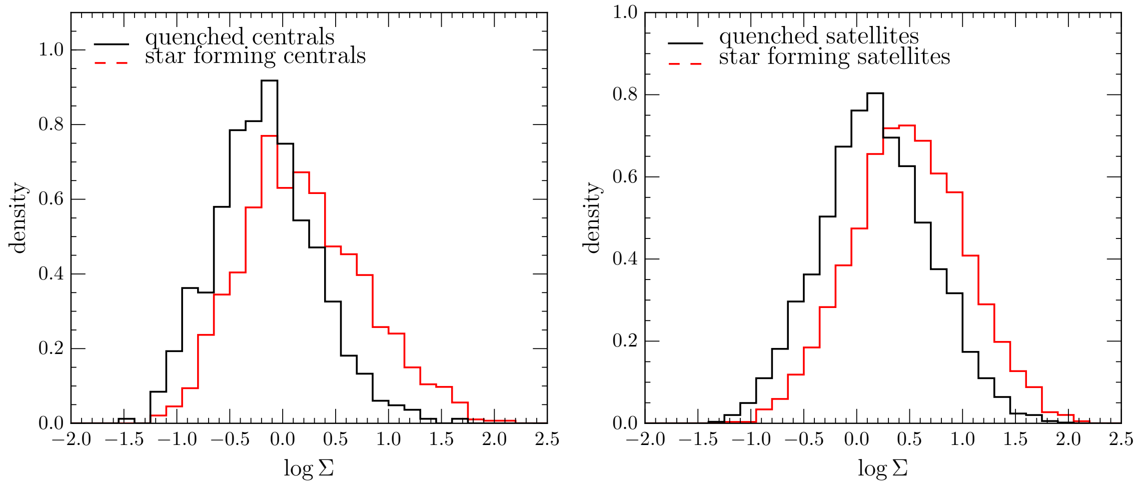

Figure 5.2: Local environment density, $\log \Sigma$, distributions of star forming (black) and quenching/quenched (red) central (left) and satellite (right) galaxies in the GZ2-GROUP sample.

galaxies as defined by Baldry et al., 2006). I chose to use both of these environmental density measures to ensure a pure sample of candidate field galaxies.

This sample of field galaxy candidates was then matched in redshift and stellar mass firstly to the central galaxies of the GZ2-GROUP sample to give $2,309$ field galaxies with $z < 0.084$. In this work I shall focus on galaxies which are either quenching or quenched and are more than 1σ below the SFS and so the same constraints must be placed on this field control sample. This encompasses $1,596$ field galaxies with $z < 0.084$ which will be referred to as the GZ2-CENT-FIELD-Q sample. It will be used as a control sample when investigating the trends with central galaxy properties of the inferred quenching parameters. The redshift distribution of the GZ2-CENT-FIELD-Q sample is shown in comparison to the distribution of central galaxies in the GZ2-GROUP sample in the left panel of Figure 5.3.

Secondly, the field galaxy candidates were then matched in redshift and stellar mass to the satellite galaxies of the GZ2-GROUP sample to give $5,004$ field galaxies with $z < 0.084$ which will be referred to as the GZ2-SAT-FIELD sample. These galaxies in the GZ2-SAT-FIELD sample will be used as a control when investigating the morphological trends of satellite galaxies with environment. Note that the sample is not restricted to being 1σ below the SFS in this case. 237 galaxies are found in both the GZ2-CENT-FIELD-Q and GZ2-SAT-FIELD samples. The redshift distribution

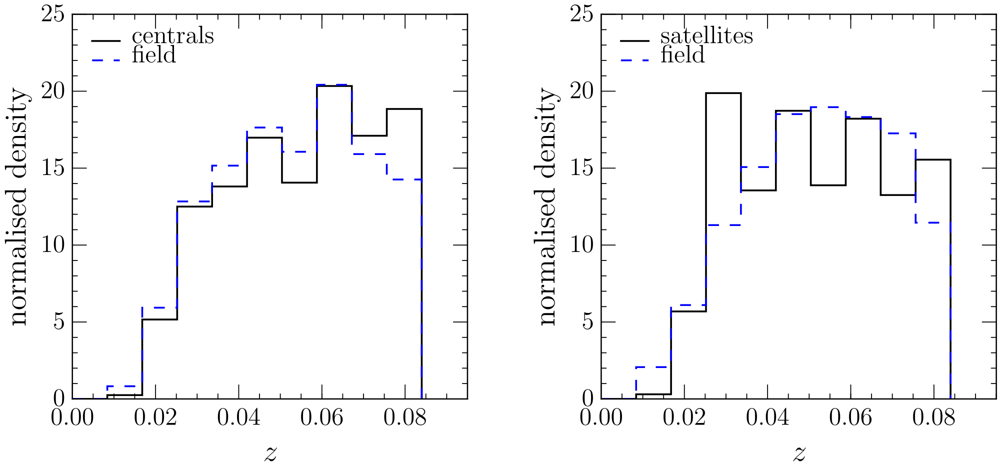

Figure 5.3: Redshift distributions of central (left) and satellite galaxies (right) in the GZ2-GROUP sample (black solid line) in comparison the redshift matched GZ2-CENT-FIELD-Q (left; blue dashed line) and GZ2-SAT-FIELD samples (right; blue dashed line).

of the GZ2-SAT-FIELD sample is shown in comparison to the distribution of satellite galaxies in the GZ-GROUP sample in the right panel of Figure 5.3

We obtain SFRs and stellar velocity dispersions of galaxies for all of the field samples described above from the MPA-JHU catalogue (Kauffmann et al., 2003b; Brinchmann et al., 2004). Stellar masses were already calculated for the entire GZ2-GALEX sample using the optical photometry and the method outlined in Baldry et al. (2006, see Section 1.3.4).

5.1.3 Morphological fractions

I once again utilise the GZ2 vote fraction to quantity the morphology of galaxies in the GZ2-GROUP sample, in order to investigate the morphological trends with group radius. As in previous Chapters, I shall utilise $p_{\rm disc}$ and $p_{\rm smooth}$ but will also use $p_{\rm bar}$, $p_{\rm bulge}$ and $p_{\rm merger}$ to calculate the bar, bulge and merger fractions in the GZ2-GROUP sample respectively.

Fractions are calculated considering the number of barred (with $p_{\rm bar} > 0.5$; see Masters et al. 2011; Cheung et al. 2013) and bulged (with $p_{\rm obvious\ or\ dominant} > 0.5$ and $p_{\rm none\ or\ noticeable} > 0.5$ from Task 4 in the GZ2 decision tree shown in Figure 1.5) galaxies over the number of disc galaxies ($p_{\mathrm{disc}} > 0.43$, $p_{\mathrm{edge\_on,no}} > 0.715$, $N_{\mathrm{edge\_on,no}} > 20$; see Table 1.1 in Chapter 1) in the GZ2-GROUP satellite sample. The merger fraction considers the number of merging galaxies (with $p_{\mathrm{merger}} > 0.4$; see Darg et al. 2010) over the number of galaxies in the GZ2-GROUP satellite sample.

5.2 Results

5.2.1 Mass dependance with radius

Since morphological features have been shown to be dependent on the stellar mass of a galaxy (e.g. the increase in the bar fraction with stellar mass; see Nair & Abraham, 2010b; Skibba et al., 2012), before investigating trends in the morphology with group radius in the GZ2-GROUP sample, the mass dependence on the group radius must be considered. This is shown in Figure 5.4. The mean stellar mass is roughly flat and consistent with the median field value with increasing group radius, until the most central group radius bin at $R \sim 0.01\ R_{200}$. This trend is present for both morphologies, with early-type galaxies showing a larger increase in the average stellar mass. I note that if this inner bin at $0.1R/R_{200}$ is ignored in the results that follow, my conclusions still hold.

5.2.2 Dependence of detailed morphological structure with environment

I perform an initial sanity check on the GZ2-GROUP sample by recreating the morphology-density relation of Dressler (1980, see Figure 1.3) in Figure 5.5, which shows the mean disc and smooth vote fractions as a function of group radius. The mean disc vote fraction decreases from the mean field value (blue line) within 1 virial radius, as the mean smooth vote fraction increases, in agreement with previous studies on the morphology-density relation (Dressler, 1980; Smail et al., 1997; Poggianti et al., 1999; Postman et al., 2005; Bamford et al., 2009). The extensive morphological classifications provided by GZ2 also allow for the investigation of how more detailed morphological structure is affected by the group environment.

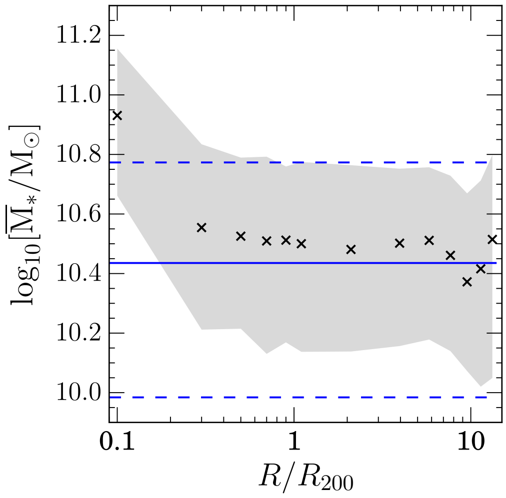

Figure 5.4: The average stellar mass as a function of radius from the group centre. The shaded regions show the $\pm 1\sigma$ in each bin of R/R_{200}. The average stellar mass of the GZ2-SAT-FIELD sample is also shown (blue solid line) with $\pm 1\sigma$ (blue dashed line).

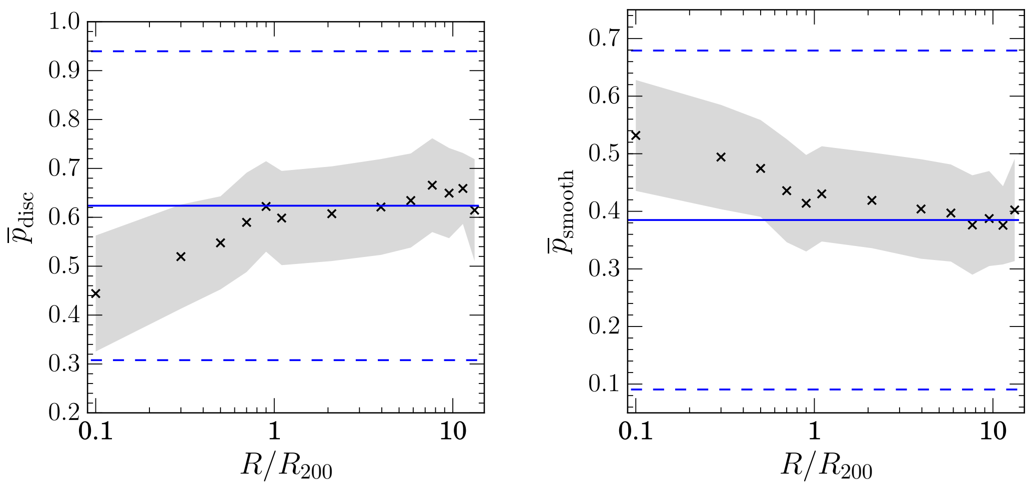

Figure 5.5: Mean GZ vote fraction for disc (top) and smooth (bottom) galaxies in the GZ2-GROUP sample binned in projected group-centric radius, normalised by R_{200}, a proxy for the virial radius of a group. The shaded region shows $\pm 1\sigma$ on the mean vote fraction. The mean vote fraction of the GZ2-SAT-FIELD sample are also shown (blue solid lines) with $\pm 1\sigma$ (blue dashed lines).

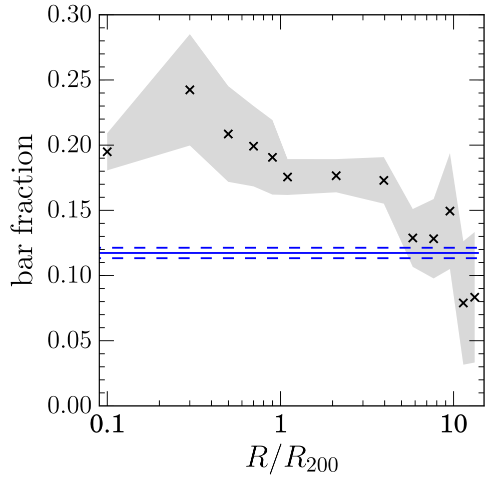

Figure 5.6: Bar fraction (number of barred disc galaxies over number of disc galaxies) in the GZ2-GROUP sample binned in projected group-centric radius, normalised by R_{200}, a proxy for the virial radius of a group. The shaded region shows $\pm 1\sigma$ on the bar fraction. The bar fraction of the GZ2-SAT-FIELD sample is also shown (blue solid line) with $\pm 1\sigma$ (blue dashed line).

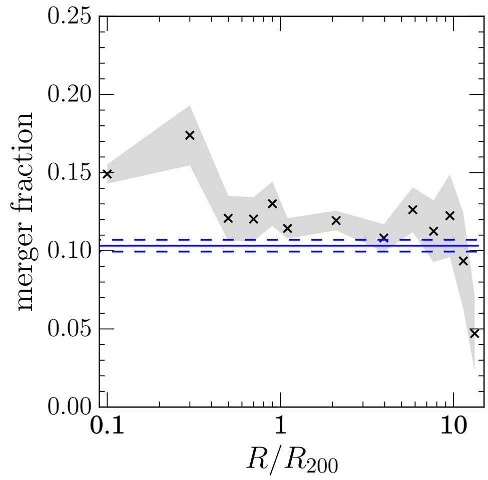

Figure 5.7: Merger fraction in the GZ2-GROUP sample binned in projected group-centric radius, normalised by R_{200}, a proxy for the virial radius of a group. The shaded region shows $\pm 1\sigma$ on the merger fraction. The merger fraction of the GZ2-SAT-FIELD sample is also shown (blue solid line) with $\pm 1\sigma$ (blue dashed line).

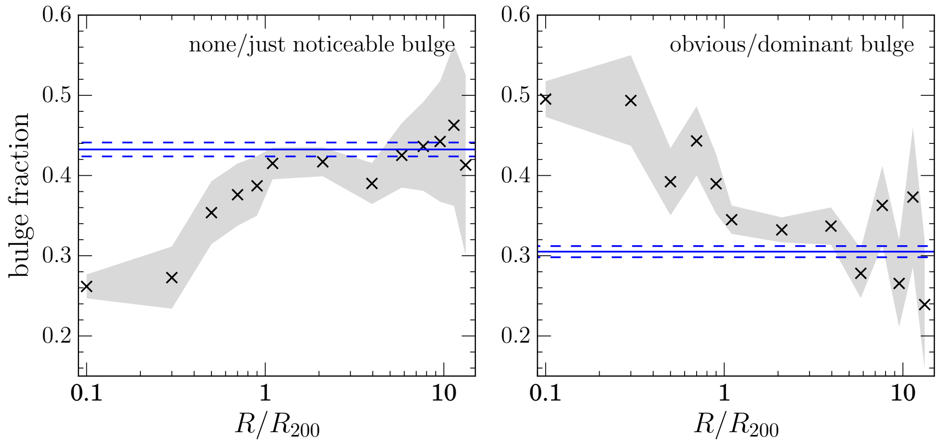

Figure 5.8: Fraction of galaxies with none/just noticeable bulge classifications (left) and with obvious/dominant bulge classifications (right) in the GZ2-GROUP sample binned in projected group-centric radius, normalised by R_{200}, a proxy for the virial radius of a group. The shaded regions shows $\pm 1\sigma$ on the bulge fractions. The bulge fractions of the GZ2-SAT-FIELD sample are also shown (blue solid lines) with $\pm 1\sigma$ (blue dashed lines).

Figure 5.6 shows how the bar fraction (number of barred disc galaxies over the number of disc galaxies; see Section 5.1.3) with decreasing group-centric radius increases significantly over the field fraction (blue solid line). Figure 5.7 shows how the merger fraction does not significantly deviate from the field fraction (blue solid line) except for galaxies found within a virial radius. As discussed in Chapter 4, mergers are thought to grow bulges and so similarly, Figure 5.8 shows how the fraction of galaxies with obvious/dominant bulges increases over the field value in the inner regions of the group and the fraction of those with none/just noticeable bulges decreases below the field value within 1 virial radius.

5.2.3 Quenching histories in the group environment

The SFHs of all galaxies in both the GZ2-GROUP and GZ2-CENT-FIELD-Q samples were analysed using STARPY, providing the posterior probability distribution across the two-parameter space for an individual galaxy. Whereas in Chapters 3 & 4 the POPSTARPY method was then used to combine and weight the individual distributions to give an overall distribution representing the population of galaxies, due to the

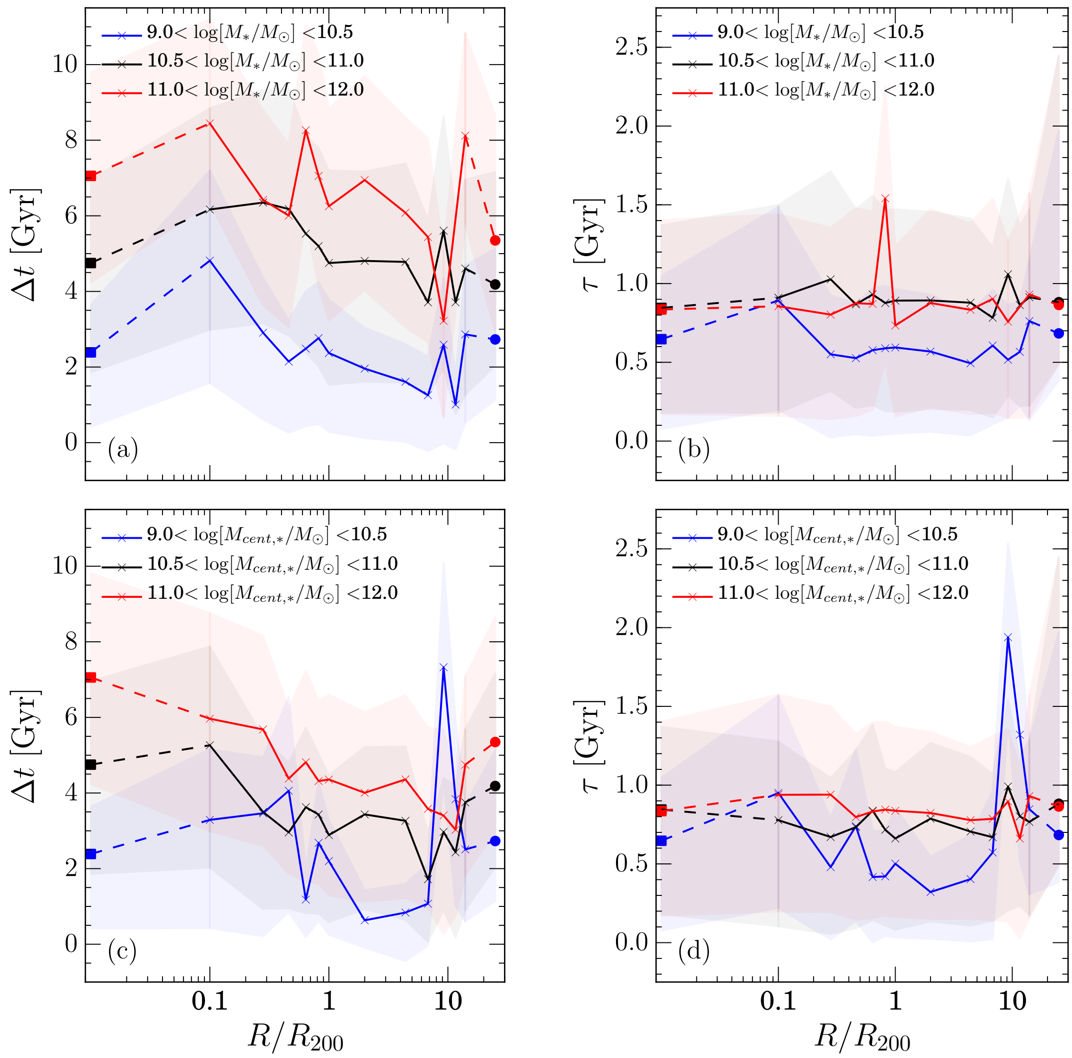

Figure 5.9: The time since quenching onset ($\Delta t = t_{obs} - t_q$; left) and rate of quenching (τ; right) binned in group radius, R/R_{200}, for satellite galaxies (crosses) split into bins of stellar mass (top) and stellar mass of the corresponding central galaxy (bottom; a proxy for halo mass of a group). The corresponding values for central galaxies (squares, plotted at $0.01R/R_{200}$) and galaxies in the GZ2-CENT-FIELD-Q sample (circles, plotted at $25R/R_{200}$) are shown and connected by the dashed lines to help guide the eye. The shaded regions show the $\pm1\sigma$ on Δt and τ in each bin of R/R_{200}.

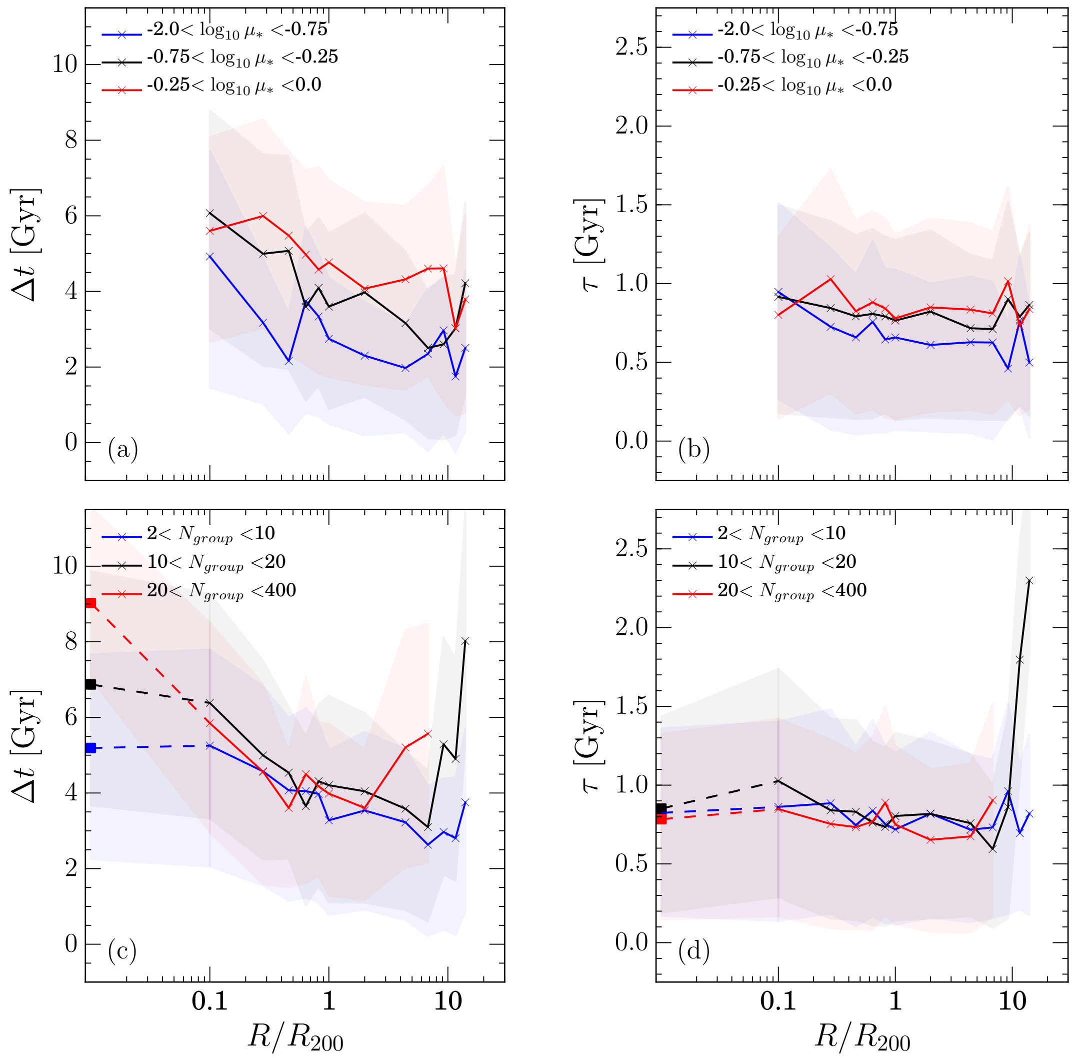

Figure 5.10: The time since quenching onset ($\Delta t = t_{obs} - t_q$) and rate of quenching (τ; right) binned in group radius, R/R_{200}, for satellite galaxies (crosses) split into bins of number of group members (N_{group}, top) and stellar mass ratio ($\mu_* = M_*/M_{cent,*}$, bottom). The corresponding values for central galaxies (squares, plotted at $0.01R/R_{200}$) and galaxies in the GZ2-CENT-FIELD-Q sample (circles, plotted at $25R/R_{200}$) are shown, where possible, and connected by the dashed lines to help guide the eye. The shaded regions show the $\pm1\sigma$ on Δt and τ in each bin of R/R_{200}.

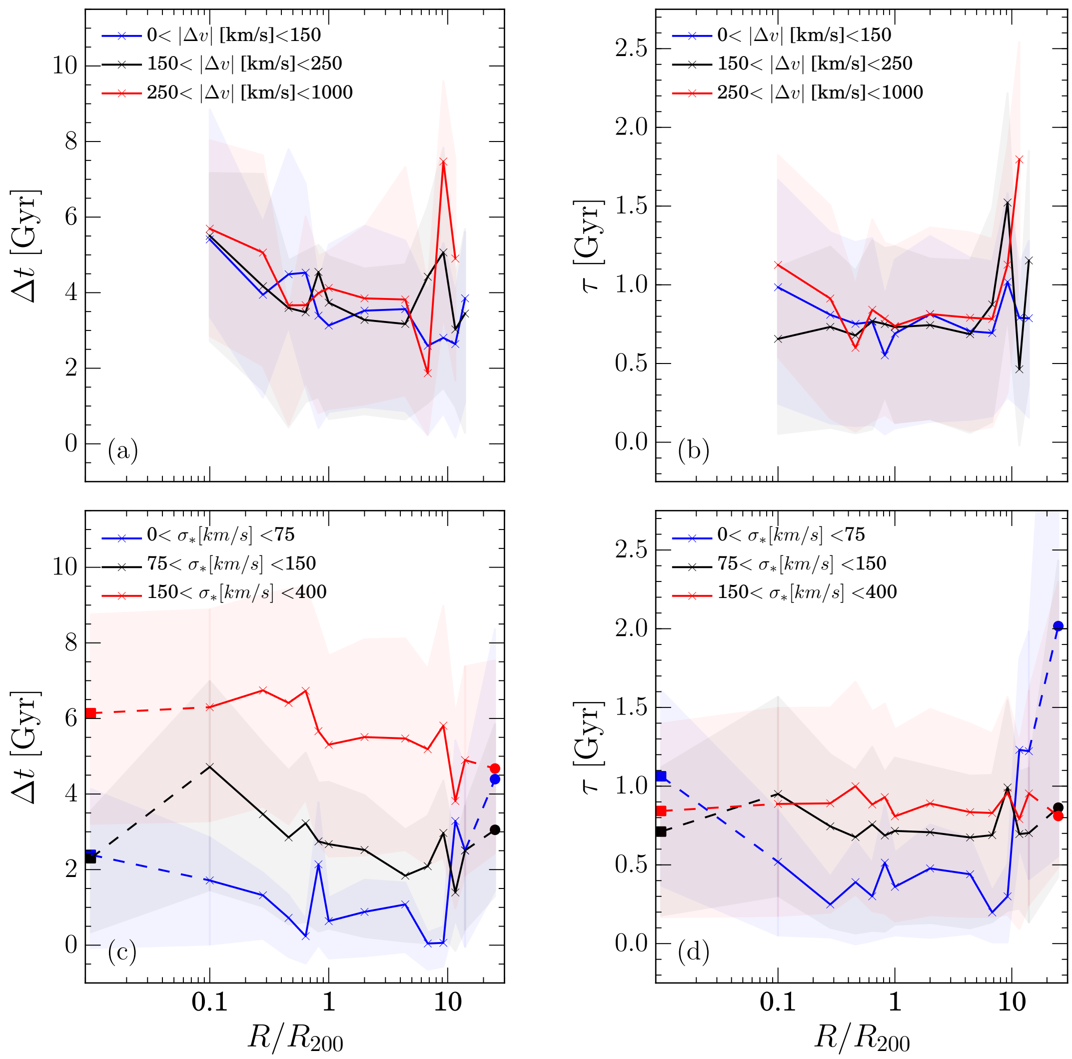

Figure 5.11: The time since quenching onset ($\Delta t = t_{obs} - t_q$; left) and rate of quenching (τ; right) binned in group radius, R/R_{200}, for satellite galaxies (crosses) split by the absolute relative velocity of the satellite to its central galaxy ($|\Delta v|$, top) and stellar velocity dispersion (σ_*, bottom). The corresponding values for central galaxies (squares, plotted at $0.01R/R_{200}$) and galaxies in the GZ2-CENT-FIELD-Q sample (circles, plotted at $25R/R_{200}$) are shown, where possible, and connected to the satellite values by the dashed lines to help guide the eye. The shaded regions show the $\pm1\sigma$ on Δt and τ in each bin of R/R_{200}.

complex nature of the group environment, the environmental effects will be washed out using this method. In this Chapter, I instead take the 50th percentile walker position of an individual posterior probability distribution to give the most likely quenching time, t_q and quenching rate, τ, for each galaxy (shown by the solid blue lines in Figure 2.4).

This simplifies the output from STARPY for each galaxy from a probability distribution to just two values, with $\pm 1\sigma$ uncertainties (shown by the dashed blue lines in Figure 2.4) which encompass the spread of the individual galaxy's SFH posterior probability distribution. In this Chapter I will calculate the time since quenching onset, Δt, for a given galaxy by calculating $\Delta t = t^{\mathrm{obs}} - t_q$ (where t^{obs} is the age of the Universe at a galaxy's observed redshift; see Section 2.1).

With the output from STARPY I can observe the trends in the time since quenching onset, Δt, and quenching rate, τ, with group radius, R/R_{200}, for satellite galaxies and central galaxies in the GZ2-GROUP sample, compared with galaxies in the GZ2-CENT-FIELD-Q sample. This is shown in Figures 5.9 - 5.11 wherein the GZ2-GROUP galaxies are binned by stellar mass (Figures 5.9a-b), halo mass (Figures 5.9c-d), mass ratio (Figures 5.10a-b), number of group galaxies (Figures 5.10c-d), relative velocity (Figures 5.11a-b) and stellar velocity dispersion (Figures 5.11c-d). All bin thresholds were chosen to give approximately the same number of galaxies in each bin.

Across all the left panels in Figures 5.9 - 5.11 a general trend for increasing time since quenching onset with group radius can be seen. As in Figures 5.5−5.8 significant differences from the mean field values arise at radii less than a virial radius. However, no trend with group radius is seen for the rate at which quenching occurs for satellites in the GZ2-GROUP sample (right panels Figures 5.9 - 5.11). This suggests that whatever mechanisms causes quenching in a group will do so at the same rate in both the dense inner and sparse outer regions.

In Figure 5.9a the GZ2-GROUP sample is split by stellar mass, M_*, and a clear trend for increasing Δt with increasing stellar mass for satellite, central and field galaxies can be seen. However, this trend is less apparent for the rate of quenching seen in Figure 5.9b. The central galaxies (shown by the square points at $\sim 0.01R/R_{200}$) appear to have quenched more recently than the inner satellites (at $\sim 0.1R/R_{200}$) of the same mass but have done so at the same quenching rate.

In the bottom panels of Figure 5.9 I split the GZ2-GROUP sample by halo mass by using the stellar mass of the corresponding central galaxy of a group, $M_{c,*}$ as a proxy. I find a clear trend for increasing time since quenching onset with increasing halo mass for satellite, central and field galaxies (Figure 5.9c) but once again this trend is less apparent for the rate of quenching (Figure 5.9d) suggesting the halo mass does not affect which quenching mechanism acts upon either central or satellite galaxies.

To account for the effects of conformity, whereby satellites of higher mass tend to be found in higher mass halos (Weinmann et al., 2006; Kauffmann et al., 2013; Hearin et al., 2015; Hatfield & Jarvis, 2016), I also split the satellites of the GZ2-GROUP sample by the stellar mass ratio of the satellite to its central galaxy, $\mu_* = M_*/M_{cent,*}$, in the top panels of Figure 5.10. Δt increases more steeply with group radius (particularly within $\sim$ a virial radius; Figure 5.10a) for satellite galaxies with much smaller masses than their group central ($-2.0 < \log_{10} \mu_* < -0.75$, shown by the blue curve). Once again this is not the case for the rate that quenching occurs, as shown in Figure 5.10b.

Another property of the group which is expected to affect the satellite quenching histories is the number of group members, N_{group}, which should be roughly correlated with a satellite's local density in a group. The bottom panels of Figure 5.10 show that there is no trend with time since quenching onset or rate of quenching with increasing N_{group} for satellite galaxies. The central galaxies (shown by the square points at $\sim 0.01R/R_{200}$) however, do show a trend for increasing time since quenching as the number of group galaxies increases (Figure 5.10c), but the rate at which they quench is the same (Figure 5.10d) suggesting the mechanism by which this occurs is the same for all centrals regardless of halo mass.

In the top panels of Figure 5.11 the GZ2-GROUP satellite galaxies are split into bins of their relative velocity to their central galaxies, i.e. the velocity at which they move through the dense group environment. There is no trend with either time since onset of quenching (Figure 5.11a) or rate of quenching (Figure 5.11b) with increasing relative velocity for galaxies in the GZ2-GROUP sample. This suggests that whatever quenching mechanism is occurring in groups, it is not correlated with the velocity at which satellites move through the dense environment.

The bottom panels of Figure 5.11 show the trend with group radius for the GZ2-GROUP satellites when split into bins of galaxy stellar velocity dispersion σ_* (note

Table 5.1: Summary of results shown in Figures 5.9-5.11 denoting whether there is, ✓, or isn't, ×, a trend with Δt when the GZ2-GROUP satellite galaxies are split by the stated property.

	M_*	$M_{\mathrm{cent},*}$	μ_*	N_{group}	$\lvert\Delta v\rvert$	σ_*
Shown in Figure	5.9a	5.9c	5.10a	5.10c	5.11a	5.11c
Trend with Δt when split by ...?	✓	✓	✓	×	×	✓

that this is not the velocity dispersion of the group) which is often used as a proxy for the galaxy potential. The stellar velocity dispersion show the largest trend in Δt (Figure 5.11c) for satellite galaxies of all of the group or satellite galaxy properties studied, with galaxies with the smallest stellar velocity dispersions having quenched more recently. Although this trend is less apparent in Figure 5.11d for the rate that quenching occurs with σ_*, it is the largest trend see across the right panels of Figures 5.9-5.11. Also, field galaxies (shown by the circles at $\sim 25R/R_{200}$) with low velocity dispersions are seen to quench at much slower rates than their satellite counterparts. This suggests that the rapid quenching observed for the low stellar velocity dispersion satellites is directly caused by the environment.

The results shown in Figures 5.9-5.11 are summarised in Table 5.1.

5.3 Discussion

I shall now consider the results presented in Section 5.2 in the context of possible quenching mechanisms which could be responsible.

5.3.1 The role of mergers as quenching mechanisms in the group environment

The merger classification in GZ2 has been shown to preferentially identify major mergers (Darg et al., 2010); while bulge formation in disc galaxies is often associated with evolutionary histories driven by minor mergers (Croton et al., 2006; Tonini et al., 2016). Although we see evidence for an enhanced merger fraction in the inner regions of the group environment in Figure 5.7, the bulge fractions in Figure 5.8 vary much more significantly from the field value than the merger fraction. This suggests that minor mergers may be more dominant than major mergers for satellites in the group environment, particularly at $R/R_{200} > 0.5$.

If mergers are a dominant evolutionary mechanism for satellite galaxies, as the morphological evidence in Figures 5.7 & 5.8 suggests, we would expect to see a difference in the quenching histories of satellites residing in groups with a larger number of members. However, the bottom panels of Figure 5.10 show there is no trend with time since quenching onset or rate of quenching with increasing N_{group} for the satellite galaxies. This suggests that mergers are not the dominant quenching mechanism for satellite galaxies, but that whatever mechanism is the cause of the quenching occurs at the same rate irrespective of group size.

Central galaxies however, do show a trend for increasing time since quenching with increasing N_{group} (square points at $0.01R/R_{200}$ in Figure 5.10c) occurring at a rate of $\tau \sim 1$Gyr (which as discussed in Chapter 3, was attributed to mergers and galaxy interactions which could transform a galaxy's morphology). Therefore, the larger the number of group members, the more likely a central galaxy has a history dominated by mergers. This is in agreement with the findings of Lin et al. (2010), Ellison et al. (2010), Lidman et al. (2013) and McIntosh et al. (2008). The latter found in a sample of local groups and clusters that half of the mergers they identified involved the central galaxy. Liu et al. (2009) also found that the fraction of merging centrals increases with the richness of a cluster (a measure of the number of galaxies within $1\mathrm{h}^{-1}$Mpc of the central galaxy).

This idea is supported by the result in Figure 5.9a showing that centrals of a given mass have quenched more recently than the inner satellites (at $\sim 0.1R/R_{200}$) of a given mass. This suggests that an episode of more recent star formation, such as a starburst, may have occurred in the central galaxies but not in the inner satellites. Mergers are thought to cause an energetic burst of star formation which can in turn quench the remnant galaxy (Hopkins et al., 2005; Treister et al., 2012; Pontzen et al., 2016, as discussed in Section 3.3.1). This result is also suggestive of a merger dominated history for central galaxies but not for satellite galaxies.

5.3.2 The role of mass quenching in the group environment

A trend is seen for increasing time since quenching with increasing stellar mass and velocity dispersion (a proxy or galaxy potential) for centrals, satellites and field galaxies in Figure 5.9a and Figure 5.11c respectively. This is suggestive of mass quenching occurring across the entire galaxy population irrespective of environmental density, supporting the work of Peng et al. (2010, 2012); Gabor et al. (2010) and Darvish et al. (2016).

5.3.3 The role of morphological quenching in the group environment

The increasing bar fraction toward the central group regions shown in Figure 5.6 (in agreement with Skibba et al., 2012), suggests that bars may be partly responsible for the relation between quenched fraction and environmental density. This is consistent with findings that show that bars themselves may be the cause of morphological quenching through the funnelling of gas toward the central regions of galaxies (Athanassoula, 1992b; Sheth et al., 2005) which is then used in star formation, exhausting the available gas[2].

We must therefore consider whether the environment itself may play a role in triggering the disk instabilities which can produce a bar. Indeed harassment and tidal interactions, believed to be common in the group environment, have been shown to both promote and inhibit bar formation dependent on the stellar mass (Noguchi, 1988; Moore et al., 1996; Skibba et al., 2012). If the environment was indeed triggering a bar, then morphological quenching would be occurring in the group environment but indirectly due to environmental quenching. This suggests that the polarity between internal secular processes ('nature') and external environmental processes ('nurture') may not be as extreme as first thought, in agreement with Skibba et al. (2012).

[2]The gas which is funnelled to the centre by the bar may also be used to fuel an AGN. The AGN-environment connection has been extensively studied with conflicting results; (Miller et al., 2003; Pimbblet et al., 2013; Ehlert et al., 2014; de Souza et al., 2016, e.g. see). I attempted to study this in this investigation. However, only 204 satellites and 128 centrals of the GZ2-GROUP sample were identified as obscured Type 2 AGN using a BPT diagram. These low numbers of AGN mean that when split into bins of group radius we are well and truly dancing precariously on the low number statistics volcano and so no robust conclusions can be drawn.

5.3.4 The role of the environment in quenching

Across all panels of Figures 5.9-5.11 a trend for increasing time since quenching onset with decreasing group radius is present. I interpret this as environmentally driven mechanisms causing quenching at the same rate throughout the infall time of a galaxy in a group. Those galaxies closer in, fell into the group earlier and as they did so they started to quench, giving rise to a larger inferred Δt.

More massive halos are seen to have a greater impact on the star formation histories of their satellites than less massive halos in Figure 5.9c. The halo mass is correlated with both (i) the gravitational potential of the group and (ii) the temperature of the IGM, suggesting that an environmental quenching mechanism which is correlated with one or both of these properties is responsible for this result.

Higher mass halos have hotter intra group medium (IGM) temperatures (Shimizu et al., 2003; Del Popolo et al., 2005) which can have a greater impact on a galaxy through ram pressure stripping (RPS) of cold gas. Gunn & Gott (1972) define the ram pressure as:

$$\rho_{\mathrm{IGM}} \cdot v^2 = 2\pi G \cdot \sigma_*(R) \cdot \sigma_g(R), \tag{5.4}$$

where ρ_{ICM} is the density of the IGM, $\sigma_*(R)$ the star surface density, $\sigma_g(R)$ the gas surface density of the galaxy disc and v the velocity of the galaxy through the IGM. Therefore if RPS is indeed a dominant environmental quenching mechanism we should see a trend in Δt with the velocity of a satellite relative to its central galaxy. However in Figure 5.11a we see that this is not the case. This therefore rules out RPS as the dominant environmental quenching mechanism, in support of the simulations of Emerick et al. (2016); Fillingham et al. (2016) which showed that RPS could only remove $40-60\%$ of a satellite's gas. and observations by McGee et al. (2014). However, this conclusion may be due to the stellar mass range spanned by the GZ2-GROUP satellite galaxies which all have $M_* \geq 10^9\mathrm{M}_\odot$, as simulations by Fillingham et al. (2016) suggest that RPS only becomes effective in lower mass satellites with $M_* \leq 10^{8-9}\mathrm{M}_\odot$, in agreement with Hester (2006).

Above this mass threshold in the simulations of Fillingham et al. (2016), a 'starvation' (or strangulation) mode (Larson et al., 1980; Balogh et al., 2000) dominantes, where a galaxy's extended gaseous halo is removed causing a quench, as cold gas for use in star formation is no longer be fed from the extended halo. This idea is supported by observations by Peng et al. (2010) which show that strangulation is a dominant mechanism for galaxies with $M_* < 10^{11}\ M_\odot$ with a quenching timescale of 4 Gyr. Such a mechanism will be correlated with the galaxy potential, as galaxies with a lower potential will be most easily stripped of their halos. This is apparent in Figure 5.11d where satellites with lower velocity dispersion (a proxy for the galaxy potential) are more rapidly quenched than their higher velocity dispersion counterparts and those in the field. Such a starvation mechanism is also correlated with halo mass, for which similar trends in Δt are see in Figure 5.9c. The dominant environmental quenching mechanism occurring in the group environment must therefore be correlated with the group potential. This suggests that satellite galaxies may be most affected by gravitationally driven environmental effects, such as starvation, thermal evaporation of the galaxy halo and galaxy harassment.

We can calculate an infall timescale for the satellite galaxies in the GZ2-GROUP sample. We can assume that galaxies begin their infall into a group at a radius of $\sim 10\mathrm{R}_{200}$ and stop infalling at $\sim 0.1\mathrm{R}_{200}$[3]. The difference in the time since quenching onset, Δt, between these two locations in a group will provide an estimate for how long it takes a satellite to infall. This assumes (i) that the galaxy starts to quenching immediately when it enters the group and (ii) that the same environmentally driven quenching process is the only quenching mechanism affecting the satellites throughout their infall. I will define this property as $\delta\Delta t = \Delta t_{0.1R_{200}} - \Delta t_{10R_{200}}$. In Figure 5.10c the trend seen in Δt with group radius is the same regardless of the number of galaxies in the group, so this gives us an estimate for the average Δt in each group-centric radius bin across the satellite population. We can therefore estimate an average infall time of $\delta\Delta t \sim 3$ Gyr for the GZ2-GROUP satellites. The rate of quenching occurring across the group radius in Figure 5.10d is $\tau \sim 1$ Gyr (this is within the range of quenching rates theorised to cause a morphological change in Section 3.2.2) and so we can also estimate the average quenching timescale (i.e. the time taken to fully quench from the SFS to 5σ below the SFS, as in Chapters 3 & 4) to be ~ 4 Gyr for the GZ2-GROUP satellites.

This infall time and quenching timescale are in agreement with the estimates of Wetzel et al. (2013) who used a high resolution cosmological N-body simulation to track satellite galaxy orbits in SDSS groups and clusters and found quenching timescales of $2-6$ Gyr. Using a similar method, Oman & Hudson (2016) derive an infall time of ~ 4 Gyr and quenching timescales between $4-6$ Gyr for galaxies in

[3]This assumes that galaxies will then merge with their central galaxy, however it is more likely that the satellite has a close pass with the central before it 'backsplashes' into the group.

the mass range of the GZ2-GROUP sample. Similarly, Hahn et al. (2016) derive a total quenching timescale of ~ 4 Gyr for satellite galaxies on infall into the group environment. However, the simulations by Fillingham et al. (2016) and Emerick et al. (2016) have shown that RPS cannot remove enough gas mass to completely quench a galaxy within ~ 2 Gyr but can assist in reducing the starvation timescale so that galaxies can be quenched within the ~ 4 Gyr quenching timescale calculated in this study. This suggests that although the effects of mechanisms correlating with the group potential are detectable in the quenching parameters of the GZ2-GROUP sample, this is only made possible by the constantly present, but less dominant effects of ram pressure stripping.

This conclusion, along with the discussion in Section 5.3.3 which concluded that morphological quenching may only be present in the group environment due to the influence of the environment itself, suggests that all mechanisms discussed here will affect a galaxy which is infalling through the group environment at some point in its lifetime,. A single mechanism may be more dominant in the evolution of an individual galaxy but to achieve the correlations between morphology, colour and quenched galaxy fraction with density observed across the entire population all mechanisms need to act in concert.

5.4 Conclusions

Using the Berlind et al. (2006) group catalog, I have constructed a sample of group galaxies in the SDSS which were cross matched with Galaxy Zoo 2 and GALEX in order to determine their most likely SFHs using STARPY. I have shown that although mass quenching, morphological quenching and mergers are all important mechanisms at work in quenching the galaxies in the group environment, the environment does play a role in quenching galaxies as they infall into the group. I have discussed the possibility that not one mechanism will dominate across the group population, with all mechanisms acting collaboratively. My findings are summarised as follows:

(i) The bar, obvious bulge and merger fractions are all seen to increase above the field value in the inner regions of the groups of the GZ2-GROUP sample in Figures 5.6, 5.8 & 5.7 respectively.

(ii) Mergers are the dominant quenching mechanism for central galaxies but not for satellite galaxies. Satellites may undergo a minor merger in the group environment but there effects are only discernible by their indirect effect on the bulge fraction (see Figure 5.8).

(iii) Mass quenching is occurring across the entire GZ2-GROUP sample for centrals and satellites irrespective of the environmental density (see Figure 5.9a).

(iv) Morphological quenching is occurring for GZ2-GROUP satellite galaxies as evidenced by the heightened bar fraction in the inner group regions (see Figure 5.6). However, this may be indirectly due to environmental quenching since galaxy interactions and harassment are believed to be able to trigger bars. This suggests the polarity between 'nature' vs. 'nurture' may not be as extreme as previously thought.

(v) The environment does cause quenching across the GZ2-GROUP sample, as evidenced by the increase in the time since quenching with decreasing group radius seen across all left panels of Figures 5.9-5.11. The results in Figures 5.9a & 5.11c suggest that this is caused by a quenching mechanism correlated with the group potential, such as harassment, interactions and starvation, rather than the velocity of a satellite through the group, such as ram pressure stripping. This quenching occurs within an average quenching timescale of ~ 4 Gyr from star forming to complete quiescence, after an average infall time of ~ 3 Gyr.

It is apparent from the results presented in this Chapter that many quenching mechanisms are all occurring simultaneously in the group environment; therefore a superposition of all of the effects of these mechanisms is seen in the quenching histories of the GZ2-GROUP sample, which in turn gives rise to the morphology-density relation observed.

Chapter 6

Discussion

In this Chapter I will discuss how my results fit into the 'big picture' of galaxy evolution and discuss their broader implications (Section 6.1). I will then discuss future work with STARPY (Section 6.2) and how I intend to adapt it so that it can be applied to IFU spectral data (Section 6.3). I will then end with a reflection on the power of Hubble Space Telescope imaging in comparison to SDSS imaging.

6.1 The Big Picture

In this thesis I have investigated quenching as a function of colour, morphology, the presence of an AGN and environment across a large galaxy population. I have found that green valley galaxies are tracing the evolution of red sequence galaxies and that though there is a morphological dependance on the rate that quenching will occur, galaxies of any morphology can quench at any rate (Chapter 3). I have found that lower mass galaxies hosting an AGN have quenched both rapidly and recently, suggesting that the AGN may be the direct cause of this quenching through feedback (Chapter 4.1). However, I have also shown that quenching in AGN host galaxies does not always proceed rapidly, suggesting a slower co-evolution of galaxies with their black holes. I investigated this slower evolutionary history with a sample of bulgeless AGN host galaxies, which are assumed to be merger free, and showed that their black holes were much more massive than predicted by typical black hole scaling relations (Chapter 4.2). I have also found evidence for environmentally driven quenching mechanisms, mass quenching and morphology quenching within the group

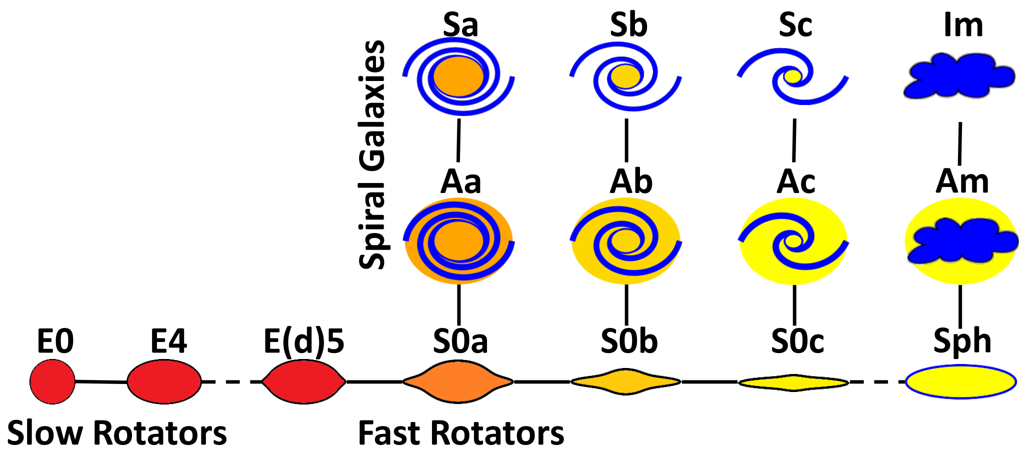

Figure 6.1: ATLAS^{3D} "comb" morphological classification scheme showing the evolution of disc galaxies along the 'tines' of the comb to the parallel fast rotator sequence. Figure 24 in Cappellari (2016)

environment; the derived timescales for which imply that environmentally driven quenching mechanisms must work in sync to quench a satellite galaxy (Chapter 5). I shall now discuss how all of these results fit into the 'big picture' of galaxy evolution.

In Chapter 3 I showed that quenching rates with $\tau < 1.5$ Gyr must be caused by mechanisms which can transform a galaxy from a disc to an elliptical. However this does not infer an immediate transition from a disc dominated to a bulge dominated galaxy. Work by the ATLAS^{3D} team (Cappellari et al., 2011) showed the majority of the visually elliptical population are rotationally supported (Emsellem et al., 2011) with ~ 7 times the number of *fast rotators*, with kinematic discs, than *slow rotators*, with dispersion dominated kinematics (see Cappellari et al., 2007; Emsellem et al., 2007). This has led to the proposal of a revision of Hubble's morphological classification scheme in the form of a "comb" (see Figure 6.1 originally from Cappellari, 2016), whereby the evolution of a disc galaxy from disc to bulge dominated takes place along a tine of the comb, until these systems become bulge dominated fast rotators. These fast rotators then evolve along the handle of the comb to become slow rotators. Given the nature of the visual morphology classifications, both fast and slow rotators will most likely have been classified as smooth galaxies and so both are expected to contribute to the smooth weighted populations shown in Chapters 3 & 4. We must therefore consider this in light of the conclusions made in Chapter 3.

Dry major mergers are considered the most likely process to produce slow rotators

(Duc et al., 2011; Naab et al., 2014) as they can destroy the disc dominated nature of a galaxy in rapid timescales (Toomre & Toomre, 1972). I find that across the red sequence smooth-weighted population in Figure 3.4 that 12% of the population density lies below $\tau < 0.2$ Gyr. Between $14 - 17 \pm 5\%$ of ellipticals are slow rotators (Emsellem et al., 2011; Stott et al., 2016), so this suggests that quenching mechanisms with these rates might give rise to a slow rotator (assuming the population densities are constant). This percentage is also therefore an estimate for the percentage of the galaxy population which have undergone a dry major merger, approximated by previous works as $\sim 10 - 20\%$ (since $z \sim 1$; Khochfar & Silk, 2009).

If we now consider fast rotators, these are theorised to be formed by the slow build up of a galaxy's bulge over time, until it eventually overwhelms the disc. This growth is thought to occur via gas-rich major and minor mergers (Duc et al., 2011) which can produce a bulge dominated, rotationally supported quenched galaxy, which would be visually classified as an elliptical. Although these mechanisms do not completely destroy the disc of a galaxy, they do cause an eventual morphological change to a completely bulge dominated system. This could be the source of the result in Section 3.2.2 suggesting all mechanisms with $\tau < 1.5$ Gyr must be able to cause a morphological change during quenching in order for the ratio of smooth to disc galaxies in the green valley to match that of the red sequence. Although this morphological change does not produce a true dispersion dominated elliptical galaxy, the resulting galaxy will be identified as smooth by visual classifications. Despite this, the STARPY method has still managed to reveal this important, slightly slower process of producing a bulge dominated galaxy and separate it from the rapid rates caused by dry major mergers (see Figures 3.4 & 3.5). The large IFU studies of MaNGA, SAMI and CALIFA will allow for larger populations of slow and fast rotators to be identified so that the relative dominance of gas-rich and dry mergers across the visually elliptical population can be determined more accurately (see Section 6.3).

Another class of galaxy which is thought to be linked with major mergers is the rare ($< 1\%$; Wong et al., 2012; Wild et al., 2016) 'missing link' post-starburst (PSB) galaxy phase (Zabludoff et al., 1996; Blake et al., 2004; Goto, 2005a; Yang et al., 2008; Pawlik et al., 2016). PSBs are thought to have undergone an intense, unsustainable period of star formation in the recent past which has then rapidly quenched (Dressler & Gunn, 1983; Abraham et al., 1996; Poggianti et al., 1999; Goto, 2003, 2005a, 2007) and can add a significant fraction ($\sim 10\%$; Wild et al., 2010) to the stellar mass of a galaxy. These PSBs are often referred to as 'E+A' galaxies, as their spectra are a combination of a typical elliptical galaxy with A star signatures, once again indicative of their post starburst nature. They appear elliptical in shape unlike 'K+A' galaxies which are disk like in shpe Wild et al. (2009), who by making assumptions for how long galaxies spend in a PSB phase, estimated that gas rich major merger induced starbursts, which can simultaneously cause a morphological change, could account for 38% of the growth of the red sequence at $z \sim 0.7$. Figure 3.4 shows that $\sim 40\%$ of the smooth weighted red population undergoes quenching at rates, $\tau < 0.7$ Gyr, suggesting that these quenching rates could be associated with this post-starburst phase.

However, earlier in this Section, I discussed how rapid quenching rates were also associated with the production of fast rotators. Work by Pracy et al. (2013) found that of the 26 'E+A' galaxies with kinematics 22 ($\sim 85\%$) were classed as fast rotators. Although at first this result seems to suggest a connection between the PSB phase and fast rotator production, this fraction is in fact similar to the overall fraction of fast rotators found in the normal elliptical galaxy population (Emsellem et al., 2011; Stott et al., 2016). These kinematic studies of PSBs also allow the locations of the recent starbursts to be determined through spectral indicators of star formation (such as $H\alpha$; Kennicutt et al., 1994). Once again, the large IFU studies of MaNGA, SAMI and CALIFA, once completed, will add to the known PSB galaxies which have be classified as either fast or slow rotators. Using STARPY to determine the spatially variant SFHs of these galaxies may help to further disentangle the theorised connection between PSBs and elliptical galaxies and the estimated contribution to the growth of the red sequence by this rare, short-lived, yet perhaps crucial evolutionary phase.

Having now considered the effects of both major and minor mergers, let us turn our attention to an internal, secular quenching mechanism. A parameter which is often investigated in quenching studies is the stellar mass surface density of a galaxy, which is found to correlate with SFR (Barro et al., 2013; Whitaker et al., 2016). As a galaxy's bulge grows it is thought to be able to stabilise a disc against collapse and effectively stop it from forming stars. This is classed as a type of morphological quenching and is effective over a few Gyr (Fang et al., 2013) even if external gas is still fed to a galaxy. This slower quenching track of bulge dominated galaxies may help to explain the slow quenching rates observed across the red and green smooth weighted population densities. Slow quenching ($\tau > 2$ Gyr) of smooth galaxies is occurring in up to 40% of the smooth weighted green population density (see Figure 3.5) and 24% of the smooth weighted red population (see Figure 3.4). With STARPY this slower quenching history caused by processes which grow the bulge then consequently trigger morphological quenching has been separated out from more rapid quenching histories caused by processes which simultaneously quench the galaxy and grow the bulge. However, even in the latter case, morphological quenching may help in either speeding up the quenching process or in ensuring the galaxy stays quenched. This is supported by the finding of Abramson et al. (2016) who found there is no threshold at which density triggered quenching occurs, but that denser systems typically redden faster than less dense galaxies. This suggests that minor mergers and morphological quenching work together to fully achieve quiescence, similar to the collaboration between starvation and stripping to achieve quiescence of satellite galaxies discussed in Chapter 5.

This sort of partnership between two quenching mechanisms was also discussed in Chapter 3; simulations have shown that without AGN feedback a major merger cannot fully quench a galaxy (Springel et al., 2005). In combination with a major merger however, a massive galaxy can be complete quenched by the heating or removal of gas and quiescence maintained (Conselice, 2003; Springel et al., 2005; Hopkins et al., 2008b; Pontzen et al., 2016). These effects are therefore easily detectable, leading to the initial theories for the links between AGN and mergers (Merritt & Ferrarese, 2001; Hopkins et al., 2006c, 2008b,a; Peng, 2007; Jahnke & Macciò, 2011). However, Figure 4.8 shows that galaxies in the AGN-HOST population don't always quench at the rapid rates caused by major mergers, suggesting that a slow co-evolution of black hole and host galaxy can occur. Alone, AGN are only an efficient quenching mechanism in low mass galaxies where they can have a greater impact on the SFR (see Figure 4.8). By studying the population as a whole with robust statistics, I have revealed the overlooked, subtle role of AGN in galaxy evolution.

Across the entire galaxy population we now have lots of examples of two quenching mechanisms working together to either quench a galaxy or ensure a galaxy stays quenched, including starvation and stripping (Section 5.3.4), mergers & AGN (Section 3.3.1), disc instabilities & environment (Section 5.3.3) and minor mergers & morphological quenching (Section 6.1). All of these mechanisms have the same end goal of galaxy quiescence (with the occasional influx of gas thwarting their progress) but no single mechanism dominates over another, except in the most extreme environments or masses. While the effects of mass and morphological quenching are more apparent for galaxies in less dense environments (Figures 5.9-5.11), they still impact galaxies in the densest environments (Chapter 5). Similarly, the effects of mergers are much more apparent in galaxies in dense environments (e.g. centrals; see

Section 5.3.1) and will often drown out the more subtle effects of slower quenching mechanisms which occurred before the merger.

I believe that it is the correct use of the morphological parameterisation that has allowed for all of these conclusions to be drawn. The evolution of a galaxy is continuous in nature from the most disc dominated to the most bulge dominated system. This nature is reflected by the continuous parameters which we use to describe this structure. This includes bulge-to-total ratios, Sérsic index (Sérsic, 1968), Gini coefficient (Abraham et al., 2003; Lotz et al., 2004), asymmetry (Conselice et al., 2000), concentration index (Morgan, 1958) and GZ vote fractions (Lintott et al., 2011). A problem arises however, when studies discretise these values by mapping them to the typical distinct Hubble classifications of morphology; either the data is mapped to T-types (Shimasaku et al., 2001; Brinchmann et al., 2004; Nair & Abraham, 2010a; Barro et al., 2015) or merely split bimodally into late and early types, e.g. with either Sérsic index, $n \leq 2.5$ (Ravindranath et al., 2004; Kelvin et al., 2012; Vika et al., 2015) or GZ vote fraction, $p_d \geq 0.8$ (Schawinski et al., 2014) to identify discs . Firstly, this discretisation no longer reflects our uncertainty in the morphological classification due to the image resolution. With increasing redshift, galaxy structures can be washed out by the PSF of the image. This means that either data must be discarded or the morphological bins made noisier by this uncertainty. Secondly, it reduces the complex internal structures of galaxies into bins which do not share common features. A single bin containing early-type galaxies (e.g. with $n \geq 2.5$ or $p_s \geq 0.8$) in a sample will have a mix of galaxies which are true ellipticals and those which are bulge dominated but rotationally supported, such as S0 galaxies. Similarly, in a single late-type galaxy bin there will be a continuum of bulge strengths along with spiral arms, bars, rings and structures which all encode very different evolutionary histories. By retaining the continuous nature of the GZ vote fractions and using them as a weight in this study, I have been able to utilise all of the possible information about a galaxy's complex history. This allowed me to infer the broad range of quenching rates seen across the colour magnitudes diagram and also reproduce the differences between the populations seen in previous results splitting by morphology (Schawinski et al., 2014, e.g.).

Just as the morphology of galaxies is continuous in nature from disc to bulge dominated, so too are the quenching mechanisms which can cause this change. The impact of mergers on the morphology and SFR of a galaxy depends on the mass ratio, a continuous variable from micro mergers (Carlin et al., 2016) through to major mergers. The strength of morphological quenching mechanisms can be measured on a continuum of stellar mass and stellar mass surface density of a galaxy; similarly the impact of environmentally driven quenching mechanisms increases with increasing halo mass. All of these processes, depending on a galaxy's environment, are likely to affect a galaxy at some point in its lifetime, acting in concert to reduce the SFR to produce the wide distribution of quenching timescales seen across the colour-magnitude diagram in Chapter 3. In previous works, efforts have been made to identify the dominant quenching mechanism in a galaxy sample (e.g. Schawinski et al., 2014; Balogh et al., 2016; Huertas-Company et al., 2016), however it is clear from this work that multiple quenching mechanisms will affect galaxies across their lifetime, working in collaboration to ensure galaxies stay quenched. Future studies should therefore focus on disentangling the effects of these various different quenching mechanisms, rather than focussing on a single process.

6.2 Future Work

Due to the flexibility of the STARPY package I believe it will have a significant number of future applications. A first development would be to investigate quenching using different wavebands as star formation indicators. For example, the $U - V$ and $V - J$ colours are used to separate star forming and quiescent galaxies on the UVJ diagram (Labbé et al., 2005; Wuyts et al., 2007; Williams et al., 2009; Brammer et al., 2011; Patel et al., 2012) at higher redshift (out to $z \sim 4$), for example in the COSMOS/UltraVISTA fields (e.g. see work by Muzzin et al., 2013). Morphological classifications are also available for the COSMOS field with the recent release of the GZ:HUBBLE classifications in Willett et al. (2016). With these morphologies, POP-STARPY can be used to investigate the SFHs inferred by these COSMOS/UltraVISTA UVJ broadband colours for galaxy populations. This will help to further constrain the relative importance of different quenching mechanisms across the galaxy population with cosmic time.

Secondly, STARPY could be adapted to consider many different possible SFHs for a galaxy and examine the Bayesian evidence to choose which is the most appropriate model to characterise the observed photometry of a galaxy. The current exponentially declining SFH (often called the "τ-model") used in STARPY is considered the simplest possible SFH one can assume and so more detail about the effects of different quenching mechanisms may be elucidated by increasing the complexity. For example, possible SFHs include a starburst model (Kauffmann et al., 2003b), an extentded τ-model (Simha et al., 2014), a Gaussian model (Feuillet et al., 2016) or a log-normal SFR (Gladders et al., 2013; Abramson et al., 2016). However, the degeneracy between all of these possible SFHs needs to be investigated in great detail before implementing this in STARPY.For example, can a starburst at early times give the same colours as a broadened Gaussian SFH? The sensitivity (or lack thereof) of the predicted colours to the features of a given model (i.e. for how long are the effects of a starburst visible in the model colours) must also be investigated.

Thirdly, it would be useful to improve the POPSTARPY analysis to use a fully hierarchical Bayesian inference method to determine the parent population quenching parameters. To do this without inferring a distribution for the unknown shape of the parent distribution, 'heat map optimisation' can be employed. This splits the two dimensional $[t_q, \tau]$ parameter space into a grid of $M \times M$ pixels (see Section 2.5.1). The values of each pixel, π_i, are the hyper Bayesian parameters which describe the population parent posterior distribution, $\vec{\theta'}$ so that Equation 2.12 for the hierarchical likelihood for a single galaxy, k, from which N_s number of random samples are drawn from its interim posterior so that there will be $N_{k,i}$ samples in a given pixel, i, becomes:

$$P(d_k|\vec{\theta'}) = \frac{1}{N_s} \sum_i \pi_i N_{k,i} = \boldsymbol{\pi} \cdot \boldsymbol{N_k}, \tag{6.1}$$

where $\boldsymbol{\pi}$ is the vector of pixel values and $\boldsymbol{N_k}$ the vector of samples drawn from the kth galaxy, since $\sum_i \frac{N_{k,i}}{N_s} = \boldsymbol{N_k}$. The hierarchical population posterior distribution is then calculated as:

$$P(\vec{\theta'}|\vec{d}) = P(\vec{\theta'}) \prod_k^N \boldsymbol{\pi} \cdot \boldsymbol{N_k}, \tag{6.2}$$

for all N galaxies and where $P(\vec{\theta'})$ is the prior on the hyper parameters. In this case, each pixel would need a prior (e.g. a basic entropic prior) and the pixel values, $\boldsymbol{\pi}$, would sum to unity, $\sum_i \pi_i = 1$. In order for this pixel map to accurately characterise the detail expected in the parent populations, the pixel grid would need to be sufficiently large, with at least a 50x50 grid of pixels (i.e. upwards of 2500 model parameters, θ' to be inferred). Determining the optimum number of pixel parameters will require a detailed investigation into the trade off between computing power and the resolution required to identify key features in the population distribution.

Along with these expansions of the STARPY module itself, several avenues of data exploration are also still available using STARPY in its current form (future work using IFU data are discussed in Section 6.3):

(i) A study of barred vs non-barred galaxies using $\{p_{\rm bar}, p_{\rm nobar}\}$ in place of $\{p_{\rm disc}, p_{\rm smooth}\}$ to weight the population densities derived with POPSTARPY may reveal the impact a bar can have on a galaxy's SFR by funnelling gas to central regions.

(ii) Studying the SFHs of low mass satellite galaxies with $M_* \leq 10^{8-9}\ M_{\odot}$, which are thought to have quenching histories dominated by ram pressure stripping (Hester, 2006; Fillingham et al., 2016), may help to constrain the quenching timescales for this mechanism. However, constructing a large sample representative of the entire population may be difficult as they are only detected at lower redshifts due to their low luminosities. For example, in the MPA-JHU catalogue of SDSS galaxies there are only $\sim 23,000$ galaxies ($\sim 2.5\%$) with calculated stellar masses of $M_* < 10^9 M_{\odot}$ (and $\sim 4,800$ with $M_* < 10^8 M_{\odot}$); matching to GALEX will further reduce these numbers.

(iii) The effect of AGN feedback could be studied further by investigating the SFHs of unobscured Type 1 AGN. However this would require either a more accurate subtraction of the unobscured nuclear emission or a change in the bandpass input to STARPY to negate this issue. AGN identified by X-ray, radio and IR selection methods could also be identified to investigate any bias with selection waveband. For example, the results of Ellison et al. (2016) show that only radio and optically selected AGN have SFRs distributed below the SFS, whereas IR selected AGN have SFRs consistent with the SFS. This suggests that different selection methods may be biased towards either star forming or quenched galaxies. Reproducing the result seen in Chapter 4.1 with these AGN would corroborate the idea that quenching is actually occurring across the entire AGN population, and provide further support for the theory of AGN unification (Antonucci, 1993; Urry & Padovani, 1995).

6.3 The use of starpy with IFU data

In Chapter 4 I discussed how the current SDSS data (both photometric and spectroscopic) cannot determine whether the AGN is the cause or the consequence of the

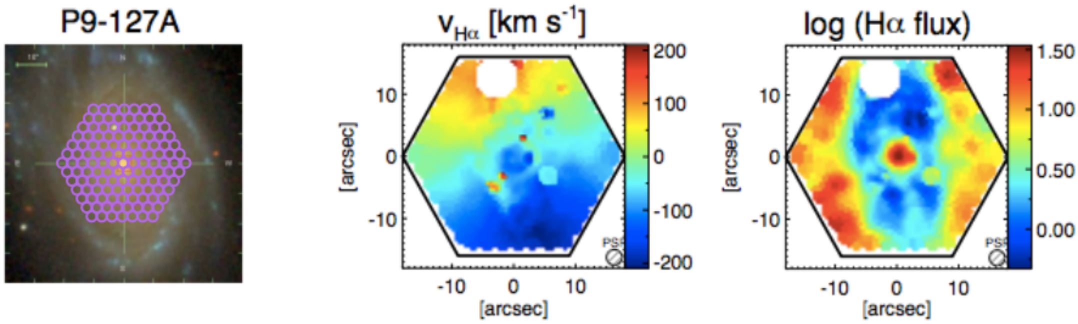

Figure 6.2: Example fibre bundle placed over a MaNGA target galaxy (left) and corresponding preliminary survey data showing the mapped velocity (middle) and flux (right) of $H\alpha$ gas emission as measured across the galaxy in each fibre. Such measurements can be utilised to calculate the star formation rate across the structure of a galaxy. Adapted from Bundy et al. (2015) Figure 14.

quenching seen across the AGN-HOST population in Figures 4.7 & 4.8. Using data from the MaNGA IFU survey (Bundy et al., 2015) I hope to determine whether feedback from the AGN is truly the cause of this quenching. MaNGA is a multi-object IFU survey which by the end of 2020 will provide IFU spectroscopy for $\sim 10,000$ galaxies with a maximum bundle of 127 fibres per galaxy (see Figure 6.2). Spectral coverage will be continuous from $3,600$Å to $10,300$Å out to 1.5 R_e for the majority of targets. Although this wavelength range does not encompass the NUV wavelength of $\sim 2,300$Å many spectral indicators of star formation, metallicity and age are all well within this range. This will allow me to modify STARPY so that spectral star formation indicators (such as $H\alpha$; Kennicutt et al., 1994) can be used as inputs to break the degeneracy inherent in the photometric colours (see Figure 2.2). The IFU data will also allow me to remove the contribution of an of any unobscured AGN in the central region of a galaxy. With the completion of the observations of $10,000$ galaxies by MaNGA, this should provide a large, representative sample of AGN to study.

Along with these improvements to STARPY, this acquisition of many spectra across the face of a galaxy will allow me to map the inferred quenching parameters as a function of radius. Any correlation of the inferred quenching parameters with radius will allow me to determine whether quenching is happening from the outside-in (i.e. quenching due to environmental mechanisms, as in Pan et al., 2015; Clarke et al., 2016; Schaefer et al., 2017) or inside-out, as in work with preliminary MaNGA survey data by Belfiore et al. (2016) and with CALIFA data by González Delgado et al. (2016). I will investigate how this preference for outside-in or inside-out quenching is correlated with the presence of an AGN and with a galaxy's environment. This will not only help to answer the question of *cause* vs. *consequence*, discussed in Section 4.1.4, but also further constrain the timescales of quenching mechanisms possibly caused by AGN or the environment.

A large IFU survey such as MaNGA (with up to $\sim 10,000$ galaxies with no cuts on colour or morphology; see Bundy et al. 2015) will also make possible the comparison of large populations of fast and slow rotators (see work with the first results from MaNGA by Penny et al., 2016). This would aid in the understanding of the different quenching timescales of gas-rich and dry major mergers. I would also like to consider how this kinematic morphological classification of early-type galaxies is linked with the rare PSB phase discussed in Section 6.1. However, considering that $< 1\%$ of galaxies are thought to be in this phase at any one time (Wong et al., 2012; Wild et al., 2016), within the MaNGA survey only $\lesssim 100$ PSB galaxies are expected to be identified. MaNGA is currently the largest IFU survey planned, therefore to investigate the link between PSBs and fast rotators with robust statistics, an IFU survey with ~ 1 million target galaxies will be required.

There is therefore still lots of work that can be done with STARPY. Investigating all of the ideas proposed in this Chapter will most likely take years to complete. However, what I have established in this thesis is a foundation of results which can be built upon with the new influx of large IFU survey data. I have found that the green valley is a transition population between the blue cloud and red sequence, with the rate of transition dependent on morphology. A second key result is the detection of rapid, recent quenching within the AGN-HOST population suggesting that AGN may be the cause of this quenching via AGN feedback. Not all of the AGN host galaxies however have quenched rapidly, suggesting a slower co-evolution of a galaxy and its black hole. This is supported by the finding that black holes in bulgeless galaxies, with assumed merger free histories, are more massive than predicted by scaling relations between black hole and bulge mass. Along with AGN feedback as a mechanism for quenching, I have found evidence for mergers, environmentally driven quenching mechanisms, mass quenching and morphology quenching all occurring in the group environment, often acting in concert with each other to both achieve and ensure quiescence for a galaxy.

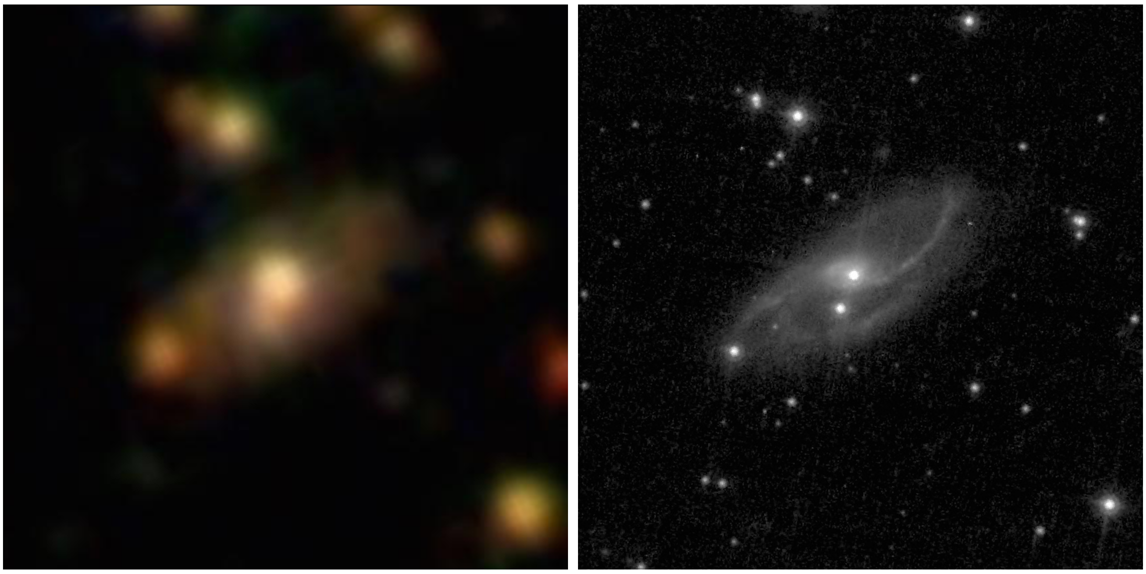

Figure 6.3: Example SDSS urgiz image (left) for J192250.74-055259.15, part of the BULGELESS sample, described in Section 4.2.1.1, in comparison to space based imaging from the HST (right). The higher resolution HST image reveals finer structure than the SDSS image, including spiral arms, a ring and a possible bar along with the true disc dominated nature of the galaxy.

6.4 And one more for the road...

In Chapter 4, I discussed how accurate fits to the bulge-to-total ratio could not be made for galaxies of the BULGELESS sample hosting AGN due to the resolution of ground based SDSS imaging. This led to the derivation of upper limits on the bulge masses of this sample. The *Hubble Space Telescope* (HST) however, provides both an extremely stable and well understood point spread function, enabling reliable separation of the AGN from the host galaxy, and high spatial resolution which is needed to distinguish between classical, merger driven bulges and pseudo bulges grown by secular processes. Observations with the HST of the galaxies in the BULGELESS sample will enable extremely robust measures of bulge-to-total ratios for each host galaxy and allow the identification of truly secular systems with growing black holes. Such measurements will also allow the dominance of merger driven (building classical bulges) and merger free (growing pseudo-bulges or retaining a pure disc) co-evolutionary histories to be determined.

We received image data from the HST Advanced Camera for Surveys Wide Field Channel (Proposal ID: 14606, Cycle 24) of the galaxy J192250.74-055259.15 from the

BULGELESS sample on October 26th 2016, on which date I was writing Section 4.2 of this thesis. Figure 6.3 demonstrates the difference in resolution provided by the HST with this first image received (right), in comparison with the ground based SDSS ugriz image (left; also shown in Figure 4.11). This galaxy has an estimated black hole mass of $M_{\mathrm{BH}} = 10^{7.4\pm0.1}\ M_{\odot}$ but a bulge-to-total mass ratio could not be derived from the SDSS image. The HST image will allow for an accurate derivation of the bulge mass of this galaxy, allowing for a more concrete conclusion to be drawn on the controversial issue of secularly driven galaxy-black hole co-evolution.

With all of this newly available data, I am excited to continue investigating the processes responsible for the complex nature of galaxy evolution.

Bibliography

Aarseth S. J., Turner E. L., Gott, III J. R., 1979, ApJ, 228, 664

Abadi M. G., Moore B., Bower R. G., 1999, MNRAS, 308, 947

Abell G. O., 1958, ApJS, 3, 211

Abraham R. G. et al., 1996, ApJ, 471, 694

Abraham R. G., van den Bergh S., Nair P., 2003, ApJ, 588, 218

Abramson L. E., Gladders M. D., Dressler A., Oemler A., Poggianti B., Vulcani B., 2016, ArXiv e-prints, 1604.00016

Ahn C. P. et al., 2012, ApJS, 203, 21

Aihara H. et al., 2011, ApJS, 193, 29

Aird J. et al., 2012, ApJ, 746, 90

Alexander D., Hickox R., 2012, New Astronomy Reviews, 56, 93

Ann H. B., Seo M., Ha D. K., 2015, ApJS, 217, 27

Antonucci R., 1993, ARA&A, 31, 473

Astropy Collaboration et al., 2013, A&A, 558, A33

Athanassoula E., 1992a, MNRAS, 259, 328

Athanassoula E., 1992b, MNRAS, 259, 345

Azadi M. et al., 2016, ArXiv e-prints, 1608.05890

Baldry I. K., Balogh M. L., Bower R. G., Glazebrook K., Nichol R. C., Bamford S. P., Budavari T., 2006, MNRAS, 373, 469

Baldry I. K., Glazebrook K., Brinkmann J., Ivezić Ž., Lupton R. H., Nichol R. C., Szalay A. S., 2004, ApJ, 600, 681

Baldwin J. A., Phillips M. M., Terlevich R., 1981, PASP, 93, 5

Ball N. M., Loveday J., Brunner R. J., 2008, MNRAS, 383, 907

Balogh M. L. et al., 2016, MNRAS, 456, 4364

Balogh M. L., Navarro J. F., Morris S. L., 2000, ApJ, 540, 113

Bamford S. P. et al., 2009, MNRAS, 393, 1324

Barnes J., Efstathiou G., 1987, ApJ, 319, 575

Barnes J. E., Hernquist L., 1996, ApJ, 471, 115

Barro G. et al., 2015, ArXiv e-prints, 1509.00469

Barro G. et al., 2013, ApJ, 765, 104

Barth A. J. et al., 2015, ApJS, 217, 26

Baugh C. M., Cole S., Frenk C. S., Lacey C. G., 1998, ApJ, 498, 504

Baugh C. M., Lacey C. G., Frenk C. S., Granato G. L., Silva L., Bressan A., Benson A. J., Cole S., 2005, MNRAS, 356, 1191

Beckmann V., Shrader C. R., 2012, Active Galactic Nuclei. John Wiley and Sons

Bekki K., 1998, ApJ, 496, 713

Belfiore F. et al., 2016, ArXiv e-prints, 1609.01737

Bell E. F., Phleps S., Somerville R. S., Wolf C., Borch A., Meisenheimer K., 2006, ApJ, 652, 270

Bell E. F. et al., 2004, ApJ, 608, 752

Bell E. F., Zheng X. Z., Papovich C., Borch A., Wolf C., Meisenheimer K., 2007, ApJ, 663, 834

Bellovary J., Brooks A., Volonteri M., Governato F., Quinn T., Wadsley J., 2013, ApJ, 779, 136

Benson A. J., Bower R. G., Frenk C. S., Lacey C. G., Baugh C. M., Cole S., 2003, ApJ, 599, 38

Bentz M. C. et al., 2006, ApJ, 651, 775

Berlind A. A. et al., 2006, ApJS, 167, 1

Béthermin M. et al., 2012, ApJ, 757, L23

Bialas D., Lisker T., Olczak C., Spurzem R., Kotulla R., 2015, A&A, 576, A103

Binney J., Merrifield M., 1998, Galactic astronomy. Galactic astronomy / James Binney and Michael Merrifield. Princeton, NJ : Princeton University Press, 1998. (Princeton series in astrophysics) QB857 .B522 1998 ($35.00)

Birnboim Y., Dekel A., 2003, MNRAS, 345, 349

Blake C. et al., 2004, MNRAS, 355, 713

Blandford R. D., McKee C. F., 1982, ApJ, 255, 419

Blanton M. R., Eisenstein D., Hogg D. W., Schlegel D. J., Brinkmann J., 2005, ApJ, 629, 143

Blanton M. R., Roweis S., 2007, AJ, 133, 734

Bluck A. F. L., Mendel J. T., Ellison S. L., Moreno J., Simard L., Patton D. R., Starkenburg E., 2014, MNRAS, 441, 599

Bluck A. F. L. et al., 2016, MNRAS, 462, 2559

Booth C. M., Schaye J., 2010, MNRAS, 405, L1

Boquien M., Buat V., Perret V., 2014, A&A, 571, A72

Bower R. G., Balogh M. L., 2004, Clusters of Galaxies: Probes of Cosmological Structure and Galaxy Evolution, 325

Bower R. G., Benson A. J., Malbon R., Helly J. C., Frenk C. S., Baugh C. M., Cole S., Lacey C. G., 2006, MNRAS, 370, 645

Bower R. G., Lucey J. R., Ellis R. S., 1992, MNRAS, 254, 601

Boylan-Kolchin M., Ma C.-P., Quataert E., 2005, MNRAS, 362, 184

Brammer G. B. et al., 2011, ApJ, 739, 24

Brammer G. B. et al., 2009, ApJ, 706, L173

Brinchmann J., Charlot S., White S. D. M., Tremonti C., Kauffmann G., Heckman T., Brinkmann J., 2004, MNRAS, 351, 1151

Brinchmann J., Ellis R. S., 2000, ApJ, 536, L77

Bruzual G., Charlot S., 2003, MNRAS, 344, 1000

Buat V. et al., 2005, ApJ, 619, L51

Bundy K. et al., 2015, ApJ, 798, 7

Bundy K., Treu T., Ellis R. S., 2007, ApJ, 665, L5

Butcher H., Oemler, Jr. A., 1978, ApJ, 226, 559

Campbell D., van den Bosch F. C., Hearin A., Padmanabhan N., Berlind A., Mo H. J., Tinker J., Yang X., 2015, MNRAS, 452, 444

Cappellari M., 2016, ARA&A, 54, 597

Cappellari M. et al., 2007, MNRAS, 379, 418

Cappellari M. et al., 2011, MNRAS, 413, 813

Cappellari M. et al., 2012, Nature, 484, 485

Cardelli J. A., Clayton G. C., Mathis J. S., 1989, ApJ, 345, 245

Carlberg R. G., 2004, Clusters of Galaxies: Probes of Cosmological Structure and Galaxy Evolution, 343

Carlin J. L. et al., 2016, ApJ, 828, L5

Chabrier G., 2003, PASP, 115, 763

Charlot S., Longhetti M., 2001, MNRAS, 323, 887

Chen X. Y., Liang Y. C., Hammer F., Prugniel P., Zhong G. H., Rodrigues M., Zhao Y. H., Flores H., 2010, A&A, 515, A101

Chester C., Roberts M. S., 1964, AJ, 69, 635

Cheung E. et al., 2013, ApJ, 779, 162

Cheung E. et al., 2015, MNRAS, 447, 506

Cid Fernandes R., Mateus A., Sodré L., Stasińska G., Gomes J. M., 2005, MNRAS, 358, 363

Cisternas M. et al., 2013, ApJ, 776, 50

Cisternas M. et al., 2011, ApJ, 741, L11

Clarke A. J., Debattista V. P., Roškar R., 2016, ArXiv e-prints, 1610.04030

Coil A. L. et al., 2008, ApJ, 672, 153

Cole S. et al., 2001, MNRAS, 326, 255

Conroy C., Gunn J. E., White M., 2009, ApJ, 699, 486

Conroy C., van Dokkum P. G., 2012, ApJ, 760, 71

Conselice C. J., 2003, ApJS, 147, 1

Conselice C. J., Bershady M. A., Jangren A., 2000, ApJ, 529, 886

Constantin A., Hoyle F., Vogeley M. S., 2008, ApJ, 673, 715

Cowie L. L., Barger A. J., 2008, ApJ, 686, 72

Cowie L. L., Songaila A., 1977, Nature, 266, 501

Cowie L. L., Songaila A., Hu E. M., Cohen J. G., 1996, AJ, 112, 839

Cowley M. J. et al., 2016, MNRAS, 457, 629

Cox T. J., Younger J., Hernquist L., Hopkins P. F., 2008, in IAU Symposium, Vol. 245, Formation and Evolution of Galaxy Bulges, Bureau M., Athanassoula E., Barbuy B., eds., pp. 63–66

Crockett R. M. et al., 2011, ApJ, 727, 115

Croom S. M. et al., 2012, MNRAS, 421, 872

Croton D. J. et al., 2006, MNRAS, 365, 11

Cucciati O. et al., 2010, A&A, 520, A42

Daddi E. et al., 2007, ApJ, 670, 156

Danese L., de Zotti G., di Tullio G., 1980, A&A, 82, 322

Darg D. W. et al., 2010, MNRAS, 401, 1043

Darvish B., Mobasher B., Sobral D., Rettura A., Scoville N., Faisst A., Capak P., 2016, ApJ, 825, 113

Davis M., Efstathiou G., Frenk C. S., White S. D. M., 1985, ApJ, 292, 371

de Jong R. S., 1996, A&A, 313, 377

de Souza R. S. et al., 2016, MNRAS, 461, 2115

de Vaucouleurs G., 1953, MNRAS, 113, 134

Dekel A., Birnboim Y., 2006, MNRAS, 368, 2

Dekel A., Silk J., 1986, ApJ, 303, 39

Del Popolo A., Hiotelis N., Peñarrubia J., 2005, ApJ, 628, 76

Di Matteo T., Springel V., Hernquist L., 2005, Nature, 433, 604

Di Teodoro E. M., Fraternali F., 2014, A&A, 567, A68

Dieleman S., Willett K. W., Dambre J., 2015, MNRAS, 450, 1441

Djorgovski S., Davis M., 1987, ApJ, 313, 59

Dressler A., 1980, ApJ, 236, 351

Dressler A., 2004, in IAU Colloq. 195: Outskirts of Galaxy Clusters: Intense Life in the Suburbs, Diaferio A., ed., pp. 341–346

Dressler A., Gunn J. E., 1983, ApJ, 270, 7

Dressler A., Lynden-Bell D., Burstein D., Davies R. L., Faber S. M., Terlevich R., Wegner G., 1987, ApJ, 313, 42

Driver S. P. et al., 2006, MNRAS, 368, 414

Duc P.-A. et al., 2011, MNRAS, 417, 863

Edelson R., Malkan M., 2012, ApJ, 751, 52

Efstathiou G., Eastwood J. W., 1981, MNRAS, 194, 503

Ehlert S. et al., 2014, MNRAS, 437, 1942

Eke V. R. et al., 2004, MNRAS, 348, 866

Elbaz D. et al., 2007, A&A, 468, 33

Ellison S. L., Mendel J. T., Scudder J. M., Patton D. R., Palmer M. J. D., 2013, MNRAS, 430, 3128

Ellison S. L., Patton D. R., Simard L., McConnachie A. W., 2008, AJ, 135, 1877

Ellison S. L., Patton D. R., Simard L., McConnachie A. W., Baldry I. K., Mendel J. T., 2010, MNRAS, 407, 1514

Ellison S. L., Teimoorinia H., Rosario D. J., Mendel J. T., 2016, MNRAS, 458, L34

Elvis M., Risaliti G., Zamorani G., 2002, ApJ, 565, L75

Emerick A., Mac Low M.-M., Grcevich J., Gatto A., 2016, ApJ, 826, 148

Eminian C., Kauffmann G., Charlot S., Wild V., Bruzual G., Rettura A., Loveday J., 2008, MNRAS, 384, 930

Emsellem E. et al., 2011, MNRAS, 414, 888

Emsellem E. et al., 2007, MNRAS, 379, 401

Emsellem E., Renaud F., Bournaud F., Elmegreen B., Combes F., Gabor J. M., 2015, MNRAS, 446, 2468

Erwin P., Sparke L. S., 2002, AJ, 124, 65

Faber S. M. et al., 2007, ApJ, 665, 265

Fabian A. C., 2012, ARA&A, 50, 455

Falkenberg M. A., Kotulla R., Fritze U., 2009, MNRAS, 397, 1954

Fall S. M., Efstathiou G., 1980, MNRAS, 193, 189

Fang J. J., Faber S. M., Koo D. C., Dekel A., 2013, ApJ, 776, 63

Ferrarese L., Pogge R. W., Peterson B. M., Merritt D., Wandel A., Joseph C. L., 2001, ApJ, 555, L79

Feuillet D. K., Bovy J., Holtzman J., Girardi L., MacDonald N., Majewski S. R., Nidever D. L., 2016, ApJ, 817, 40

Fillingham S. P., Cooper M. C., Pace A. B., Boylan-Kolchin M., Bullock J. S., Garrison-Kimmel S., Wheeler C., 2016, MNRAS

Finn R. A. et al., 2005, ApJ, 630, 206

Fiore F. et al., 2012, A&A, 537, A16

Fitzpatrick P. J., Graves G. J., 2015, MNRAS, 447, 1383

Foreman-Mackey D., Hogg D. W., Lang D., Goodman J., 2013, PASP, 125, 306

Frenk C. S., White S. D. M., 2012, Annalen der Physik, 524, 507

Friedli D., Benz W., 1993, A&A, 268, 6585

Gabor J. M., Capelo P. R., Volonteri M., Bournaud F., Bellovary J., Governato F., Quinn T., 2016, A&A, 592, A62

Gabor J. M., Davé R., 2015, MNRAS, 447, 374

Gabor J. M., Davé R., Finlator K., Oppenheimer B. D., 2010, MNRAS, 407, 749

Gabor J. M. et al., 2009, ApJ, 691, 705

Ganda K., Peletier R. F., Balcells M., Falcón-Barroso J., 2009, MNRAS, 395, 1669

Gavazzi G., Bonfanti C., Sanvito G., Boselli A., Scodeggio M., 2002, ApJ, 576, 135

Gelman A., Roberts G., Gilks W., 1996, Bayesian statistics 5. Oxford University Press, pp. 599–607

Genel S. et al., 2008, ApJ, 688, 789

Genel S. et al., 2014, MNRAS, 445, 175

Gladders M. D., Oemler A., Dressler A., Poggianti B., Vulcani B., Abramson L., 2013, ApJ, 770, 64

Gómez P. L. et al., 2003, ApJ, 584, 210

Gonçalves T. S., Martin D. C., Menéndez-Delmestre K., Wyder T. K., Koekemoer A., 2012, ApJ, 759, 67

González V., Labbé I., Bouwens R. J., Illingworth G., Franx M., Kriek M., Brammer G. B., 2010, ApJ, 713, 115

González Delgado R. M. et al., 2016, A&A, 590, A44

Goodman J., Weare J., 2010, CAMCS, 5, 65

Goto T., 2003, PhD thesis, The University of Tokyo

Goto T., 2005a, MNRAS, 357, 937

Goto T., 2005b, MNRAS, 359, 1415

Goto T., 2007, MNRAS, 381, 187

Gott, III J. R., Rees M. J., 1975, A&A, 45, 365

Gott, III J. R., Turner E. L., Aarseth S. J., 1979, ApJ, 234, 13

Goulding A. D., Alexander D. M., 2009, MNRAS, 398, 1165

Graham A. W., 2001, AJ, 121, 820

Greene J. E., Ho L. C., 2007, ApJ, 670, 92

Greene J. E., Ho L. C., Barth A. J., 2008, ApJ, 688, 159

Greene J. E. et al., 2010, ApJ, 721, 26

Gunn J. E., Gott, III J. R., 1972, ApJ, 176, 1

Guth A. H., Pi S.-Y., 1982, Physical Review Letters, 49, 1110

Hahn C., Tinker J. L., Wetzel A. R., 2016, ArXiv e-prints, 1609.04398

Haines T., McIntosh D. H., Sánchez S. F., Tremonti C., Rudnick G., 2015, MNRAS, 451, 433

Hao L. et al., 2005, AJ, 129, 1795

Häring N., Rix H.-W., 2004, ApJ, 604, L89

Harrison C. M. et al., 2016, MNRAS, 456, 1195

Hart R. E. et al., 2016, MNRAS, 461, 3663

Hatfield P. W., Jarvis M. J., 2016, ArXiv e-prints, 1606.08989

Hawking S. W., 1982, Physics Letters B, 115, 295

Hayward C. C., Torrey P., Springel V., Hernquist L., Vogelsberger M., 2014, MNRAS, 442, 1992

Hearin A. P., Watson D. F., van den Bosch F. C., 2015, MNRAS, 452, 1958

Heavens A. F., Jimenez R., Lahav O., 2000, MNRAS, 317, 965

Heckman T. M., Kauffmann G., Brinchmann J., Charlot S., Tremonti C., White S. D. M., 2004, ApJ, 613, 109

Heinis S. et al., 2014, MNRAS, 437, 1268

Hester J. A., 2006, ApJ, 647, 910

Hickox R. C. et al., 2009, ApJ, 696, 891

Hill D. T. et al., 2011, MNRAS, 412, 765

Hilz M., Naab T., Ostriker J. P., Thomas J., Burkert A., Jesseit R., 2012, MNRAS, 425, 3119

Hirschmann M., De Lucia G., Wilman D., Weinmann S., Iovino A., Cucciati O., Zibetti S., Villalobos Á., 2014, MNRAS, 444, 2938

Ho L. C., Filippenko A. V., Sargent W. L. W., 1997, ApJ, 487, 591

Ho L. C., Kim M., 2014, ApJ, 789, 17

Homan D. C., 2012, International Journal of Modern Physics Conference Series, 8, 163

Hopkins P. F., Cox T. J., Kereš D., Hernquist L., 2008a, ApJS, 175, 390

Hopkins P. F., Cox T. J., Younger J. D., Hernquist L., 2009, ApJ, 691, 1168

Hopkins P. F., Hernquist L., 2009, ApJ, 694, 599

Hopkins P. F., Hernquist L., Cox T. J., Di Matteo T., Robertson B., Springel V., 2006a, ApJS, 163, 1

Hopkins P. F., Hernquist L., Cox T. J., Kereš D., 2008b, ApJS, 175, 356

Hopkins P. F., Hernquist L., Cox T. J., Robertson B., Di Matteo T., Springel V., 2006b, ApJ, 639, 700

Hopkins P. F. et al., 2005, in Bulletin of the American Astronomical Society, Vol. 37, American Astronomical Society Meeting Abstracts, p. 1354

Hopkins P. F., Kereš D., Murray N., Quataert E., Hernquist L., 2012, MNRAS, 427, 968

Hopkins P. F., Somerville R. S., Hernquist L., Cox T. J., Robertson B., Li Y., 2006c, ApJ, 652, 864

Hoyle B., Jimenez R., Verde L., 2011, MNRAS, 415, 2818

Hu J., 2008, MNRAS, 386, 2242

Hu J., 2009, ArXiv e-prints, 0908.2028

Huang J.-S., Glazebrook K., Cowie L. L., Tinney C., 2003, ApJ, 584, 203

Hubble E. P., 1936, Science, 84, 509

Huertas-Company M. et al., 2016, MNRAS, 462, 4495

Ishibashi W., Fabian A. C., 2012, MNRAS, 427, 2998

Jahnke K., Macciò A. V., 2011, ApJ, 734, 92

Jiang Y.-F., Greene J. E., Ho L. C., 2011a, ApJ, 737, L45

Jiang Y.-F., Greene J. E., Ho L. C., Xiao T., Barth A. J., 2011b, ApJ, 742, 68

Johnston E. J. et al., 2016, ArXiv e-prints, 1611.00609

Jones L. R., Ponman T. J., Forbes D. A., 2000, MNRAS, 312, 139

Jones L. R., Ponman T. J., Horton A., Babul A., Ebeling H., Burke D. J., 2003, MNRAS, 343, 627

Kaspi S., Maoz D., Netzer H., Peterson B. M., Vestergaard M., Jannuzi B. T., 2005, ApJ, 629, 61

Kauffmann G., 1996, MNRAS, 281, 487

Kauffmann G., Colberg J. M., Diaferio A., White S. D. M., 1999a, MNRAS, 303, 188

Kauffmann G., Colberg J. M., Diaferio A., White S. D. M., 1999b, MNRAS, 307, 529

Kauffmann G., Heckman T. M., 2009, MNRAS, 397, 135

Kauffmann G. et al., 2003a, MNRAS, 346, 1055

Kauffmann G. et al., 2003b, MNRAS, 341, 33

Kauffmann G., Li C., Zhang W., Weinmann S., 2013, MNRAS, 430, 1447

Kauffmann G., White S. D. M., Heckman T. M., Ménard B., Brinchmann J., Charlot S., Tremonti C., Brinkmann J., 2004, MNRAS, 353, 713

Kaviraj S., 2014a, MNRAS, 440, 2944

Kaviraj S., 2014b, MNRAS, 437, L41

Kaviraj S. et al., 2013, MNRAS, 428, 925

Kaviraj S., Tan K.-M., Ellis R. S., Silk J., 2011, MNRAS, 411, 2148

Kelly B. C., 2007, ApJ, 665, 1489

Kelvin L. S. et al., 2012, MNRAS, 421, 1007

Kennicutt R. C., 1997, in Astrophysics and Space Science Library, Vol. 161, Astrophysics and Space Science Library, pp. 171–195

Kennicutt, Jr. R. C., 1998, ApJ, 498, 541

Kennicutt, Jr. R. C., Tamblyn P., Congdon C. E., 1994, ApJ, 435, 22

Kewley L. J., Groves B., Kauffmann G., Heckman T., 2006, MNRAS, 372, 961

Kewley L. J., Heisler C. A., Dopita M. A., Lumsden S., 2001, ApJS, 132, 37

Khochfar S., Silk J., 2009, MNRAS, 397, 506

Kimm T. et al., 2009, MNRAS, 394, 1131

Kimm T., Yi S. K., Khochfar S., 2011, ApJ, 729, 11

Kitzbichler M. G., White S. D. M., 2006, MNRAS, 366, 858

Knobel C. et al., 2012, ApJ, 753, 121

Knobel C., Lilly S. J., Woo J., Kovač K., 2015, ApJ, 800, 24

Ko J., Hwang H. S., Lee J. C., Sohn Y.-J., 2013, ApJ, 767, 90

Kocevski D. D. et al., 2012, ApJ, 744, 148

Kochanek C. S. et al., 2001, ApJ, 560, 566

Koester B. P. et al., 2007, ApJ, 660, 239

Kormendy J., Bender R., 1996, ApJ, 464, L119

Kormendy J., Bender R., Cornell M. E., 2011, Nature, 469, 374

Kormendy J., Drory N., Bender R., Cornell M. E., 2010, ApJ, 723, 54

Kormendy J., Kennicutt, Jr. R. C., 2004, ARA&A, 42, 603

Koss M., Mushotzky R., Veilleux S., Winter L. M., Baumgartner W., Tueller J., Gehrels N., Valencic L., 2011, ApJ, 739, 57

Kriek M. et al., 2010, ApJ, 722, L64

Labbé I. et al., 2005, ApJ, 624, L81

Lacerna I., Rodríguez-Puebla A., Avila-Reese V., Hernández-Toledo H. M., 2014, ApJ, 788, 29

Lahav O., Bridle S. L., Hobson M. P., Lasenby A. N., Sodré L., 2000, MNRAS, 315, L45

Lan T.-W., Ménard B., Mo H., 2016, MNRAS, 459, 3998

Larson R. B., Tinsley B. M., Caldwell C. N., 1980, ApJ, 237, 692

Lee G.-H., Woo J.-H., Lee M. G., Hwang H. S., Lee J. C., Sohn J., Lee J. H., 2012, ApJ, 750, 141

Lee S.-K., Ferguson H. C., Somerville R. S., Wiklind T., Giavalisco M., 2010, ApJ, 725, 1644

Lidman C. et al., 2013, MNRAS, 433, 825

Lin L. et al., 2010, ApJ, 718, 1158

Lin L.-H., Wang H.-H., Hsieh P.-Y., Taam R. E., Yang C.-C., Yen D. C. C., 2013, ApJ, 771, 8

Linde A. D., 1982, Physics Letters B, 116, 335

Lintott C. et al., 2011, MNRAS, 410, 166

Lintott C. J. et al., 2009, MNRAS, 399, 129

Lintott C. J. et al., 2008, MNRAS, 389, 1179

Liu F. S., Mao S., Deng Z. G., Xia X. Y., Wen Z. L., 2009, MNRAS, 396, 2003

Lotz J. M., Jonsson P., Cox T. J., Croton D., Primack J. R., Somerville R. S., Stewart K., 2011, ApJ, 742, 103

Lotz J. M., Jonsson P., Cox T. J., Primack J. R., 2008, MNRAS, 391, 1137

Lotz J. M., Primack J., Madau P., 2004, AJ, 128, 163

MacArthur L. A., Courteau S., Bell E., Holtzman J. A., 2004, ApJS, 152, 175

Maciejewski W., Teuben P. J., Sparke L. S., Stone J. M., 2002, MNRAS, 329, 502

Mackay D. J. C., 2003, Information Theory, Inference and Learning Algorithms. Cambridge University Press, p. 640

Madau P., Pozzetti L., Dickinson M., 1998, ApJ, 498, 106

Magorrian J. et al., 1998, AJ, 115, 2285

Maier C. et al., 2016, A&A, 590, A108

Malkan M. A., Gorjian V., Tam R., 1998, ApJS, 117, 25

Maraston C., 2005, MNRAS, 362, 799

Marconi A., Hunt L. K., 2003, ApJ, 589, L21

Martig M., Bournaud F., Croton D. J., Dekel A., Teyssier R., 2012, ApJ, 756, 26

Martin D. C. et al., 2005, ApJ, 619, L1

Martin D. C. et al., 2007, ApJS, 173, 342

Martini P., Weinberg D. H., 2001, ApJ, 547, 12

Masters K. L. et al., 2010a, MNRAS, 405, 783

Masters K. L. et al., 2010b, MNRAS, 404, 792

Masters K. L. et al., 2012, MNRAS, 424, 2180

Masters K. L. et al., 2011, MNRAS, 411, 2026

Mathur S., Fields D., Peterson B. M., Grupe D., 2012, ApJ, 754, 146

McConnell N. J., Ma C.-P., Gebhardt K., Wright S. A., Murphy J. D., Lauer T. R., Graham J. R., Richstone D. O., 2011, Nature, 480, 215

McDermid R. M. et al., 2015, MNRAS, 448, 3484

McGee S. L., Bower R. G., Balogh M. L., 2014, MNRAS, 442, L105

McIntosh D. H., Guo Y., Hertzberg J., Katz N., Mo H. J., van den Bosch F. C., Yang X., 2008, MNRAS, 388, 1537

McIntosh D. H. et al., 2014, MNRAS, 442, 533

McLure R. J., Dunlop J. S., 2001, MNRAS, 327, 199

McLure R. J., Kukula M. J., Dunlop J. S., Baum S. A., O'Dea C. P., Hughes D. H., 1999, MNRAS, 308, 377

Medling A. M. et al., 2015, ApJ, 803, 61

Melbourne J. et al., 2012, ApJ, 748, 47

Mendez A. J. et al., 2013, ApJ, 770, 40

Mendez A. J., Coil A. L., Lotz J., Salim S., Moustakas J., Simard L., 2011, ApJ, 736, 110

Merchán M., Zandivarez A., 2002, MNRAS, 335, 216

Merchán M. E., Zandivarez A., 2005, ApJ, 630, 759

Merritt D., Ferrarese L., 2001, MNRAS, 320, L30

Michel-Dansac L., Lambas D. G., Alonso M. S., Tissera P., 2008, MNRAS, 386, L82

Mihos J. C., Hernquist L., 1994, ApJ, 431, L9

Mihos J. C., Hernquist L., 1996, ApJ, 464, 641

Miller C. J., Nichol R. C., Gómez P. L., Hopkins A. M., Bernardi M., 2003, ApJ, 597, 142

Miller C. J. et al., 2005, AJ, 130, 968

Miner J., Rose J. A., Cecil G., 2011, ApJ, 727, L15

Mo H., van den Bosch F. C., White S., 2010, Galaxy Formation and Evolution. Cambridge University Press

Montuori M., Di Matteo P., Lehnert M. D., Combes F., Semelin B., 2010, A&A, 518, A56

Moore B., Katz N., Lake G., Dressler A., Oemler A., 1996, Nature, 379, 613616

Morgan W. W., 1958, PASP, 70, 364

Muñoz-Cuartas J. C., Müller V., 2012, MNRAS, 423, 1583

Muldrew S. I. et al., 2012, MNRAS, 419, 2670

Muzzin A. et al., 2013, ApJ, 777, 18

Naab T. et al., 2014, MNRAS, 444, 3357

Nair P. B., Abraham R. G., 2010a, ApJS, 186, 427

Nair P. B., Abraham R. G., 2010b, ApJL, 714, L260L264

Navarro J. F., Frenk C. S., White S. D. M., 1995, MNRAS, 275, 56

Nelson C. H., Green R. F., Bower G., Gebhardt K., Weistrop D., 2004, ApJ, 615, 652

Netzer H., 1990, AGN Emission Lines, Springer Berlin Heidelberg, Berlin, Heidelberg, pp. 57–158

Netzer H., 2015, ARA&A, 53, 365

Nipoti C., Londrillo P., Ciotti L., 2003, MNRAS, 342, 501

Noeske K. G. et al., 2007, ApJ, 660, L43

Noguchi M., 1988, A&A, 203, 259

Nulsen P. E. J., 1982, MNRAS, 198, 1007

Oemler, Jr. A., Dressler A., Gladders M. G., Fritz J., Poggianti B. M., Vulcani B., Abramson L., 2013, ApJ, 770, 63

Oh K., Sarzi M., Schawinski K., Yi S. K., 2011, ApJS, 195, 13

Oh K., Yi S. K., Schawinski K., Koss M., Trakhtenbrot B., Soto K., 2015, ApJS, 219, 1

Oman K. A., Hudson M. J., 2016, MNRAS, 463, 3083

Onken C. A., Ferrarese L., Merritt D., Peterson B. M., Pogge R. W., Vestergaard M., Wandel A., 2004, ApJ, 615, 645

Paccagnella A. et al., 2016, ApJ, 816, L25

Padmanabhan N. et al., 2008, ApJ, 674, 1217

Pan Z., Li J., Lin W., Wang J., Fan L., Kong X., 2015, ApJ, 804, L42

Pasquali A., Gallazzi A., Fontanot F., van den Bosch F. C., De Lucia G., Mo H. J., Yang X., 2010, MNRAS, 407, 937

Pasquali A., Gallazzi A., van den Bosch F. C., 2012, MNRAS, 425, 273

Pastrav B. A., Popescu C. C., Tuffs R. J., Sansom A. E., 2013, A&A, 553, A80

Patel S. G., Holden B. P., Kelson D. D., Franx M., van der Wel A., Illingworth G. D., 2012, ApJ, 748, L27

Pawlik M. M., Wild V., Walcher C. J., Johansson P. H., Villforth C., Rowlands K., Mendez-Abreu J., Hewlett T., 2016, MNRAS, 456, 3032

Peng C. Y., 2007, ApJ, 671, 1098

Peng C. Y., Ho L. C., Impey C. D., Rix H.-W., 2002, AJ, 124, 266

Peng C. Y., Ho L. C., Impey C. D., Rix H.-W., 2010, AJ, 139, 2097

Peng Y., Maiolino R., Cochrane R., 2015, Nature, 521, 192

Peng Y.-j., Lilly S. J., Renzini A., Carollo M., 2012, ApJ, 757, 4

Penny S. J. et al., 2016, MNRAS, 462, 3955

Pérez I., Sánchez-Blázquez P., 2011, A&A, 529, A64

Peterson B. M., 2001, in Astronomical Society of the Pacific Conference Series, Vol. 224, Probing the Physics of Active Galactic Nuclei, Peterson B. M., Pogge R. W., Polidan R. S., eds., p. 1

Peterson B. M., 2014, Space Sci. Rev., 183, 253

Phillips J. I., Wheeler C., Cooper M. C., Boylan-Kolchin M., Bullock J. S., Tollerud E., 2015, MNRAS, 447, 698

Pierce C. M. et al., 2007, ApJ, 660, L19

Pimbblet K. A., Shabala S. S., Haines C. P., Fraser-McKelvie A., Floyd D. J. E., 2013, MNRAS, 429, 1827

Pimbblet K. A., Smail I., Kodama T., Couch W. J., Edge A. C., Zabludoff A. I., O'Hely E., 2002, MNRAS, 331, 333

Pipino A., Matteucci F., 2008, A&A, 486, 763

Planck Collaboration, 2016, A&A, 594, A13

Poggianti B. M., Smail I., Dressler A., Couch W. J., Barger A. J., Butcher H., Ellis R. S., Oemler, Jr. A., 1999, ApJ, 518, 576

Ponman T. J., Allan D. J., Jones L. R., Merrifield M., McHardy I. M., Lehto H. J., Luppino G. A., 1994, Nature, 369, 462

Pontzen A., Tremmel M., Roth N., Peiris H. V., Saintonge A., Volonteri M., Quinn T., Governato F., 2016, ArXiv e-prints, 1607.02507

Postman M., 2002, in Astronomical Society of the Pacific Conference Series, Vol. 268, Tracing Cosmic Evolution with Galaxy Clusters, Borgani S., Mezzetti M., Valdarnini R., eds., p. 3

Postman M. et al., 2005, ApJ, 623, 721

Powell L. C., Slyz A., Devriendt J., 2011, MNRAS, 414, 3671

Pracy M. B. et al., 2013, MNRAS, 432, 3131

Press W. H., Schechter P., 1974, ApJ, 187, 425

Ravindranath S. et al., 2004, ApJ, 604, L9

Regan M. W., Teuben P. J., 2004, ApJ, 600, 595

Richards G. T. et al., 2006, ApJS, 166, 470

Roberts I. D., Parker L. C., Karunakaran A., 2016, MNRAS, 455, 3628

Robertson B., Bullock J. S., Cox T. J., Di Matteo T., Hernquist L., Springel V., Yoshida N., 2006, ApJ, 645, 986

Robotham A. S. G. et al., 2011, MNRAS, 416, 2640

Rupke D. S. N., Kewley L. J., Barnes J. E., 2010, ApJ, 710, L156

Sánchez S. F. et al., 2004, ApJ, 614, 586

Saintonge A. et al., 2012, ApJ, 758, 73

Sakamoto K., 1996, ApJ, 471, 173

Salim S. et al., 2007, ApJS, 173, 267

Salpeter E. E., 1955, ApJ, 121, 161

Sánchez S. F. et al., 2012, A&A, 538, A8

Sánchez-Blázquez P., Ocvirk P., Gibson B. K., Pérez I., Peletier R. F., 2011, MNRAS, 415, 709

Sanders D. B., Soifer B. T., Elias J. H., Madore B. F., Matthews K., Neugebauer G., Scoville N. Z., 1988, ApJ, 325, 74

Sarzi M. et al., 2006, MNRAS, 366, 1151

Sarzi M. et al., 2010, MNRAS, 402, 2187

Schaefer A. L. et al., 2017, MNRAS, 464, 121

Schawinski K., Koss M., Berney S., Sartori L. F., 2015, MNRAS, 451, 2517

Schawinski K., Thomas D., Sarzi M., Maraston C., Kaviraj S., Joo S.-J., Yi S. K., Silk J., 2007a, MNRAS, 382, 1415

Schawinski K., Thomas D., Sarzi M., Maraston C., Kaviraj S., Joo S.-J., Yi S. K., Silk J., 2007b, MNRAS, 382, 1415

Schawinski K., Treister E., Urry C. M., Cardamone C. N., Simmons B., Yi S. K., 2011, ApJ, 727, L31+

Schawinski K. et al., 2014, MNRAS, 440, 889

Schawinski K. et al., 2010, ApJ, 711, 284

Schawinski K., Virani S., Simmons B., Urry C. M., Treister E., Kaviraj S., Kushkuley B., 2009, ApJ, 692, L19

Schiminovich D. et al., 2007, ApJS, 173, 315

Schlegel D. J., Finkbeiner D. P., Davis M., 1998, ApJ, 500, 525

Schmidt M., 1959, ApJ, 129, 243

Scoville N. et al., 2007, ApJS, 172, 1

Scudder J. M., Ellison S. L., Torrey P., Patton D. R., Mendel J. T., 2012, MNRAS, 426, 549

Searle L., Sargent W. L. W., Bagnuolo W. G., 1973, ApJ, 179, 427

Sérsic J. L., 1968, Atlas de galaxias australes. Cordoba, Argentina: Observatorio Astronomico, 1968

Shankar F. et al., 2014, MNRAS, 439, 3189

Shen J., Vanden Berk D. E., Schneider D. P., Hall P. B., 2008, AJ, 135, 928

Shen Y. et al., 2011, ApJS, 194, 45

Sheth K., Melbourne J., Elmegreen D. M., Elmegreen B. G., Athanassoula E., Abraham R. G., Weiner B. J., 2012, ApJ, 758, 136

Sheth K., Vogel S. N., Regan M. W., Thornley M. D., Teuben P. J., 2005, ApJ, 632, 217

Shimasaku K. et al., 2001, AJ, 122, 1238

Shimizu M., Kitayama T., Sasaki S., Suto Y., 2003, ApJ, 590, 197

Silk J., Mamon G. A., 2012, Research in Astronomy and Astrophysics, 12, 917

Silk J., Rees M. J., 1998, A&A, 331, L1

Simard L., 1998, in Astronomical Society of the Pacific Conference Series, Vol. 145, Astronomical Data Analysis Software and Systems VII, Albrecht R., Hook R. N., Bushouse H. A., eds., p. 108

Simard L., Mendel J. T., Patton D. R., Ellison S. L., McConnachie A. W., 2011, ApJS, 196, 11

Simha V., Weinberg D. H., Conroy C., Dave R., Fardal M., Katz N., Oppenheimer B. D., 2014, ArXiv e-prints, 1404.0402

Simmons B. D. et al., 2013, MNRAS, 429, 2199

Simmons B. D. et al., 2016, ArXiv e-prints, 1610.03070

Simmons B. D., Urry C. M., 2008, ApJ, 683, 644

Simmons B. D., Van Duyne J., Urry C. M., Treister E., Koekemoer A. M., Grogin N. A., The GOODS Team, 2011, ApJ, 734, 121

Singh R. et al., 2013, A&A, 558, A43

Sivia D., Skilling J., 2006, Data Analysis: A Bayesian Tutorial, Oxford science publications. OUP Oxford

Skibba R. A. et al., 2009, MNRAS, 399, 966

Skibba R. A. et al., 2012, MNRAS, 423, 1485

Skrutskie M. F. et al., 2006, AJ, 131, 1163

Smail I., Dressler A., Couch W. J., Ellis R. S., Oemler, Jr. A., Butcher H., Sharples R. M., 1997, ApJS, 110, 213

Smethurst R. J. et al., 2016, MNRAS, 463, 2986

Smethurst R. J. et al., 2015, MNRAS, 450, 435

Smith D. J. B., Hayward C. C., 2015, MNRAS, 453, 1597

Smith R. et al., 2015a, MNRAS, 454, 2502

Smith R. J., Lucey J. R., Conroy C., 2015b, MNRAS, 449, 3441

Snyder G. F., Cox T. J., Hayward C. C., Hernquist L., Jonsson P., 2011, ApJ, 741, 77

Somerville R. S., Hopkins P. F., Cox T. J., Robertson B. E., Hernquist L., 2008, MNRAS, 391, 481

Somerville R. S., Primack J. R., Faber S. M., 2001, MNRAS, 320, 504

Sparre M., Springel V., 2016, ArXiv e-prints, 1610.03850

Springel V., Di Matteo T., Hernquist L., 2005, ApJ, 620, L79

Starobinsky A. A., 1982, Physics Letters B, 117, 175

Stern D. et al., 2005, ApJ, 631, 163

Stott J. P. et al., 2016, MNRAS, 457, 1888

Strateva I. et al., 2001, AJ, 122, 1861

Tago E., Einasto J., Saar E., Tempel E., Einasto M., Vennik J., Müller V., 2008, A&A, 479, 927

Tago E., Saar E., Tempel E., Einasto J., Einasto M., Nurmi P., Heinämäki P., 2010, A&A, 514, A102

Taranu D., Dubinski J., Yee H. K. C., 2015, ApJ, 803, 78

Tempel E. et al., 2014, A&A, 566, A1

Thomas D., Maraston C., Schawinski K., Sarzi M., Silk J., 2010, MNRAS, 404, 1775

Tinker J., Wetzel A., Conroy C., 2011, ArXiv e-prints, 1107.5046

Tinsley B. M., 1972, A&A, 20, 383

Tojeiro R., Heavens A. F., Jimenez R., Panter B., 2007, MNRAS, 381, 1252

Tojeiro R. et al., 2013, MNRAS, 432, 359

Tonini C., Mutch S. J., Croton D. J., Wyithe J. S. B., 2016, MNRAS, 459, 4109

Toomre A., 1977, in Evolution of Galaxies and Stellar Populations, B. M. Tinsley & R. B. G. Larson D. Campbell, ed., p. 401

Toomre A., Toomre J., 1972, ApJ, 178, 623

Torrey P., Cox T. J., Kewley L., Hernquist L., 2012, ApJ, 746, 108

Tortora C., Antonuccio-Delogu V., Kaviraj S., Silk J., Romeo A. D., Becciani U., 2009, MNRAS, 396, 61

Treister E., Schawinski K., Urry C. M., Simmons B. D., 2012, ApJ, 758, L39

Tremonti C. A. et al., 2004, ApJ, 613, 898

Tucker D. L. et al., 2000, ApJS, 130, 237

Turner E. L., Aarseth S. J., Blanchard N. T., Mathieu R. D., Gott, III J. R., 1979, ApJ, 228, 684

Urry C. M., Padovani P., 1995, PASP, 107, 803

Urry C. M., Scarpa R., O'Dowd M., Falomo R., Pesce J. E., Treves A., 2000, ApJ, 532, 816

van de Voort F., Bahé Y. M., Bower R. G., Correa C. A., Crain R. A., Schaye J., Theuns T., 2016, ArXiv e-prints, 1611.03870

van der Wel A., Rix H.-W., Holden B. P., Bell E. F., Robaina A. R., 2009, ApJ, 706, L120

van Dokkum P. G., 2008, ApJ, 674, 29

Varela J., Moles M., Márquez I., Galletta G., Masegosa J., Bettoni D., 2004, A&A, 420, 873

Vázquez G. A., Leitherer C., 2005, ApJ, 621, 695

Veilleux S., Kim D.-C., Sanders D. B., 2002, ApJS, 143, 315

Vika M., Vulcani B., Bamford S. P., Häußler B., Rojas A. L., 2015, A&A, 577, A97

Vogelsberger M. et al., 2014, MNRAS, 444, 1518

Voges W. et al., 1999, A&A, 349, 389

Volonteri M., Natarajan P., Gültekin K., 2011, ApJ, 737, 50

Walker I. R., Mihos J. C., Hernquist L., 1996, ApJ, 460, 121

Wang W., Sales L. V., Henriques B. M. B., White S. D. M., 2014, MNRAS, 442, 1363

Weigel A. K., Schawinski K., Bruderer C., 2016, MNRAS, 459, 2150

Weiner B. J. et al., 2006, ApJ, 653, 1049

Weinmann S. M., van den Bosch F. C., Yang X., Mo H. J., 2006, MNRAS, 366, 2

Wetzel A. R., Tinker J. L., Conroy C., van den Bosch F. C., 2013, MNRAS, 432, 336

Wetzel A. R., Tinker J. L., Conroy C., van den Bosch F. C., 2014, MNRAS, 439, 2687

Whitaker K. E. et al., 2016, ArXiv e-prints, 1607.03107

White S. D. M., Rees M. J., 1978, MNRAS, 183, 341

Wild V., Almaini O., Dunlop J., Simpson C., Rowlands K., Bowler R., Maltby D., McLure R., 2016, MNRAS, 463, 832

Wild V., Heckman T., Charlot S., 2010, MNRAS, 405, 933

Wild V., Walcher C. J., Johansson P. H., Tresse L., Charlot S., Pollo A., Le Fèvre O., de Ravel L., 2009, MNRAS, 395, 144

Wilkinson D. M., 2015, PhD thesis, University of Portsmouth

Willett K. W. et al., 2016, ArXiv e-prints, 1610.03068

Willett K. W. et al., 2013, MNRAS, 435, 2835

Williams R. J., Quadri R. F., Franx M., van Dokkum P., Labbé I., 2009, ApJ, 691, 1879

Willmer C. N. A. et al., 2006, ApJ, 647, 853

Wong O. I. et al., 2012, MNRAS, 420, 1684

Woo J., Carollo C. M., Faber S. M., Dekel A., Tacchella S., 2016, ArXiv e-prints, 1607.06091

Worthey G., 1994, ApJS, 95, 107

Wright E. L. et al., 2010, AJ, 140, 1868

Wuyts S. et al., 2007, ApJ, 655, 51

Wyder T. K. et al., 2007, ApJS, 173, 293

Xiao T., Barth A. J., Greene J. E., Ho L. C., Bentz M. C., Ludwig R. R., Jiang Y., 2011, ApJ, 739, 28

Yan R., Blanton M. R., 2012, ApJ, 747, 61

Yang X., Mo H. J., van den Bosch F. C., 2009, ApJ, 695, 900

Yang X., Mo H. J., van den Bosch F. C., Jing Y. P., 2005, MNRAS, 356, 1293

Yang X., Mo H. J., van den Bosch F. C., Pasquali A., Li C., Barden M., 2007, ApJ, 671, 153

Yang Y., Zabludoff A. I., Zaritsky D., Mihos J. C., 2008, ApJ, 688, 945

Yesuf H. M., Faber S. M., Trump J. R., Koo D. C., Fang J. J., Liu F. S., Wild V., Hayward C. C., 2014, ApJ, 792, 84

York D. G. et al., 2000, AJ, 120, 1579

Yu Q., Tremaine S., 2002, MNRAS, 335, 965

Zabludoff A. I., Zaritsky D., Lin H., Tucker D., Hashimoto Y., Shectman S. A., Oemler A., Kirshner R. P., 1996, ApJ, 466, 104

Zinn P.-C., Middelberg E., Norris R. P., Dettmar R.-J., 2013, ApJ, 774, 66

Zurita A., Relaño M., Beckman J. E., Knapen J. H., 2004, A&A, 413, 73

Zwicky F., 1938, PASP, 50, 218

Zwicky F., 1952, PASP, 64, 247